



UNIVERSITAT
POLITÈCNICA
DE VALÈNCIA

UNIVERSITAT POLITÈCNICA DE VALÈNCIA

Department of Mechanical and Materials Engineering

PhD THESIS

Development of innovative methodologies to reduce
railway rolling noise through Genetic
Algorithm-based shape optimization techniques

Presented by: Xavier Garcia Andrés

Supervised by: Prof. Francisco David Denia Guzmán

Dr. José Martínez Casas

Valencia, February, 2021

PhD THESIS

**Development of innovative methodologies to reduce
railway rolling noise through Genetic
Algorithm-based shape optimization techniques**

for the degree of

Doctor in Engineering and Industrial Production

presented by

Xavier Garcia Andrés

at the

Department of Mechanical and Materials Engineering

Universitat Politècnica de València

Supervised by

Prof. Francisco David Denia Guzmán

Dr. José Martínez Casas

Valencia, February, 2021

PhD THESIS

**DEVELOPMENT OF INNOVATIVE METHODOLOGIES TO
REDUCE RAILWAY ROLLING NOISE THROUGH GENETIC
ALGORITHM-BASED SHAPE OPTIMIZATION TECHNIQUES**

Presented by: Xavier Garcia Andrés

Supervised by: Prof. Francisco David Denia Guzmán

Dr. José Martínez Casas

EXAMINERS

Prof. Jorge Patricio Arenas Bermúdez

Dr. Luís Manuel Cortesão Godinho

Dr. Emilio Velasco Sánchez

QUALIFYING TRIBUNAL

PRESIDENT: Prof. Francisco Javier Fuenmayor Fernández

VOCAL: Prof. Jorge Patricio Arenas Bermúdez

SECRETARY: Prof. Jordi Romeu Garbí

Valencia, February, 2021

This Thesis has been supported by the Agencia Estatal de Investigación and the European Regional Development Fund (projects TRA2013-45596-C2-1-R and TRA2017-84701-R).



Abstract

Rolling noise phenomenon is produced due to the wheel/track interaction and induced by the small unevenness present in their surfaces. Such unevenness, known as “roughness”, causes that vibrations arise in both the wheel and track when the train passes by with a certain speed, that consequently leads to the appearance of acoustic radiation. This kind of noise is one of the most relevant sources of annoyance and the principal focus of the railway acoustic pollution produced by trains operating through highly populated urban regions.

Thus, the main goal of the present Thesis is the development of a comprehensive methodology to achieve suitable railway wheel designs through the use of Genetic Algorithms (GAs) with the aim of minimizing the associated rolling noise.

When developing the aforementioned optimization algorithms, the Finite Element Method (FEM) is combined with the geometric parametrization of the different wheel design typologies analysed, described as a function of those parameters most relevant for the current research. In order to describe the dynamic behaviour of each component involved in the wheel/track interaction, use is made of linearised models in the frequency domain capable of solving the whole coupled dynamic response from the corresponding cross-section meshes. Subsequent derivation of the radiated sound power from the dynamic information is carried out by applying a semi-analytical formulation that allows for the wheel acoustic efficiency computation, on one hand, and by making use of an Equivalent Sources Model (ESM) in the track, on the other hand. Be-

sides, such theoretical development is validated with the reference commercial software in the field, TWINS, on which it is based.

Throughout the optimization procedures, a fatigue analysis is performed on every wheel design considered to assure structural feasibility, that acts as a “death penalty” constraint in the algorithm. Furthermore, a modal identification procedure is developed, which allows to characterize modeshapes and to classify them according to their number of nodal diameters and circumferences. Then, two different formulations of the objective function are explored: one focused on directly reducing radiated noise, named $L_{A,W}$ -min; and another centred on decreasing rolling noise by maximizing the average natural frequency of the modeshapes, called NF-max. Hence, in the $L_{A,W}$ -min methodology, radiated noise is directly reduced by minimizing the sum in energy of the wheel Sound poWer Level (SWL) expressed in dB(A). For the NF-max case, maximizing natural frequencies shifts them to frequency regions where the roughness amplitude content is lower, consequently lowering rolling noise.

In the usage of such optimization tools, different approaches are considered in order to modify wheel geometry: the inclusion of perforation schemes, using as a base wheel both a curved and a straight web shape; and the variation of its cross-sectional shape, setting the radius as a constant value in one case and using it as an optimization parameter in another. Moreover, the influence on the noise of changing the rail geometric and track viscoelastic properties is also studied.

As a result of the present Thesis, several quieter models of railway wheels have been achieved, with rolling noise reductions of up to 5 dB(A). When the whole railway system with all the components is considered, improvements in the radiated sound power remain achieved with the resulting wheel designs. Besides, correlations between maximization of natural frequencies and SWL mitigation are analysed, establishing the NF-max as a suitable methodology for cases when computational efficiency is prioritized. The sensitivity of the problem to selected design domains and the suitability of the use of GAs are also studied with the obtention of Response Surfaces (RSs) for the geometric parameters used. Additionally, correlations are established between the variation of the geometric parameters and the decrease in the associated acoustic radiation, while the shifting of the modeshapes along the frequency domain is proposed as a physical mechanism responsible of the observed sound power decrease.

Resum

El soroll de rodament és un fenomen causat per la interacció entre la roda i el carril i induït per les xicotetes irregularitats presents a les seues superfícies. Aquestes irregularitats, conegudes amb el nom de “rugositat”, provoquen que es genere una vibració tant a la roda com al carril en circular el tren a una certa velocitat, el que conseqüentment du a l’aparició de radiació acústica. Açò conforma una de les fonts de molèsties més rellevants i el principal origen de la contaminació acústica generada pels trens al seu pas per regions urbanes densament poblades.

Així, l’objectiu d’aquesta Tesi és el desenvolupament d’una metodologia integral per a l’obtenció de dissenys de roda viables mitjançant l’ús d’Algoritmes Genètics (AG) amb la finalitat de minimitzar el soroll de rodament associat.

Al desenvolupar els esmentats algoritmes d’optimització, el Mètode d’Elements Finites (MEF) es combina amb la parametrització geomètrica de les diferents tipologies de disseny de roda analitzades, descrites en funció d’aquells paràmetres més rellevants per a aquesta investigació. Amb la finalitat de descriure el comportament dinàmic de cadascun dels components involucrats en la interacció roda/carril, es fa ús de models linealitzats en el domini de la freqüència, capaços de resoldre la dinàmica completa del sistema a partir les corresponents malles de secció transversal. La subseqüent obtenció de la potència acústica radiada a partir de la informació de la dinàmica es du a terme mitjançant la utilització d’una formulació semi-analítica per al càlcul de l’eficiència acústica de la roda, per una banda, i a l’ús d’un Model de Fonts Equivalents (MFE) amb el carril, per l’altra. El desenvolupament teòric, a més a més, s’ha validat

amb el software comercial de referència al camp d'investigació, TWINS, en el qual es basa.

Al llarg dels procediments d'optimització, es realitza una anàlisi de fatiga a cada disseny de roda considerat amb la finalitat d'assegurar la seua viabilitat estructural, el que actua com una restricció de “pena de mort” en l'algoritme. A més a més, s'ha desenvolupat un procediment d'identificació modal que permet caracteritzar els modes de vibració i classificar-los d'acord al seu número de diàmetres i circumferències nodals. Seguidament, s'exploren dos formulacions diferents de la funció objectiu: una centrada en reduir directament el soroll radiat, anomenada $L_{A,W}$ -min; i altra centrada en disminuir el soroll de rodament maximitzant la mitja de les freqüències naturals dels modes de vibració, coneguda com NF-max. D'aquesta manera, en la metodologia $L_{A,W}$ -min, el soroll radiat es redueix directament mitjançant la minimització de la suma en energia del nivell de potència acústica expressat en dB(A). Per al cas de NF-max, maximitzar les freqüències naturals les desplaça a regions de freqüència on l'amplitud de rugositat és menor, rebaixant en conseqüència el soroll de rodament.

Durant l'ús d'aquestes ferramentes d'optimització es consideren diverses aproximacions per modificar la geometria de la roda: la inclusió d'esquemes de perforació, utilitzant com a rodes base tant una forma de vel corba com una de recta; i la modificació de la forma de la seua secció transversal, establint el radi com un valor fixe en un cas i utilitzant-lo com un paràmetre d'optimització més en l'altre. A més a més, s'ha estudiat la influència en el soroll de la variació de les propietats geomètriques del carril i viscoelàstiques de la via.

Com a resultat d'aquesta Tesi s'han aconseguit diversos models de roda ferroviària més silenciosos, amb reduccions en el soroll de rodament de fins a 5 dB(A). Quan es considera el sistema ferroviari complet amb tots els seus components, es segueixen aconseguint millores en la potencia acústica radiada amb els dissenys de roda resultants. A més a més, s'analitzen les correlacions entre la maximització de les freqüències naturals i l'atenuació del nivell de potencia acústica, establint NF-max com una metodologia adequada pels casos en que es prioritza l'eficiència computacional. La sensibilitat del problema als espais de disseny escollits i l'adequació de l'ús de AG s'estudia també mitjançant l'obtenció de Superfícies de Resposta (SRs) per als paràmetres geomètrics utilitzats. Adicionalment, s'han establert relacions entre la variació dels paràmetres geomètrics i la disminució en la radiació acústica associada, així com s'ha proposat la reubicació dels modes de vibració al voltant de l'espectre en freqüència com a mecanisme físic responsable de les reduccions en potència acústica observades.

Resumen

El ruido de rodadura es un fenómeno producido debido a la interacción entre la rueda y el carril e inducido por las pequeñas irregularidades existentes en la superficie de ambos. Dichas irregularidades, conocidas como “rugosidad”, provocan que se genere una vibración tanto en la rueda como el carril cuando el tren circula a una cierta velocidad, lo que consecuentemente lleva a la aparición de radiación acústica. Esto conforma una de las fuentes de molestias más relevantes y principal origen de la contaminación acústica producida por los trenes al circular por regiones urbanas densamente pobladas.

Así, el objetivo de esta Tesis es el desarrollo de una metodología integral para la obtención de diseños de rueda viables mediante el uso de Algoritmos Genéticos (AG) con la finalidad de minimizar el ruido de rodadura asociado.

Al desarrollar los mencionados algoritmos de optimización, el Método de Elementos Finitos (MEF) se combina con la parametrización geométrica de las diferentes tipologías de diseño de rueda analizadas, descritas en función de aquellos parámetros más relevantes para la presente investigación. A fin de describir el comportamiento dinámico de cada uno de los componentes implicados en la interacción rueda/carril, se hace uso de modelos linealizados en el dominio de la frecuencia, capaces de resolver la dinámica completa del sistema a partir de las correspondientes mallas de la sección transversal. La subsiguiente obtención de la potencia acústica radiada a partir de la información de la dinámica se lleva a cabo mediante el empleo de una formulación semi-analítica para el cálculo de la eficiencia acústica de la rueda, por un lado, y al uso de un Modelo de Fuentes Equivalentes (MFE) en el carril por el otro. El

desarrollo teórico, además, es validado con el software comercial de referencia en el campo de investigación, TWINS, en el cual se basa.

A lo largo de los procedimientos de optimización, se realiza un análisis de fatiga en cada diseño de rueda considerado con el fin de asegurar su viabilidad estructural, lo que actúa como una restricción de “pena de muerte” en el algoritmo. Además, se desarrolla un procedimiento de identificación modal que permite caracterizar los modos de vibración y clasificarlos según su número de diámetros y circunferencias nodales. Seguidamente, se exploran dos formulaciones diferentes de la función objetivo: una centrada en reducir directamente el ruido radiado, llamada $L_{A,W}$ -min; i otra centrada en disminuir el ruido de rodadura maximizando la media de las frecuencias naturales de los modos de vibración, conocida como NF-max. De este modo, en la metodología $L_{A,W}$ -min, el ruido radiado se reduce directamente mediante la minimización de la suma en energía del nivel de potencia acústica expresado en dB(A). Para el caso de NF-max, maximizar las frecuencias naturales las desplaza a regiones de frecuencia donde la amplitud de rugosidad es menor, rebajando en consecuencia el ruido de rodadura.

Durante el uso de estas herramientas de optimización se consideran diversas aproximaciones para modificar la geometría de la rueda: la inclusión de esquemas de perforación, usando como ruedas base tanto una forma de velo curva como una recta; y la modificación de la forma de su sección transversal, estableciendo el radio como un valor fijo en un caso y usándolo como un parámetro de optimización en otro. Además, también se ha estudiado la influencia en el ruido de la variación de las propiedades geométricas del carril y viscoelásticas de la vía.

Como resultado de esta Tesis se han conseguido diversos modelos más silenciosos de rueda ferroviaria, con reducciones en el ruido de rodadura de hasta 5 dB(A). Cuando se considera el sistema ferroviario completo con todos sus componentes, se siguen consiguiendo mejoras en la potencia acústica radiada con los diseños de rueda resultantes. Además, se analizan las correlaciones entre la maximización de las frecuencias naturales y la atenuación del nivel de potencia acústica, estableciendo NF-max como una metodología adecuada para los casos en que se priorice la eficiencia computacional. La sensibilidad del problema a los espacios de diseño seleccionados y la adecuación del uso de AG se estudian también con la obtención de Superficies de Respuesta (SR) para los parámetros geométricos utilizados. Adicionalmente, se han establecido relaciones entre la variación de los parámetros geométricos y la disminución en la radiación acústica asociada, así como se ha propuesto la reubicación de

los modos de vibración a lo largo del espectro en frecuencia como mecanismo físico responsable de las reducciones de potencia acústica observadas.

Agraïments

En primer lloc, m'agradaria expressar el meu més sincer agraïment als meus directors de Tesi, Francisco D. Denia i José Martínez. Paco y José, gracias por todas vuestras aportaciones y la exhaustiva revisión. Sin vuestra guía y ayuda nunca habría podido llevar a buen puerto este trabajo.

També a tota la gent del DIMM i, en especial, a tots els companys de la sala de becaris, tant els que estan com els que passaren. Ricardo, Norberto, Marta, Borja, David, Héctor, Raquel, Jorge Gutiérrez, Jorge Gómez, Víctor, Jaime, Santi, José Manuel, Vicente, Luca, Eva, Juan Tudela, José Vicente, Edu, Sandra, Estivaliz, Onofre, Camila: sense la vostra companyia i el vostre suport les innumerables hores passades a la sala hagueren paregut més llargues i aquests últims 5 anys hagueren sigut menys feliços. Moltes gràcies per estar sempre presents quan se us ha necessitat. A Jaime per la portada i els consells pel que fa al disseny (and thanks Jeanne for the finishing touches). És impossible no mencionar a Marga i a Eva Vázquez, que fan fàcil el difícil; moltes gràcies per l'ajuda, la paciència i les explicacions cada vegada que he necessitat fer algun tràmit. I que dir de Fede, cada volta que la informàtica ha fallat, ací has estat tu, sempre disposat a ajudar. Sense tu ja fa temps que la sala de becaris haguera col·lapsat!

No puc deixar passar l'oportunitat de destacar la inestimable ajuda de Jorge i Víctor. Han sigut moltes hores de compartir faena, discutir i interpretar resultats i explicacions obtuses. Aquesta Tesi també és en part vostra.

I would also never forget the time spent at the University of Southampton. Ander, Niko, Thanasis, Angelis, Felipe, Anaïs, Reuben, Domenico, Simone, you made the city shine. It was a pleasure to meet you. Gràcies a Luis Baeza per acollir-me allí i pel seu acompanyament durant eixe temps.

D'altra banda, no tot en la vida es redueix a la universitat. Han sigut 5 anys molt intensos en què he tingut molt bons amics i amigues al meu costat. El vostre suport ha sigut fonamental, tant en les penes com les alegries. Sou imprescindible. A més a més, tinc la sort de tindre una família increïble que sempre s'ha mostrat disposada a ajudar-me en el que fera falta. En especial els meus pares, qui sempre han sigut els meus referents en aquesta vida. Tot el que soc avui dia és gràcies a vosaltres, sou els millors pares que podria haver tingut. Tampoc m'oblido del tio Lluís, qui ha exercit de mentor en tot aquest viatge, des que comencí els estudis universitaris fins a l'actualitat. Sense la teua saviesa i consell mai haguera arribat tan lluny. També dedicar-li un sentit record a la iaia, qui de segur estaria orgullosa de veure com el seu net segueix la tradició familiar.

Per últim, moltes gràcies Anna. Per estar sempre al meu costat. Per donar-me suport quan més ho he necessitat. Per ser la meua companya de vida. Per ser tu.

Contents

Abstract	iii
Resum	iv
Resumen	vii
Contents	xiii
List of acronyms	xvii
List of symbols	xix
1 Introduction	1
1.1 Motivation and background	1
1.2 Objectives.	2
1.3 Organization and development of the Thesis.	3

2	Acoustic characterization of wheel and track rolling noise	5
2.1	Introduction	5
2.2	State of the art	6
2.2.1	Rolling noise	6
2.2.1.1	Studying wheel behaviour in rolling noise	8
2.2.1.2	Studying track behaviour in rolling noise	11
2.2.1.3	Wheel/track interaction and contact	15
2.2.1.4	Rolling noise comprehensive modelling: TWINS	18
2.2.1.5	Rolling noise distribution among sources	20
2.2.2	Tackling rolling noise: mitigation measures	21
2.2.3	Tackling rolling noise: optimization techniques in the search for quieter trains	28
2.2.4	Beyond rolling noise: additional noise sources	30
2.2.4.1	Squeal noise	30
2.2.4.2	Aerodynamic noise	31
2.2.4.3	Bridge noise	31
2.3	Wheel dynamic model	32
2.3.1	Railway wheel characterization	32
2.3.2	Wheel receptance function	33
2.3.3	Wheel response in the frequency domain	34
2.3.4	Wheel response in the time domain: simplified formulation	37
2.4	Track dynamic model	38
2.4.1	Timoshenko beam	39
2.4.2	Rail receptance function	42
2.4.3	Deformable track cross-section model	44
2.4.4	Rail response	51
2.5	Wheel/track interaction model	52
2.5.1	The contact patch	52
2.5.2	Contact receptance function	55
2.5.3	Roughness filter	57
2.6	Sound power radiation	57
2.6.1	Wheel sound power	58
2.6.1.1	Wheel radiation efficiencies	60
2.6.1.2	Wheel noise in the three-dimensional case	62

2.6.2	Track sound power	63
2.6.2.1	Contribution of the rail	63
2.6.2.2	Contribution of the sleeper.	66
2.6.2.3	Equivalent Sources Model	66
3	Wheel shape optimization procedures for rolling noise minimization	71
3.1	Introduction	71
3.2	Genetic Algorithms	72
3.2.1	Theoretical foundations	73
3.2.2	GA operators.	75
3.2.3	Constraint-handling in GAs	76
3.3	Optimization algorithms: from the general methodology to the specificities of each procedure	78
3.3.1	Perforation scheme optimization algorithm.	80
3.3.2	Wheel shape optimization algorithm.	81
3.3.3	Preliminary approach to the track shape influence on rolling noise.	82
3.4	High-cycle fatigue analysis.	83
3.5	Geometry parametrization of wheel shapes	86
3.5.1	Finite Element model for the perforation scheme	87
3.5.2	Finite Element model for the railway wheel cross-section	88
3.5.2.1	Geometry parametrization	89
3.5.2.2	Axisymmetric elements	90
3.6	Modal identification and modeshape characterization	92
3.6.1	Nodal diameters and modal amplitudes.	93
3.6.2	Displacement of the contact point	96
3.6.3	Nodal circumferences	97
3.6.4	Modal damping	98
3.7	Objective functions	98
3.7.1	$L_{A,W}$ -min.	99
3.7.2	NF-max	100
4	Results	103
4.1	Introduction	103

4.2 Methodology validation	104
4.3 Optimization of wheel perforated schemes	113
4.3.1 Straight web	113
4.3.2 Curved web	117
4.3.3 Response Surfaces	122
4.3.4 Accuracy assessment of the acoustic model.	124
4.4 Cross-sectional wheel shape optimization	128
4.4.1 Optimization with fixed radius	128
4.4.2 Optimization with all the geometric parameters.	135
4.4.3 Response Surfaces	138
4.4.4 Studies on the correlation between natural frequencies and radiated noise.	142
4.5 Preliminary studies of the track shape influence on rolling noise.	143
5 Conclusions and future work	149
5.1 Conclusions.	149
5.2 Future work	152
Bibliography	155
List of Publications	185
International journals (JCR)	185
International congresses	185
National congresses	186

List of acronyms

Notation	Description
BEM	Boundary Element Method
BFS	Best Found Solution
ESM	Equivalent Sources Model
FEM	Finite Element Method
FSI	Fluid-Structure Interaction
GA	Genetic Algorithm
NF	Natural Frequency
RS	Response Surface
RSM	Response Surface Methodology
SPL	Sound Pressure Level
SWL	Sound Power Level

List of symbols

Notation	Description
f	Frequency
V	Speed of train
λ	Wavelength
n	Number of nodal diameters
m	Number of nodal circumferences
\mathbf{M}	Mass matrix
\mathbf{C}	Damping matrix
\mathbf{K}	Stiffness matrix
$\tilde{\mathbf{u}}$	Displacement amplitude
$\tilde{\mathbf{F}}$	Force amplitude
ω	Angular frequency
Ψ_{nm}	Modeshape (n, m)
\tilde{Q}_{nm}	Modal force amplitude of modeshape (n, m)
m_{nm}	Modal mass of modeshape (n, m)
ξ_{nm}	Modal damping ratio of modeshape (n, m)
ω_{nm}	Natural frequency of modeshape (n, m)
\mathbf{F}_c	Contact force
$\mathbf{u}_w, \mathbf{u}_r, \mathbf{u}_c$	Wheel, rail and contact response
\bar{r}	Roughness
$\mathbf{H}_w, \mathbf{H}_r, \mathbf{H}_c$	Wheel, rail and contact receptance
\mathbf{H}_{sys}	Combined receptance of the system
E	Young modulus

Notation	Description
M_{bend}	Bending moment
γ_{strain}	Shear strain
I	Second moment of area
F_{shear}	Shear force
G	Shear modulus
κ	Shear coefficient
A	Cross-section area
ρ	Density
η_r, η_p, η_b	Rail, rail pad and ballast loss factor
k_{stiff}	Rail foundation combined stiffness
k'_p, k'_b	Rail pad and ballast stiffness per unit length
m'_s	Sleeper mass per unit length
L_X	Rail cross receptance factor level
\tilde{q}_L, \tilde{q}_R	Rail solution for left-side and right-side d.o.f
\tilde{F}_L, \tilde{F}_R	Force in left-side and right-side d.o.f
k_n	Wavenumber for rail n th waveshape
Ψ_n	Waveshape for rail n th waveshape
$\tilde{q}_L^{S,A}$	Rail solution for left-side symmetric(S) or anti-symmetric (A) d.o.f
A_n, B_n	Generalized coordinates for the n th right and left travelling waveshape
$\overline{u_r^2}$	Spatially-averaged squared response
$\overline{A_n^2}$	Spatially-averaged squared generalized coordinate
δ_n	Real propagating part of wavenumber k_n
ζ_n	Imaginary decaying part of wavenumber k_n
F_0	Normal load
a, b	Semi-axis of contact patch ellipse
E^*	Plain elastic modulus
ν	Poisson's ratio
r_e	Effective curvature radius of surfaces in contact
K_H	Linearized contact stiffness
K_L	Linearized transverse contact stiffness
$ H(k) $	Contact filter transfer function
k	Wavenumber
\tilde{v}	Velocity amplitude
W_w, W_r, W_{sl}	Wheel, rail and sleeper sound power
c_0	Speed of sound

Notation	Description
$\langle \bar{v}^2 \rangle$	Mean squared velocity averaged over time and surface
$S_{a,j}$	Area of the j th ring of the wheel
$f_i^{a,r}$	Transition frequency in the axial or radial radiation efficiency formulation
N_S	Number of triangular radiating surfaces
$\bar{v}_{S,i}$	Effective velocity in the normal direction of the triangular surface i in the time domain model
$W'_{r,n}$	Equivalent sound radiation of rail for the n th waveshape
N_r	Number of rail waveshapes
k_{air}	Air wavenumber
C_r	Correction factor for rail sound power
$W'_{sl,n}$	Equivalent sound radiation of sleeper for the n th waveshape
b_{sl}	Width of the sleeper
d_{sl}	Distance between sleepers
h_{sl}	Sleeper height
$A_{i,m}$	Strength i of m th triplet
$H_n^{(2)}$	Hankel function of second kind and order n
v_r^{eq}	Rail equivalent velocity generated by triplets
v_n^s	Normal velocity to the surface generated by each rail waveshape
I_r^{eq}	Equivalent surface intensity generated by triplets
\mathbf{X}_i	Set of design candidates for the i th generation
N_{pop}	Initial population of the GA algorithm
$\bar{\mathbf{x}}_j$	Design candidate in a given generation
$\Delta\sigma_c$	Maximum stress variation
N_m	Number of modeshapes used for the computation of objective functions
h	Size of elements in FE mesh
$Obj_{NF}, Obj_{L_A,W}$	Objective function for NF-max and $L_{A,W}$ -min methodologies
tol_m	Convergence tolerance
$N_{gen,max}$	Maximum number of generations allowed to be computed by the GA
n_{layer}	Number of layers of circumferentially equidistant perforations.

Notation	Description
N_l	Number of holes in the l th layer.
X_l	Distance from hole centres in the l th layer to the wheel axis of rotation.
R_l	Radius of the holes in the l th layer.
n_f	Number of Fourier terms used in the general axisymmetric elements
F_x, F_{y2}, F_{y3}	Loads applied in structural analysis
$\sigma_{max}, \sigma_{min}$	Maximum and minimum principal stresses
x_1, x_2, x_3, x_4	Geometric parameters defining the wheel cross-sectional design: wheel radius x_1 , fillet radius x_2 , web thickness x_3 and web offset x_4
N_{cs}	Number of cross-sections defined for the axisymmetric meshing
W_{ref}	Reference value for converting power to dB
$\hat{\omega}_m$	Mean value of the wheel natural frequencies computed by the algorithm
$L_{A,W}, L_{A,R}, L_{A,Sl}, L_{A,Ss}, L_{A,T}$	Sum in energy of the SWL of the wheel, rail, sleeper, superstructure or total component expressed in dB
$E_{L_{A,W}}$	Energy contribution share in $L_{W,A}$ of one given modeshape of the wheel compared to that of the whole modeshapes set of the wheel

Chapter 1

Introduction

1.1 Motivation and background

Railways are a highly efficient, cost-effective and low polluting transportation system. Indeed, among the most established mass transport systems, the train is the least polluting system of all [1]. This, combined with the need to confront and adjust to the challenge that climate change represents for today's societies, makes the railway one of the transport systems of the future.

There are, unfortunately, some problems that need to be addressed so that the railway network can continue to grow, especially as it advances across urban environments. Such issues are mainly related to acoustic pollution, which has been a growing concern for citizens in recent years. This becomes especially relevant in high population density regions, where one of the main factors contributing to environmental noise are the different vehicles that circulate within them. Among these, the sound emitted by railway vehicles is the origin of severe nuisance and prejudice to nearby inhabitant. It is estimated that about 12 million people during the day and 6 million during the night are affected daily in Europe by this phenomenon [2] and it is well known that a prolonged exposure to the levels emitted by railway vehicles is associated with major health problems, such as cardiovascular diseases and difficulties when falling asleep [3]. As a consequence, it is generally a necessity to adopt

expensive measures to mitigate such nuisance, therefore limiting the growth of the railway network and effectively discouraging the increase in its use among citizenship.

Some of the most relevant types of noise emitted by railway vehicles are squeal, aerodynamic and rolling noise [4]; and it is the later which is predominant for the usual operating conditions of railway vehicles in urban environments. Rolling noise is generated by the vibration of the wheel and track induced when moving along by the interaction force generated due to the irregularities present in their surfaces [5]. Both the wheel and track play a fundamental role in it and, in order to attempt decreasing their radiation, the effect of the proposed measures in both components at the same time must be taken into account [6].

In that sense, through the different range of possible approaches that can be followed for railway noise mitigation, those considering its control at source have emerged as considerable cost-effective measures [7]. This would be the case of, for example, designing and modifying railway components properties best fitted for acoustic radiation attenuation.

It is in this context where this research is presented with the purpose of exploring the effect of different wheel and track designs on rolling noise as well as the feasibility of the application of optimization algorithms in this search of quieter railway components.

1.2 Objectives

The aim of the present Thesis is the reduction of railway rolling noise by achieving optimal wheel geometries that minimize sound radiation. Such purpose is accomplished by the development and implementation of a comprehensive railway vibroacoustic methodology that makes use of an optimization technique based on GAs [8–11]. To this end, the following objectives are proposed:

- Development and implementation of dynamic and acoustic models capable of considering the whole wheel/track interaction process as well as the partial contribution of each component to the total rolling noise radiation. Such implementations must consider not only the structural and dynamic properties of the components but also the influence of their corresponding geometries.

- Definition of geometric parametrizations of the wheel in which their shapes are expressed as functions of those geometric parameters that have the greatest influence on rolling noise. Additionally, these parametrizations are later combined with FEM in order to perform eigenanalysis in an accurate and efficient manner. Wheel axisymmetric properties are used, allowing for the derivation of the full three-dimensional modal information from the two-dimensional cross-section mesh.
- Creation of methodologies that make use of the above mentioned models to optimize wheel shapes through the use of GAs. Definition of those objective functions that better suit the intended goals and study of their effectiveness.
- Achievement of a perforated scheme applied to a railway wheel that minimizes computed rolling noise through the use of GA-based techniques. Use of GA-based approaches for the computation of the optimal wheel cross-sectional shape from the point of view of acoustic radiation mitigation.
- Exploration of the influence of each geometric parameter on rolling noise and the physical causes underlying the changes in the generated sound.
- Performing preliminary studies on the influence of rail shape and track viscoelastic properties in rolling noise.

1.3 Organization and development of the Thesis

The Thesis is structured in five different chapters. Aside from the present introductory part, these are organized as follows:

In Chapter 2, the theoretical basis of the rolling noise phenomenon and its characterization is presented. In this chapter, the state of the art of the research field is exposed and the dynamic and acoustic models developed in the work are presented. That includes the description of the dynamic behaviour of wheel and track with different approaches and their interaction, as well as the computation procedure for their radiated sound power.

In Chapter 3, the procedure followed throughout each optimization is explained in detail. The chapter begins with a brief introduction on the elemental concepts regarding GA methodologies. Then, the general algorithm flowcharts are illustrated as a whole. Each step of the process is later revisited and further developed. Special attention is paid to the geometric parametrization

used for the wheel cross-section and for the perforation schemes, along with the modal identification procedure used for classifying and characterizing the wheel modeshapes. Objective functions defined in the current investigation are also described at the end of the chapter: first the $L_{A,W}$ approach, based in the straight forward minimization of the computed Sound poWer Level (SWL); and then the NF-max method, centred in maximizing the natural frequencies of the modeshapes.

In Chapter 4, the results provided by the methodologies developed in the Thesis are presented and discussed in detail. The implementation of the models exposed in previous chapters is validated with the commercial program TWINS for the different results obtained. Then, the best perforated scheme and wheel cross-sections found for each proposed objective function are shown. In the case of the wheel, the aforementioned analysis are performed on two different typologies of wheel shapes: curved and straight web. Findings of the influence of each defined parameter on rolling noise are also explored, including a RS analysis. Insights on the underlying physical causes behind the acoustic radiation changes of the different designs analysed are also treated in this chapter. Moreover, a preliminary study of the effects on the rolling noise of the variation of the track geometric and structural parameters is also performed.

In Chapter 5, the main conclusions and contributions are summarized. Relevant possible future research lines are proposed and briefly described.

Acoustic characterization of wheel and track rolling noise

2.1 Introduction

As previously introduced, the study of ways to decrease the noise emitted by trains is a very active field of research at the moment. In particular, this Thesis focuses on the study of the use of geometric optimization techniques with the goal of reducing rolling noise. Such kind of pursuit requires, among other things, the ability to model the dynamic behaviour of all components involved in this particular noise, as well as being able to translate their vibratory response to the corresponding acoustic radiation. Thus, in the following chapter, a review is first made in Section 2.2 of the research undertaken so far on those topics relevant to the present work. Then, in Sections 2.3, 2.4 and 2.5, the models used for the description of the dynamic behaviour of the wheel, rail and contact, respectively, are explained in detail. Finally, in Section 2.6, the procedure for the calculation of the sound power is presented.

2.2 State of the art

With the aim of providing a comprehensive review of the main literature available on the subject at hand, first, rolling noise and its related phenomena are introduced. Then, it follows an explanation of different existing approaches for tackling the associated acoustic radiation, with special detail in the application of optimization techniques. Later, for the sake of completeness, a brief statement on other important sources of railway noise is granted.

2.2.1 Rolling noise

Rolling noise is defined as the noise from railway operations caused by the interaction of wheel and rail while running on a straight track and, together with other contributions to the railway noise like curve squeal or aerodynamic noise, is one of the main sources of sound emission from a train pass-by [4]. Specifically, it is the most relevant noise in trains circulating on a straight track at speeds from approximately 50 to 300 km/h [6].

It is caused by the interaction of the system conformed by the railway wheel and the rail at their contact patch or contact area [12]: due to the irregularities present at both the wheel and rail running surfaces, when the train is moving on its track there is a relative movement between wheel and rail. As a consequence of the resulting wheel/track contact interaction, a force appears which excites the system with a frequency dependent on the moving velocity of the train and the running surfaces irregularities wavelength. Such a force generates vibrations in the components involved in the rolling noise phenomenon, which in turn causes them to emit this characteristic noise. These irregularities mentioned above, which are ultimately the cause of rolling noise, are referred to as roughness. Its wavelength, together with the speed of operation of the train, are the parameters fixing the frequency at which the system is excited. When the train passes at a speed V in presence of a roughness with wavelength λ , a force will be produced that will excite the system at a frequency [5, 13]:

$$f = \frac{V}{\lambda} \quad (2.1)$$

As rolling noise acts in a broadband frequency spectrum, the range of wavelengths which results of relevance for noise emission can be established from Eq. (2.1), corresponding to the range that covers wavelengths from 0.005 m to around 0.05 m [4]. Thus, the combined roughness spectrum of both wheel and



(a)



(b)

Figure 2.1: Example of roughness (corrugation) on: (a) rail running surface; (b) wheel tread. Originally published in [23] and [30], respectively.

rail presents typically a magnitude of between -20 to 15 dB re $1\mu\text{m}$ [14–16], although under some operation conditions as in the tramway network these values can increase with differences of up to 10 dB [17]. It is worth mentioning that, even though the linear approximation of roughness behaviour is generally good, when disturbances are large enough to produce loss of contact to occur, then non-linearities should be included [18].

There are several mechanisms that lead to the development of this unevenness on the running surfaces of rails and/or wheels, but the main ones [4] are: manufacturing variability; variable wear, caused by rolling and sliding that take place in the contact area [19, 20]; corrugation, a quasi-sinusoidal type of irregularity that appears on the rail rolling surface with wavelength between few centimetres and 2 meters [21–23]; and the effects of wheel brake systems [24, 25], generally due to apparition of out-of-roundnesses [26] or temperature-dependent wear in tread brakes [27–29]. For illustrative purposes, an example of the corrugation present in a rail and wheel can be seen together in Fig. 2.1.

Furthermore, with respect to the relationship between train speed of operation and the level of rolling noise emitted, it has been observed that the higher

the speed, the higher the Sound Pressure Level (SPL) generated, following a proportional logarithmic relationship. This is expressed as:

$$L_p = L_{p0} + N \cdot \log_{10}\left(\frac{V}{V_0}\right) \quad (2.2)$$

where V_0 is a reference speed, L_{p0} its sound level, V the speed of the train, L_p the resulting SPL and N a factor determined from experimental measures with a typical value of 30 [4, 31, 32]. The increase in the noise with V does not vary uniformly along the frequency domain, with the biggest frequency content being located at low frequencies for the case of trains with low speeds while, at high speeds, the spectrum peaks shift towards the high frequency regions [4]. It is worth noting, though, that some doubts have been raised about the effectiveness of the logarithmic relation of speed and noise [33].

As seen, the modelling and description of rolling noise is a complex task with several aspects associated. From the point of view of the railway components involved in this noise emission, the most relevant are the wheel and track, with their influence depending on the frequency studied [4, 34–38]. In the subsequent sections, a detailed review of each component behaviour is done together with a description of the attempts of achieving a comprehensive understanding of the generation mechanisms.

2.2.1.1 Studying wheel behaviour in rolling noise

Since the beginning, it has been clear the necessity to assess the dynamic and acoustic nature of the wheel for an accurate approach to rolling noise research. Early in 1975, P. J. Remington described its radial impedance by the combination of that of a simple mass, for frequencies under 1000 Hz, and that of an infinite beam with the same cross-section of the tread [39]. Later on, as knowledge of the resonant behaviour of wheels improved [40], new approximations proposed a switch to the use of disks for the dynamic description. So, in [41] a mechanical model based on Midlin's plate theory [42] is used for a wheel disc with flat web but considering only its rim. Then, natural frequencies for a disk with one point on its outer edge elastically supported under are computed and the point impedance of the disk when harmonically excited is established. This publication is later expanded in [43] with the implementation of a FE model and with the computation of the sound power, which is also compared with experimental data from four different types of wheelsets. Besides, an acousti-

cal quality factor level is introduced to assess the geometric differences effect in the radiated noise.

Meanwhile, in [34, 44], the disk approximation is improved with the inclusion of a stiffness to account for the compression of the web and a solid mass for the hub and axle. Thus, with classical normal mode techniques the impedance is obtained for both axial and radial directions. Modifications in the performance under 500 Hz are introduced to make the radial mobility behave as a rigid mass and, as no rotary inertia or shear in the wheel tread are included, some specific major deviations of the 10% - 20% order arise. In any case, such variations are not directly translated to the noise calculation outputs, where the wheel is considered to radiate as a monopole point source.

Then, with the increase in the understanding of the phenomenon granted by the reported research, D. J. Thompson publishes in [45, 46] the model chosen in the present Thesis for the description of the wheel vibrational behaviour. In [45], a modal approximation is used for the stationary case in which mode-shapes are categorized according to the number of nodal diameters n and nodal circumferences m , being labelled by the two numbers as (n, m) . For the characterization of the modes, a FEM approximation is applied with the use of axi-harmonic elements. When considering a forced vibration, the results of the derived frequency agree with the experimental data provided for those mode-shapes with $n \geq 2$, which are considered to be the most important in rolling noise [4]. If $n = 0$ or $n = 1$ modeshapes are to be described more accurately, axle should also be considered or as an intermediate solution, the hub should be taken as fixed [4]. Additionally, in [46] the model is completed with the inclusion of rotation, which has the effect of splitting natural frequencies into closely positioned pairs in the same manner as the imperfections in the axial symmetry does [47], the pairs differing in its angular frequency proportionally to the rotational velocity Ω by $\Delta f = 2n\Omega$. This exact same phenomenon is observed in [48], where a 2.5D FEM and BEM formulation are proposed for sound power computation. Also, [45, 46] approaches consider the wheel as a low damped structure in which each modal damping ratio cannot be predicted. Therefore they must be either approximated or experimentally derived. Hence, in [49] damping values vary between $1 \cdot 10^{-4}$ and $5 \cdot 10^{-4}$ for modeshapes with $n \geq 2$; in [50] the described pattern is also followed with low damping measures that increase to $\sim 10^{-3}$ for $n \leq 2$; and in [51] measures for five different monobloc wheels found no systematic differences between each of them, with damping average values of $0.8 \cdot 10^{-4} - 1.3 \cdot 10^{-4}$ for $n \geq 2$, damping ratios of $\sim 10^{-3}$ for $(0, 0)$ and $(1, 0)$ modeshapes and evidence of higher ratios for $n = 1$. Also, damping magnitudes could differ between measures for a free wheel and

those for the wheel on the track, with the later case presenting loss factor values at least 10 times greater than the free wheel counterparts [49]. To sum up, [4] concludes that for rolling noise calculations, the modal damping ratio value is not critical and reasonable predictions can be made by approximating it to 10^{-4} for $n \geq 2$ modeshapes, 10^{-3} for cases with $n = 0$ and 10^{-2} when $n = 1$. However, it is worth noting that Merideño et al. defend in [52] that small changes in modal damping, when it affects those modeshapes most relevant for the studied noise, can have great effects on the resulting acoustic pressure.

Also, time domain models of the whole wheelset behaviour have been developed, with the capability of accounting for the rotation of the wheel and the gyroscopic effects it generates, the high frequency dynamics associated with the flexibility of the solids and the non-linearity present in the wheel-rail contact [53, 54], together with the inclusion of phenomena specific to train negotiating curves [55]. Although computationally demanding, such models are fitted for research of not yet well understood problems as the relation of corrugation and rolling noise in curves and tangent tracks [56] or higher frequency events as squeal.

With the dynamic portrayal clarified, it just rests to appropriately assess acoustic efficiencies for a complete depiction of wheel behaviour. In this sense, an initial formulation is proposed in [57] that, despite the good results for the acoustic radiation offered in [36, 58], presents some nuances. On one hand, it is observed that axial efficiencies, when compared with results obtained with a BEM, lead to underprediction of the radiation ratios at frequencies $f < 200 - 1000$ Hz depending on the number of nodal diameters. On the other hand, the computed radial radiation ratios have several changes in gradient through the frequency, implying the need of a higher number of critical frequencies in the formulation. Furthermore, when different types of web and tyre dimensions are considered, a radiation ratio drop is detected at low frequencies. These issues are considered in [59] where a new semi-analytic formulation is derived from a series of BEM based calculations, for wheels with different radial size and web shapes. This time, to determine their values accurately, scaling factors are used whose numerical quantities are assigned to those that minimize the mean squared error of the fittings. Besides, the fitted radial efficiencies curves are normalized to a factor depending on the wheel radius and more realistic critical frequencies are considered.

Once a comprehensive noise radiation methodology is established, the acoustic characteristics for rolling noise emission observed in literature with each modeshape contribution should be studied. With this regard, in [50] it is ex-

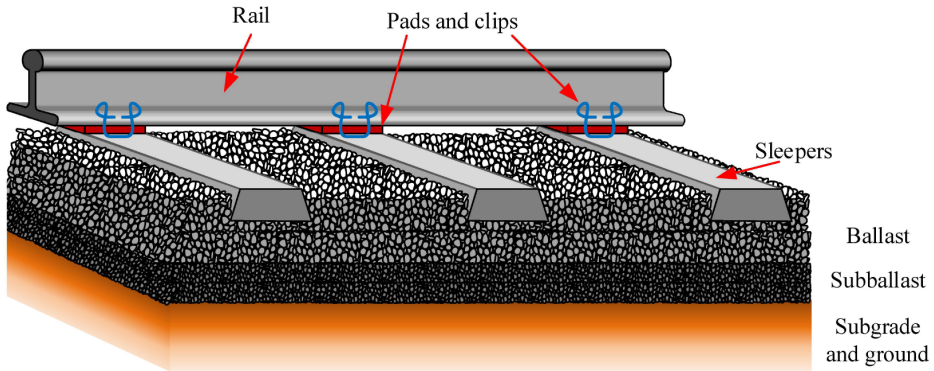


Figure 2.2: Typical track structure composed by rails, clips, rail pad, sleepers and ballast. Originally published in [62].

perimentally found that radial modeshapes are those most involved in rolling noise emission up to 5000 Hz. In [59, 60] the modeshapes that appear as more relevant to the rolling noise in measures of a standard 920 mm freight wheel are those radial and axial with one nodal circumference, each with two or more nodal diameters. This pre-eminence of radial modeshapes is also found [61] if viscoelastic wheels are also taken into account. In addition, [4] states that the modeshapes most important for noise radiation in rolling noise are those with a number of nodal diameters $n \geq 2$.

2.2.1.2 Studying track behaviour in rolling noise

Track, and in particular the rail, constitutes the other most important component in the rolling noise radiation together with the wheel [4]. It is generally supported onto transverse positioned sleepers that lay on a bed of stones named ballast or, in the case of ballastless tracks, directly attached to concrete slabs. An example of track structure is found in Fig. 2.2, where it can be seen how they are held to sleepers, or slabs, by clips and in-between them a rubber pad or rail pad is placed for protection purposes. The analysis of such a complex structure poses many challenges, which have been historically approached in two ways: time domain and frequency domain techniques.

Time domain techniques have the advantage of being able to produce accurate predictions of dynamic phenomena and the capability of including non-linearities. As a down side, they require a great number of steps during the

problem solution computation if an appropriate precision is wanted, with the associated high computational cost. Examples of track modelling in the time domain can be found in [63–65], the latter case applied to the particular case of a sleeper. Due to the fact that the calculation time required would not be viable for the optimization procedures developed in the present Thesis, this section will focus on the several existing frequency domain-based models. If the reader is interested in a more detailed literature review for the time approach, the thorough review realized by K.Knothe and S. L. Grassie [66] is recommended as starting point.

Frequency domain techniques are based on finding appropriate transfer functions for the system under a point load excitation. They have the advantage that, when the functions are known, it is easy to calculate the response of the system to a moving distortion [66]. On their side have the first dynamic analysis made for the rail, where Timoshenko modelled it as a continuously supported Bernoulli beam excited by a harmonic stationary point load or a varying irregularity [67]. This model offers a proper representation of rail response for frequencies under 500 Hz, but above that becomes inaccurate as transverse deformation gains influence [66]. Improvements are made in the case of [68–70], where a Timoshenko beam on a continuous two-layer mass-spring foundation is used to characterize the rail in the vertical, longitudinal and lateral directions. With that formulation a precise description is obtained when the cross-section deformation is not significant, giving a good approximation up to 2500 kHz for the vertical and longitudinal response [66] and up to 1500 Hz for the lateral case [71]. For overcoming such limitations, [72] introduces a detailed semi-analytical model including the effects of torsion, shear centre eccentricity, warping and foundation eccentricity. Such work produces good predictions of the mobility and decay rates for both supported and free cases in the range of up to 2000 Hz. Also, [73, 74] introduce a double beam model of rail that allow for a basic display of the cross-sectional deformation in the form of foot-flapping. By dividing the rail in an upper part corresponding to the head and web and a lower part representing the foot, reliable results are offered under the range of 6500 Hz and 500 Hz for the vertical and lateral vibration, respectively. Additionally, both continuously and periodically supported models are implemented, with the periodically supported layer offering more appropriate results and a better description of the rail decay rate. Another example of a periodically supported structure model can be found in [75], where sleepers are considered as discrete flexible lumped inertias and the rail idealized as a simple beam. Unfortunately, comparison with experimental results suggested discrepancies in the model likely caused by the choice of track parameters [76]. Later, in [77] M. Heckl continues the previously cited inves-

tigation by including an infinitely long Timoshenko beam on infinitely many supports, improving the formulation efficiency by the use of Bloch's theorem for periodic waves [78]. It is seen that the inclusion of the effects of the periodicity of sleepers cause the point mobility to change severely within a sleeper span and "pinned-pinned" modes together with passing/stopping band behaviour arise [4, 77]. From the noise radiation perspective, though, "pinned-pinned" resonances have at most an effect of 1.4 dB in the 1000 Hz band and, when the random variation in sleeper spacing is accounted, the results obtained for the spatially-average vibration are similar to those of the continuously supported models [4, 79].

Another approach followed when dealing with cross-section deformation produced at high frequency vibration is the use of FEM formulations. Thus, in [76, 80], by meshing a short length of rail and applying symmetric/anti-symmetric boundary conditions at the ends the whole dynamic behaviour is predicted. It makes use of the periodic structure theory and generalized wave propagation [81] and considers a continuous support layer, offering good agreement with the experimental data in the range above 1500 Hz for both vertical and lateral direction. Gry propose in [82] an approach using waves travelling in a track span and a FE approach. Later, Gry and Gontier, in the seek of a FE less time consuming method, introduce in [83] a process describing track behaviour based on deformation patterns called "cross-section modes", that allows a reduction of FE matrices size. In [84] a 2.5D FEM is also used to calculate the wavenumbers, waveshapes and dispersion curves of a free rail for up to 6000 Hz. Then, in [85] the semi-analytical FEM is extended with the inclusion of multiple frequency dependent support layers combined with the use of real track measured properties. The effect of the moving load is also studied for the wavenumber-based approximation in [86], where the response of a periodically supported rail is derived for both a multiple-beam model and a 2.5D FEM case through a Fourier transform-based method. This work is generalized in [87] to include rails with non-uniform periodic structures (e.g. when rail dampers are present in the track) and, in [88], a so-called Fourier-series approach based on that of [86] is proposed to study wheel-rail interactions caused by a multiple number of moving wheels. Lastly, a discretely supported railway track coupled with the sleepers by multiple springs representing the pad is presented in [89]. Besides the infinite discrete supports and rail cross-section deformation, the proposal also includes the flexible ballasted sleepers by using an analytical Timoshenko beam and the surface dimension of pads, represented by several springs across the rail foot. In such research, a precise agreement with measured data is found for the decay rates, vertical and lateral

track point mobilities in the range of up to 5000 - 6000 Hz, depending on the rail pad stiffness.

Once the dynamic properties of the track are derived, it is time to determine the rolling noise radiated by its components. Therefore, with regard to noise focused work, in [90], Thompson et al. conclude that a two-dimensional acoustic model is enough to predict rail noise radiation accurately. If the decay rate or wavenumber of waveshapes remain lower than those of the air radiation, the two-dimensional approach predictions remain within a margin of error of ~ 2 dB. It is below the range of 250 Hz where the three-dimensional effects should be accounted, although two-dimensional models are still applicable if appropriate corrections are made in the low frequency range. Thus, [91] uses an alternative implementation to BEM based on the estimation of rail and sleepers noise radiation. It finds the strengths of equivalent source triplets, each one consisting of a monopole and two dipoles, positioned inside the corresponding cross-sections that minimize the difference of the derived surface vibration velocity with that obtained through solving the dynamic problem. Then, makes use of the triplets to obtain the corresponding acoustic radiation pressure and intensity. In [92], it is applied a waveguide FE methodology combined with a wavenumber BEM application [93] for solving the problem of noise radiation in an open and embedded rail. This way, evidence is found that the embedded case could considerably reduce sound radiation with a proper design, as it is less radiating in the range under 600 Hz where its embedded mass is not included in the procedure. Centred in the other components of track, X. Zhang et al. characterize in [94] the sleeper sound with a three-dimensional BEM model and in [95, 96] the authors study the effects of ground and ballast on rail radiation. Then, the information granted by these researches is merged in [97], where a comprehensive track radiation model is detailed. The acoustic behaviour of the track is described by considering ground noise reflection and absorption, differences between ballasted and slabs tracks, periodic supports, coupling between sleepers due to the rail, and an infinite rail model. Results are compared with those of a three-dimensional BEM track section, the previously cited TWINS model and measured data, showing a good agreement in all cases for the whole frequency range and an improvement of accuracy with respect previous methodologies.

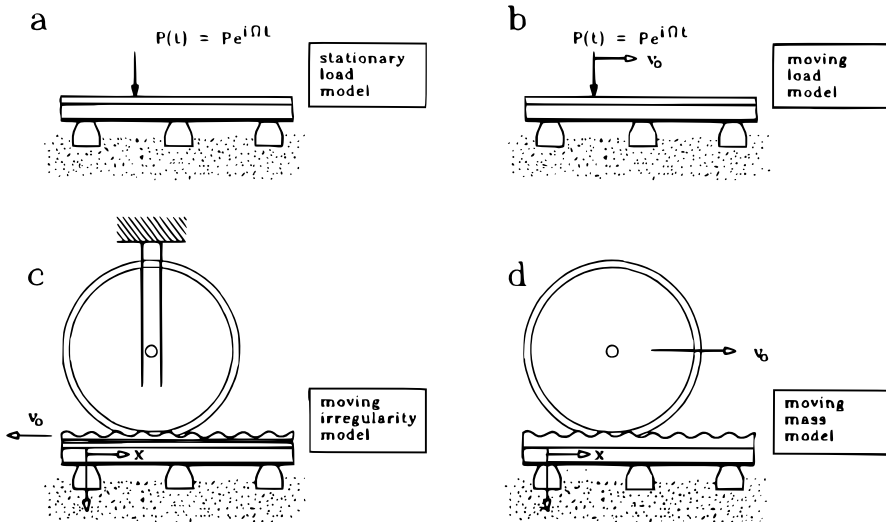


Figure 2.3: Classification of excitations models. Originally published in [66].

2.2.1.3 Wheel/track interaction and contact

At the beginning of the section, it is explained that due to the roughness present in the wheel and rail surfaces, a contact force appears as both components interact when the train moves. Accordingly, it is necessary to characterize this interaction if an accurate representation of rolling noise is wanted.

According to Knothe and Grassie [66], excitation models can be divided into four types: stationary load, moving load, moving irregularity and moving mass. A representation of them can be seen in Fig. 2.3. The first model is just appropriate for calculating the response produced by a stationary periodic or transient force and the second case (e.g. [98]) does not consider roughness, fundamental for rolling noise. The wheel moving on an irregularity (e.g. [99, 100]) is the most realistic choice but also that introducing the most difficulties [66]. In contrast, the moving irregularity model allows to study the dynamic response of both wheel and track under rolling noise conditions with lower complexity. Therefore, the wheelset remains in a fixed position on the rail, and the irregularities representing roughness are treated as moving. Thus, in the present Thesis models used are based on the third mentioned case, using an approach in the frequency domain [4, 5].

For Remington [34, 44], the wheel/track system is represented by two dynamic systems which are joined at the contact point. Thus, the excitation of the

system is described by means of a contact spring connected in series to the other two components. This is done with the help of a contact impedance describing the contact springs connecting each component with the defined roughness acting in the vertical direction. The lateral displacement at the contact, on the contrary, is taken as rigid. Thompson later improves this by adding further coordinates to the coupling in [5], including longitudinal displacement and three rotations. Feldman, instead, introduces an external force excitation at the wheel-rail interface in a similar manner than a series impedance model [101].

In order to derive the receptance corresponding to the contact interface, it is necessary to account for the local deformations produced at the interaction region. Also, the zone in where contact is produced depends on the normal load, in a load-deflection relation that is non-linear [4]. In [34, 44, 102], the Hertz contact theory [103] is used for this problem. According to Hertz theory, the stiffness between bodies in contact is described by the radii of curvature of these bodies at the contact [104]. Hence, [4, 102] derive the vertical stiffness from an effective radius of curvature composed by each radius of curvature of the components involved, using a linearised formulation based on that in [105, 106]. For the stiffness in the lateral direction, the transverse compliance defined by Mindlin [107] is considered. If creepage, i.e. small relative motion occurring during rolling, is to be considered, resulting reaction forces named creep forces must be derived. Kalker in [108] extracts such forces in relation to a series of coefficients called Kalker coefficients. These coefficients, which establish the relationship between creepage itself and the resulting force, are a function of the contact ellipse and Poisson's ratio and are calculated considering the system in steady state [109–112]. Afterwards, Knothe and Gross-Thebing include harmonic motion in Kalker's analysis developing frequency-dependent Kalker coefficients [113].

Additionally, if a more detailed depiction of the creepage phenomenon is desired, saturation of creepage should be taken into consideration. When slipping, there are simultaneously sliding and adhesion zones in the contact region. Besides, transverse stresses caused during elastic deformations in rolling contact present a local friction limit, with the transverse force in the case where the slip zones covers entirely the contact area limited to μF_0 , μ being the friction coefficient and F_0 the normal load [4]. Thus, in [114] Vermeuinen and Johnson present an approximate analytic model for this phenomenon where transversal and longitudinal forces are represented by a composite function, whose value depends on a normalized creep parameter. Reference [115] includes the case

of combined longitudinal and lateral forces in this formulation, allowing the inclusion of spin effects.

Also, in an attempt to fully account for the non linear behaviour of contact, Kalker develops the CONTACT algorithm for non-Hertzian, non-steady contact problem [116]. By the use of the variational method, it computes normal and tangential forces distribution through the potential contact area, which is previously discretized in rectangular elements. As indicated in [21], the CONTACT algorithm is one of the most rigorous contact models available. Even though, its high computational requirements make it difficult to integrate such algorithm in multi-body codes [117]. Computing time issues are addressed in a simplified approximate algorithm, FASTSIM [118], which allows for solution in the precision range of $\sim 10\%$ with respect to CONTACT with a 1000 times faster solution [21, 116]. Later, the model is broadened by the addition of non-elliptic contact regions [119] and a creep dependent friction coefficient [120]. In [121] a new version called FASTSIM2 with improved precision and efficiency is presented. Moreover, in [18] Wu and Thompson publish a study on the effects of non-linear wheel/track interaction. It concludes that linear approximations grant good precision for large static normal loads, with a global deviation not higher than 2 dB in the force spectrum due to non-linearities for a 50 kN load.

If a correct representation of the roughness effect on contact is required, it is important to include the relation between the contact patch size and the roughness excitation. In the so-called “contact filter” phenomenon, when roughness presents wavelengths shorter than the length of the contact region in the rolling direction its effect on the noise radiation is attenuated. In order to deal with this, an analytical model is developed by Remington in [12] by considering a circular patch and defining a filter transfer function depending on a parameter indicating the degree of correlation among parallel roughness profiles at a given wavenumber. Thompson simplifies it further in [4], avoiding the need of integral computations. A more precise procedure for estimating the resulting non-linear behaviour due to roughness in the contact patch is the “distributed point reacting spring” (DPRS) method [122]. In the DPRS procedure, non-linear point reacting springs are distributed on the running surface and the magnitude of stiffness and deflection of each spring is obtained for the smooth surface case. Once these parameters are derived, roughness can be added and the changes in the interaction force and stresses distribution computed. Results are compared with those extracted from solving the Boussinesq integral equations [123], offering a good agreement for all the range of studied wavelengths. Then, with the results extracted from the DPRS and by considering a blocked force, it is possible to obtain later an equivalent filtered roughness

[124]. In [125], a two-dimensional DPRS based model is presented for calculations requiring less demanding computation complexity, where the set of independent springs is located just along a single line. Proposals have also been made to extend the contact filter effect into time-domain problems [126, 127].

2.2.1.4 Rolling noise comprehensive modelling: TWINS

One of the first comprehensive studies on the train noise was the work developed in a five-part publication [12, 128–131] in which a wide range of the phenomenology involved in railway noise radiation, as rolling, squeal or impact noises are analysed through theoretical and experimental research. Later this research lead to a complete analytical model of the rolling noise [34, 44] which served as foundations for posterior developments more focused on rolling noise. Hence, in [5, 45, 46, 76, 102], D. J. Thompson refines and expands the work initiated in [71], that also conforms the core of his PhD thesis [132], establishing an extensive description of the rolling noise generation mechanisms and its behaviour. In this five-part work, the wheel-rail noise generation is characterized as a function of the combined roughness of wheel and rail, which is ultimately the responsible of the appearance of a the contact force that causes the vibration, and therefore noise emission, of these components [5]. The dynamics of the whole system is computed in the frequency domain, using Frequency Response Functions (FRFs) to detail how the rail [76], wheel [45, 46] or contact [102] behave dynamically and acoustically.

At the same time, this research is now integrated in one of the most used commercial software in the field: TWINS [91, 133]. TWINS, acronym of "Track-Wheel Interaction Noise Software", is a computer program produced by the TNO Institute of Applied Physics capable of computing the SWL and SPL of wheel, track and superstructure for different operating conditions and geometries. The theory and literature behind the wheel, track and their interaction modules are further described in posterior sections. For the other parts, e.g. the superstructure module, as they are out of the scope of the present Thesis, the reader is referred to [91] for more information. In Fig. 2.4, a flow diagram extracted from [60] of the aforementioned calculation procedure is shown for the sack of completeness and clarity.

Additionally, there is an extensive and meticulous groundwork validating the results provided by TWINS [36, 37, 49, 58, 134]. More precisely, the works presented in [36, 58] belong to a two-part publication with the first experimental validation of TWINS executed by D. J. Thompson et al. In them, SPL

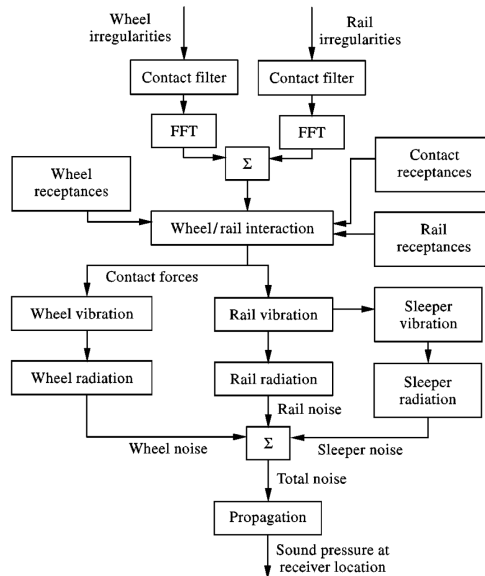


Figure 2.4: Complete flow diagram for rolling noise calculation in TWINS. Originally published in [60].

and vibrational measurements for trains passing by in 25 cases, consisting of a number of combinations of three different wheels and three different types of track, are registered and compared with the corresponding predictions of the software, showing an overall good agreement between the experimental data and theoretical models. Later, in [49] field measurements of wheels with sinusoidal profiles are tested; their vibration amplitude, together with that of the track, are compared with TWINS methodology and, additionally, an estimation of the effects of the contact filter is made. Besides, in [37, 134], a more recent set of updates of the validations with the last theoretical improvements is added. In the first case, in a series of 34 experimental measurements of different wheel/track combinations, a difference lower than 2 dB is shown between measured and predicted data. In the last case, 4 different wheels and a single track with a 60-type rail on monobloc concrete sleepers were tested for speeds ranging between 70 - 160 km/h. Here, the matching between measured and predicted data improves and a good agreement is found again for all sets of data, with a mean difference in noise predictions with respect to measured data of ± 1.5 dB.

2.2.1.5 Rolling noise distribution among sources

Although it is the total combined noise what is perceived when a train pass-by occurs, it is important to know up to which extent contributes each of the components to tackle rolling noise effectively. Early attempt of doing so provided unclear not concordant results. This way, Bender and Remington studied in [135] the contribution of the rail to total train noise. Results show rail radiation dominating in most frequency ranges, between $\sim 500 - 5000$ Hz. In another work [136], in predictions made from vibration data measured during a train passage is found that all sources contribute significantly from 315 to 630 Hz, the rail dominates in the 800 - 2500 Hz range and above 2500 Hz is the wheel the primary source. Ten Wolde and van Ruitten, instead, found in [137] that it is the wheel what dominates between 250 to 400 Hz and the rail from 400 Hz up to 1250 Hz, with no reliable predicted data above that frequency. Contrary to such results, on a study by the Japanese National Railways, Arai [138] concluded the wheel contribution to rolling noise on straight tracks was negligible for the Japanese case. Also, W. F. King III and D. Bechert, with a series of measures at different heights with an array of 14 microphones of radiated noise generated by trains at speeds between 160 and 250 km/h, obtained results indicating a dominant contribution of the rail at low frequencies and of the wheel at mid frequencies around 800 - 2500 Hz, while above this range both components seemed to contribute equally [139].

With the development of advanced comprehensive rolling noise models, more detailed experiments have been done. In [140], combined measurements are made on a laboratory coach and at the trackside for a corrugated and uncorrugated rail and four test speeds, with a total of 11 different runs. For the track type and wheel used in the experiment, the averaged results show that the wheel is found to radiate significantly only over 1250 Hz, being the predominant source at high frequencies, with the rail being relevant in the whole frequency spectrum. In the validation of Remington's model [34] a similar procedure is followed with on-board and wayside measurements. This time, the rail is found to be the most significant part up to ~ 2500 Hz, where wheel noise begins to dominate. Results obtained for the TWINS validations [36] agree, presenting noise radiation distributions in which the rail is the most influential at low to mid frequencies and the wheel above ~ 2500 Hz for test at 160 km/h and ~ 1500 Hz for the freight test at 100 km/h. Besides, sleeper, although with a small contribution to the overall sound level, appears to be the main contributor in the range below 250 Hz. Analysis done in Japanese railways [134, 141], showed that sleeper is the most significant below $\sim 250 - 400$ Hz and the wheel is the important source above 2000 Hz. As for the

middle frequencies, depending on the wheel type used, either it is the rail the most relevant component or this significance is shared between wheel and rail. Additionally, in an assessment of different methodologies for separating wheel and track contributions, in the reference results generated with the TWINS model and the experimental data collected [142], a similar pattern is observed with the wheel dominating above 2000 Hz and the rail between 315 and 1600 Hz. Also, following the work in [139], an analysis is carried out in [143], purely based on the data gathered by an array of microphones, using its directional capabilities to locate the dominant sources. Noise is seen to comprise four strong spectral peaks all in frequencies above 1700 Hz, and whose radiation area is concentrated in the lower half of the wheel. This pre-eminence of the wheel, could be explained by a phenomenon observed in the aforementioned work of Kitagawa [134], where it is demonstrated how microphone arrays oriented perpendicular to the track are not capable to fully register track radiated noise. Therefore, this kind of noise source determination could undermine the rail contribution. This is later confirmed by the measurements of a study on rail noise directivity and its implications on the use of microphone arrays published by Kitagawa and Thompson [144]. Reference [145] reassures the need of considering the rail directivity in field tests and that its omission when analysing data may produce to incorrectly attribute the radiation to the wheel.

As a summary, it can be stated with the current data available that rail is the most relevant at low to mid frequencies, wheel becomes predominant above 2000 - 2500 Hz and the sleeper, while not significant in most of the frequency range of interest, plays a relevant role in rolling noise radiation beneath 250 Hz. Besides, there is evidence that rail significance at high frequencies could be underestimated due to the influence of its directivity in experimental tests. For illustrative purposes, an example of radiated sound spectra derived with the TWINS formulation and experimental data published in [142] is shown in Fig. 2.5.

2.2.2 Tackling rolling noise: mitigation measures

Over the course of the years, many measures have been taken to tackle the noise emitted by railway vehicles. Among those aimed at reducing rolling noise, most of them have focused on acting on the track and/or wheel since, as it is described in the previous sections, they are the main sources of noise radiation. Therefore, besides the building of noise barriers, studies emphasize noise control at source, which has proven to be considerably more cost-effective and less visually intrusive than construction of barriers [7].

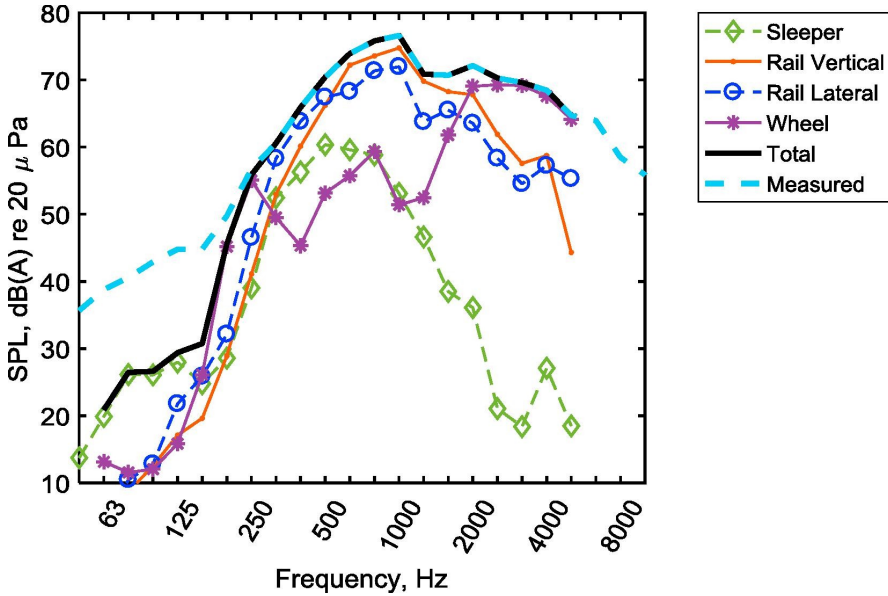


Figure 2.5: Contribution to rolling noise of each component involved for data measured from a run at 80 km/h. Originally published in [142].

As explained in Section 2.2.1, the mechanism responsible of the appearance of rolling noise is the roughness present on the running surfaces. Therefore, one of the most immediate approaches to prevent acoustic radiation is to try to minimize it. In this sense, the substitution of traditional cast-iron block brakes, which favours the presence of corrugation in wheels [25], by disc brakes is proven to be a successful measure. When changing brakes, reductions of up to 10 dB are observed [24]. For freight wagons, the retrofitting with composite brake-blocks is a low-cost option that allows a noise decrease of up to 12 - 14 dB [146]. Focused on the rail, rail grinding is another option. Despite being done mainly to prevent defects and fatigue cracks [4], the use of rotating grinding stones also smooths the rail surface. However, a tonal peak is left at a wavelength of $\sim 20 - 30$ mm, corresponding to resonances of the grinding stones and drive system [6]. To avoid it, a practical grinding strategy has been developed consisting in giving a second grind at a lower speed, reducing the frequency at which the tonal sound was present to another less relevant to noise radiation [6]. Deutsche Bahn AG has developed an “Acoustic grinding”, a rail grinding designed specifically to lower noise, which is estimated to accomplish a decline of 3 dB [147]. It consists of a two step process: first planing or milling, and then grinding using oscillating stones [147]. Examples of roughness differences

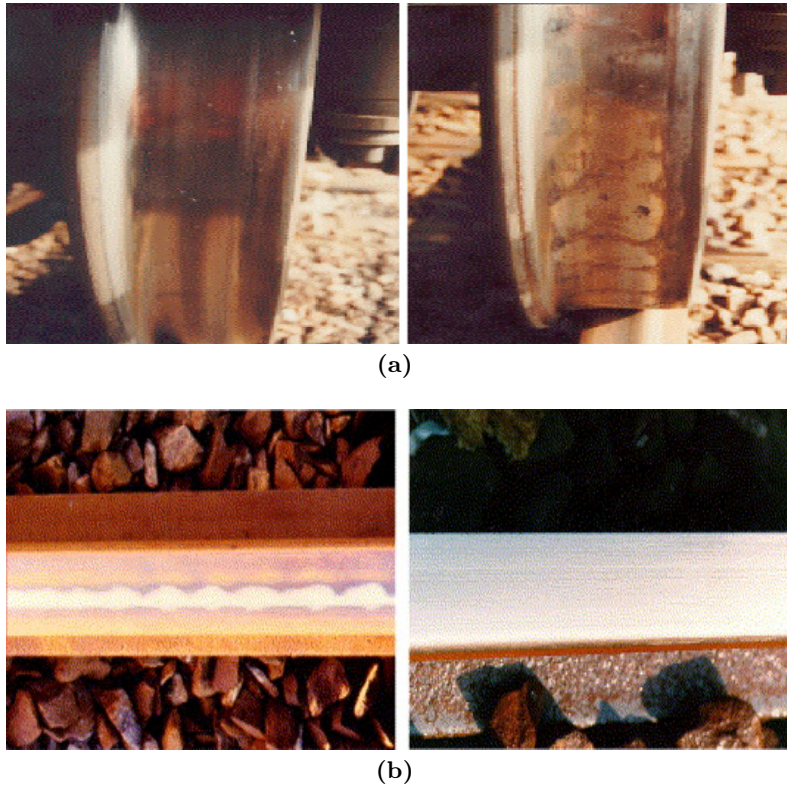


Figure 2.6: (a) Running surface of wheels equipped with: (left) disk brakes, (right) cast-iron block brakes. (b) Running surface of rail: (left) Before grinding, (right) after grinding with oscillating stones. Published in [4] and [147], respectively.

in the respective running surfaces due to brake change and grinding are exposed in Fig. 2.6. Also, it has been proposed to reduce roughness influence by modifying transverse curvatures of wheel and rail running surfaces in order to minimize contact force excitation [148], but more detailed calculations lead to inconclusive results [149]. Wheel/rail force mitigation in rolling noise through the use of fluid films has been also theorized, although no significant attenuation of interaction force has been achieved [150].

Leaving roughness minimization aside, several other techniques have been explored. A sample is shown as an example in Fig. 2.7. Thus, for the rail, tuned absorber systems are attached continuously along the beam in order to introduce higher damping and attenuate structural waves present [151]. In general,

tuned absorber systems are well-known devices useful for noise attenuation whose efficiency highly depends on track characteristics, in particular the pad stiffness [4]. In [152], field tests accomplish a broadband decrement in noise of ~ 6 dB in the range of 500 - 2000 Hz by using these devices combined with soft pads. Additionally, two types of damper tested in France, for example, show an overall reduction of 2 - 4 dB [153]. Similar rail damper tested in Germany, a picture of which is displayed in Fig. 2.7a, offered declines between 1.4 - 4 dB, depending on pad stiffness [154]. Indeed, variation of pad stiffness can have significant effects on railway noise. Through several experimental projects, improvements between 3 to 5 dB have been achieved by the use of stiffer and more damped pads [4]. Nonetheless, it should be borne in mind that an increase in the rigidity of the pad may lead to an increase in the radiation emitted by the sleeper. Hence, Vincent et al. state that the stiffness that equals rail and sleeper contribution would minimize global track radiation [155]. It is also important to note that using stiffer pads could lead to undesirable effects as a lesser protection of sleepers and ballast from impact loading [156] or an increase of rail corrugation growth [157].

If less conventional track types are considered, as ballastless tracks or slab tracks, different acoustic treatments have been explored in a search for re-dressing their noisier specifications, of about 2 - 4 dB greater than ballasted tracks [4]. With a combination of an absorption layer under the rail, covering the rail as much as possible with absorbent material and installing small barriers, as depicted in Fig. 2.7b, a less radiating track than ballasted is attained with a lowering of 6 dB [158]. An acoustically optimized “silent slab track” is also proposed in [159] by embedding the rail in a stiffer moulding material. With this method, an enhancement of 4 to 6 dB(A) is observed.

The use of local shielding measures as the small barriers mentioned above can be extended to other track systems. Thus, for a combination similar to that in Fig. 2.7c of low track-side barriers and bogie shrouds, i.e. skirts fixed on the bogie that shield wheel radiation, reductions of ~ 8 dB(A) are found in tests made for both tread-braked and disc-braked coaching stock [160]. When independently implemented, each appliance is expected to contribute in 3 - 4 dB(A) in the bogie shrouds case and 0 - 3 dB(A) for the low rail screens [161]. Wheel web shielding has been also tested with a result of a decrease of 5 - 6 dB on the wheel component of noise, depending on the speed [4, 60].

With regard to wheel-oriented rolling noise mitigation measures, there are multiple existing proposals, with different examples presented in Fig. 2.8. As with the track, wheel damping treatments are an effective way of noise attenuation. Thus, using tuned absorbers has been proven successful in increasing modal

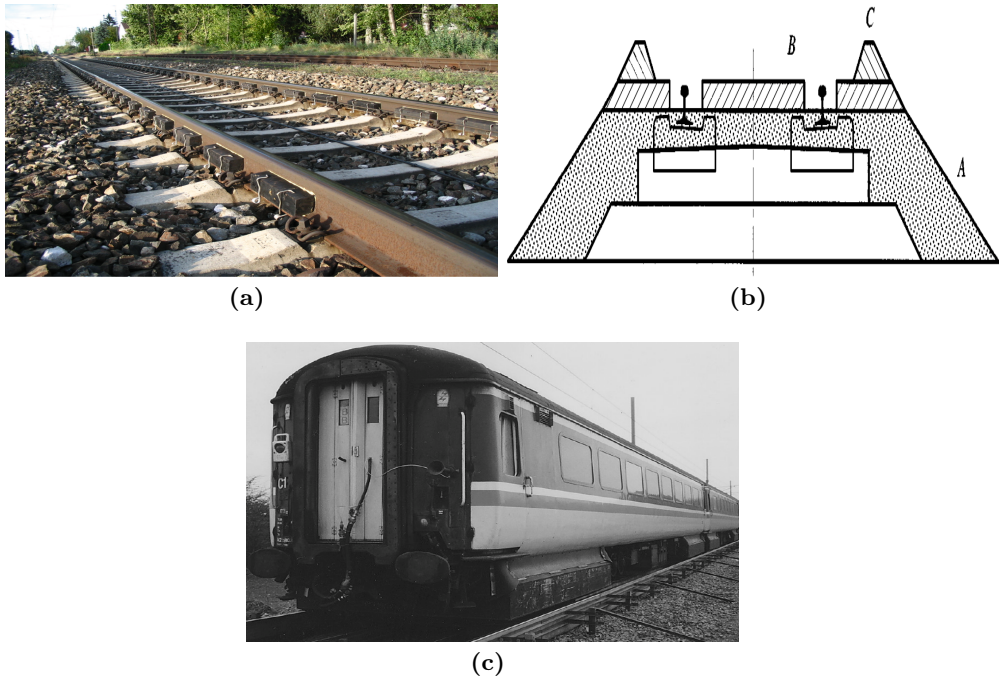


Figure 2.7: (a) Track section equipped with rail dampers. (b) Cross-section of ballastless track with absorption layer (A), rail shielding (B) and barrier (C). (c) Car with bogie shrouds on rails with barriers. Published in [154], [158] and [160], respectively.

damping ratios of the wheel [162] with a decrease in wheel noise from 4 to 8 dB [6] in configuration similar to that in 2.8a. For example, reductions of 5 - 8 dB(A) were reported in German trains at speeds of 200 km/h, although when applied to lower speeds, more modest cuts of 1 - 3 dB(A) were measured [4]. In [163], by using a configuration consisting of plate dampers divided into tuned absorber fins, displayed in 2.8b, improvements of 1 to 3 dB are achieved at 80 and 200 km/h, respectively. An alternative choice for adding damping is to apply a constrained layer treatment, that is, applying a thin layer of a highly-damped viscoelastic material in-between the wheel and a constraining plate. A schematic of this is observed in Fig. 2.8c. Decrements in wheel sound level of 3 - 5 dB are predicted in [61] for the case of a 1 mm layer of viscoelastic material and 1 mm of steel constraining plate, and in field tests for high speed train wheels, an overall rolling noise improvement of 4 - 5 dB has been observed [4]. Additionally, both tuned absorbers and constrained layer treatments are the only solutions capable of concentrating the damping strength in specific

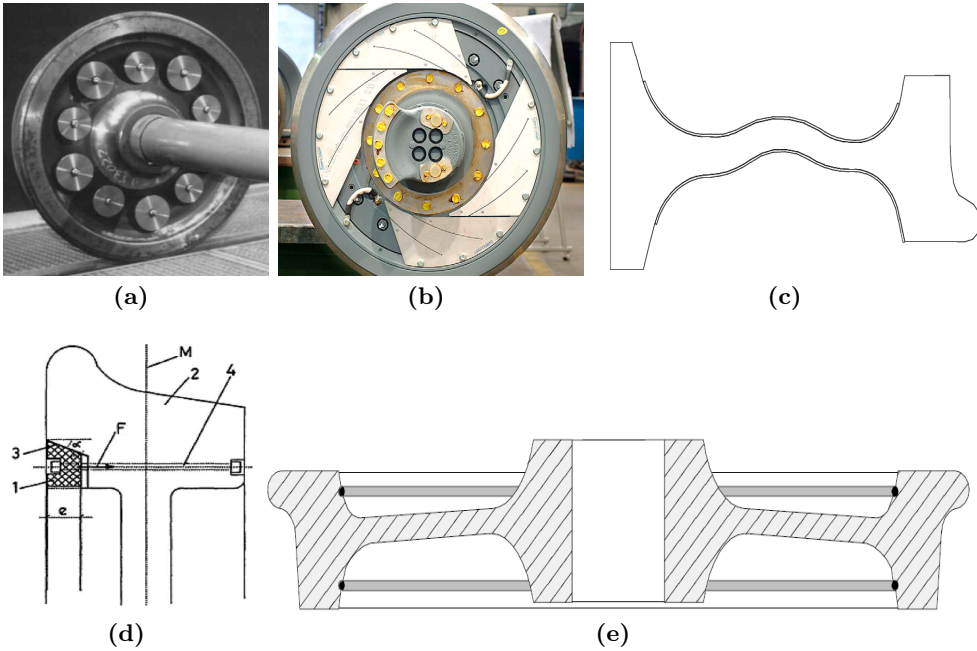


Figure 2.8: (a) Tuned absorbers in a wheel. (b) Plate wheel dampers divided into tuned absorber fins. (c) Cross-section of wheel with constrained layer damping. (d) Example of friction damper patented by CAF. (e) Cross-section schematic of a ring damped wheel. Extracted from [6], [4] (both (b) and (c)), [164] and [167], respectively.

frequency ranges [164]. Remaining damping focused techniques are friction dampers and damping rings, shown in Figs. 2.8d and 2.8e, respectively. The latter corresponds to a circular metallic ring placed in a groove created under the rim. The former is a variation of damping rings, where a ring with friction properties is screwed under the rim surface. They are usually designed for squeal noise attenuation with influence only at high frequencies [164], although some modest effect is observed in rolling noise [165] and they can be used to increase modal damping of the modes with more relevance to it [166]. Additional, their effectiveness is highly depending on the preload applied [167].

Another option for the wheel is to change its structure, creating new types of wheel. In this way, it is possible to find resilient and perforated wheels. Resilient wheels are made of two parts with rubber blocks in the middle of them. The positive effects on rolling noise can be: uncoupling of the web and tread, increase of damping, and decrease of mechanical impedance [168]. Thus, albeit

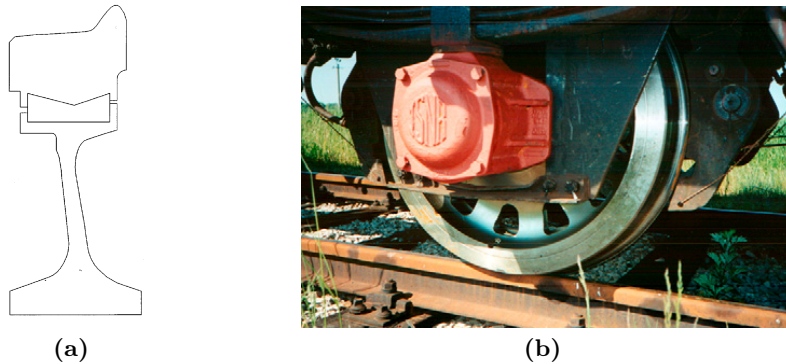


Figure 2.9: (a) Diagram of a resilient cross-section. (b) Wheel with a perforated web. Images are extracted from [61] and [4], respectively.

initially designed for squeal noise cancellation, Bouvet et al. show in [168] that it can be optimized for rolling noise mitigation. An overall reduction of 2.6 - 3.6 dB(A) is expected by tuning the resilient wheel to an uncoupling frequency amid 700 - 800 Hz, depending on the track. Besides, in [169], it is established that the resilient block properties are determinant to minimize acoustic emission for the case of rolling noise rather than the geometric properties of wheel. Then, Suarez et al., by the use of a FE model, also predict a lowering of the radiated noise with cutbacks of up to 7.2 dB for wheel radiation, but without taking into account possible track noise variations [170]. In the case of perforated wheels, the web is designed with a hole pattern in an attempt of reducing low frequency noise due to acoustic short circuiting [171]. This short circuiting is observed in [172–174], where perforated pattern is seen to have a considerable effect on acoustic radiation in baffled and unbaffled plates, with the number and size of the holes having a determinant effect. Later, Tong et al. predict a 2 dB reduction of wheel radiation in a parametric study using different numbers of circular or elliptic holes with the use of BEM [175]. In [171] a quieter wheel with a 6 - 9 dB improvement in the range below 1000 Hz is conjectured when holes are applied. Despite such promising expectations, when constructed and tested in field experiments, no noise decline was found, and just a more modest cut of 2.5 dB was reached when combined with a damped ring [4]. Examples of both wheel typologies can be seen in Fig. 2.9.

Up to this point, the use of geometric optimization techniques for both the wheel and rail with the intention of minimizing rolling noise radiation has

been omitted. This is due to the fact that they will be dealt separately in the following section.

2.2.3 Tackling rolling noise: optimization techniques in the search for quieter trains

Several examples of optimization techniques, in the broad sense, and in particular GA techniques, which are further explained in Section 3.2, can be found in the literature applied to the railway field. For example, in [176] GAs are used to minimise the maximum dynamic loads in transition zones between slab and ballasted tracks; or in [177] where a GA deals with finding a catenary geometry that improves current collection quality. This section will aim at those works focusing on the components more involved in rolling noise radiation.

Hence, one of the first works in which optimization techniques are applied to the track is reference [178]. In this work, Nielsen studies with a so-called fractional factorial design method the dynamic properties of a total of 16 different track configurations with the aim of minimizing the bending stresses in three positions: at railseat, at the centre of upper side of sleepers and under the rail cross-section positioned between sleepers. For this, beam elements are used to model a rail, 14 resilient pads and 14 sleepers on ballast treated to behave as Euler-Bernoulli beams on a Winkler foundation. Thus, rail or sleeper shape is not explicitly considered in the research. Unfortunately, no sound power calculation is made and, therefore, no noise related conclusions are extracted. By contrast, in [155] Vincent et al. do consider rolling noise, using SWL as the quantity to minimize in the parametric study. Radiated noise is computed using TWINS and for computations a ballasted track with two different models of a UIC60 rail on a bi-bloc sleeper with a 920 mm diameter wheel running at a speed of 100 km/h is used. The parameter assessment deals with rail pad properties as well as the use of external damping on the rail, and neither changes on the rail cross-section nor in the sleeper cross-section are accounted. With the described methodology, a configuration which offered gains of 3 dB less track radiated SWL is achieved, increasing this gain to 6 dB when using external damping devices. Additionally, it is found that, when varying the rail pad stiffness, a minimum in the track radiation occurs when the radiated sound power of the rail vertical and sleeper components becomes even. Nielsen also publishes an acoustic optimization in [179], this time focused on the railway sleeper. The author presents a dynamic model in where rail and sleepers are described with linear finite beam elements on a Winkler base, with rail pad represented as a damped spring system. With regard to the acoustic behaviour, a BEM model is implemented and, this time, sleeper shape is ex-

plicitly examined. The most important parameters determining noise radiation for the sleeper case are rail pad stiffness and ballast properties, with the influence of the sleeper shape on the sound radiation efficiency being negligible. As a result, an optimized bi-bloc sleeper is proposed capable of a predicted noise emission reduction of 2 - 3 dB. Attempts have also been made to find an optimal rail shape that minimizes noise, although no optimization techniques have been systematically used in them. Thus, by shortening rail size, both the radiating area and the radiation ratio would be affected in a way that leads to a diminishing sound emission [4]. From this perspective, British Steel and British Rail Research designed a short rail with a height of 110 mm, but field tests yielded inconclusive results. A rail with a narrower foot was also tried, lowering the rail component in 3 dB [4]. In [180], the gutter cross-section of an embedded track is optimized by using a combined BEM and FEM approach, arriving to designs radiating 3 dB(A) less noise, 4 dB(A) if the correct set of material parameters is chosen.

In the same manner, it is also feasible to look for a wheel shape that radiates the minimum possible noise. Three are the main principles behind this search [156]: minimizing the radiating area, conceiving a cross-section as symmetric as possible with the aim of decoupling radial and axial motion, and maximizing natural frequencies. With the aforementioned guidelines, different wheel designs have been projected with improvements ranging from 3 to 6 dB(A) [4, 156, 161]. It is with Efthimeros et al. [181], though, when one of the first exploratory research in the application of optimization algorithms to the wheel noise problem is developed, using GA optimization techniques for a geometric optimization of a railway wheel. For this, a parametric FE model with linear three-dimensional elements was used, with a cross-section geometry of the wheel defined by a set of parameters composed of thread and hub thicknesses and the fillet radii. Although the results obtained were promising, the objective function employed, based on the vibrating energy of the wheel, did not include a specific SWL calculation and the methodology did not completely approach some of the most influential aspects concerning rolling noise generation in wheels. The wheel-rail interaction model was not included in the work and, therefore, neither the dynamics of wheel nor the rail were considered. Thus, the magnitude used for accounting the emitted noise was purely based on the modal displacements of each modeshape, adopting a simplified radiation model that did not consider radiation efficiencies. Even so, a candidate with a 48.3% reduction of calculated radiated energy was achieved. When manufactured and acoustically tested, results showed the optimized wheel as 3 dB quieter than reference. Nielsen and Fredö [182] also published a Response Surface Methodology (RSM) with the purpose of tackling rolling noise

in wheels with a constrained damping layer. Specifically, the scope of the work was to develop a methodology capable of minimizing, under high speed operation, both dynamic wheel-rail contact loads and rolling noise while preventing weight increase. For the acoustic and dynamic modelling, TWINS was used, thus ensuring a full SWL calculation methodology that includes wheel/track interaction. The study was organized as a 3-level full factorial design, with a total of 81 wheel designs tested. For the FEM model, linear hexaedral elements were applied in a cross-section built from four different geometric parameters: wheel radius, web width, offset between hub and rim, and a fillet radii value. The track was introduced as a continuously supported Timoshenko beam and constrained layer damping effect was included through modified loss factors and a function of the Young modulus. In the results, a lessening of 3 dB with 9 kg of weight increase is achieved with the optimized design when no constrained layer damping is considered, and 11 dB with a gain of 14 kg when it is taken into account.

2.2.4 Beyond rolling noise: additional noise sources

Rolling noise is not the only source contributing to the railway sound. Although it is the most relevant under the operation conditions considered throughout this Thesis, there are other relevant types of sound that should not be omitted. Among these, the most significant are squeal and aerodynamic noise, but in some specific cases there are also additional noise sources that could be the prominent ones, as impact and bridge noise.

As all these typologies of noise are outside the scope of this study, they will not be discussed in detail. However, for the sake of completeness, the following section will provide a brief introduction to the basic notions of each.

2.2.4.1 Squeal noise

Squeal noise is a strongly tonal noise emitted at high frequencies that usually occurs when the railway vehicle negotiates sharp curves. It arises from the self-excited vibration of the wheel [4] and its tonal frequency is attributed to modeshapes of axial wheel modes with zero nodal circumferences [183–185]. Usually, this sound is found in the range between 2000 and 8000 Hz [186], and in some occasions, even up to frequencies as high as 10000 Hz [187].

It is more likely to appear in small radius curves. Indeed, a ratio between the curve radius and the bogie wheelbase can be used to determine the probability

of this noise to happen [129, 188]. More precisely, if the curve radius $R < 100b$, with b being the bogie wheel base, squeal noise is expected to emerge [189].

Regarding its generation mechanism, the main consensus nowadays is to consider that unsteady lateral creepage between wheel tyre and the top of the rail is the most likely reason [4]. In this stick-slip contact behaviour phenomenon, unstable vibration can materialize as a result of a falling behaviour of the wheel/rail friction coefficient [189].

2.2.4.2 Aerodynamic noise

Aerodynamic noise is generated by the flow of air over the train created by railway vehicles operating at high speeds [4]. It is the main source of noise from trains when travelling at speeds of 300 - 350 km/h or above. The pantograph, whose noise generation is mainly due to vortex shedding around its cylindrical parts [190], is considered to be the main radiation source of this particular noise [191]. Additionally, as it is located on the roof of the train, they are less affected by possible presence of noise barriers [191]. Other relevant sources for aerodynamic radiation are the bogie, the inter-coach spacing, the nose of the power car, the coach walls, the rear power car, the louvres and the cooling fans [192]. Its radiated noise level is considered to have a dependency on the vehicle speed V of $60 \log_{10} V$ [4]. Besides, although relatively broadband, is dominated by tonal contributions and, most of its acoustic energy is concentrated in the low frequency range under 500 Hz and tonal contributions [4, 193, 194].

2.2.4.3 Bridge noise

The term bridge noise refers to the particular specifications of railway emitted noise when running across a bridge. In this situation, it usually produces more noise with increases that vary depending on the characteristics of the bridge, typically of ~ 5 dB for concrete bridges and ~ 10 dB for steel bridges [4, 195]. In the concrete case, sound is concentrated just below 300 Hz [196], but in steel bridges it can be important up to 1000 Hz [197].

Two effects are the main responsible of such increment. Firstly, vibrations generated during the train pass by are transmitted to the bridge, making the structure to radiate noise. Secondly, depending on the rail fastening system, vibrations of the rail in that section could be greatly enhanced [4].

2.3 Wheel dynamic model

The vibration of the wheel is one of the main contributors to sound radiation associated with rolling noise. Therefore, a model capable of describing the wheel dynamic behaviour is needed. With this aim, a description and characterization of the dynamic properties of the wheel is achieved on the basis of its modeshapes and natural frequencies [4, 45]. Throughout this section, the wheel models employed in the research developed in the present Thesis are further explained: first, details on the railway wheel characterization are offered, later the derivation of the wheel receptance and response in the frequency domain is explained and, lastly, a simplified time domain model, used for the perforation scheme optimization described in Section 3.3.1, is presented.

2.3.1 Railway wheel characterization

As any other structure, railway wheels can have a set of resonances associated with natural frequencies and, due to their light damping and axisymmetric nature, these resonances strongly characterize their vibration [4]. Therefore, the first step for describing the wheel vibration is to determine and classify its modeshapes or modes of vibration, which are later used in the modelling of the dynamic behaviour. Such modeshapes resemble those of a flat circular plate, with the modes being categorized by the number of nodal diameters and nodal circumferences they have [45]. Hence, modeshapes can be classified with a (n, m) notation according to the number of nodal diameters n , which determines the distribution of the amplitude of vibration along the perimeter of the disc, and nodal circumferences m , which determines the vibration amplitude through the radial coordinate [45, 50]. This way, a modeshape takes the form of $A \cos(n \Theta)$ around a perimeter of the wheel, where A is the maximum amplitude achieved in the perimeter and Θ is the angular coordinate. The same description would apply for the amplitude distribution through the radial direction but using the number of nodal circumferences m instead. For illustration purposes Fig. 2.10 shows several modeshapes and their respective classification.

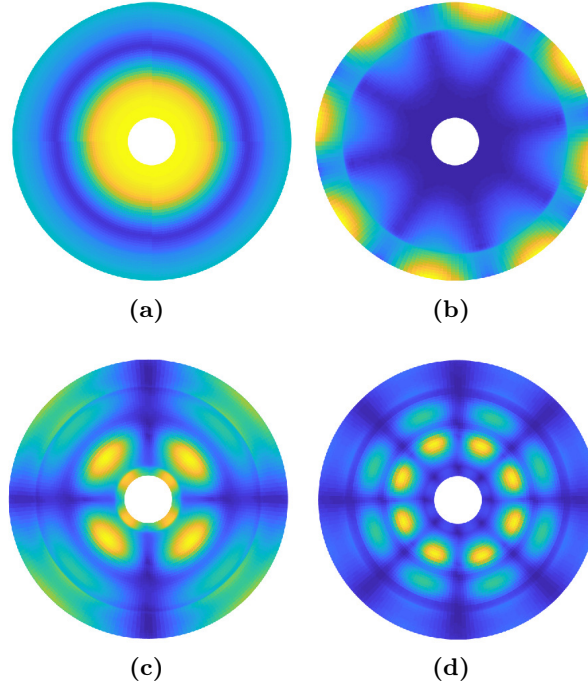


Figure 2.10: Example of modeshapes of a railway wheel and its corresponding (n, m) classification. (a): $(n = 0, m = 1)$; (b): $(n = 4, m = 0)$; (c): $(n = 2, m = 1)$; (d): $(n = 4, m = 2)$.

2.3.2 Wheel receptance function

In order to derive the receptance of the wheel, its response is formulated by considering a mass-spring system with damping [4]. Then, such system with N degrees of freedom (d.o.f). is described as [198]:

$$\mathbf{M} \ddot{\mathbf{u}} + \mathbf{C} \dot{\mathbf{u}} + \mathbf{K} \mathbf{u} = \mathbf{F} \quad (2.3)$$

where mass matrix \mathbf{M} describes the inertial properties, \mathbf{C} the damping of the system, stiffness matrix \mathbf{K} the elastic properties, \mathbf{u} is the displacement vector and \mathbf{F} the external force. Then, if a harmonic solution $\mathbf{u} = \tilde{\mathbf{u}} e^{i\omega t}$ and force $\mathbf{F} = \tilde{\mathbf{F}} e^{i\omega t}$ oscillating at angular frequency ω are assumed, Eq. (2.3) can now be written as

$$-\omega^2 \mathbf{M} \tilde{\mathbf{u}} + i\omega \mathbf{C} \tilde{\mathbf{u}} + \mathbf{K} \tilde{\mathbf{u}} = \tilde{\mathbf{F}} \quad (2.4)$$

Consequently, as the modal matrix Ψ_{nm} , in which its columns are formed by the eigenvectors (modeshapes), is known, it is possible to express Eq. (2.4) in modal coordinates \tilde{q}_{nm} for mode (n, m) as

$$-\omega^2 m_{nm} \tilde{q}_{nm} + i\omega c_{nm} \tilde{q}_{nm} + k_{nm} \tilde{q}_{nm} = \tilde{Q}_{nm} \quad (2.5)$$

where \tilde{Q}_{nm} is the modal force amplitude, m_{nm} is the modal mass defined as $m_{nm} = \Psi_{nm}^T \mathbf{M} \Psi_{nm}$, the modal stiffness k_{nm} is given by $k_{nm} = m_{nm} \omega_{nm}^2$, and considering a spectral modal damping $c_{nm} = 2 \xi_{nm} m_{nm} \omega_{nm}$.

It is now possible from Eq. (2.5) to finally obtain wheel receptance \mathbf{H}_w . Hence, by making use of modal superposition, the receptance in the case of a stationary wheel is derived as [45]

$$H_{w,jk}(\omega) = \sum_{n=0}^{\infty} \sum_{m=0}^{\infty} \frac{\Psi_{nm,j} \Psi_{nm,k}}{m_{nm} (\omega_{nm}^2 - \omega^2 + 2i\xi_{nm} \omega_{nm} \omega)} \quad (2.6)$$

where, as stated above, $\Psi_{nm,j}$ and $\Psi_{nm,k}$ are the modal amplitudes of the modeshape (n, m) for direction j and k , respectively, m_{nm} is the modal mass of the corresponding modeshape, ξ_{nm} its modal damping ratio, ω_{nm} is the natural frequency of the corresponding modeshape and ω the angular frequency at which the receptance is calculated. It should be noted that both radial and axial modeshapes are included in the modal superposition.

2.3.3 Wheel response in the frequency domain

The system describing rolling noise generation mechanism is composed by a continuously supported rail and a wheel interacting at the contact point. The rail is described either as a Timoshenko beam [199], as described in Section 2.4.2, or by the complex rail cross-section model described in Section 2.4.3, while the wheel/track interaction in the radial and axial directions is modelled by a contact spring. In regard to the excitation of the system, it is generated by the introduction of a roughness amplitude which is assumed to act only in the vertical direction [5]. Therefore, when the wheel travels along the rail, this roughness amplitude generates a relative movement between the wheel/track system which produces a contact force \mathbf{F}_c . In addition, a contact filter [4, 12]

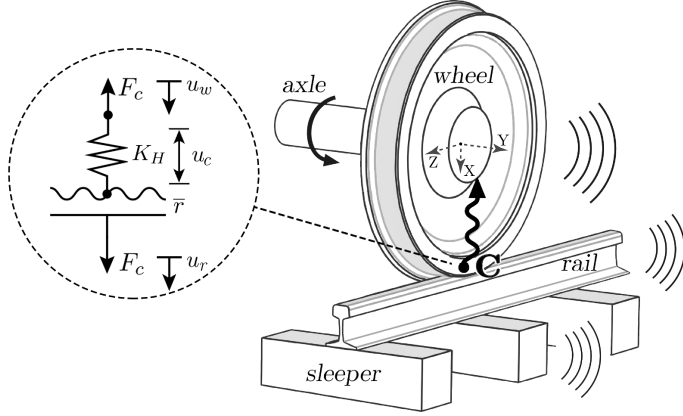


Figure 2.11: Wheel/track interaction model.

is applied in order to consider the attenuation effect of the contact patch size in the force. A diagram of the model can be seen in Fig. 2.11.

Then, assuming a roughness amplitude r , the displacements in the system are related as [5]

$$\mathbf{u}_w = \mathbf{u}_r + \mathbf{u}_c - \bar{\mathbf{r}} \quad (2.7)$$

where \mathbf{u}_w , \mathbf{u}_r and \mathbf{u}_c are the displacements of the wheel, rail and contact, respectively, and $\bar{\mathbf{r}}$ is a vector with amplitude r in the vertical direction. This is clearly seen in the zoomed area of Fig. 2.11. Under a contact force \mathbf{F}_c acting on the systems, the displacements are defined by

$$\mathbf{u}_w = -\mathbf{H}_w \mathbf{F}_c \quad (2.8)$$

$$\mathbf{u}_r = \mathbf{H}_r \mathbf{F}_c \quad (2.9)$$

$$\mathbf{u}_c = \mathbf{H}_c \mathbf{F}_c \quad (2.10)$$

Combining Eqs. (2.8)-(2.10) in Eq. (2.7) and rearranging, the dynamics of the system can be expressed as

$$\bar{\mathbf{r}} = \mathbf{H}_{sys} \mathbf{F}_c \quad (2.11)$$

where \mathbf{H}_{sys} is the combined receptance of the system defined as [4]

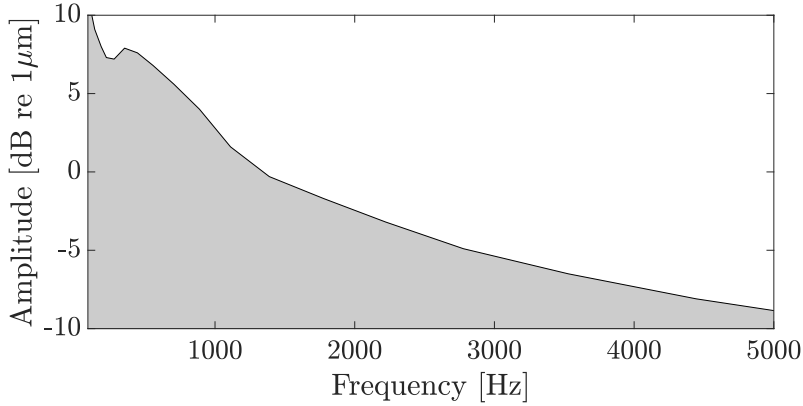


Figure 2.12: Frequency spectrum of the roughness defined by DIN-prEN 13979-1 [200] for a vehicle moving at 80 km/h and cast-iron block brakes.

$$\mathbf{H}_{sys} = \mathbf{H}_w + \mathbf{H}_r + \mathbf{H}_c \quad (2.12)$$

with \mathbf{H}_w , \mathbf{H}_r and \mathbf{H}_c being the receptances in matrix form of the wheel, rail and contact, respectively, which are defined later.

Regarding the excitation of the system used throughout the present Thesis, when the approach being considered is the above explained frequency model, the roughness considered is defined by the standard DIN-prEN 13979-1 [200] for the corresponding train speed. An example of this roughness for a speed of $V = 80$ km/h is expressed in one-third octave bands in Fig. 2.12.

Once the contact force \mathbf{F}_c has been derived, it is immediate to obtain the response of the wheel for the j th d.o.f.

$$u_{w,j} = - \sum_{i=1}^3 H_{w,ji} F_{c,i} \quad (2.13)$$

where $H_{w,ji}$ is the receptance of the wheel for the j th d.o.f. when the force is applied at the contact point in the i th direction and $F_{c,i}$ is the value of the contact force in the i th direction; directions 1, 2 and 3 represent directions x (radial), y (axial) and z (longitudinal), respectively.

As for the derivation of \mathbf{H}_w , it has already been explained in Section 2.3.2. Meanwhile, the rest of receptances corresponding to each component of the system necessary to build the global receptance and to solve the dynamic interaction problem, \mathbf{H}_r and \mathbf{H}_c , are studied with further detail in the Sections 2.4.2 and 2.5.2, respectively.

2.3.4 Wheel response in the time domain: simplified formulation

For the study of the effect of perforated schemes in wheels, whose optimization algorithm and results are described in Sections 3.3.1 and 4.3, respectively, a simplified time domain model is adopted for the computation of the wheel velocity response [11, 201].

In such procedure, first, a previously computed time dependent force spectrum $\mathbf{F}_c(t)$ is considered with t_{sam} time samples number. This dynamic contact force, acting on the wheel contact point, is obtained by solving the wheel-rail interaction problem while considering a Hertzian contact model. The excitation applied is composed through using the roughness central wavelengths and amplitude values defined according to the standard ISO3095, and combining each with a pseudo-random generated phase [202]. In addition, the contact force taken into account in such approach considers a train velocity of $V = 160$ km/h and a system of wheel-set and track parameters extracted from the interaction model described in [55]. The resulting force is displayed on Fig. 2.13 both as a function of time (a) and frequency (b).

Then, similar to Eq. (2.5), it is possible to express Eq. (2.3) in modal coordinates for each modeshape (n, m) as

$$\ddot{q}_{nm} + \omega_{nm}^2 q_{nm} = Q_{nm} \quad (2.14)$$

with modal displacements q_{nm} normalized to unitary modal mass m_{nm} , considering no modal damping and with the generalized force Q_{nm} defined by

$$Q_{nm} = \Psi_{nm}^T \mathbf{F}_c(t) \quad (2.15)$$

By solving Eq. (2.14), the modal velocity is derived and, lastly, it is transformed into physical coordinates as

$$\mathbf{v}(t) = \sum_n \sum_m \Psi_{nm} \dot{q}_{nm} \quad (2.16)$$

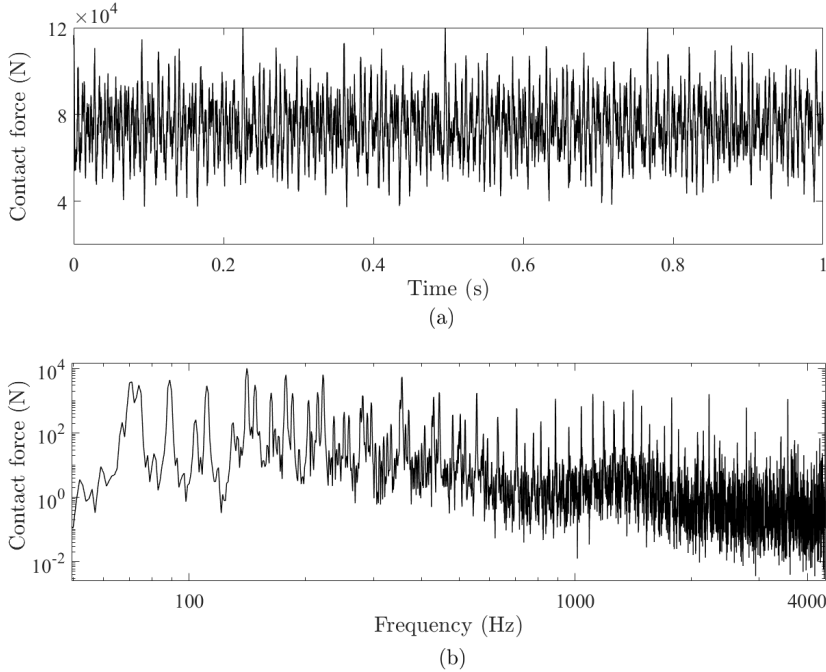


Figure 2.13: Contact force signal in: (a) time domain and (b) frequency domain.

where $\mathbf{v}(t)$ is the velocity response needed for the posterior derivation of wheel SWL.

2.4 Track dynamic model

Rail is the other major contributor to the rolling noise together with the wheel. A standard track structure is composed by the rails themselves and a support consisting of a sleeper with rail pad in between on a foundation of a layer of stones named ballast, as schematically shown in the previous section in Fig. 2.2.

In this case, its behaviour can not be predicted using as a base a set of vibration modes as, contrary to the wheel, the track is essentially a highly damped infinite structure and, therefore, it has no proper resonance modes. Instead, it acts as a waveguide where different structural waves can coexist at a particular frequency [4].

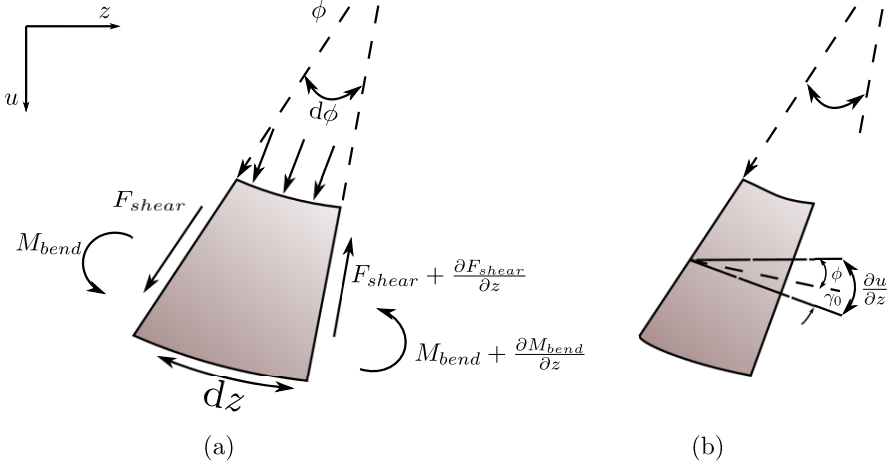


Figure 2.14: (a) Differential element of beam subjected to a load. (b) Detail on kinematic effects of shearing deformation. Figure based on [204].

As with the wheel, FRFs are used in order to describe the dynamics of the rail. Accordingly, two approaches are followed for the receptance derivation: by considering a rail behaving as a Timoshenko beam on a continuously supported foundation, allowing the inclusion of shear deformation and rotational inertia [4, 68, 203] (Section 2.4.1); or by a 2.5D finite element approach developed with the inclusion of periodic system properties [81] capable of including the cross-section deformation [76] (Section 2.4.3).

2.4.1 Timoshenko beam

Timoshenko beam theory was first developed in [205] with the aim of improving the accuracy of Euler-Bernoulli beams, which neglected the shear deformation due to the hypothesis that plane sections remain plane and, as rotary inertia effects were not included, predicted infinite phase velocities [204]. These inaccuracies are tackled in the Timoshenko beam by establishing a relationship between bending moment and curvature in a beam element and implementing a shear force. Hence, a beam element as the one described in Fig. 2.14, subjected to a distributed load $q(z, t)$, shear force F_{shear} and bending moment M_{bend} , is considered. Also, a coordinate ϕ , which represents the rotation of the cross-section relative to the undeformed axis, is introduced to measure the cross-section slope caused by bending. In the described element, the slope of the centroidal axis is given by

$$\frac{\partial u}{\partial z} = \phi + \gamma_0 \quad (2.17)$$

with γ_0 representing the contribution attributed to the shear effects. Besides, the relationship between bending moment and curvature in a beam element is established as [204]

$$\frac{M_{bend}}{EI} = -\frac{\partial \phi}{\partial z} \quad (2.18)$$

where E is the Young modulus and I is the second moment of area of the cross-section. As with regard of the shear force F_{shear} at the cross-section, it is given in terms of the shear strain γ_{strain} by

$$F_{shear} = G \int_A \gamma_{strain} dA = AG\kappa\gamma_0 \quad (2.19)$$

where A the cross-section area, G the shear modulus and κ is the shear coefficient. Therefore, if Eq. (2.17) is combined with Eq. (2.19), the shear force can be finally expressed as

$$F_{shear} = AG\kappa \left(\frac{\partial u}{\partial z} - \phi \right) \quad (2.20)$$

where u corresponds to the deflection. Hence, the resulting governing equations are [204]

$$GA\kappa \left(\frac{\partial \phi}{\partial z} - \frac{\partial^2 u}{\partial z^2} \right) + \rho A \frac{\partial^2 u}{\partial t^2} = q(z, t) \quad (2.21)$$

$$GA\kappa \left(\frac{\partial u}{\partial z} - \phi \right) + EI \frac{\partial^2 \phi}{\partial z^2} = \rho I \frac{\partial^2 \phi}{\partial t^2} \quad (2.22)$$

with ρ being the density and $q(z, t)$ the function describing the load. Thompson in [4] adapts Eqs. (2.21) and (2.22) by considering a harmonic point excitation force F acting on the rail over a continuous elastic foundation, where rail pads, sleepers and ballast are included and which is described by a spring-mass-spring system [58] illustrated in Fig. 2.15. Additionally, damping of the rail is included by introducing a loss factor η_r in the Young modulus $\tilde{E} = E(1 + i\eta_r)$

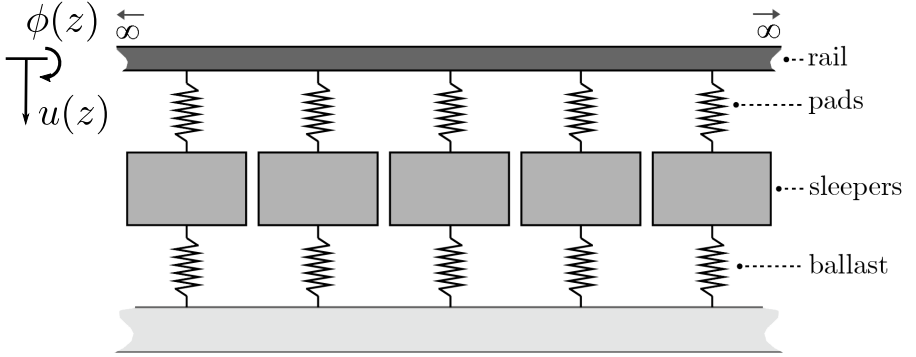


Figure 2.15: Rail track modelled as a Timoshenko beam on an elastic continuous foundation described by a spring-mass-spring system .

and shear factor $\tilde{G} = G(1 + i\eta_r)$, the resulting equations of motion being [4, 91]:

$$\tilde{G}A\kappa \left(\frac{\partial \phi}{\partial z} - \frac{\partial^2 u}{\partial z^2} \right) + \tilde{k}_{stiff} u + \rho A \frac{\partial^2 u}{\partial t^2} = F\delta(z)e^{i\omega t} \quad (2.23)$$

$$\tilde{G}A\kappa \left(\phi - \frac{\partial u}{\partial z} \right) - \tilde{E}I \frac{\partial^2 \phi}{\partial z^2} + \rho I \frac{\partial^2 \phi}{\partial t^2} = 0 \quad (2.24)$$

with $\delta(z)$ is the Kronecker delta [206] and \tilde{k}_{stiff} represents the combined stiffness of the foundation

$$\tilde{k}_{stiff} = \frac{\tilde{k}'_p(\tilde{k}'_b - m'_s\omega^2)}{\tilde{k}'_p + \tilde{k}'_b - m'_s\omega^2} \quad (2.25)$$

where $\tilde{k}'_p = k'_p(1 + i\eta_p)$ and $\tilde{k}'_b = k'_b(1 + i\eta_b)$. k'_p , k'_b and m'_s are the rail pad stiffness, ballast stiffness and sleeper mass respectively, divided by the spacing between sleepers (stiffness and mass per unit length); and η_b and η_p represent the ballast and pad damping loss factor, respectively.

2.4.2 Rail receptance function

For an adequate description of wheel/track interaction, the direct receptance of the rail in the contact point is needed. With the intention of deriving it, free wave solutions for Eqs. (2.23) and (2.24) are considered with the form

$$u_r(z, t) = U e^{i\omega t} e^{-ikz} \quad (2.26)$$

$$\phi_r(z, t) = U_\phi e^{i\omega t} e^{-ikz} \quad (2.27)$$

where u_r and ϕ_r refer to the corresponding free wave solutions for the rail, U and U_ϕ are complex amplitudes corresponding to each wave and ω and k correspond to the angular frequency and wavenumber, respectively. Introducing these in Eq. (2.24) results in

$$U_\phi = U \frac{\tilde{G}A\kappa s}{\tilde{G}A\kappa - \rho I\omega^2 - \tilde{E}I s^2} \quad (2.28)$$

with $s = -ik$ being a complex propagation factor. Then, substituting Eqs. (2.27) and (2.28) into Eq. (2.23) and rearranging yields [91]

$$\frac{U}{F} = -\frac{1}{\tilde{G}A\kappa} \frac{s^2 + C_1(\omega)}{s^4 + C_2(\omega) s^2 + C_3(\omega)} \quad (2.29)$$

with

$$C_1(\omega) = \frac{-\tilde{G}A\kappa + \rho I\omega^2}{\tilde{E}I} \quad (2.30)$$

$$C_2(\omega) = \frac{\rho I\omega^2}{\tilde{E}I} - \frac{1}{\tilde{G}A\kappa} \left(\frac{\tilde{k}'_p(\tilde{k}'_b - m'_s\omega^2)}{\tilde{k}'_p + \tilde{k}'_b - m'_s\omega^2} - \rho A\omega^2 \right) \quad (2.31)$$

$$C_3(\omega) = \frac{\tilde{G}A\kappa - \rho I\omega^2}{\tilde{G}A\kappa\tilde{E}I} \left(\frac{\tilde{k}'_p(\tilde{k}'_b - m'_s\omega^2)}{\tilde{k}'_p + \tilde{k}'_b - m'_s\omega^2} - \rho A\omega^2 \right) \quad (2.32)$$

Thus, the direct receptance of the rail in the contact point for a given direction $H_{r,jj}$ is obtained by [203]

$$H_{r,jj}(\omega) = \frac{1}{2\pi i} \int_{-i\infty}^{i\infty} -\frac{1}{\tilde{G}A\kappa} \frac{s^2 + C_1(\omega)}{s^4 + C_2(\omega) s^2 + C_3(\omega)} ds \quad (2.33)$$

This way, Eq. (2.33) is integrated in the complex domain by means of the Theory of Residues [207], which yields

$$H_{r,jj}(\omega) = \sum_{\substack{k \text{ with} \\ \operatorname{Re}(s_k) < 0}} \operatorname{Res}(s_k) \quad (2.34)$$

with

$$\operatorname{Res}(s_k) = \frac{-1}{\tilde{G}A\kappa} \frac{s_k^2 + C_1(\omega)}{4s_k^3 + 2C_2(\omega)s_k} \quad (2.35)$$

where s_k corresponds to the permissible complex propagation constants of free vibration for a given excitation frequency ω . As indicated previously, structural damping is included in the definition of the Young modulus, such as $\tilde{E} = E(1 + i\eta_r)$, and in the shear modulus $\tilde{G} = G(1 + i\eta_r)$, η_r being the loss factor of the rail [4]. Therefore, by using the physical properties of the rail for the vertical and lateral directions with the above described formulation the direct receptances in each those directions, $H_{r,xx}$ and $H_{r,yy}$ respectively, are computed.

With respect to the cross receptance $H_{r,xy}$, due to the absence of coupling between motion in the x and y direction it is not possible to predict it with the Timoshenko formulation. Still, in practice, this cross-coupling between a vertical force and a lateral response is not negligible and should be therefore computed. Consequently, it is derived in the form of a geometrical average of vertical receptance $H_{r,xx}$ and lateral receptance $H_{r,yy}$ as [58]

$$H_{r,xy}(\omega) = X \sqrt{H_{r,xx}(\omega)H_{r,yy}(\omega)} \quad (2.36)$$

where the parameter X is obtained from an empirically estimated factor from track characterization tests with

$$L_X = 20 \log |X| \quad (2.37)$$

using a value of $X = 0.1778$ and $L_X = -15$ dB in this work, being the best value to fit the numerical and experimental results in the track type used (bibloc track) [36, 58].

Besides, it should be noted that there is a frequency limit for the application of the described model, defined by that frequency where the condition $\rho I \omega^2 \geq GA\kappa$ is met. As a consequence, the sign of C_3 is inverted and all four solutions are imaginary, therefore defining the range from which the Timoshenko beam formulation is no longer valid [91]. The frequency range used for the results presented in Chapter 4 lies completely within this range.

2.4.3 Deformable track cross-section model

When higher precisions than that offered by the Timoshenko beam approach are required, it is necessary to take into account the cross-section deformation of the rail. Such deformation is especially relevant at high frequencies, particularly above 1500 Hz for the lateral vibration and 2000 Hz for the vertical one [4]. In the model detailed through the present section, this is done by considering a short length of a continuously supported track section and, later, solving the dynamics of the whole track by considering its periodical properties.

This track section element is connected end to end forming an infinite structure by making use of transfer matrix theory [81]. The element nodes are divided between left-side and right-side nodes and the response of each set is related to one another. Then, the infinite track is assumed to be conformed by an infinite repetition of the defined element structure, in which the left-side nodes of the $p + 1$ th element would equal the right-side ones of the p th element. This way, by solving the dynamics considering just one of the periodic elements, the whole dynamic behaviour of the track is characterized. A brief schematic diagram of the described methodology is presented in Fig. 2.16. It is also worth noting that each element would incorporate one node representing the track foundation to be able to derive its dynamic and acoustic properties if needed.

In the studied case, therefore, the behaviour of the track can be explained through the combination of waveshapes propagating along the structure and their corresponding wavenumbers, from which receptance is derived. Thus, by considering an infinite structure of length L , the equation of motion in matrix form is defined by [198]

$$((\mathbf{I} + i\mathbf{C})\mathbf{K} - \omega^2\mathbf{M})\tilde{\mathbf{q}} = \tilde{\mathbf{F}} \quad (2.38)$$

where \mathbf{K} is the stiffness matrix, \mathbf{M} is the mass matrix, ω is the angular frequency, $\tilde{\mathbf{q}}$ represents the vector with the corresponding d.o.f. and $\tilde{\mathbf{F}}$ the force

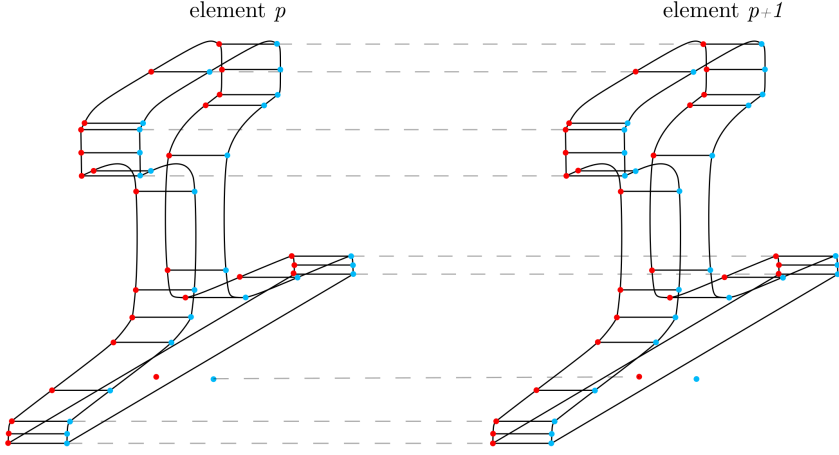


Figure 2.16: Schematic representation of the track element p and $p + 1$ interconnected in the $p_{\text{right}}-(p + 1)_{\text{left}}$ boundary. Left-side nodes are presented in red and right-side nodes in blue.

applied. Damping is introduced with the structural damping loss factor matrix \mathbf{C} , each of whose components corresponds to the assigned damping loss factor associated with each component of \mathbf{K} and are conformed by a combination of rail η_r , rail pad η_p and ballast η_b loss damping factors. This way, the combination $(\mathbf{I} + i\mathbf{C})\mathbf{K}$ is analogous to a complex stiffness matrix with the structural damping incorporated. In such matrix, the elements corresponding to nodes of the rail foot would correspond to the addition in parallel of rail and pad stiffnesses, those corresponding to the sleeper node would be assigned with the composed stiffness of pad and ballast while, in the d.o.f. corresponding to the sleeper-rail foot union, the stiffness used would be that of the rail pad.

Now, coordinates are divided into two groups: $\tilde{\mathbf{q}}_L$, which correspond to those on the element left end, and $\tilde{\mathbf{q}}_R$, representing those in the right end. Forces and matrices are correspondingly re-arranged, resulting in

$$\begin{bmatrix} \mathbf{D}_{LL} & \mathbf{D}_{LR} \\ \mathbf{D}_{RL} & \mathbf{D}_{RR} \end{bmatrix} \begin{Bmatrix} \tilde{\mathbf{q}}_L \\ \tilde{\mathbf{q}}_R \end{Bmatrix} = \begin{Bmatrix} \tilde{\mathbf{F}}_L \\ \tilde{\mathbf{F}}_R \end{Bmatrix} \quad (2.39)$$

with $\mathbf{D}_{LL,LR,RL,RR}$ being the left-left, left-right, right-left and right-right, respectively, of matrix \mathbf{D} defined as

$$\mathbf{D} = (\mathbf{I} + i\mathbf{C})\mathbf{K} - \omega^2\mathbf{M} \quad (2.40)$$

In the case of free wave motion, it is characterized by the displacements of one element being equal to that of the adjacent element times e^s [81], s being a propagation constant. Therefore, taking into account that track is a continuous structure, elements are connected and that there should be an equilibrium in the inter-connecting forces between adjacent elements, it is established that

$$\tilde{\mathbf{q}}_R = e^s \tilde{\mathbf{q}}_L \quad (2.41)$$

$$\tilde{\mathbf{F}}_R = -e^s \tilde{\mathbf{F}}_L \quad (2.42)$$

By introducing Eqs. (2.41) and (2.42) into Eq. (2.39), free wave response of the system can be derived, reformulated as

$$\left(\begin{bmatrix} \mathbf{D}_{RL} & \mathbf{D}_{RR} \\ \mathbf{0} & \mathbf{I} \end{bmatrix} + e^s \begin{bmatrix} \mathbf{D}_{LL} & \mathbf{D}_{LR} \\ -\mathbf{I} & \mathbf{0} \end{bmatrix} \right) \begin{Bmatrix} \tilde{\mathbf{q}}_L \\ \tilde{\mathbf{q}}_R \end{Bmatrix} = \mathbf{0} \quad (2.43)$$

which can be solved as an eigenvalue problem in which each $s_n = -ik_n$ and eigenvectors $\{\tilde{\mathbf{q}}_L, \tilde{\mathbf{q}}_R\}_n^T = \Psi_n$, with k_n and Ψ_n being the corresponding wavenumber and waveshape, respectively.

It is seen that, as $\tilde{\mathbf{q}}_L$ and $\tilde{\mathbf{q}}_R$ are related according to Eq. (2.41), in order to solve the problem only N equations of the $2N$ composing Eq. (2.43) are needed. Thus, the problem can be reduced by considering just the solutions corresponding to one end, which corresponds to the left end in the present case. Consequently, Eq. (2.43) reduces to

$$((e^s)^2 \mathbf{D}_{LR} + e^s(\mathbf{D}_{RR} + \mathbf{D}_{LL}) + \mathbf{D}_{RL}) \tilde{\mathbf{q}}_L = \mathbf{0} \quad (2.44)$$

that, for ulterior simplification reasons, is reformulated as

$$(\mathbf{D}_{RR} + \mathbf{D}_{LL} + e^s \mathbf{D}_{LR} + e^{-s} \mathbf{D}_{RL}) \tilde{\mathbf{q}}_L = \mathbf{0} \quad (2.45)$$

Additionally, as the track element is taken as periodic along the z direction, a series of symmetry conditions must be made in the edge of the element. This way, if continuity of the structure is to be granted, the displacements of nodes on the left side of the n th element in the x and y directions must be symmetric

with respect displacements of right side nodes of element $n - 1$ and vice-versa. The contrary applies for the z direction, where an anti-symmetry condition occurs. Consequently, depending on whether the d.o.f. are symmetric (i.e. that corresponding to x and y) or antisymmetric (i.e. corresponding to z), $\mathbf{D}_{LL,LR,RL,RR}$ elements fulfil

$$\begin{aligned} D_{RR,ij} &= D_{LL,ij} \\ D_{RL,ij} &= D_{LR,ij} \end{aligned} \quad \text{for } i, j \text{ both sym. or antisym.} \quad (2.46)$$

and

$$\begin{aligned} D_{RR,ij} &= -D_{LL,ij} \\ D_{RL,ij} &= -D_{LR,ij} \end{aligned} \quad \text{for } i, j \text{ of different kind} \quad (2.47)$$

Now, if the symmetry conditions are considered, matrix values of Eq. (2.45) can be expressed by

$$\begin{aligned} D_{RR,ij} + D_{LL,ij} + e^s D_{LR,ij} + e^{-s} D_{RL,ij} &= \\ 2D_{LL,ij} + (e^s + e^{-s})D_{LR,ij} &= \quad \text{for } i, j \text{ both sym. or antisym.} \\ 2(D_{LL,ij} + \cosh(s)D_{LR,ij}) & \end{aligned} \quad (2.48)$$

or

$$\begin{aligned} D_{RR,ij} + D_{LL,ij} + e^s D_{LR,ij} + e^{-s} D_{RL,ij} &= \\ (e^s - e^{-s})D_{LR,ij} &= \quad \text{for } i, j \text{ of different kind} \\ 2 \sinh(s)D_{LR,ij} & \end{aligned} \quad (2.49)$$

By using the developments in Eqs. (2.48) and (2.49), and by splitting the solutions between symmetric d.o.f. (S) and antisymmetric d.o.f. (A), Eq. (2.45) is reformulated as

$$\begin{bmatrix} \cosh(s) \mathbf{D}_{LR}^{SS} + \mathbf{D}_{LL}^{SS} & \sinh(s) \mathbf{D}_{LR}^{SA} \\ \sinh(s) \mathbf{D}_{LR}^{AS} & \cosh(s) \mathbf{D}_{LR}^{AA} + \mathbf{D}_{LL}^{AA} \end{bmatrix} \begin{Bmatrix} \tilde{\mathbf{q}}_L^S \\ \tilde{\mathbf{q}}_L^A \end{Bmatrix} = \mathbf{0} \quad (2.50)$$

where $\mathbf{D}_{LL,LR}^{SS,AA}$ and $\mathbf{D}_{LL,LR}^{SA,AS}$ contain the sym.-sym. (SS), sym.-antisym. (SA) or vice-versa (AS) and antisym.-antisym. (AA) components of the corresponding \mathbf{D} matrices; and $\tilde{\mathbf{q}}_L^{S,A}$ represents the $\tilde{\mathbf{q}}_L$ components corresponding to the symmetric and antisymmetric d.o.f., respectively.

Now, in order to rearrange Eq. (2.50) in a form in which it could be solved as an eigenproblem, it is multiplied as

$$\begin{bmatrix} \cosh(s) + 1 & 0 \\ 0 & \sinh(s) \end{bmatrix} \cdot \begin{bmatrix} \cosh(s) \mathbf{D}_{LR}^{SS} + \mathbf{D}_{LL}^{SS} & \sinh(s) \mathbf{D}_{LR}^{SA} \\ \sinh(s) \mathbf{D}_{LR}^{AS} & \cosh(s) \mathbf{D}_{LR}^{AA} + \mathbf{D}_{LL}^{AA} \end{bmatrix} \begin{Bmatrix} \tilde{\mathbf{q}}_L^S \\ \tilde{\mathbf{q}}_L^A \end{Bmatrix} = \mathbf{0} \quad (2.51)$$

which, by applying a little algebra and making use of hyperbolic trigonometric functions identities, it can be expressed as

$$\begin{bmatrix} \cosh(s) \mathbf{D}_{LR}^{SS} + \mathbf{D}_{LL}^{SS} & (\cosh(s) + 1) \mathbf{D}_{LR}^{SA} \\ (\cosh(s) - 1) \mathbf{D}_{LR}^{AS} & \cosh(s) \mathbf{D}_{LR}^{AA} + \mathbf{D}_{LL}^{AA} \end{bmatrix} \cdot \begin{bmatrix} \cosh(s) + 1 & 0 \\ 0 & \sinh(s) \end{bmatrix} \begin{Bmatrix} \tilde{\mathbf{q}}_L^S \\ \tilde{\mathbf{q}}_L^A \end{Bmatrix} = \mathbf{0} \quad (2.52)$$

that can be reformulated as the eigenvalue problem equation

$$\left(\begin{bmatrix} \mathbf{D}_{LL}^{SS} & \mathbf{D}_{LR}^{SA} \\ -\mathbf{D}_{LR}^{AS} & \mathbf{D}_{LL}^{AA} \end{bmatrix} + \cosh(s) \begin{bmatrix} \mathbf{D}_{LR}^{SS} & \mathbf{D}_{LR}^{SA} \\ \mathbf{D}_{LR}^{AS} & \mathbf{D}_{LR}^{AA} \end{bmatrix} \right) \begin{Bmatrix} \tilde{\mathbf{q}}_L^S \\ \tilde{\mathbf{q}}_L^A \end{Bmatrix} = \mathbf{0} \quad (2.53)$$

with

$$\tilde{\mathbf{q}}_L^S = (\cosh(s) + 1) \tilde{\mathbf{q}}_L^S \quad (2.54)$$

$$\tilde{\mathbf{q}}_L^A = \sinh(s) \tilde{\mathbf{q}}_L^A \quad (2.55)$$

Once solved, it will be possible to derive the two existing solutions for $\tilde{\mathbf{q}}_L^S$ and $\tilde{\mathbf{q}}_L^A$ associated with waves travelling to the left ($s > 0$) or to the right ($s < 0$), choosing in the present case the right propagating waves and obtaining this way the solutions for the d.o.f. of the nodes in the left $\tilde{\mathbf{q}}_L$. By combining all the resulting solution vectors $\tilde{\mathbf{q}}_L$ for each $s_n = -ik_n$, the waveshape matrix of the rail Ψ is obtained. Meanwhile, the respective right-side solutions $\tilde{\mathbf{q}}_R$ are immediately available by the definition in Eq. (2.41).

Additionally, from Eqs. (2.54) and (2.55) it is possible to define the matrix of the left propagating waveshape Ψ^* . Thus, for each wavenumber $-k_n$, the corresponding left-propagating waveshape values Ψ_{jn}^* are given by

$$\Psi_{jn}^{*S} = \Psi_{jn}^S \quad (2.56)$$

$$\Psi_{jn}^{*A} = -\Psi_{jn}^A \quad (2.57)$$

As soon as the derivation of the free wave response is completed by solving Eq. (2.43), and having computed Ψ , it is possible to proceed with the receptance. Considering the force \tilde{F} acting on the boundary between two rail elements as the one defined at the beginning of the section, named $(-)$ and $(+)$ respectively, and setting there $z = 0$, it is immediate that a continuity boundary condition can be defined. Therefore,

$$\tilde{q}_R^{(-)} = \tilde{q}_L^{(+)} \quad (2.58)$$

In addition, motion in physical coordinates for the positive and negative sides of the beam is described by the superposition of N waves as [82]

$$u_{r,j}(z) = \sum_{n=1}^N A_n \Psi_{jn} e^{-ik_n z} \text{ for } z \geq 0 \quad (2.59)$$

$$u_{r,j}(z) = \sum_{n=1}^N B_n \Psi_{jn}^* e^{ik_n z} \text{ for } z \leq 0 \quad (2.60)$$

where Ψ_{jn} , Ψ_{jn}^* are the j th component of the n th waveshape propagating in the positive and negative direction, respectively, k_n refers to the n th wavenumber and A_n and B_n the generalized coordinates corresponding to the n th waveshape.

Hence, taking into account Eq. (2.58), it is immediate that

$$\Psi \mathbf{A}_n = \Psi^* \mathbf{B}_n \quad (2.61)$$

with \mathbf{A}_n and \mathbf{B}_n being vectors including each A_n and B_n , respectively. For $(+)$ element right and left coordinates:

$$\tilde{q}_L^{(+)} = \Psi A_n \quad (2.62)$$

$$\tilde{q}_R^{(+)} = \Psi' A_n \quad (2.63)$$

where $\Psi'_n = \Psi_n e^{-ik_n L}$, L being the element length. In the case of element $(-)$,

$$\tilde{q}_R^{(-)} = \Psi^* B_n = \Psi A_n \quad (2.64)$$

$$\tilde{q}_L^{(-)} = \Psi^{*'} B_n \quad (2.65)$$

with $\Psi_n^{*'} = \Psi_n^* e^{-ik_n L}$.

Thus, by introducing Eqs. (2.62)-(2.65) in Eq. (2.39), the force component for each element side can be written as

$$\tilde{F}_L^{(+)} = (\mathbf{D}_{LL} \Psi + \mathbf{D}_{LR} \Psi') A_n \quad (2.66)$$

$$\tilde{F}_R^{(-)} = (\mathbf{D}_{RL} \Psi^{*'} + \mathbf{D}_{RR} \Psi^*) B_n \quad (2.67)$$

Additionally, by considering that $B_n = \Psi^{*-1} \Psi A_n$, which is immediate to observe from Eq. (2.61), right side force of element $(-)$ is rewritten as

$$\tilde{F}_R^{(-)} = (\mathbf{D}_{RL} \Psi^{*'} \Psi^{*-1} \Psi + \mathbf{D}_{RR} \Psi) A_n \quad (2.68)$$

Consequently, force can be stated as

$$\tilde{F} = \tilde{F}_L^{(+)} + \tilde{F}_R^{(-)} = \left(\mathbf{D}_{LL} \Psi + \mathbf{D}_{LR} \Psi' + \mathbf{D}_{RL} \Psi^{*'} \Psi^{*-1} \Psi + \mathbf{D}_{RR} \Psi \right) A_n \quad (2.69)$$

Finally, in order to obtain the point receptance used for the rail $\mathbf{H}_r(\omega)$, given that $\mathbf{u}_r = \Psi A_n$ at $z = 0$, the following expression can be used

$$H_r(\omega) = \Psi \left(\mathbf{D}_{LL} \Psi + \mathbf{D}_{LR} \Psi' + \mathbf{D}_{RL} \Psi^{*'} \Psi^{*-1} \Psi + \mathbf{D}_{RR} \Psi \right)^{-1} \quad (2.70)$$

for the given angular frequency ω at which waveshapes have been computed.

2.4.4 Rail response

The rail response is calculated in an identical manner than that used for the wheel in Section 2.3.3. Thus, after having obtained \mathbf{H}_{sys} and \mathbf{F}_c , it would be immediate to compute the rail response \mathbf{u}_r with Eq. (2.9). Accordingly, response for the j th d.o.f. is given by

$$u_{r,j} = \sum_{i=1}^3 H_{r,ji} F_{c,i} \quad (2.71)$$

where $H_{r,ji}$ is the receptance of the rail for the j th d.o.f. when the force is applied at the contact point in the i th direction and $F_{c,i}$ is the value of the contact force in the i th direction. Again, directions 1, 2 and 3 represent directions x (radial), y (axial) and z (longitudinal) respectively.

Besides, it is also useful to calculate the average response of the rail over a given length, averaged quantity that would be later used in the rail SWL expression as detailed in Section 2.6.2. For a rail length L defined in the positive longitudinal region $z \geq 0$, its response along z direction would be expressed by Eq. (2.59). Then, the spatially-averaged squared response for a given d.o.f. j reads

$$\begin{aligned} \overline{u_{r,j}^2} &= \frac{2}{L} \int_0^\infty |u_{r,j}(z)|^2 dz \approx \sum_n |\psi_{jn}|^2 |A_n|^2 \left(\frac{2}{L} \int_0^\infty e^{-2\delta_n z} dz \right) = \\ &= \sum_n |\psi_{jn}|^2 |A_n|^2 \left(\frac{1}{\delta_n L} \right) \end{aligned} \quad (2.72)$$

where δ_n is the real part of the complex wavenumber k_n . The approximation followed in Eq. (2.72), consisting in taking the summation over n outside the square, is justified by the fact that when the wavelengths of any two waves differ, the integral of their cross terms tends to 0 for a long enough length L [58].

From Eq. (2.72) it is now possible to define the spatially-averaged squared generalized coordinate $\overline{A_n^2}$ for wave n in a way that

$$\overline{u_{r,j}^2} \approx \sum_n |\psi_{jn}|^2 \overline{A_n^2} \quad (2.73)$$

where

$$\overline{A_n^2} = |A_n|^2 \left(\frac{1}{\delta_n L} \right) \quad (2.74)$$

2.5 Wheel/track interaction model

The wheel/track interaction and the corresponding contact force resulting from the roughness excitation are modelled in this work with the use of Hertzian contact springs. Thus, the interaction described by the contact springs is expressed in the form of a contact receptance in both the radial and transversal direction. Additionally, as the contact is not produced in a single point and instead is given around an area, the effect such phenomenon has in the excitation is also considered with the use of a contact filter.

2.5.1 The contact patch

The contact patch, that is, the area where interaction between wheel and rail occurs, is produced as a result of the local elastic deformation of each body involved [102] and its size is directly related to the normal load present in the system. Even though the contact model developed in the Thesis is based on a single contact point, it is necessary to include this contact patch effect in the computation.

More specifically, the region depends on the normal load F_0 following a non-linear relation and, as schematically presented in Fig. 2.17, it presents an elliptical shape whose size is determined through the use of Hertz theory [103]. Its semi-axis in the rolling direction a and in the transverse direction b , which are later used in the contact receptance calculation in Section 2.5.2, are given by [4]

$$a = \mu \left(\frac{3F_0 r_e}{2E^*} \right)^{\frac{1}{3}} \quad (2.75)$$

$$b = \sigma \left(\frac{3F_0 r_e}{2E^*} \right)^{\frac{1}{3}} \quad (2.76)$$

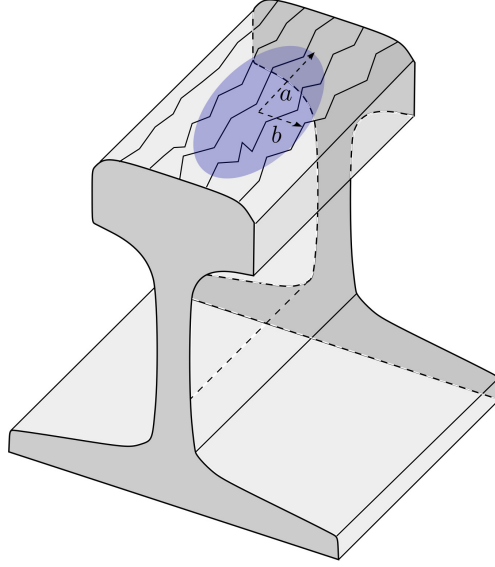


Figure 2.17: Diagram of a rail section with irregular lines representing roughness and the contact patch with semi-axis a and b depicted by the purple ellipse.

where $E^* = E/(1 - \nu^2)$ is the plain strain elastic modulus assuming both wheel and rail have the same material properties, with ν being the Poisson's ratio, and r_e is the effective curvature radius of surfaces in contact derived from

$$r_e = 2 \left(\frac{1}{r_1^W} + \frac{1}{r_2^W} + \frac{1}{r_1^R} + \frac{1}{r_2^R} \right)^{-1} \quad (2.77)$$

with r_1^W and r_1^R being the radii in the rolling direction of wheel and rail, respectively, and r_2^W and r_2^R the radii in the transverse direction. In any case, it is worth mentioning that, due to the usual operating conditions of railway vehicles, it is generally considered that $r_1^R \rightarrow \infty$ [4]. In Fig. 2.18, a scheme with a representation of the above mentioned radii is presented for clarification.

Parameters μ and σ , whose theoretical derivation is developed in [105, 106], are obtained through interpolation in Table 2.1, in where Θ equals to

$$\Theta = \cos^{-1} \left(\frac{r_e}{2} \left(-\frac{1}{r_1^W} + \frac{1}{r_2^W} - \frac{1}{r_1^R} + \frac{1}{r_2^R} \right) \right) \quad (2.78)$$

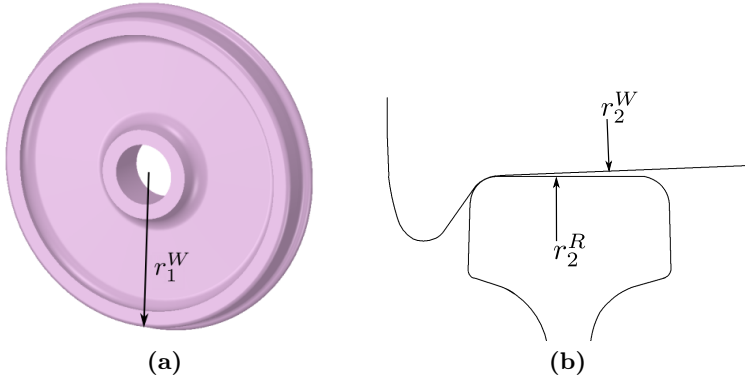


Figure 2.18: Example of radii of curvature in the radial direction for the wheel r_1^W and the transverse direction for each component r_2^W and r_2^R .

For the sake of completeness, it is worth mentioning that both μ and σ can be explicitly derived from the expressions [4, 105, 106]

$$\mu = \left(\frac{2g^2 \mathbf{E}(e)}{\pi} \right)^{\frac{1}{3}} \quad (2.79)$$

$$\sigma = \left(\frac{2\mathbf{E}(e)}{\pi g} \right)^{\frac{1}{3}} \quad (2.80)$$

where \mathbf{E} is the complete elliptic integral of the second kind and

$$g = \frac{a}{b} \quad (2.81)$$

$$e = 1 - \frac{1}{g^2} \quad (2.82)$$

Table 2.1: Values of parameters μ and σ as a function of Θ .

Θ [°]	30	35	40	45	50	55	60	65	70	75	80	85	90
μ	2.731	2.397	2.136	1.926	1.754	1.611	1.486	1.378	1.284	1.202	1.128	1.061	1.0
σ	0.493	0.530	0.567	0.604	0.641	0.678	0.717	0.759	0.802	0.846	0.893	0.944	1.0

2.5.2 Contact receptance function

As mentioned, the interaction between wheel and rail is described by means of a contact spring which allows modelling the contact receptance through a stiffness caused by local contact deformations. Hence, using Hertz theory, if small displacement amplitudes produced through the interaction are considered, a contact receptance in the vertical direction can be defined as [102]

$$H_{c,xx} = \frac{1}{K_H} \quad (2.83)$$

where K_H is the linearised contact stiffness for the vertical direction. Following the formulation of Eqs. (2.79) and (2.80), the approach of two bodies u_0 resulting from a load F_0 is given by

$$u_0 = \frac{\xi}{2r_e} \left(\frac{3F_0 r_e}{2E^*} \right)^{\frac{2}{3}} \quad (2.84)$$

and the linearised contact stiffness is related as

$$K_H^{-1} = \frac{du_0}{dF_0} \quad (2.85)$$

Combining Eqs. (2.84) and (2.85) results in

$$K_H = \frac{2}{\xi} \left(\frac{3E^{*2} r_e F_0}{2} \right)^{1/3} \quad (2.86)$$

where r_e is the effective radius of curvature of the surfaces in contact, F_0 is the normal load and ξ is a dimensionless factor that depends on the radii of curvature of the surfaces in contact and is derived with Kalker's methodology [208] from Table 2.2.

Table 2.2: Values of parameter $\xi/2$ as a function of Θ .

Θ [°]	30	35	40	45	50	55	60	65	70	75	80	85	90
$\xi/2$	0.727	0.775	0.817	0.855	0.887	0.913	0.938	0.957	0.972	0.985	0.993	0.998	1.000

Table 2.3: Non-linear Kalker creep coefficient C_{22} as a function of g and ν . (a) $b > a$ case; (b) $a > b$ case.

(a)				(b)			
$g = \frac{a}{b}$	ν			$g = \frac{b}{a}$	ν		
	0	$\frac{1}{4}$	$\frac{1}{2}$		0	$\frac{1}{4}$	$\frac{1}{2}$
0.1	2.51	2.52	2.53	1	3.40	3.67	3.98
0.2	2.59	2.63	2.66	0.9	3.51	3.81	4.16
0.3	2.68	2.75	2.81	0.8	3.65	3.99	4.39
0.4	2.78	2.88	2.98	0.7	3.82	4.21	4.67
0.5	2.88	3.01	3.14	0.6	4.06	4.50	5.04
0.6	2.98	3.14	3.31	0.5	4.37	4.90	5.56
0.7	3.09	3.28	3.48	0.4	4.84	5.48	6.31
0.8	3.19	3.41	3.65	0.3	5.57	6.40	7.51
0.9	3.29	3.54	3.82	0.2	6.96	8.14	9.79
				0.3	10.7	12.8	16.0

For the receptance in the lateral direction, the lateral contact stiffness is combined with the creep forces present in the low frequency region [113]. A simplified equivalent formulation [132] is used where the lateral receptance is defined as

$$H_{c,yy} = \frac{1}{K_L} - i \frac{V}{Gc^2 C_{22} \omega} \quad (2.87)$$

V being the train speed, G is the shear modulus, $c^2 = ab$, C_{22} is the corresponding non-dimensional creep coefficient developed by Kalker [108] and extracted from Table 2.3 [209], and

$$K_L = K_H \left[1 + \frac{\nu}{1 - \nu} \left(\frac{1}{4} + \frac{1}{\pi} \arctan\left(\frac{a}{b}\right) \right)^{1/3} \right]^{-1} \quad (2.88)$$

is the transverse contact stiffness in the lateral direction.

2.5.3 Roughness filter

When modelling rolling noise phenomenon, the way the roughness is perceived during the wheel/track interaction is susceptible to the size of the contact patch surface. In the cases where the roughness wavelength is small compared to the size of the contact patch in the rolling direction, the running surface of the wheel moves over the surface of the rail without noticing this precise irregularity in the interaction area and, therefore, the excitation generated becomes attenuated [12]. This effect is known as the “contact filter”.

In order to account for this phenomenon, a contact filter transfer function is defined which modifies the calculated sound power. The formulation is derived from a simplified version of the work of P. J. Remington [12] which shows that, for a circular contact patch of radius a , the transfer function is given by

$$|H(k)|^2 = \frac{4}{\beta(ka)^2} \int_0^{\arctan(\beta)} J_1^2(ka \sec(\psi)) d\psi \quad (2.89)$$

with $k = 2\pi/\lambda$ being the wavenumber along the length of the rail or around the circumference of the wheel (λ denotes the wavelength), β is a constant determining the degree of correlation among parallel roughness profiles at a given wavenumber and J_1 is the Bessel function of the first kind and order 1.

Eq. (2.89) can be approximated to the simplified filter function [4] used in the present work

$$|H(k)|^2 = \left(1 + \frac{\pi}{4}(ka)^3\right)^{-1} \quad (2.90)$$

where a will take the value of the semi-axis in the rolling direction. A representation of the simplified contact filter function for different values of ka is shown in Fig. 2.19.

2.6 Sound power radiation

A detailed study of the rolling noise and the search for ways of reducing it require not only the dynamic properties of the system to be obtained but also the ability to calculate the resulting acoustic power. Thereby, in this section the models used for the calculation of the main components of the rolling noise are described. Hence, first the procedure followed for the wheel is detailed in

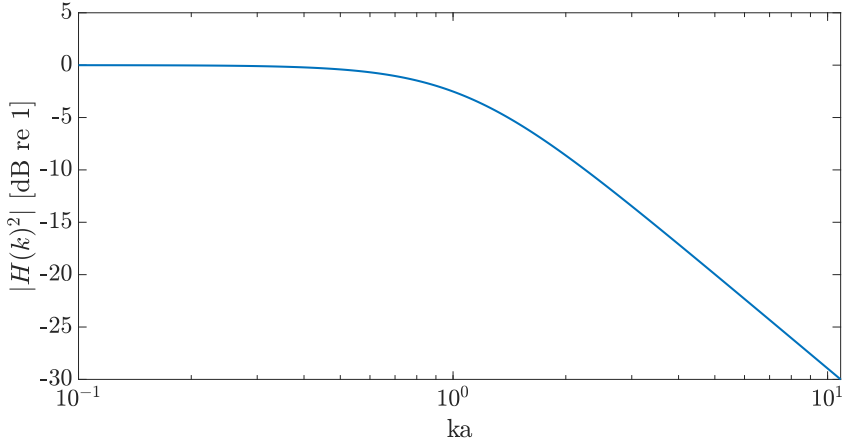


Figure 2.19: Simplified contact filter function $|H(k)|^2$ for different values of ka .

Section 2.6.1 and, thereafter, the same is done for the track case in Section 2.6.2.

2.6.1 Wheel sound power

One of the main purposes of the present Thesis is achieving less sound radiating designs for railway wheels and, evidently, in doing so it is necessary to explicitly compute the sound power radiated by them. To this end, the wheel surface is initially divided into six concentric rings, whose areas and velocities are used for calculating the axial contribution to the sound radiation [91]. For illustrative purposes, an exemplification of a wheel divided into six circular areas (from r_1 to r_7) is presented in Fig. 2.20, together with their velocities and the geometric parameters used in the sound power computation. In addition, for the case of the radial contribution to acoustic radiation, the combined surfaces of the external and internal side of the tyre are used (with r_{int} and r_w).

Once the wheel/track system dynamics is solved by means of the methodology described in this chapter, and due to the harmonic behaviour of motion considered, the velocity for each of the concentric rings and for the contact point is calculated as

$$\tilde{v} = i\omega \tilde{u} \quad (2.91)$$

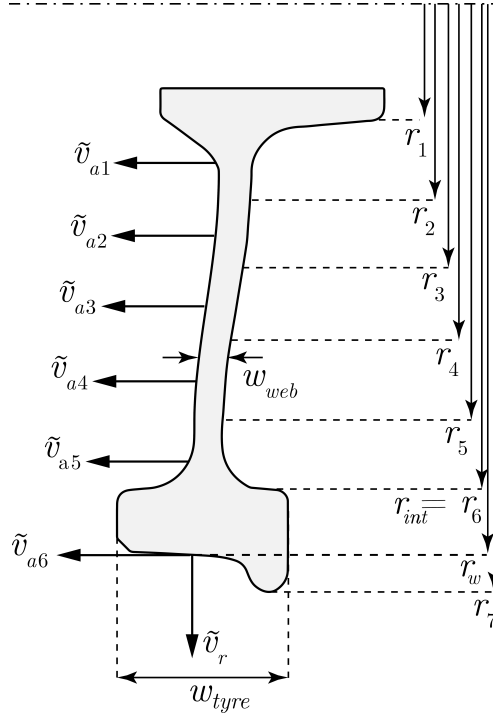


Figure 2.20: Cross-sectional illustration of geometry parameters used in wheel radiation model.

where \tilde{u} refers to the wheel vibration displacement amplitude.

After that, it is possible to extend the sound power formulation [4] to the wheel through

$$W_w = \rho c_0 \sum_{l=1}^{N_m} \left(\sigma_l^a \sum_{j=1}^6 (S_{a,j} \langle \tilde{v}_{a,jl}^2 \rangle) + \sigma_l^r S_r \langle \tilde{v}_{r,l}^2 \rangle \right) \quad (2.92)$$

where W_w is the wheel sound power, index l refers to each the N_m modeshapes, $\langle \tilde{v}_{a,jl}^2 \rangle$ and $\langle \tilde{v}_{r,l}^2 \rangle$ to the mean squared velocity averaged over time and surface area for the axial and radial directions, respectively, associated with l^{th} mode-shape and surface ring j ; ρ is the air density, c_0 the speed of sound, $S_{a,j}$ the area of the j^{th} ring, S_r the area used for the radial radiation and σ_l^a and σ_l^r

are the radiation efficiencies [210] for the l^{th} mode for the axial and radial contribution, respectively. Surfaces used in the calculation are defined by

$$S_{a,j} = 2\pi (r_{j+1}^2 - r_j^2) \quad (2.93)$$

$$S_r = 2\pi (r_w w_{tyre} + r_{int}(w_{tyre} - w_{web})) \quad (2.94)$$

where r_j and r_{j+1} are the radii defining the concentric rings as shown in Fig. 2.20, r_w is the wheel radius, r_{int} is the inner tyre radius, w_{tyre} is the tyre width and w_{web} is the web width.

2.6.1.1 Wheel radiation efficiencies

Radiation efficiencies are defined as the ratio expressing the amount of actual acoustic power radiated to that of a piston of the same area on an infinite wall vibrating uniformly with the same average quadratic velocity at a frequency such that the diameter of the piston considerably exceeds the acoustic wavelength, or in other words, that the Helmholtz number $ka \gg 1$ [210].

For the acoustic efficiencies computation, the formulation developed explicitly for railway wheels in [59] is used, as it meets the requirements needed, i.e. allowing a fast method to calculate each of the acoustic efficiencies while maintaining the required accuracy. To do so, a semi-analytical formulation is developed, defining them as a function of frequency, radius of the wheel and number of nodal diameters.

In the case of the axial acoustic radiation, the formula applied is

$$\sigma^a = \frac{1}{1 + \left(\frac{f_1^a}{f}\right)^{2n+4}} \quad (2.95)$$

where n is the number of nodal diameters of the modeshape under consideration and f_1^a is a transition frequency defined as

$$f_1^a = \frac{c_0 l}{2\pi r_w} \quad (2.96)$$

in which l is a scaling parameter with value:

$$l = 1.90 + 1.015 n - 0.0189 n^2 \quad (2.97)$$

For the radial case, instead, the acoustic efficiency is defined by

$$\sigma^r = \begin{cases} \frac{\Gamma}{1 + \left(\frac{f_2^r}{f}\right)^2} & \text{if } n = 0 \\ \frac{\Gamma}{1 + \left(\frac{f_1^r}{f}\right)^{2n}} \frac{1}{1 + \left(\frac{f_3^r}{f}\right)^2} & \text{if } n > 0 \end{cases} \quad (2.98)$$

with

$$\Gamma = \begin{cases} \sqrt{\frac{S_{ext} - S_{int}}{S_{ext} + S_{int}}} & \text{for } f < f_3^r \\ 1 & \text{for } f \geq f_3^r \end{cases} \quad (2.99)$$

and

$$f_1^r = \frac{120 n}{\sqrt{r_w/0.42}} \quad (2.100)$$

$$f_2^r = \frac{800}{\sqrt{r_w/0.42}} \quad (2.101)$$

$$f_3^r = \frac{280 + 150 n}{\sqrt{r_w/0.42}} \quad (2.102)$$

where S_{int} and S_{ext} are the areas of the inner and outer surfaces of the tyre, respectively. Those areas, that composed yields the total radial surface S_r , defined in Eq. (2.94), are calculated as follows

$$S_{int} = 2\pi r_{int} (w_{tyre} - w_{web}) \quad (2.103)$$

$$S_{ext} = 2\pi r_w w_{tyre} \quad (2.104)$$

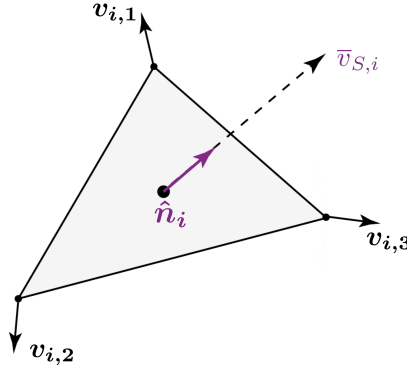


Figure 2.21: Velocities of vertices and projected surface velocity of an arbitrary surface i .

2.6.1.2 Wheel noise in the three-dimensional case

When the perforated wheel approach is used, the sound power W_w is computed over the whole three-dimensional surface. Instead of the six rings division, wheel is divided into N_s triangular radiating surfaces, each one vibrating in the normal direction with an effective mean squared surface velocity $\langle \tilde{v}_S^2 \rangle$ averaged over space and time.

Once the velocity for each d.o.f. is obtained, following the procedure explained in Section 2.3.4, v_S is derived by averaging the velocity of the surface triangle vertices and projecting that onto the vector normal to the surface. The methodology is illustrated for a triangular surface shown in Fig. 2.21 with respective vertex velocities, effective surface velocity and normal unit vector. Each $\bar{v}_{S,i}(t)$ corresponding to the effective velocity of the triangular surface i in the time domain is written as

$$\bar{v}_{S,i}(t) = \frac{\sum_{l=1}^3 \mathbf{v}_{i,l}(t)}{3} \cdot \hat{\mathbf{n}}_i \quad (2.105)$$

where $\hat{\mathbf{n}}_i$ refers to the normal unit vector to the surface i and $\mathbf{v}_{i,l}(t)$ corresponds to each vertex l of the i th triangle.

Then, in order to compute sound power W_w , the velocity $\langle \tilde{v}_{S,i}^2 \rangle$ in the frequency domain is derived through the Fourier transform of $\bar{v}_{S,i}^2(t)$. W_w can be expressed now as

$$W_w = \rho c_0 \sum_{i=1}^{N_S} \langle \bar{v}_{S,i}^2 \rangle S_i \quad (2.106)$$

with S_i being the area of the i th triangle. It has to be noted that, in this case, no acoustic efficiency is considered. As the three-dimensional model is applied in the present Thesis to a perforated wheel and no analytical formulation exists for the acoustic efficiency of this kind of wheels, an alternative choice is to explicitly solve the fluid-structure interaction problem, which is computationally unaffordable for its posterior use in an optimization process [11]. There is evidence [172] that, in the case of perforated rectangular plates, their acoustic efficiency σ approaches unity at higher frequencies, perforations having their predominant effect in the low frequency range. Such trend is also observed in current non perforated wheels, whose acoustic efficiency approaches 1 at approximately 1500 Hz [59], where they begin to conform as the dominating component of rolling noise [36]. Therefore, it is believed that such simplification would only imply an underestimation of the acoustic reduction achieved in the optimization procedure described in Section 3.3.1.

2.6.2 Track sound power

As the other most influential component together with the wheel, it is important to determine the sound power radiated by the track if the noise is to be reduced. By using its dynamic properties, derived with the formulation described in Section 2.4.3, the rail and sleeper sound powers are computed separately and then summed in energy in order to obtain the global noise radiated by the track.

2.6.2.1 Contribution of the rail

Regarding the rail emitted sound power, contrary to the procedure followed for the wheel noise, this time no analytic formulation is available for some possible rail radiation efficiencies to be used. Instead, an Equivalent Sources Model (ESM) approach [91, 211], described in Section 2.6.2.3, is used in order to find the equivalent sound emission $W'_{r,n}$ of each of the rail waveshapes. These, combined with their average amplitude $\overline{A_n^2}$ and the rail length L considered, would provide the corresponding radiated power. Thus, mathematically expressed, summing over all the N_r rail waveshapes, rail sound power W_r is defined as

$$W_r = \sum_{n=1}^{N_r} \overline{A_n^2} W'_{r,n} L \quad (2.107)$$

It should be taken into account that such methodology for the rail sound power poses some implicit assumptions. First, radiation energy is added energy-wise, which ignores phase information. That is, when two different waves are averaged over an appropriately large length, cross terms will tend to 0 meanwhile both wavenumbers differ, as it is generally the case. Therefore, interference caused phenomena cancel [58]. Second, cross-section deformation variation within calculation frequencies is not great. Such premise is mandatory if the Timoshenko beam model is used but also is a valid supposition when the deformable track cross-section model is applied [91]. Third, the radiation from a spatially decaying wave is equivalent to that of a wave with no decay and with the same amplitude but spatially averaged and mean squared. This is considered reasonable for waves with low decay rates, which dominate emitted noise [76, 90]. Notwithstanding, if decay rates become great enough, the line source assumption is no longer valid and corrections must be implemented to include the three-dimensional related effects [90].

Such corrections depend on each wavenumber $k_n = \delta_n + i\zeta_n$, particularly on the relation of its real propagating part δ_n and its imaginary decaying part ζ_n with k_{air} , where k_{air} is the wavenumber in the air, i.e. $k_{air} = \omega/c_0$ with c_0 being the speed of sound. Hence [90], for the region where the decay rate is low no correction is needed, as the rail acts as an effectively infinitely long structure; then, when the decay rate grows, rail stops radiating noise as a line source and shifts towards a point source; and in those cases where there is low decay simultaneously with large propagating wavenumbers or short wavelengths, noise is specially reduced due to short-circuiting effects appearing. In the described model, this phenomenon translates in $W'_{r,n}$ being multiplied by a correction function C_r , whose value will vary depending on the region of k_n/k_{air} in which is placed for each frequency. Therefore, the value of C_r , depicted in Fig. 2.22, is defined according to the following cases [91]:

- If $\delta_n/k_{air} \geq 0.3$:

$$C_r = \frac{1}{\frac{1.215(\zeta_n/k_{air})^2}{\delta_n/k_{air} (1+(k_{air}/\zeta_n)^2)} + \sqrt{1 + (1.215 \delta_n/k_{air})^2}} \quad (2.108)$$

- If $\delta_n/k_{air} < 0.3$ and $\zeta_n/k_{air} < 1$:

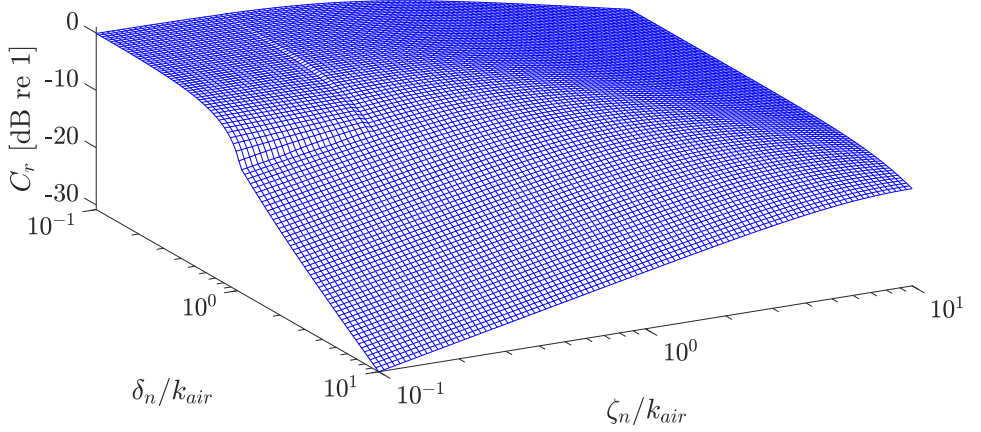


Figure 2.22: Sound power correction function C_r for different values of δ_n/k_{air} and ζ_n/k_{air} .

$$C_r = \frac{\sin^2\left(\arctan\left(\sqrt{(k_{air}/\zeta_n)^2 - (1 - \delta_n/(0.8 k_{air}))^2}\right)\right)}{\sqrt{1 + (1.215 \delta_n/k_{air})^2}} \quad (2.109)$$

- If $\delta_n/k_{air} < 0.3$ and $1 < \zeta_n/k_{air} < 1/(1 - \delta_n/(0.8 k_{air}))$:

$$C_r = \max\left(\frac{\sin^2\left(\arctan\left(\sqrt{(k_{air}/\zeta_n)^2 - (1 - \delta_n/(0.8 k_{air}))^2}\right)\right)}{\sqrt{1 + (1.215 \delta_n/k_{air})^2}}, \frac{1}{\frac{1.215(\zeta_n/k_{air})^2}{\delta_n/k_{air} (1 + (k_{air}/\zeta_n)^2)} + \sqrt{1 + (1.215 \delta_n/k_{air})^2}}\right) \quad (2.110)$$

- If $\delta_n/k_{air} < 0.3$ and $\zeta_n/k_{air} \geq 1/(1 - \delta_n/(0.8 k_{air}))$:

$$C_r = \frac{1}{\frac{1.215(\zeta_n/k_{air})^2}{\delta_n/k_{air} (1 + (k_{air}/\zeta_n)^2)} + \sqrt{1 + (1.215 \delta_n/k_{air})^2}} \quad (2.111)$$

2.6.2.2 Contribution of the sleeper

Sleeper radiation is derived with a similar methodology to that of the rail. In this case, a simplified two-dimensional quadrilateral is defined as the sleeper geometry, which is considered to only radiate noise through its upper side. Hence, the top is considered to vibrate uniformly in the x direction according to the value of each waveshape Ψ_n for the d.o.f. corresponding to the sleeper, mentioned in Section 2.4.3, and their associated average amplitude $\overline{A_n^2}$. Accordingly, by using the sleeper d.o.f. Ψ_n value in the ESM approach, it is possible to compute the equivalent radiated sound power corresponding to the sleeper for each waveshape $W'_{sl,n}$. Additionally, as sleepers are not continuous structures along the longitudinal direction z , each resulting sound power $W'_{sl,n}$ has to be conveniently scaled. Consequently, sound power radiated by the sleeper W_{sl} is defined by

$$W_{sl} = \frac{b_{sl}}{d_{sl}} \sum_{n=1}^{N_r} \overline{A_n^2} W'_{sl,n} L \quad (2.112)$$

where b_{sl} and d_{sl} are the width of the sleeper and the distance between sleepers, respectively.

2.6.2.3 Equivalent Sources Model

With the intention of computing each wave $W'_{r,n}$, an ESM is used [211]. For a given two-dimensional shape, e.g. the rail or sleeper cross-section, and assuming everything as uniform along the longitudinal direction, it should be possible to define a set of radiating sources inside the body whose radiation replicates that produced by the body when an enclosing surface S (the rail surface in the present methodology) vibrates at a velocity \tilde{v}_n^S observed at a given position (x, y) outside the body.

Thus, a set of N_{trip} triplets is defined, each consisting of a monopole and two dipoles, with position (x_m, y_m) and strengths $A_{i,m}$ with $i = 1, 2, 3$ for the strength of the monopole, dipole along the x axis and dipole along the y axis, respectively. Regarding the location of the triplets, it is done according to a collection of rules. First, the rail cross-sectional shape is approximated by four quadrilaterals representing the head, web, upper and lower part of the foot. Then, triplets are distributed along each quadrilateral centreline, each separated from each other by one half of the quadrilateral thicknesses. In addition, sources should not be located nearer to the rail surface than one third

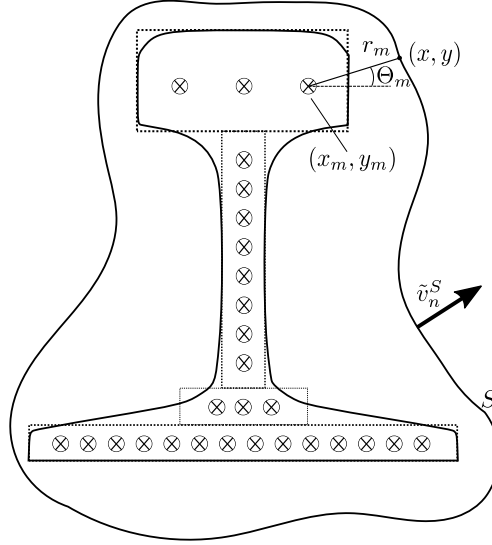


Figure 2.23: Example of rail section divided into four box regions, with the corresponding triplets defined inside at positions (x_m, y_m) , and a surface S that encloses the sources vibrating at \tilde{v}_n^S .

of the assigned triplets separation. In Fig. 2.23, an example of a rail cross-section with its corresponding triplets along with the defined boxes regions is shown.

Then, if a local set of polar coordinates is now defined relative to triplets position

$$r_m = \sqrt{(x - x_m)^2 + (y - y_m)^2} \quad (2.113)$$

$$\Theta_m = \text{atan}\left(\frac{y - y_m}{x - x_m}\right) \quad (2.114)$$

acoustic pressure p is defined at point (x, y) by [91]

$$p(x, y) = \sum_{m=1}^{N_{trip}} \left(A_{1,m} H_0^{(2)}(k_{air} r_m) + A_{2,m} H_1^{(2)}(k_{air} r_m) \cos(\Theta_m) + A_{3,m} H_1^{(2)}(k_{air} r_m) \sin(\Theta_m) \right) \quad (2.115)$$

where $H_n^{(2)}$ represents a Hankel function of the second kind and order n . In addition, rail velocity equivalent field generated by triplets is given by [212]

$$\tilde{v}_r^{eq} = \frac{-1}{i\omega\rho} \nabla p(x, y) \cdot \hat{\mathbf{n}} \quad (2.116)$$

with ρ being the air density and $\hat{\mathbf{n}}$ refers to the normal unit vector in the surface at point (x, y) . Thus, by combining Eqs. (2.115) and (2.116), velocity can be expressed as

$$\begin{aligned} \tilde{v}_r^{eq}(x, y) = \frac{-1}{i\omega\rho} \sum_{m=1}^{N_{trip}} \left(A_{1,m} \nabla H_0^{(2)}(k_{air}r_m) + \right. \\ \left. A_{2,m} \nabla \left(H_1^{(2)}(k_{air}r_m) \cos(\Theta_m) \right) + \right. \\ \left. A_{3,m} \nabla \left(H_1^{(2)}(k_{air}r_m) \sin(\Theta_m) \right) \right) \cdot \hat{\mathbf{n}} \end{aligned} \quad (2.117)$$

Up to the moment, the values of source strengths $A_{i,m}$ are unknown. Though, the Kirchhoff-Helmholtz integral establishes that if two sound sources generate the same normal velocity field around a closed boundary enclosing a surface, then the corresponding radiated sound fields must be also equivalent [212]. Therefore, using the already computed waveshape amplitude $\omega\Psi_{\mathbf{n}}$ in the normal direction as the velocity over the rail surface S for each wave \tilde{v}_n^S , it is desired to find the value $A_{i,m}$ that generates a velocity field in the surface \tilde{v}_r^{eq} as close as possible to the original \tilde{v}_n^S . As the ultimate goal of the methodology is the proper computation of the radiated sound power, the above can be expressed mathematically as finding the set of $A_{i,m}$ that minimizes [91]

$$\int_S |\tilde{v}_n^S p^* - I_r^{eq}|^2 dS \quad (2.118)$$

where equivalent surface intensity I_r^{eq} is given by

$$I_r^{eq} = \tilde{v}_r^{eq}(x, y) p^*(x, y) \quad (2.119)$$

This way, introducing Eq. (2.117) into Eq. (2.118) and differentiating with respect $A_{i,m}$, yields

$$-i\omega\rho \int_S \tilde{v}_n^S \alpha_1^*(j) = \sum_{m=1}^{N_{trip}} (A_{1,m}\beta_{11}(j, m) + A_{2,m}\beta_{12}(j, m) + A_{3,m}\beta_{1,3}(j, m)) \quad (2.120)$$

$$-i\omega\rho \int_S \tilde{v}_n^S \alpha_2^*(j) = \sum_{m=1}^{N_{trip}} (A_{1,m}\beta_{21}(j, m) + A_{2,m}\beta_{22}(j, m) + A_{3,m}\beta_{2,3}(j, m)) \quad (2.121)$$

$$-i\omega\rho \int_S \tilde{v}_n^S \alpha_3^*(j) = \sum_{m=1}^{N_{trip}} (A_{1,m}\beta_{31}(j, m) + A_{2,m}\beta_{32}(j, m) + A_{3,m}\beta_{3,3}(j, m)) \quad (2.122)$$

where j varies from 1 to N_{trip} as the index m , * represents the conjugate, and α_j and β_{pq} are defined as

$$\alpha_1(m) = H_0^{(2)}(k_{air}r_m) \quad (2.123)$$

$$\alpha_2(m) = H_1^{(2)}(k_{air}r_m) \cos(\Theta_m) \quad (2.124)$$

$$\alpha_3(m) = H_1^{(2)}(k_{air}r_m) \sin(\Theta_m) \quad (2.125)$$

$$\beta_{pq}(j, m) = \int_S \alpha_p^*(j) \gamma_q(m) dS \quad (2.126)$$

with

$$\gamma_1(m) = \nabla H_0^{(2)}(k_{air}r_m) \cdot \hat{\mathbf{n}} = -\frac{k_{air}H_1^{(2)}(k_{air}r_m)}{r_m} \begin{Bmatrix} x - x_m \\ y - y_m \end{Bmatrix}^T \cdot \hat{\mathbf{n}} \quad (2.127)$$

$$\begin{aligned} \gamma_2(m) = \nabla \left(H_1^{(2)}(k_{air}r_m) \cos(\Theta_m) \right) \cdot \hat{\mathbf{n}} = \\ \left(\frac{k_{air}(H_0^{(2)}(k_{air}r_m) - H_2^{(2)}(k_{air}r_m)) \cos(\theta_m)}{2r_m} \begin{Bmatrix} x - x_m \\ y - y_m \end{Bmatrix}^T + \right. \\ \left. \frac{H_1^{(2)}(k_{air}r_m) \sin(\theta_m)}{r_m^2} \begin{Bmatrix} y - y_m \\ -(x - x_m) \end{Bmatrix}^T \right) \cdot \hat{\mathbf{n}} \end{aligned} \quad (2.128)$$

$$\begin{aligned} \gamma_3(m) = \nabla \left(H_1^{(2)}(k_{air}r_m) \sin(\Theta_m) \right) \cdot \hat{\mathbf{n}} = \\ \left(\frac{k_{air}(H_0^{(2)}(k_{air}r_m) - H_2^{(2)}(k_{air}r_m)) \sin(\theta_m)}{2r_m} \begin{Bmatrix} x - x_m \\ y - y_m \end{Bmatrix}^T + \right. \\ \left. \frac{H_1^{(2)}(k_{air}r_m) \cos(\theta_m)}{r_m^2} \begin{Bmatrix} -(y - y_m) \\ x - x_m \end{Bmatrix}^T \right) \cdot \hat{\mathbf{n}} \end{aligned} \quad (2.129)$$

referring $\hat{\mathbf{n}}$ to the normal unit vector to surface element dS .

Next, the system of equations conformed by Eqs. (2.120)-(2.129) can be expressed in matrix form as

$$-i\omega\rho \int_S \tilde{v}_n^S \boldsymbol{\alpha}^* = \boldsymbol{\beta}_{mat} \cdot \mathbf{A}_{trip} \quad (2.130)$$

where $\boldsymbol{\alpha}^*$ and \mathbf{A}_{trip} are vectors whose components correspond to

$$\boldsymbol{\alpha}^* = \{\alpha_1^*(1) \alpha_2^*(1) \alpha_3^*(1) \cdots \alpha_1^*(N_{trip}) \alpha_2^*(N_{trip}) \alpha_3^*(N_{trip})\}^T \quad (2.131)$$

$$\mathbf{A}_{trip} = \{A_{1,1} \ A_{2,1} \ A_{3,1} \ \cdots \ A_{1,N_{trip}} \ A_{2,N_{trip}} \ A_{3,N_{trip}}\}^T \quad (2.132)$$

and the matrix $\boldsymbol{\beta}_{mat}$ is defined as

$$\boldsymbol{\beta}_{mat} = \begin{bmatrix} \beta_{mat,11} & \cdots & \beta_{mat,1N_{trip}} \\ \vdots & \ddots & \vdots \\ \beta_{mat,N_{trip}1} & \cdots & \beta_{mat,N_{trip}N_{trip}} \end{bmatrix} \quad (2.133)$$

with each $\beta_{mat,jm}$ component corresponding to

$$\beta_{mat,jm} = \begin{bmatrix} \beta_{11}(j,m) & \beta_{12}(j,m) & \beta_{13}(j,m) \\ \beta_{21}(j,m) & \beta_{22}(j,m) & \beta_{23}(j,m) \\ \beta_{31}(j,m) & \beta_{32}(j,m) & \beta_{33}(j,m) \end{bmatrix} \quad (2.134)$$

Accordingly, by solving the system associated with Eq. (2.130), all $A_{i,m}$ values are obtained. Once $A_{i,m}$ are known, it is immediate to compute the pressure corresponding to the source strengths through Eq. (2.115) and derive $W'_{r,n}$ by integrating over a surface enclosing the rail cross-section boundary, that includes the rail boundary itself, with

$$W'_{r,n} = \frac{1}{2} \int_S \text{Re}(p(x,y) v_n^{S*}) ds \quad (2.135)$$

where ds is a length element, as $dS = b ds$ with a width $b = 1$ m.

Wheel shape optimization procedures for rolling noise minimization

3.1 Introduction

In the course of the work undertaken in the present Thesis, two optimization methodologies have been developed, one focused on obtaining suitable perforation schemes and another on the shape of the wheel cross-section. Additionally, a study on the influence of rail geometry on rolling noise has been carried out.

This chapter focuses on detailing the methodology followed for the different optimizations processes developed, as well as explaining thoroughly the operation of each of the modules of the algorithms. Additionally, for the sake of completeness, the chapter begins with a brief theoretical introduction to GA and its related concepts in Section 3.2, as it is the optimization method chosen in the development of this Thesis.

Thus, after the introduction mentioned above, in Section 3.3, the general algorithm used for both optimization procedures is described and, to continue,

focus is centred on the specificities of each approach. Then, the characteristics of the applied structural analysis are described in Section 3.4 and, afterwards, the FE models and corresponding settings of both the perforation scheme and the wheel cross-section are discussed in Section 3.5. Next, Section 3.6 details the process of modal identification applied on wheel candidates and how the different values associated with each mode are obtained. Finally, the different target functions used throughout the research are defined in Section 3.7.

3.2 Genetic Algorithms

A GA is a stochastic global search method that, together with Evolution Strategies [213] and Evolutionary Programming [214], belongs to a larger class of algorithms called Evolutionary Algorithms (EA) [215]. One of its main characteristics is that is inspired by Darwin's theory of evolution [216] and tries to mimic the process of natural selection [9]. Simplifying, the theory states that individual specimens of a population compete between each other for resources, shelter or to attract mates who they can reproduce with. In this practice, those most adapted individuals have greater chances to survive and produce larger number of offspring. At the same time, in the course of reproduction the genetic traits of each individual are recombined and transposed to the next generation of specimens, which produces that, as the best fit individuals have a larger rate of mating, each generation become more adapted to its environment as the characteristics that make individuals more suitable and produce better offspring have a higher probability of being transposed. The GA tries to import all these features into a computer algorithm which serves for solving complicated optimization problems, i.e. timetabling, job-shop scheduling or, as in the present case, engineering vibro-acoustic problems [9].

They were first developed in the 1960s, when computer scientists were studying evolutionary systems with the idea that evolution could be used as an optimization tool for engineering problems [217]. More precisely, they were first theorized by John Holland at the University of Michigan, whose original goal was to formally study the phenomenon of adaptation in the way it occurs in nature and to develop methodologies to include the mechanisms of natural adaptation into computer systems [217]. The main findings were embodied in the book *Adaptation in Natural and Artificial Systems*, where the crossover and mutation operations were first introduced for a population-based algorithm [8].

In the problem addressed in the present Thesis, a GA is selected as the optimization method used because, as part of the derivative-free optimization

methods, allows for an effective approach in complex non-linear problems where no analytical expression of the objective function exists and no derivative information is available [218], like the one addressed in this work. Since GAs do not require gradient information, they can be successful regardless of the nature of the objective functions and constraints and, as a global optimization technique, there is a greater chance of convergence to a global solution rather than to a local one [219]. In addition, they are suited for large scale problems, as the number of function evaluations required can be scaled independent of the problem dimension [220]. Additionally, other features that GAs present and make them differ with respect to alternative available techniques are [221]: the possibility to search population points in parallel, the use of probabilistic transition rules instead of deterministic ones and working on an encoding of the parameter set rather than the parameter set itself.

3.2.1 Theoretical foundations

A general optimization problem in which GAs are applied has the form [222]

$$\begin{aligned} & \text{minimize} && f_0(\mathbf{x}) \\ & \text{subject to} && g_i(\mathbf{x}) \leq b_i, \quad i = 1, \dots, m \end{aligned} \quad (3.1)$$

where the vector $\mathbf{x} = x_1, \dots, x_n$ is the optimization variable of the problem, $f_0: \mathbf{R}^n \rightarrow \mathbf{R}$ is the objective function, $g_i: \mathbf{R}^n \rightarrow \mathbf{R}$ are the inequality or the equality constraints and b_i are the associated bounds. The goal of such a problem is to find a vector \mathbf{x}^* that has the smallest objective function between all the possible ones, that is, for any \mathbf{x} that fulfils the constraints $g_i(\mathbf{x}) \leq b_i$ it is accomplished that $f_0(\mathbf{x}^*) \leq f_0(\mathbf{x})$. Thus, in an average optimization problem, the available solutions related to the problem are known. This forms the solution space, that should not be confused with the space conformed by all possible combination of variables of the problem, as it is exemplified in Fig. 3.1

With the intention of finding \mathbf{x}^* , GA encodes the variables of the problem $\mathbf{x} = x_1, \dots, x_n$ in the form of what is called chromosomes and creates an initial population of n_{ini} individuals with a different combination of chromosomes usually chosen with the use of a stochastic methodology. Each individual is evaluated with the objective function, alternatively named fitness function, and the resulting information is used in the initialization of subsequent offspring, which defines a new set of individuals to be computed. This set of steps is called a generation. Then, the process goes until the Best Found Solution

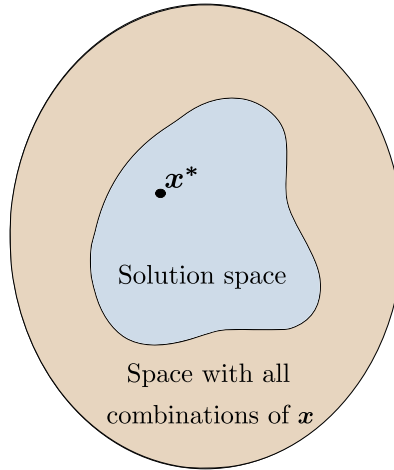


Figure 3.1: Diagram representing the solution space (in brown) and optimum solution x^* inside the space conformed by all possible combinations of x (in blue).

(BFS), that is, the candidate that is considered to be closer to x^* , is found. Moreover, during this course of events a series of operators is used in the generation and selection of candidates. In the simplest form of GA and also in the present work, these operators, which are described with further detail in Section 3.2.2, are: selection, crossover and mutation.

In a more structured way, a simple GA would proceed as follows [9, 217, 223]:

- 1: A population of n_{ini} chromosomes, i.e. candidate solutions to the problem, is randomly generated.
- 2: The fitness of each chromosome x in the population is derived by evaluating the objective function $f(x)$.
- 3: Until n_{ini} offspring have been created, repeat:
 - 3a: A pair of chromosomes is selected based on their fitness.
 - 3b: Two new offspring are generated by crossing over the parents with a crossover probability p_c . In case that no crossover is performed, offspring are exact copies of their parents.
 - 3c: New offspring are mutated at each position in chromosome (*locus*) with probability p_m .

- 3d: New offspring are placed in the new population. In case n_{ini} is odd, one new member of the population can be discarded randomly.
- 4: Current population is replaced by the new generation.
- 5: Convergence is tested. If fulfilled, the algorithm is stopped and BFS \mathbf{x}^* is selected.
- 6: If convergence has not happened in step 5, return to step 2 and repeat the loop.

Additionally, the required criteria for a proper implementation of a GA approach can be established as [9]:

- **Completeness:** all solutions should have their encoding.
- **Non redundancy:** solutions and codes should have an univocal correspondence.
- **Soundness:** any code that has been produced by genetic operators has to be associated with a solution.
- **Characteristic perseverance:** characteristics transmitted from parents to offspring should be useful.

In the case of the optimization of a railway wheel presented in the Thesis, where the genes are the geometric parameters defining the cross-section, all these criteria are followed: the whole solution space can be represented with the adequate selection of parameters, each set of parameters defines a unique wheel and the geometric aspects chosen are those more relevant for the acoustic radiation, as explained in section 3.5.2.

3.2.2 GA operators

In the course of GA procedures, several operators are used for different specific purposes. For example, there exists the dominance operator with the intention of including diploidy, i.e. diploid or double stranded chromosomes [224, 225], or the crowding operator [226], which is inspired by the ecological phenomenon of individuals competing against each other for limited resources [227].

As stated above, in the present work just the three main basic operators are used. Those, whose behaviour is briefly outlined in Fig. 3.2, are defined as [217]:

- **Selection:** is the operator in charge of selecting those chromosomes more suitable for the problem treated, choosing them according to the objective function of its candidates. The selection function chosen is the Matlab ‘ga’ function option **Stochastic uniform** [228], whose behaviour is the following: first, it arranges a line divided into sections corresponding to each parent whose length is proportional to its fitness; then, it moves through the line in steps of equal size, selecting in each step a parent corresponding to the individual associated with the section of line where the algorithm is on.
- **Crossover:** randomly chooses a locus and exchange the genes before and after the locus between parents to form a new pair of children or offspring. The crossover function chosen in the this case is the Matlab ‘ga’ function option **Scattered** [228], which creates a random binary vector and selects the genes of one parent when the vector is the unity and from the other when is zero to generate the offspring. According to the default options set for ‘ga’, the number of crossover individuals in each generation is $n_{cross} = 0.8(n_{ini} - n_{elite})$, where $n_{elite} = 0.05 n_{ini}$ is the number of candidates with the best fitness values that are assured to survive to the subsequent generation and the resulting crossover probability is $p_c = 0.76$.
- **Mutation:** it makes stochastic changes in the parents genes to create new children. It assures diversity for the genes available and helps for a broader exploration of the whole space, hindering the algorithm in getting caught in a local minimum [9]. The mutation function used is the Matlab ‘ga’ function option **Gaussian** [228], which adds to the geometric parameters random numbers taken from a Gaussian distribution among the initial range of values with mean 0. The number of mutated individuals in every iteration is $n_{mut} = n_{ini} - (n_{elite} + n_{cross})$, giving a mutation probability of $p_m = 0.19$ when default parameters are used.

3.2.3 Constraint-handling in GAs

In engineering application of GAs, there are usually several constraints that the problem must comply to consider the resulting design adequate. In the case of the railway wheel, for example, there are structural requirements that the wheel should accomplish for considering it feasible, as will be detailed in Section 3.4. Therefore, such constraints have to be incorporated into the fitness function.

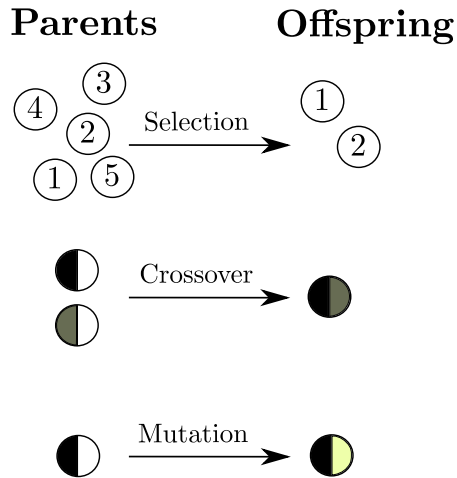


Figure 3.2: Diagram with the behaviour of GA operators: Selection, Crossover and Mutation.

From the several ways there are to handle these limitations, the most common is the use of penalty functions [229, 230] consisting in transforming a constrained problem in an unconstrained problem by penalizing infeasible solutions through the modification of the objective function in some amount [231]. Yet, due to difficulties associated with penalty functions [229] researchers have developed multiple approaches to manage this problem [232]. Some examples are techniques aiming to simplify the search space by developing special representation schemes, e.g. ‘random key encoding’ [233] and GENCOOP approach [234], or methodologies able to handle constraints and objectives separately, as co-evolution [235] or behavioural memory [236].

In the procedure presented here, a ‘death penalty’ method is chosen for including the constraint that imposes structural requirements of the wheel. ‘Death penalty’ belongs to the group of penalty constraint methods and consists in the rejection of infeasible individuals, its advantages being ease of implementation and computational efficiency [232]. Therefore, all those wheel candidates that do not fulfil the appropriate structural requirements are neither considered for offspring generation nor as a candidate for the BFS.

3.3 Optimization algorithms: from the general methodology to the specificities of each procedure

In the present Thesis, both optimization methodologies share a common structure on how the in-house code behaves and how it moves through the modules needed. This shared algorithm in which GA is embedded, called here the “general algorithm” and represented in the form of a flow diagram in Fig. 3.3, is broadly described through this section, although the details of each step and particularities of the different optimization approaches are further explained in the subsequent sections.

As observed in Fig. 3.3, the very first step of the algorithm developed is to provide the initial set of wheel candidates \mathbf{X}_0 , that, at the same time, conforms the first generation. Also, \mathbf{X}_0 , as the rest of series \mathbf{X}_i , is composed by an initial population N_{pop} . Then, the algorithm iterates over all the peers in the generation and compute its corresponding objective function.

To do so, it starts by defining a perforation scheme or cross-section for every candidate $\bar{\mathbf{x}}_j$ in \mathbf{X}_i , making use of its corresponding geometric parameters. In the case of first generation designs, these parameters are randomly generated inside the design domain defined by the selected lower and upper boundaries, therefore not considering the information of the previous evaluations. In the subsequent groups computed, though, the procedure does consider such information for the initialization of new candidates, as the GA applies a stochastic uniform function [228] for the selection process.

Next to the proposal of a candidate wheel geometry, a structural analysis, carried out following the standard UNE-EN 13979-1 [237], is performed to check whether the design is feasible or not from an endurance point of view. If the resulting maximum stress variation $\Delta\sigma_c$ is smaller than the maximum permissible range of dynamic stresses ΔA_m , the candidate is considered feasible and its evaluation process goes on, otherwise it is discarded and the next candidate proceeds to be tested. Therefore, such control acts as a “death penalty” constraint in the optimization procedure [232].

If the candidate is not rejected, the next step is to carry on with a modal analysis to obtain the modeshapes Ψ_{nm} and natural frequencies ω_{nm} needed to compute the selected objective function, the number of extracted modeshapes being N_m . Such analysis is executed by the FEM software ANSYS® APDL¹ using general axisymmetric elements of size h (details will be provided later).

¹Using version ANSYS Academic Research Mechanical (18.2)

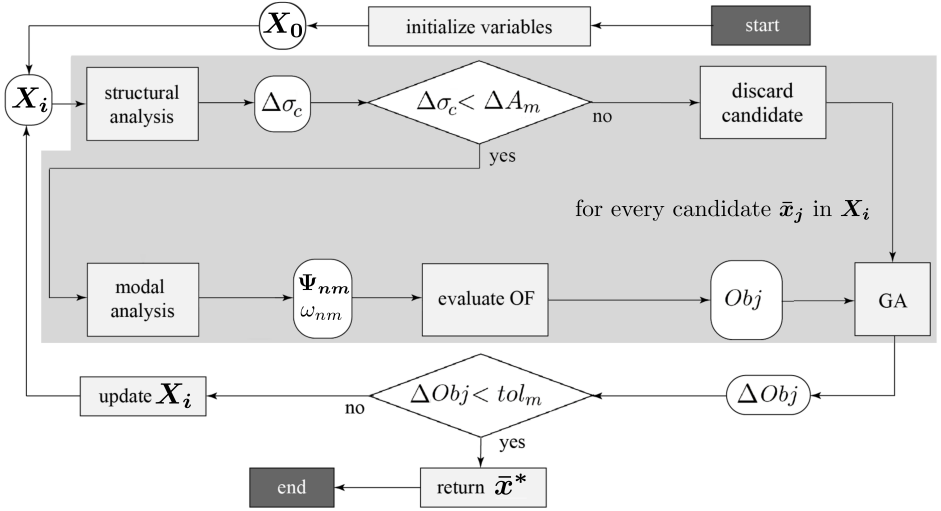


Figure 3.3: Flow diagram describing the general optimization procedure.

Then, the objective function Obj is evaluated and the GA is fed with this information. After computing Obj for each viable iteration of the set, the variation in the best fitness value obtained is checked. Then, if the maximum change in the objective function in 50 generations is less than the defined convergence tolerance tol_m , set in the present Thesis to $tol_m = 10^{-6}$, the stopping criterion $\Delta Obj < tol_m$ is met. Fulfilling the stopping condition implies that the optimization workflow ends and the wheel design with the best fitness \bar{x}^* between all evaluated wheels is selected as the Best Found Solution (BFS). On the other hand, if $\Delta Obj < tol_m$ is not accomplished, the optimization procedure continues and a new set of geometric parameters \mathbf{X}_i is initialized, taking into account the geometrical information of the previous candidates. Additionally, when a number of $N_{gen,max}$ generations is computed without achieving this ending condition, the algorithm considers that convergence is not fulfilled and ends anyway.

3.3.1 Perforation scheme optimization algorithm

Now, the procedure followed through the optimization process of a perforation scheme for a railway wheel is detailed. In this case, the above-mentioned optimization algorithm is applied with the intention of finding a perforation scheme for the wheel that minimizes its radiated rolling noise in terms of sound power level $L_{W,A}$.

For this purpose, up to 9 parameters defining the configurations of the wheel are used as genes. These are: the number of layers n_{layer} of circumferentially equidistant holes, with $n_{layer} = 1, 2$ or 3 ; the number of holes N_l in each l layer; the distance X_l from hole centre to the wheel axis of rotation in each layer l ; and the radius R_l of holes in a layer l . Thus, for every layer, a set of independent parameters N_l , X_l and R_l is considered and, therefore, the total number of parameters defining one design depends on the value assigned to n_{layer} for each generated candidate. Although using n_{layer} as a gen increases the complexity of the problem, it is necessary for an accurate search of the design space [238, 239]. The resulting configuration is applied for two different typologies of wheel, with curved and straight web. More details on how the wheel geometry is built when using this algorithm are given in Section 3.5.1.

In this scenario, the objective function Obj is always computed with the $L_{A,W}$ -min methodology defined in Section 3.7.1, considering the number of mode-shapes N_m in the frequency range below 6 kHz. Additionally, in the dynamic analysis described in Section 2.3.4, the contact force $\mathbf{F}_c(t)$ considered in the computations is taken into account as an external constant, not varying among the different perforation scheme candidates $\bar{\mathbf{x}}_j$. Regarding the mesh, which is further explained at Section 3.5.1, SOLID 45 tetrahedral elements [240] are used with a maximum size $h = 0.03$ m. Besides, an initial population of $N_{pop} = 50$ individuals is used for every evaluated set \mathbf{X}_i and the maximum number of generations is fixed to $N_{gen,max} = 1000$.

For further clarification, the modified flow diagram describing the process for the present case is illustrated in Fig. 3.4.

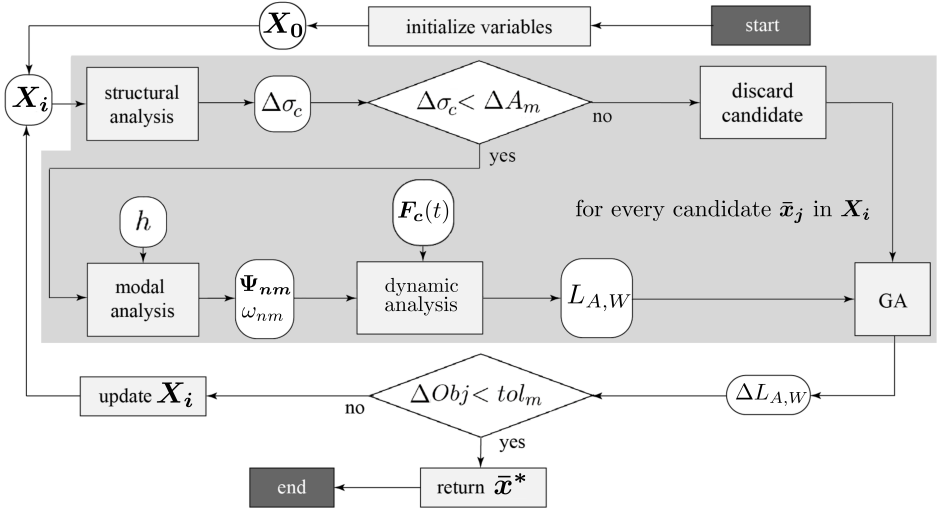


Figure 3.4: Flow diagram describing the optimization procedure for perforation schemes.

3.3.2 Wheel shape optimization algorithm

In the case of the wheel cross-sectional shape optimization, some additional features are introduced in the general procedure previously described, as it can be observed in the modified diagram shown in Fig. 3.5.

In this occasion, the genes used for every conformed cross-section candidates are wheel radius x_1 , fillet radius x_2 , web thickness x_3 and web offset x_4 (see Fig. 3.12 for further information). Again, more details on the wheel geometry definitions are offered in the posterior Section 3.5.2. Furthermore, different objective functions Obj can be chosen depending on the desired optimization approach: NF-max or $L_{A,W}$ -min, both defined later in Section 3.7. A new modal identification module (“modal ID”) is added due to the specificities of the computation when using the wheel shape methodology, as it is necessary to classify the modeshapes according to the number of nodal diameters n and nodal circumferences m in the $L_{A,W}$ -min approach. More on this is explained in Section 3.6. Additionally, when performing the dynamic analysis, required for the sound power calculations, this time the whole dynamic system is solved and the contact force is internally computed, instead of loaded as an external constant. All information on the derivation of the dynamic behaviour used in this kind of optimization is clarified through Chapter 2.

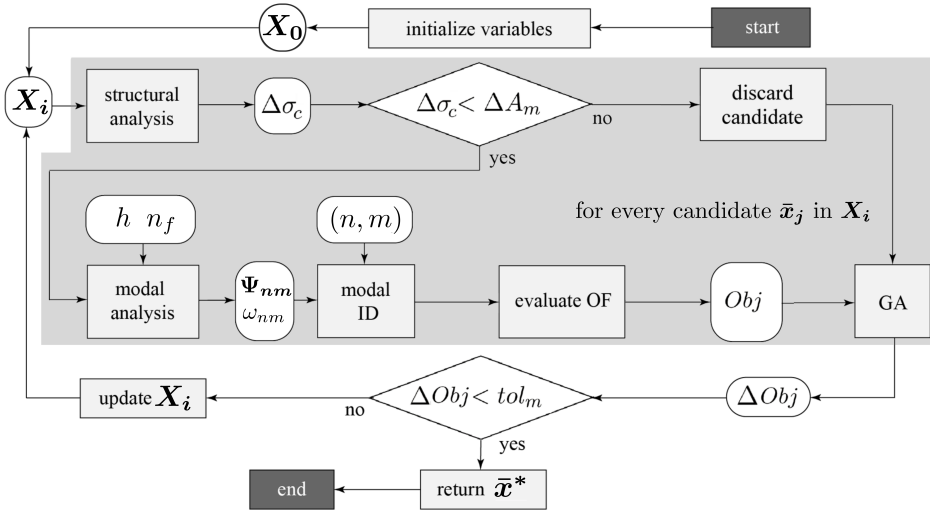


Figure 3.5: Flow diagram describing the shape optimization procedure for wheel cross-sections.

With regard to mesh properties, which are exposed in Section 3.5.2, SOLID 273 general axisymmetric elements [241] are used with a maximum size $h = 0.007$ m and considering a number of Fourier terms $n_f = 12$, with the number of extracted modeshapes during the eigenanalysis being $N_m = 48$. Besides, an initial population of $N_{pop} = 50$ individuals is used for every evaluated set \mathbf{X}_i and the maximum number of generations is fixed to $N_{gen,max} = 300$.

3.3.3 Preliminary approach to the track shape influence on rolling noise.

As repeatedly mentioned throughout the present Thesis, track components also play a fundamental role in rolling noise radiation. Hence, in order to further study the effects of varying the most relevant geometrical parameters of the rail and its structural characteristics, the sound levels of different track models are studied when combined with the optimized wheel designs or the reference wheel. Therefore, first a set of tracks with different characteristics is defined. Then, total SWL is computed for each defined track model combined with both the BFS wheel, obtained with the procedure described in Section 3.3.2, and the reference wheel. The combined SWL of the system is derived by adding

together each component of the sound power expressed in terms of energy and then converting the resulting value again to dB(A). Later, every SWL curve, together with the energy sum of each of the frequency bands expressed in dB(A), are compared. Finally, several relevant conclusions are extracted.

In all the cases, a section of length $L = 0.01$ m is considered and linear triangular elements of a maximum size $h = 0.01$ m are used for meshing, solved with Matlab Partial Differential Equation toolbox [242]. Also, a two-dimensional wheel/track interaction model is taken into account in the calculation and the number of rail waveshapes used during the sound power computation is $N_r = 20$. Regarding the sleeper geometry used when deriving its SWL, whose shape is kept constant for all different track candidates, it is represented as a quadrilateral with height $h_{sl} = 0.22$ m and length $l_{sl} = 0.84$ m, whose width is set as $b_{sl} = 0.25$ m. Besides, non-geometric properties of the foundation, which are among the most relevant to the emitted noise [155, 178, 179], are also considered when defining the track. This is the case of the rail pad loss factor η_p , rail pad stiffness per unit length k'_p and ballast stiffness per unit length k'_b .

3.4 High-cycle fatigue analysis

To assess the mechanical behaviour of each wheel design, a high-cycle fatigue analysis is performed following the standard UNE-EN 13979-1. Such standard has as a goal to define the requirements that a monobloc railway wheel must meet in order to operate in the European railway network and to assess the suitability of a chosen design [237]. It defines two stages for the evaluation of mechanical behaviour and to ensure that there is no risk of crack initiation due to fatigue during its lifespan: a first stage consisting of a computer-based stress analysis and, if the outcomes are not suitable, a second one in which a test bench essay has to be performed. Depending on whether the requirement of each of the steps is exceeded or not, the wheel will be approved or dismissed for its use in the European railway network. A flow chart with the defined methodology is illustrated in Fig. 3.6.

Due to the obvious reason that the optimization procedure proposed in the Thesis is purely computational, it only focuses on the first step described. In this high-cycle fatigue analysis the risk of cracking in the railway wheel is computed by comparing the principal stresses resulting of three load cases that correspond to different vehicle operating conditions with an established threshold in every circumstance. More precisely, each of them is associated

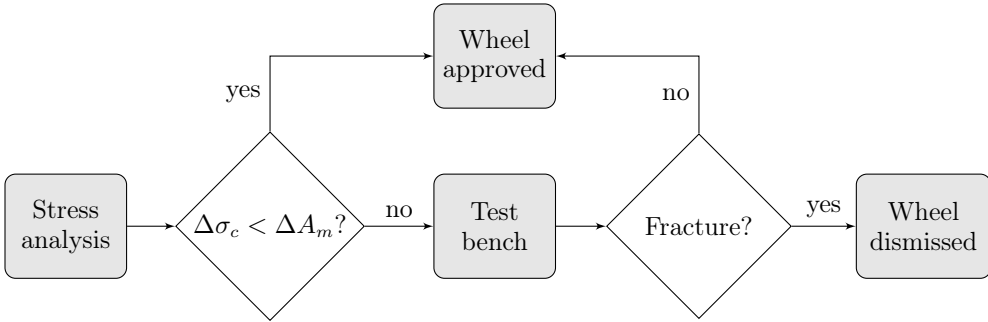


Figure 3.6: Flow diagram with the assessment of the mechanical behaviour defined by standard UNE-EN 13979-1 [237]

with the following conditions: straight track, curve and railway switches. Then, these conditions are translated into different specific points of application of a series forces, which are exemplified in Fig. 3.7. The numbers on the points of application indicate their reference case and the force values are:

- **Case 1 - Straight track:** $F_x = 1.25 P$
- **Case 2 - Curve:** $F_x = 1.25 P$ and $F_{y2} = 0.7 P$
- **Case 3 - Railway switches:** $F_x = 1.25 P$ and $F_{y3} = 0.42 P$

where P is defined as half the load by axis on track. In the cases studied in this work, a typical value $P = 60$ kN is used [18], the rest of forces being $F_x = 75$ kN, $F_{y2} = 42$ kN and $F_{y3} = 25.2$ kN.

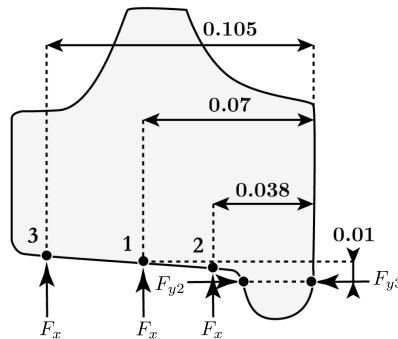


Figure 3.7: Load cases defined by the standard UNE-EN 13979-1 [237]. Distances are defined in metres.

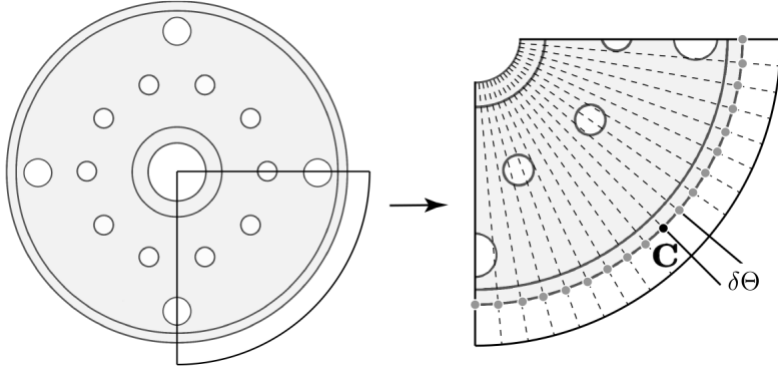


Figure 3.8: Points **C**, separated in the angular direction by $\delta\Theta$, in which defined load cases are applied when performing a structural analysis in non-axisymmetric wheels.

Also, in the case of non-axisymmetric wheels as those with perforations schemes, the cases defined in Fig. 3.7 are applied along several circumferential positions. Thus, the angular locations **C** in which the three load cases are applied are changed in steps of $\delta\Theta$ through a quarter of the wheel, using $\delta\Theta = 5^\circ$ in the perforation scheme optimization. In this manner, the evaluation of the effects the loads have on all possible positions during wheel rotation is ensured. This process is further clarified by the example depicted in Fig. 3.8.

By using a FEM software, a half of a three-dimensional wheel geometry is meshed with PLANE185 and an element size $h = 0.015$ m. The Cauchy stress tensor [243] is calculated in all nodes for each load case, using as boundary condition the restriction of movement of the axle. From there, the principal stresses and directions for each case are computed through the eigenvalue problem. In Fig. 3.9 an example of the first principal stress for each case in a wheel is shown for illustrative purposes.

As the wheel is supposed to be operated eventually under every of the defined conditions by the different cases, the dynamic range of stresses checked would be conformed by the difference between the maximum principal stress σ_{max} and the minimum one σ_{min} . Thus, in all nodes their σ_{min} is projected into σ_{max} direction and the variation between the maximum and minimum stress

$$\Delta\sigma = \sigma^{max} - \sigma^{min} \quad (3.2)$$

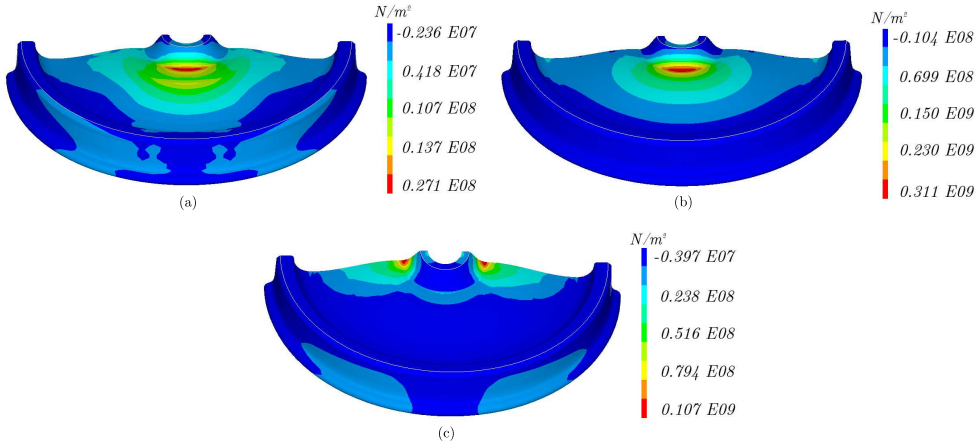


Figure 3.9: Example Principal Stress σ_1 in a wheel for each load case: (a) case 1; (b) case 2; (c) case 3. The particularities of each load case can be seen in Fig. 3.7.

is derived, obtaining a maximum variation $\Delta\sigma_c$. Those candidate wheels which meet $\Delta\sigma_c < \Delta A_m$ are considered as feasible. ΔA_m is defined as the maximum permissible range of dynamic stresses and, for the type of wheel studied in the present work, the standard fixes a value of $\Delta A_m = 360$ MPa.

3.5 Geometry parametrization of wheel shapes

As most of the calculations for the problems studied are ultimately based on the natural frequencies and modeshapes of candidate wheels, the FE model adopted and geometry parametrization are fundamental parts of the approach followed in this work. The requirements needed are being capable to define a wheel geometry from a number of discrete values, that is, the geometrical parameters or genes in GA terminology, and to calculate the required eigenproblem efficiently enough to keep computation times within an admissible range from the point of view of an optimization process. All these specifications should be met at the same time a good precision in the obtention of the results is kept.

In the following pages, a description of the parametrizations built for the optimization procedures is exposed. The first one corresponds to a perforation scheme while the latter is associated with the wheel cross-section.

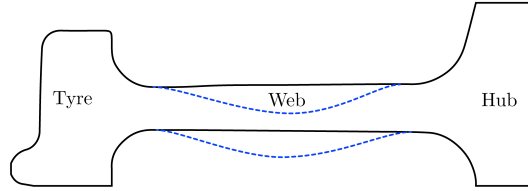


Figure 3.10: Schematic of wheel cross-sectional shapes used for the base wheel shape during the perforation scheme optimization.

3.5.1 Finite Element model for the perforation scheme

For generating the wheels with perforated schemes, a three-dimensional FE model is defined which makes use of SOLID 45 linear tetrahedral elements [240]. In the model, the tyre and hub sections are meshed with a maximum element size of $h = 0.03$ m and the inner edge of hub is constrained. As for the web, since the size and position of the perforations are variable, its volume is meshed by using an h-adaptative refinement process. This meshing strategy grants an acceptable accuracy while limiting the computational expense [244].

Regarding the building of the perforated wheels, two are the main steps followed: first, an unperforated shape is taken as the base geometry; later, the perforation scheme is applied. As the base shape, a standard monobloc wheel with typical dimensions and a radius $r_c = 0.56$ m is used. Besides, with the intention of exploring the effects of perforations in different web geometries, two different cross-sections are considered for the base wheel, differing in their web shapes. Hence, as illustrated in Fig. 3.10, cross-sections considered are either a curved web shape or straight web one.

Once the base wheel geometry is set, the perforation scheme is defined according to the following design parameters: the number of layers of circumferentially equidistant holes n_{layer} , the number of holes for the l th layer N_l , the distance from hole centres in the l th layer to the wheel axis of rotation X_l and the radius of the holes in the l th layer R_l . In all cases the subscript l denotes the layer with its value being $l = 1, 2$ or 3 . For a better understanding of the defined parametrization, Fig. 3.11 illustrates each of the aforementioned design parameters. The upper and lower design boundaries used through the optimization are shown in Table 3.1.

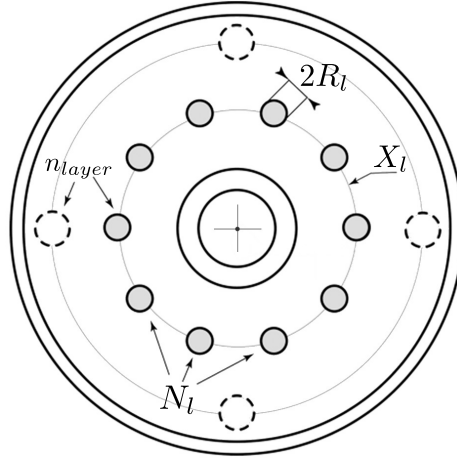


Figure 3.11: Design parameters defining the perforation scheme.

Table 3.1: Lower and upper design boundaries for the perforation scheme design parameters.

		X_1 [m]	R_1 [m]	N_1	X_2 [m]	R_2 [m]	N_2	X_3 [m]	R_3 [m]	N_3
$n_{layer} = 1$	Lower	0.2	0.02	2	-	-	-	-	-	-
	Upper	0.4	0.045	16	-	-	-	-	-	-
$n_{layer} = 2$	Lower	0.2	0.02	2	0.3	0.02	2	-	-	-
	Upper	0.3	0.045	16	0.4	0.045	16	-	-	-
$n_{layer} = 3$	Lower	0.2	0.02	2	0.267	0.02	2	0.334	0.02	2
	Upper	0.267	0.045	16	0.334	0.045	16	0.4	0.045	16

3.5.2 Finite Element model for the railway wheel cross-section

In accordance with the guidelines defined at the beginning of this section, and with the aim of meeting the needs described there, a geometric characterization of the wheel as a function of four different geometrical parameters is defined. General axisymmetric elements are used for meshing the geometry, as it is explained hereinafter in more detail.

3.5.2.1 Geometry parametrization

Wheel cross-section geometry is parametrized in the present work by four different geometric properties, using a model based on that described by Nielsen and Fredö in [182]. There, the most influential geometric characteristics for the acoustic radiation [10, 59, 182] are chosen in order to describe the wheel cross-section, resulting in a geometry defined by the subsequent variables: wheel radius x_1 , fillet radius x_2 , web thickness x_3 and web offset x_4 , which refers to the relative position between the hub and the rim along the Y axis. A scheme of the wheel cross-section together with each of the defined geometric design variables are shown in Fig. 3.12. Among these attributes, x_1 , x_2 and x_4 are absolute components whose values directly correspond to the wheel radius, fillet radius and wheel offset and, therefore, a change in their value is directly reflected in the wheel shape. Conversely, x_3 is defined as a proportionality factor which multiplies a reference base value, that is, x_3 does not directly reflect the web thickness. Instead, the relation between the physical magnitude of the thickness and the value of x_3 is derived according to

$$w_{thick} = k_{thick} (1 + x_3) \quad (3.3)$$

where w_{thick} represents the web thickness and k_{thick} is the base magnitude, which ranges from $k_{thick} = 0.028$ m at the beginning of the web to $k_{thick} = 0.024$ m at its end.

In all cases, the values of the parameters that build the designs created throughout the optimization procedure described in Section 3.3 are chosen from a space of possible solutions previously defined. The boundaries of such space, as selected for this work, are shown in Table 3.2. Additionally, for further clarification an overview of this framework is illustrated in Fig. 3.12, where the cross-sections corresponding to the use of the upper and lower boundary parameters are exemplified.

Table 3.2: Design domain of wheel for the optimization methodologies.

	x_1 [m]	x_2 [m]	x_3	x_4 [m]
Reference	0.45	0.0427	0.0681	0.0300
Lower Boundary	0.40	0.0364	-0.1000	-0.2700
Upper Boundary	0.50	0.0484	0.1000	0.2700

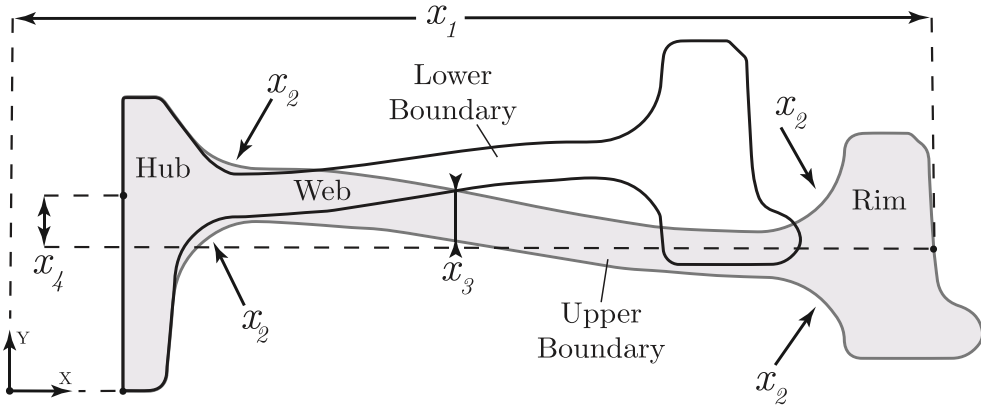


Figure 3.12: Geometric design variables of the wheel parametrization. Cross-sections corresponding to a wheel with upper (shaded) and lower (white) boundary parameters shown in Table 3.2.

3.5.2.2 Axisymmetric elements

Due to the characteristic shape of a railway wheel, it is possible to define its geometry as an axisymmetric solid, i.e. the shape of its body can be generated through a revolution of a plane area, in this case its cross-section, about an axis in the same plane, the Y-axis for the case at hand. Accordingly, it is not compulsory to mesh the whole three-dimensional body to obtain the wheel modeshapes and natural frequencies, just needing to discretize the cross-sections with two-dimensional elements which take into account the axisymmetric condition in their shape functions. More precisely, the FE model considers the use of SOLID 273 general axisymmetric quadratic elements [241], implemented in the commercial FEM software ANSYS APDL, for the wheel cross-section discretization. These elements allow to perform a full three-dimensional eigenanalysis of the wheel through a two-dimensional meshing of a defined number N_{cs} of cross-sections distributed along the angular direction. Thus, by considering Fourier series in the shape functions, whose purpose is describing the displacement field in the circumferential direction, the full three-dimensional problem can be solved. In such formulation, considering that the displacement components can be expressed as a distribution of Fourier series across the angular coordinate Θ , as it is the case of the railway wheel modeshapes, the resulting interpolation functions can be formulated as [245]

$$\begin{aligned}
 u &= h^u \left(c^u + \sum_{n=1}^{\frac{N_{cs}-2}{2}} (a_n^u \cos(n\Theta) + b_n^u \sin(n\Theta)) \right. \\
 &\quad \left. + a_{\frac{N_{cs}}{2}}^u \left(\cos\left(\frac{N_{cs}}{2}\Theta\right) + \sin\left(\frac{N_{cs}}{2}\Theta\right) \right) \right) \quad (3.4)
 \end{aligned}$$

$$\begin{aligned}
 v &= h^v \left(c^v + \sum_{n=1}^{\frac{N_{cs}-2}{2}} (a_n^v \cos(n\Theta) + b_n^v \sin(n\Theta)) \right. \\
 &\quad \left. + a_{\frac{N_{cs}}{2}}^v \left(\cos\left(\frac{N_{cs}}{2}\Theta\right) + \sin\left(\frac{N_{cs}}{2}\Theta\right) \right) \right) \quad (3.5)
 \end{aligned}$$

$$\begin{aligned}
 w &= h^w \left(c^w + \sum_{n=1}^{\frac{N_{cs}-2}{2}} (a_n^w \cos(n\Theta) + b_n^w \sin(n\Theta)) \right. \\
 &\quad \left. + a_{\frac{N_{cs}}{2}}^w \left(\cos\left(\frac{N_{cs}}{2}\Theta\right) + \sin\left(\frac{N_{cs}}{2}\Theta\right) \right) \right) \quad (3.6)
 \end{aligned}$$

for the case where N_{cs} is even; and

$$u = h^u \left(c^u + \sum_{n=1}^{\frac{N_{cs}-1}{2}} (a_n^u \cos(n\Theta) + b_n^u \sin(n\Theta)) \right) \quad (3.7)$$

$$v = h^v \left(c^v + \sum_{n=1}^{\frac{N_{cs}-1}{2}} (a_n^v \cos(n\Theta) + b_n^v \sin(n\Theta)) \right) \quad (3.8)$$

$$w = h^w \left(c^w + \sum_{n=1}^{\frac{N_{cs}-1}{2}} (a_n^w \cos(n\Theta) + b_n^w \sin(n\Theta)) \right) \quad (3.9)$$

for a case with an odd number N_{cs} . In both cases, $c^{u,v,w}$, $a_n^{u,v,w}$ and $b_n^{u,v,w}$ represent the coefficients for the Fourier terms and $h^{u,v,w}$ correspond to regular Lagrangian polynomial interpolation functions.

General axisymmetric elements also have the advantage of allowing, if necessary, the inclusion of non-axisymmetric loads. For clarification purposes, in Fig. 3.13 an example of a quadratic general axisymmetric element with $N_{cs} = 3$ is presented. Besides, in order to exemplify the precision of the el-

Table 3.3: Comparison of natural frequencies of modeshapes obtained with SOLID 273 general axisymmetric elements and with a full three-dimensional mesh with SOLID 186 hexahedrons.

Mode	1	3	4	5	15	16	26	27	35	36
SOLID 273 [Hz]	124.86	249.09	293.78	336.48	1462.90	1681.30	2552.90	2628.50	3191.90	3419.30
SOLID 186 [Hz]	124.86	249.09	293.78	336.48	1462.90	1681.30	2552.90	2628.50	3191.90	3419.30

elements used, in Table 3.3 a comparison of the natural frequencies of some modeshapes of the wheel obtained with both axisymmetric elements and with full three-dimensional quadratic hexahedrons, e.g. SOLID 186 [241] is shown. The element size used is $h = 0.007$ m and, as it can be seen, the results are identical with a precision of 10^{-2} Hz.

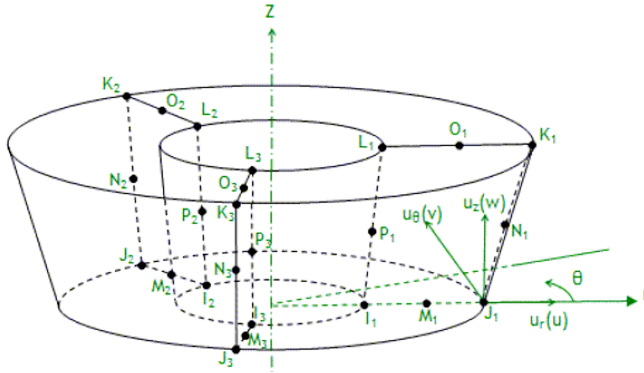


Figure 3.13: Example of a general axisymmetric quadratic element with a number of cross-sections $N_{cs} = 3$. Letters $I_i - P_i$, refer to nodes of the element conforming the i th layer and a cylindrical coordinate system is considered. Originally published in [245]

3.6 Modal identification and modeshape characterization

The evaluation of the objective functions, as repeatedly mentioned along the explanation of each procedure conducted in Section 3.3, requires to carry out a modal analysis beforehand. Moreover, when obtaining wheel SWL, it becomes necessary to solve railway dynamics and explicitly calculating the acoustic power. As a consequence, it is also compulsory to identify the modeshapes of the wheel by means of their number of nodal diameters n and circumferences m , as well as to obtain from them the modal displacements.

More precisely, in the link between the FEM module and the computing of fitnesses throughout the optimization algorithm, the following values are involved for each modeshape:

- Number of nodal diameters n .
- Number of nodal circumferences m .
- Modal damping ξ_n .
- Displacements of the node corresponding to the contact point for coordinates x , y , z , and φ_Θ .
- Modal amplitudes in the axial direction for the radial positions considered in the SWL calculation.

In the following pages, a detailed description is provided of the way each quantity is obtained.

3.6.1 Nodal diameters and modal amplitudes

The first step in the process of determining the number of nodal diameters n is to transform the modal displacement reference system for each node to one more convenient for the axisymmetric approach, as in Fig. 3.14, through

$$\Psi_{i,\rho} = \Psi_{i,x} \cos(\Theta_i) + \Psi_{i,z} \sin(\Theta_i) \quad (3.10)$$

$$\Psi_{i,\Theta} = -\Psi_{i,x} \sin(\Theta_i) + \Psi_{i,z} \cos(\Theta_i) \quad (3.11)$$

$$\Psi_{i,y'} = \Psi_{i,y} \quad (3.12)$$

where $\Psi_{i,x/y/z}$ is the modal amplitude of node i in directions x , y and z , respectively; $\Psi_{i,\rho/\Theta/y'/\varphi_\Theta}$ the modal amplitude in the new reference system; and Θ_i is the Θ coordinate corresponding to node i .

Later, the modal amplitudes in the axial direction corresponding to the nodes in the six previously defined ring radii (see Fig. 2.20 for details) are extracted from the modal matrix Ψ and sorted for the Θ direction. Now, if these modal displacements are represented, it is clearly appreciated how a harmonic function arise for each ring with a given amplitude and number of nodal positions. For illustrative purposes, in Fig. 3.15, the amplitudes of a given modeshape for each defined radii in one wheel are shown. In this example, after a visual

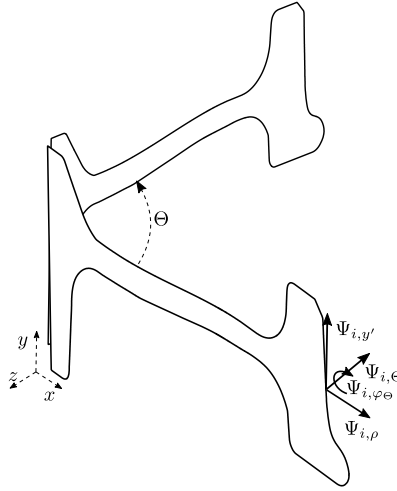


Figure 3.14: Example of modal amplitudes $\Psi_{i,\rho/\Theta/y'/\varphi_\Theta}$ in a section of wheel represented by two different cross-sections separated in different Θ positions.

inspection it is obvious that the number of nodal diameters n of the modeshape is $n = 1$.

Such harmonic pattern would repeat in every case for all modeshapes. Therefore, it is immediate to derive n by means of a *Fast Fourier Transform* (FFT) over the nodal displacements of one of the rings, where n would be just one less than the position of the fundamental harmonic. Using the same example, FFT of each of the rings displayed in Fig. 3.15 is represented in Fig. 3.16. As it is observed, in all rings the number of nodal diameters n obtained is $n = 1$, reflected in that all harmonics are placed at position 2, and the given amplitudes match that displayed for each ring r_j in Fig. 3.15.

Following with the FFT analysis, it is now possible to extract the maximum modal amplitudes for each ring, as the model uses the data of that cross-section with the maximum displacements for the SWL computation. With this purpose in mind, it is possible to describe the above mentioned harmonic behaviour given by the modal displacements for each ring and a given modeshape as

$$\Psi_{i,y'}^{r_j} = A_{real} \cos(n \alpha_i) + A_{imag} \sin(n \alpha_i) \quad (3.13)$$

where $\Psi_{i,y'}^{r_j}$ is the amplitude in direction y' at a node i inside ring r_j , n is the number of nodal diameters of the modeshape, α_i is the phase corresponding to

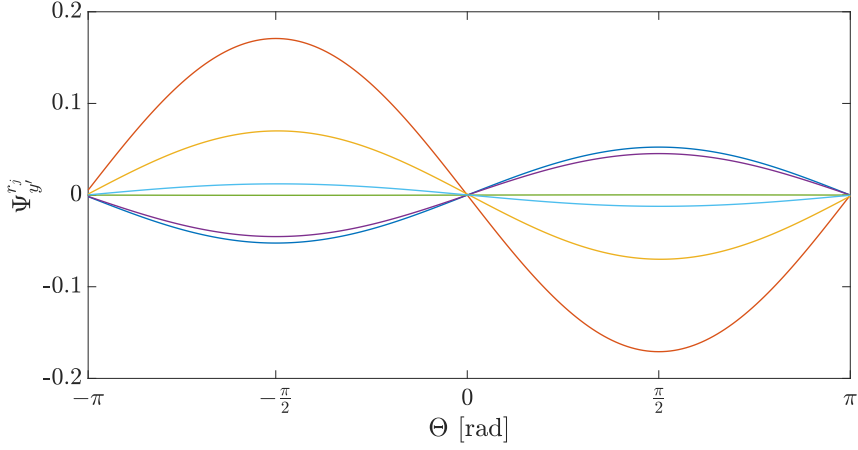


Figure 3.15: Modal amplitudes in the axial direction of a $n = 1$ modeshape for the nodes of the various rings obtained from the modal matrix Ψ . Each colour represents the corresponding amplitude $\Psi_{y'}^{r_j}$ along the ring r_j with $j = 1, \dots, 6$.

the cross-section to which the node i belongs, A_{real} corresponds to the maximum amplitude of the real component of the FFT and A_{imag} to the imaginary part. Furthermore, the maximum amplitude must obey

$$\frac{\Psi_{y'}^{r_j}}{d\alpha} = 0 \quad (3.14)$$

with $\frac{\Psi_{y'}^{r_j}}{d\alpha}$ at node i given by

$$\left(\frac{\Psi_{y'}^{r_j}}{d\alpha} \right)_i = [-A_{real} \sin(n \alpha_i) + A_{imag} \cos(n \alpha_i)] n \quad (3.15)$$

It is immediate to derive from Eqs. (3.14) and (3.15) that

$$\frac{A_{imag}}{A_{real}} = \tan(n \alpha_i) \quad (3.16)$$

and, therefore,

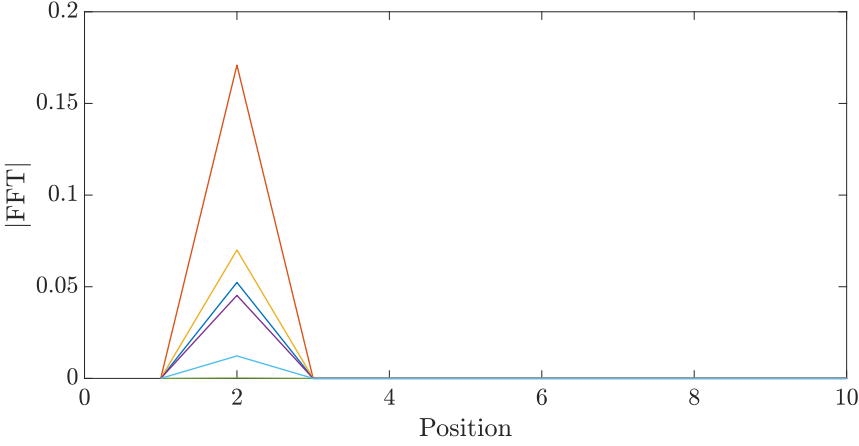


Figure 3.16: *Fast Fourier Transform* of a modeshape with $n = 1$ for every ring of nodes corresponding to each defined radii.

$$\alpha_i = \frac{1}{n} \arctan\left(\frac{A_{imag}}{A_{real}}\right) \quad (3.17)$$

Once A_{real} and A_{imag} are known, it is straightforward to derive α_i first and, later, the maximum nodal amplitude of the modeshape along the selected ring $\Psi_{y'}^{r_j}$ by substituting in Eq. (3.13). The same α_i computed for the first ring selected, would be applied for the rest of the rings, as all the amplitudes used must be in the same cross-section.

3.6.2 Displacement of the contact point

In the case of the displacement of the contact point, a similar procedure as that explained in Section 3.6.1 is followed. This time, though, the FFT also considers the nodal displacements in the radial and transversal directions Ψ_ρ and Ψ_Θ , respectively, and small differences in the methodology appear for the calculation of the displacements of rotational component φ_Θ , Ψ_{φ_Θ} .

In the first step of this procedure, those nodes conforming the contact ring r_c are selected, which in the present work will always equal to select the nodes of ring r_6 (see Fig. 2.20). Now, by applying the same procedure than Section 3.6.1 but also considering this time the displacements in the radial and transversal directions, the displacements of the contact node in Ψ_ρ , Ψ_Θ and $\Psi_{y'}$ can be

obtained. To proceed, a new set of nodes conforming a ring neighbouring r_c is needed in order to compute the rotations in φ_ρ and $\varphi_{y'}$. This ring, named as "near contact ring" or r_{nc} , is formed by the closest node to the contact node in direction y for each cross-section. Now, it is immediate to define the rotational displacements of the nodes of r_c as

$$\Psi_{i,\varphi_\Theta} = \frac{\Psi_{i,\rho}^{r_{nc}} - \Psi_{i,\rho}^{r_c}}{\Delta_{y'}} \quad (3.18)$$

where $\Delta_{y'}$ is the difference between r_c and r_{nc} in the component y' for each couple of nodes i , $\Psi_{i,\rho}^{r_{nc}}$ corresponds to the modal displacement in ρ direction for the nodes in ring r_{nc} and $\Psi_{i,\rho}^{r_c}$ the one corresponding to nodes in ring r_c . Finally, the same methodology than with the other coordinate displacements is used.

It is important to state that, for the work developed in the present Thesis, displacements corresponding to Ψ_{φ_ρ} and $\Psi_{\varphi_{y'}}$ are not computed, as it is considered that their influence is not relevant enough and they could be taken as zero.

3.6.3 Nodal circumferences

When assessing the number of nodal circumferences m , a different process is required than that presented for the nodal diameters n . Instead of using a FFT, this time m is derived by counting sign changes in the modal amplitudes. Likewise in Section 3.6.1, for each cross-section plane in the mesh, the one with the maximum displacement in the contact point is selected. This way, possible discrepancies caused by a cross-section plane located in a nodal diameter can be avoided. Then, modal amplitudes $\Psi_{y'}$ of each surface node of the internal face of the wheel are extracted and sorted by their radial component. Afterwards, the sign changes in $\Psi_{y'}$ are counted, resulting in the value of m in each given cross-section. A scheme of such procedure is depicted in Fig. 3.17.

As there could be numerical perturbations in the near zero values due to the inherent error of FEM, that would produce changes in the sign of $\Psi_{y'}$ not related to the presence of a nodal circumference, hence a tolerance value tol_{err} is considered to avoid this problem. Therefore, any node with a modal amplitude that accomplish $|\Psi_{y'}| \leq tol_{err}$ is considered as a zero value for the sign counting.

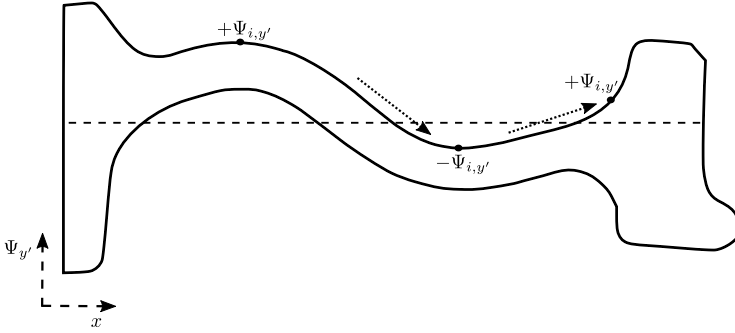


Figure 3.17: Schematic of the nodal circumference derivation procedure for a wheel mode-shape with $m = 2$. Each dotted arrow represents one sign variation in $\Psi_{y'}$, with the discontinued line indicating zero value.

3.6.4 Modal damping

Once the number of nodal diameters is established for each mode-shape, it is possible to assign the corresponding modal damping ξ_{nm} . This way, depending on the value of n , the assigned modal damping value is [4]

$$\xi_{nm} = \begin{cases} 10^{-3} & \text{for } n = 0 \\ 10^{-2} & \text{for } n = 1 \\ 10^{-4} & \text{for } n > 1 \end{cases} \quad (3.19)$$

3.7 Objective functions

In every optimization process, an objective function, also known as fitness function, is necessary in order to have the ability to sort and rank all different designs. Its purpose is to take the characteristics of each candidate and to assign them a numerical value expressing its adequacy to the set of features the optimization is looking for. Usually, when assessing the suitability of each candidate, the smaller the fitness value the better. This aspect is later used to designate the probability of wheel genes to be passed on to the next generation or to choose the final BFS.

Two different objective functions are built in the optimization algorithms developed in the present Thesis. All of them are based on the wheel natural

frequencies and modeshapes: the first one, $L_{A,W}$ -min, consists mainly on the SWL calculation and minimization explained in Chapter 2 while the other, NF-max, is founded on the maximization of the natural frequencies of all modeshapes. This way, due to the combination of a GA-based optimizer with the acoustic model explained in Chapter 2 for the SWL calculation, the first proposed methodology $L_{A,W}$ -min offers a direct, accurate and potentially effective way of minimizing the railway wheel noise taking into account the whole dynamic process. Moreover, since this approach may imply a high computational cost, the alternative presented, NF-max, attempts to indirectly minimize the radiated SWL with less computational cost and mathematical complexity. As for the case of the preliminary studies performed around the influence of track geometry on rolling noise, it should be remarked that no objective function is considered as no explicit search for a sound minimizing design is executed (see Section 4.5 for details).

Accordingly, in the subsequent sections the main features of each proposed methodology are explained with further detail.

3.7.1 $L_{A,W}$ -min

The $L_{A,W}$ -min methodology aims to directly minimize the rolling noise radiated by the wheel. To do so, the fitness of this methodology, $Obj_{L_{A,W}}$, corresponds to the sum in energy of the candidate wheel SWL, $L_{A,W}$. The SWL computed includes the effects of roughness in the excitation and is expressed in A-weighted decibels. During its computation, the roughness considered is defined by the standard DIN-prEN 13979-1 [200] for a train moving at the speed $V = 80$ km/h and expressed in one-third octave bands. Moreover, in order to take into account human perception of the noise, the radiated power is expressed as the SWL in dB(A) [246]. On that account, SWL is expressed as

$$\text{SWL} = 10 \log_{10} \left(\frac{W_w}{W_{ref}} \right) + A_{filter} \quad (3.20)$$

where W_w is the sound power of the wheel, $W_{ref} = 10^{-12}$ W and A_{filter} is the A-weighting filter for dB.

Finally, as stated above, the summation of the radiated power in each frequency band after having taken into account the effect of the A-weighting filter is used as the objective function. Therefore, Obj is defined in this case as

$$Obj_{LA,W} = 10 \log_{10} \left(\sum_{i=1}^{n_{cf}} 10^{\frac{SWL_i}{10}} \right) \quad (3.21)$$

where SWL_i is the SWL of the i th one-third octave band and n_{cf} the number of bands in the studied frequency region.

This objective function is used in both wheel related optimization procedures, either in the Wheel Shape Optimization Algorithm with the approach named as itself as well as the objective function during the Perforation Scheme Optimization.

3.7.2 *NF-max*

Vibration of wheels is highly influenced by the wheel-rail combined roughness inasmuch it is ultimately responsible of the interaction leading to rolling noise. Besides, roughness content in general reduces as the frequency increases, with a local exception in the lowest frequency region, where there is a slight irregularity in the trend. This is illustrated in Fig. 2.12 in Chapter 2, where the roughness defined by DIN-prEN 13979-1 [200] used in the present work is represented. Combining it with the effect of the contact filter, the general trend of a typical rolling noise excitation signal appears as monotonically decreasing along frequency, with the aforementioned initial exception. In addition, given the broad band frequency content in a typical rolling noise excitation signal, it is difficult to focus on a narrow frequency range in which trying to suppress or attenuate modes located in it.

Consequently, the assumption is that maximizing the natural frequencies of the modes of the wheel, i.e. shifting its natural frequencies to a higher frequency region where the roughness frequency content is lower, should generally lead to wheel candidates whose vibration modes are less excited, and therefore to quieter wheel designs [247, 248].

To this end, the NF-max methodology, abbreviation of natural frequency maximization, aims to maximize the average of the wheel natural frequencies. With this goal in mind, the objective function Obj for the present methodology is defined as

$$Obj_{NF} = \frac{1}{\hat{\omega}_m} \quad (3.22)$$

where $\hat{\omega}_m$ is the mean value of the N_m wheel natural frequencies computed by the algorithm. It is obvious that this methodology only requires performing a modal analysis for each candidate wheel, thus highly simplifying the algorithmic complexity and reducing the computational cost.

This objective function is just used in the Wheel Shape Optimization Algorithm with the approach named as itself.

Chapter 4

Results

4.1 Introduction

Throughout the optimization procedures developed in the present Thesis, several results have been achieved. Besides of the BFS wheel and perforation scheme designs attained, attention is also paid to the influence of the geometric parameters of each component in the rolling noise radiation and the physical mechanisms behind the SWL reductions accomplished.

Thus, this chapter opens in Section 4.2 with the validation of the models introduced in Chapters 2 and 3 with the reference software in the field, TWINS. Then, the different outcomes obtained in the optimizations of wheel perforated schemes are presented in Section 4.3. Later, Section 4.4 introduces the cross-sectional wheel shape optimizations as well as the survey on the relation between the different objective function adopted. Last, in Section 4.5 the study made on how the track shape impacts rolling noise radiation is introduced.

Table 4.1: Geometric parameters and ring radii of the reference wheel.

Reference Wheel						
Radii [m]	First ring	r_1	0.0650	Fifth ring	r_5	0.3807
	Second ring	r_2	0.1365	Tyre interior rad.	r_{int}	0.4100
	Third ring	r_3	0.2126	Wheel rad.	r_w	0.4500
	Fourth ring	r_4	0.3045	Tyre exterior rad.	r_7	0.4614
Widths [m]	Web width	w_{web}	0.0299	Tyre width	w_{tyre}	0.1300

4.2 Methodology validation

Before introducing the results, the validation of the radiation model presented in Chapters 2 and 3 should be discussed in order to ensure the correct development and implementation of the SWL calculation embedded in the optimization procedure. Through this section, the different results produced by the model are compared with their counterparts generated by the commercial program TWINS [91, 133], the reference program in the field.

For the simulations, the reference wheel of the cross-sectional wheel shape optimization procedure is used, with a maximum element size $h = 0.007$ established for the cross-section mesh. The six concentric rings radii, widths and the rest of geometric information of the wheel needed for the TWINS calculation are offered in Table 4.1.

With regard to the track, an UIC54 rail [91] with concrete bibloc sleeper separated 0.6 m and a rail profile radius $r_2^R = 0.3$ m is considered, whose track parameters are shown in Table 4.2. In the deformable track cross-section case, the rail mesh used has a maximum element size of $h = 0.04$ m. In relation to the sleeper geometry, the values selected are: length $l_{sl} = 0.8400$ m, height $h_{sl} = 0.2200$ m and width $b_{sl} = 0.25$ m. Steel with density $\rho = 7850$ kg/m³, Young modulus $E = 2.1 \cdot 10^{11}$ N/m² and Poisson's ratio $\nu = 0.3$ is chosen for all components selected. In all cases, a train speed of $V = 80$ km/h is considered and, when computing the SWL, a roughness defined according to the DIN-prEN 13979-1 standard [200] combined with the corresponding contact filter are used.

Table 4.2: Track parameters used in SWL calculations.

Rail UIC54	Vertical	Lateral	Foundation	Vertical	Lateral
Bending stiffness EI [Nm ²]	$4.93 \cdot 10^6$	$0.87 \cdot 10^6$	Pad stiffness k'_p [N/m ²]	$2.17 \cdot 10^9$	$1.67 \cdot 10^8$
Shear coefficient κ	0.4	0.4	Pad loss factor η_p	0.25	0.25
Loss factor η_r	0.02	0.02	Ballast stiffness k'_b [N/m ²]	$1.17 \cdot 10^8$	$5.83 \cdot 10^7$
Mass per length ρA [kg/m]	54.43		Ballast loss factor η_b	2	2
Cross receptance level	-15		Sleeper mass per length m'_s [kg/m]	203.33	

Hence, the receptances in each direction of the wheel at the contact point are compared with their TWINS equivalents at Fig. 4.1. As it can be seen, in all response functions both the curve corresponding to the TWINS calculation and that representing the model developed match for the whole frequency spectrum, with no noteworthy differences. The maximum variance observed in a resonance is of $\Delta|H_{w,xy}| = 0.0623$ dB and a divergence in phase of $\sim 6.88^\circ$, present at 336.48 Hz in Figs. 4.1c and 4.1d, respectively. This later cause a maximum difference in-between resonance peaks of ~ 0.4 dB.

In the case of the track receptances at contact for both existing models, their absolute values and phases in each direction are represented in Fig. 4.2. It should be mentioned that, in the case of the deformable track cross-section model, no cross receptance is obtained due to the symmetry in the vertical plane of the track geometry defined. As it can be appreciated, nearly an exact match occurs between the results generated and those offered by TWINS. In this occasion, the maximum differences are $\Delta|H_{r,yy}| = 0.0042$ dB in the lateral receptance for the Timoshenko beam approach, at 117.48 Hz in Fig. 4.2e, and $\Delta|H_{r,xx}| = 0.16$ dB in the vertical receptance for the deformable track cross-section case, at 300 Hz in Fig. 4.2a, with no significant discrepancies in the phase in neither of both cases. Regarding the differences observed between the receptances of both track models themselves, the changes that appear in the behaviour are consistent with those reported in the literature [4].

To proceed with the contact model validation, the contact forces computed for the radial and axial directions by using the above receptances and considering a unit roughness excitation are shown in Fig. 4.3. In this case, as the modelling of the contact behaviour considered for the y direction correspond to a simplified version of its counterpart in TWINS, some discrepancies arise. When generated with the Timoshenko beam track receptance, the most remarkable disparities for the component $|F_{c,x}|$ are given in the anti-resonances at 1469.16 Hz and 2012.14 Hz, with $\Delta|F_{c,x}| = 1.23$ dB and $\Delta|F_{c,x}| = 1.29$ dB, respectively. As for the phase in Fig. 4.3b, the greatest disparities found are 7.45° at 1968 Hz and 9.74° at 2641 Hz, both preceding the peaks in Fig. 4.3a at 1978 Hz and 2657 Hz with a divergence of ~ 0.5 dB. Regarding the force in direction y , the changes are greater as it can be clearly observed in Fig. 4.3c, with differences of up to 2.3 dB in-between peaks. Even though, no remarkable differences are found in the phase in Fig. 4.3d besides a shift in frequency of 2 - 10 Hz in some regions. If attention is centred in the $|F_{c,y}|$ peaks, the largest contrasts are found at 2958 Hz and 4452 Hz with a $\Delta|F_{c,y}| = 1.5$ dB. Meanwhile, when the contact force is derived with the deformable cross-section track receptance the agreement remains highly accurate. The maximum discrepancies observed

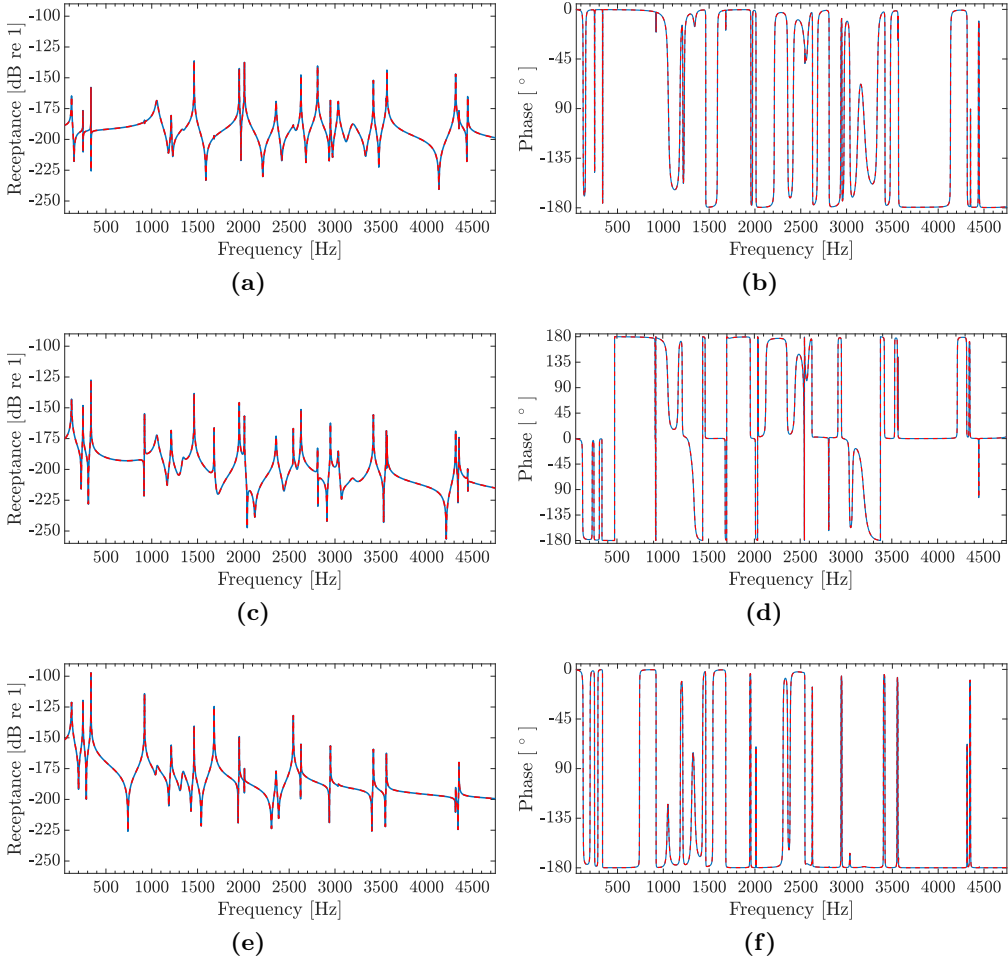


Figure 4.1: Receptance of the wheel at contact point produced by the commercial program TWINS (---) and the methodology developed (—): (a) point radial receptance (response and force in X direction) and (b) phase; (c) cross receptance (response in direction Y and force in X) and (d) phase; (e) point axial receptance (response and force in Y direction) and (f) phase.

are $\Delta|F_{c,x}| = 1.68$ dB at 3423 Hz and $\Delta|F_{c,y}| = 1.78$ dB at 3563 Hz, both corresponding to either a dip or its surroundings and, thus, having a small influence on the posterior SWL computation. In terms of the spikes, no relevant distinctions are detected, presenting an average discordance of $\sim 0.2 - 0.4$ dB.

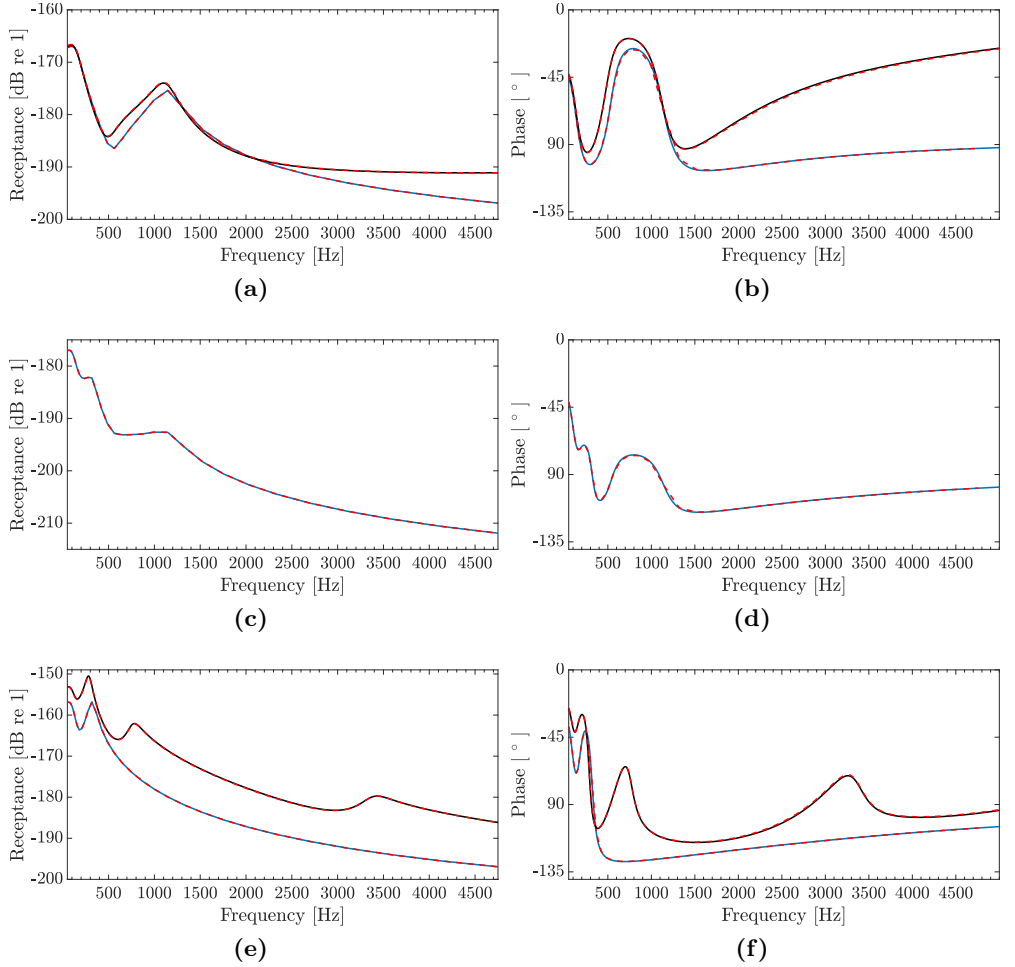


Figure 4.2: Receptance of the rail at contact point produced by the commercial program TWINS (---) and the methodologies developed (— Timoshenko beam; — deformable track cross-section model): (a) point vertical receptance (response and force in X direction) and (b) phase; (c) cross receptance and (d) phase; (e) point lateral receptance (response and force in Y direction) and (f) phase.

As for the phase in Figs. 4.3b and 4.3e, the same patterns than those described for the Timoshenko beam are found. It is worth to specify that, despite having some visible effects in the wheel response, in general terms the discrepancies found are minimal and the differences currently observed ultimately introduce

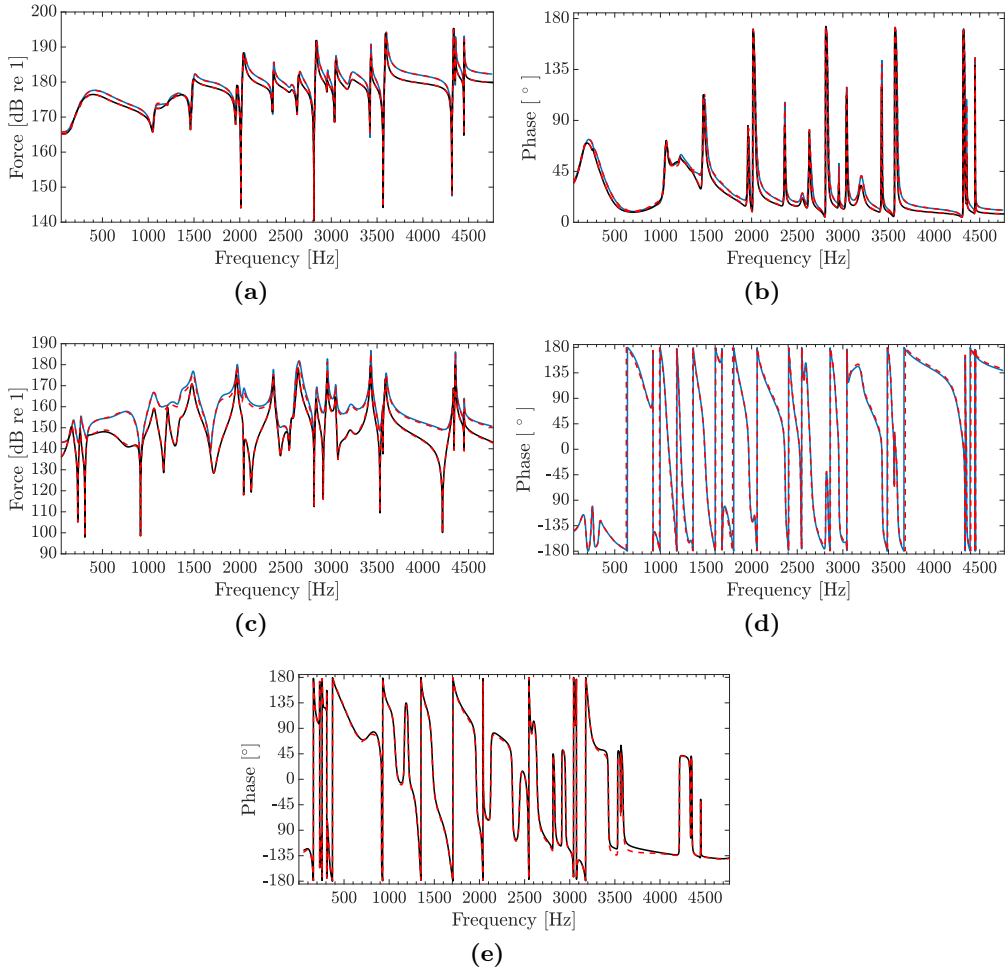


Figure 4.3: Contact force generated by a unit roughness excitation produced by the commercial program TWINS (---) and the methodologies developed (— Timoshenko beam; — deformable track cross-section model): (a) X direction and (b) phase; (c) Y direction and phase for (d) Timoshenko model and (e) deformable track cross-section model.

no significant error in the SWL expressions shown in Figs. 4.7a - 4.7d, as explained below.

Concerning the response of the wheel, the axial velocity response of each of the six previously defined rings are shown in Figs. 4.4 and 4.5. Furthermore, the

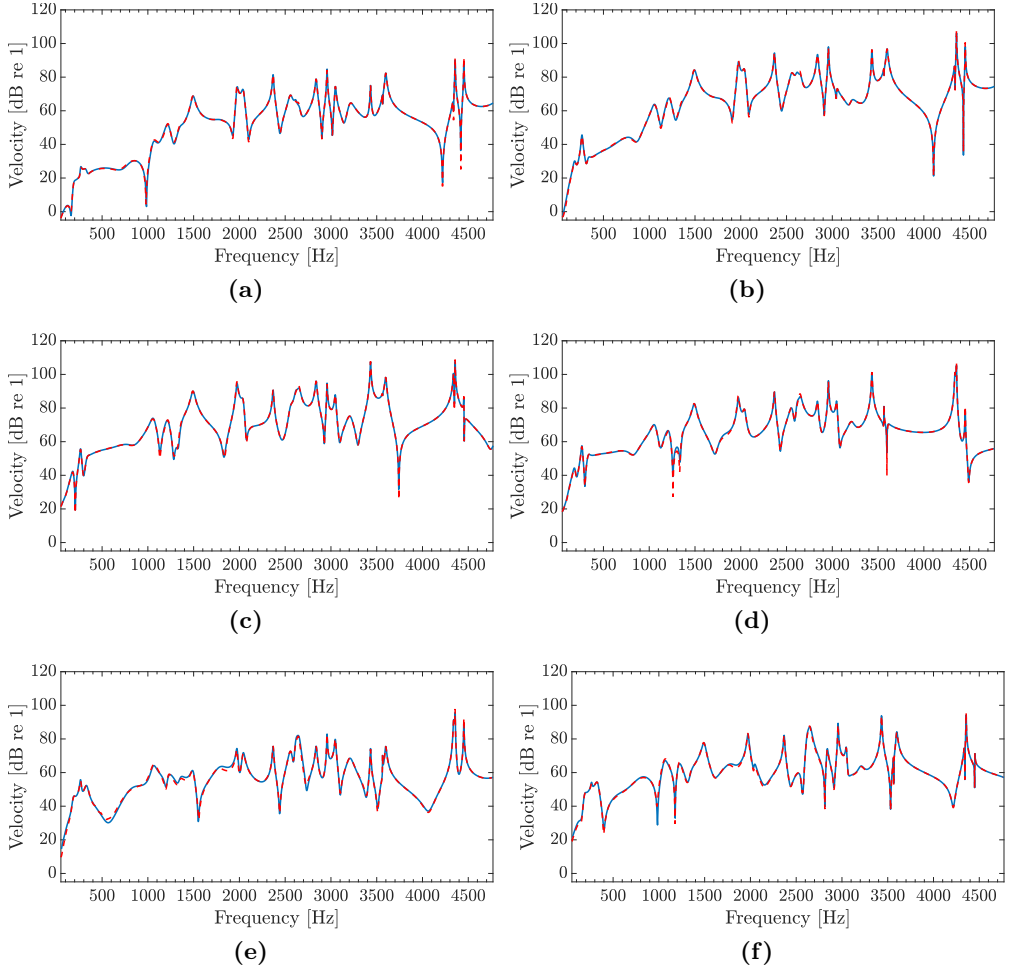


Figure 4.4: Axial response in velocity for the six different rings produced by the commercial program TWINS (---) and the methodology developed (—): (a) r_1 ; (b) r_2 ; (c) r_3 ; (d) r_4 ; (e) r_5 ; (f) r_6 .

contact point wheel velocity in the radial and rolling directions is illustrated in Figs. 4.6a-4.6d. In such cases, there are some visible contrasts as a consequence of the application of the distinct contact receptance, which can be observed in some anti-resonances position, as in the case of 1259.79 and 3595.44 Hz in Fig. 4.4d or some peaks as in 4453.27 Hz in Fig. 4.4e.

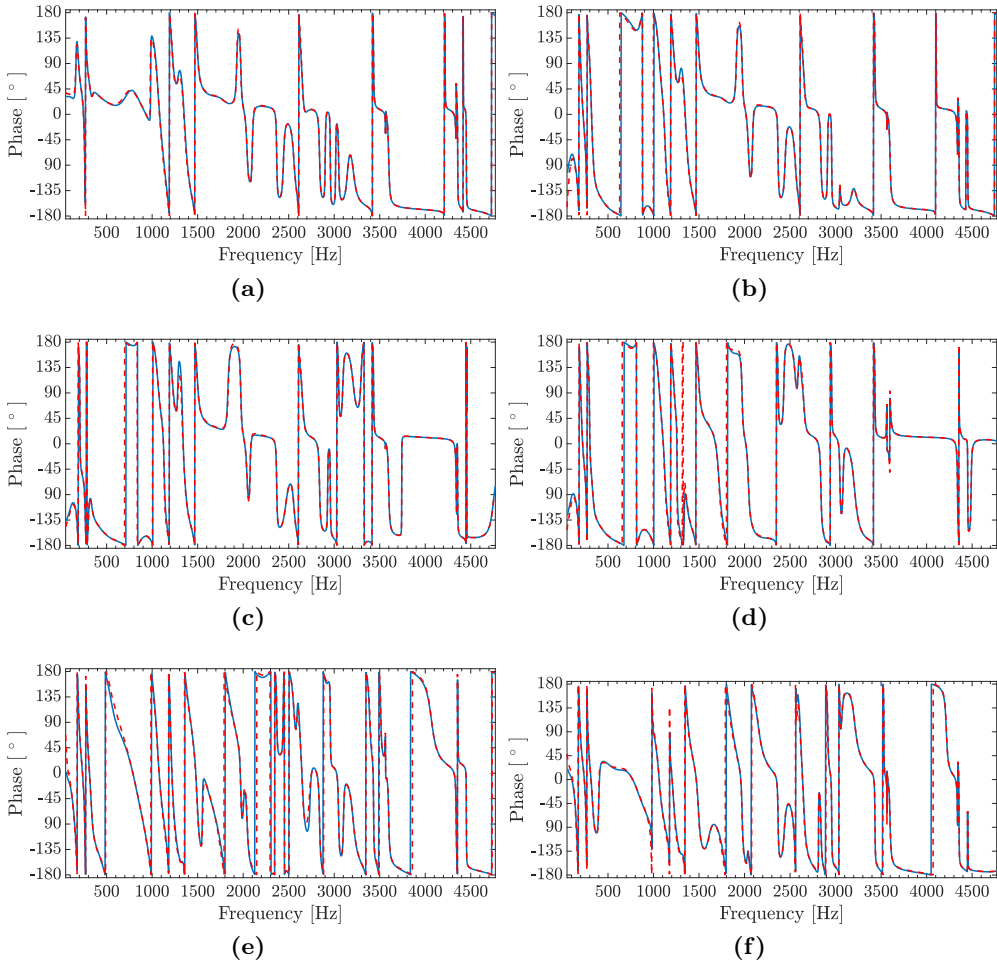


Figure 4.5: Phase of the axial response in velocity for the six different rings produced by the commercial program TWINS (---) and the methodology developed (—): (a) r_1 ; (b) r_2 ; (c) r_3 ; (d) r_4 ; (e) r_5 ; (f) r_6 .

In the same manner, the spatially-averaged squared velocity response of the track obtained with the deformable approach is displayed in Figs. 4.6e and 4.6f. It is immediate to see that the agreement between the deformable cross-section model and the outcome offered by TWINS is large, the most noticeable distinction being a ~ 0.8 dB change at 539 Hz in Fig. 4.6e. The disturbances appearing in the high frequency range of the TWINS outcome in Fig. 4.6e, as

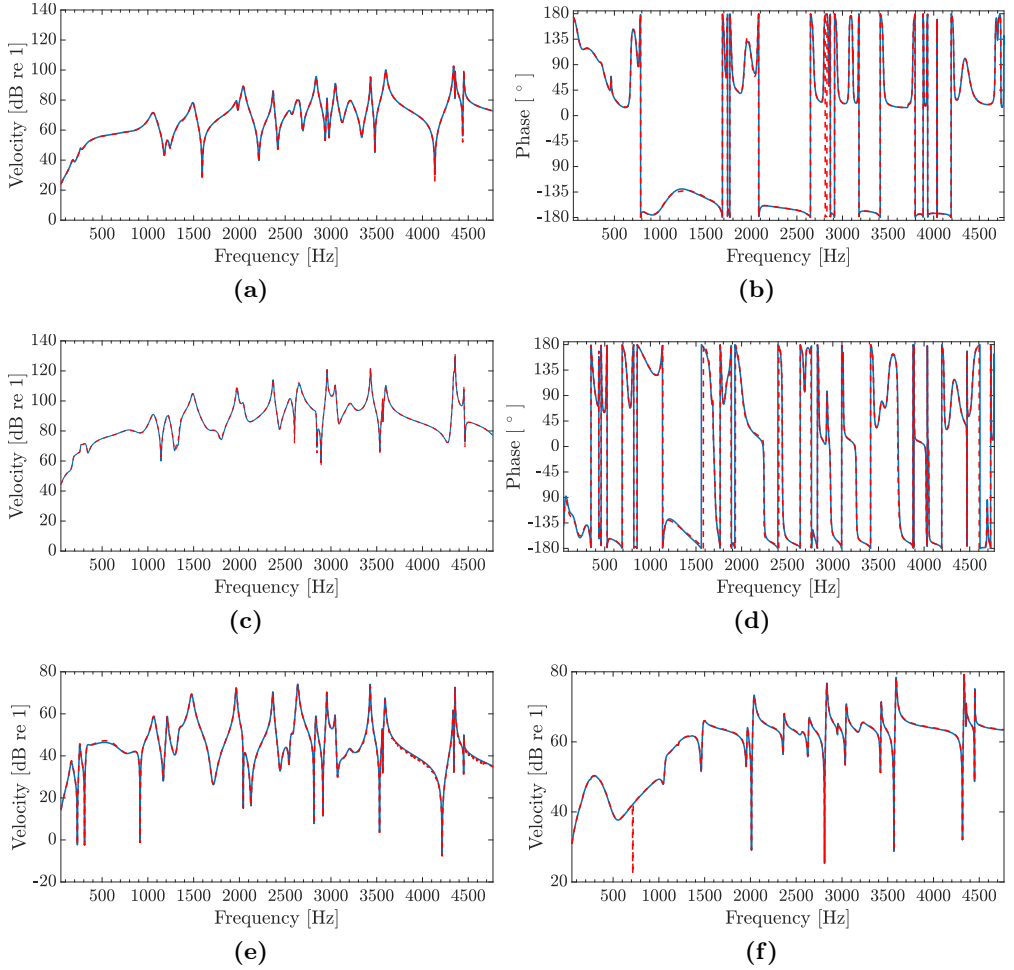


Figure 4.6: Contact point velocity response of the wheel and spatially-averaged squared velocity response of the track produced by the commercial program TWINS (---) and the methodology developed (—). Wheel velocity response: (a) radial direction and (b) phase; (c) φ_{Θ} direction and (d) phase. Track velocity response: (e) X direction; (f) Y direction.

well as the pronounced non-smooth dip located at 715 Hz in Fig. 4.6f, are not considered for the validation analysis as they are assumed to be the result of numerical inaccuracies produced during the software calculation.

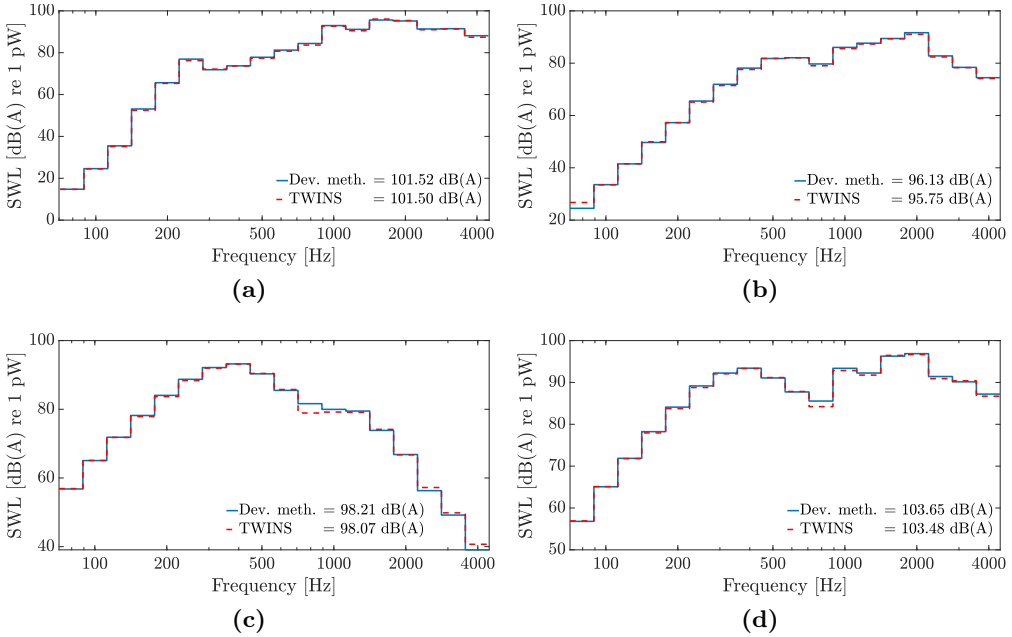


Figure 4.7: SWL produced by the commercial program TWINS (---) and the methodology developed (—): (a) wheel; (b) rail; (c) sleeper; (d) total.

To conclude the validation, in Fig. 4.7 the SWLs returned by TWINS are compared with those computed with the developed models for the chosen wheel, rail, sleeper and their combined radiation, respectively. In the wheel case in Fig. 4.7a, it can be seen that the maximum discrepancy between both curves presents a value of 0.75 dB(A) which, as earlier mentioned, is thought to be related with the contact implementation. In terms of the sum of each SWL band in terms of energy, that would be later used as an objective function in the $L_{A,W}$ -min approach, the difference between methods is just $\Delta L_{A,W} = 0.018$ dB(A). For the rail component SWL in Fig. 4.7b, it is in the 19th octave band (70 - 89 Hz) where a 2.23 dB(A) split occurs. Still, this has a minor influence due to the low energy contribution of the band, with the change in $L_{A,R}$ being $\Delta L_{A,R} = 0.37$ dB(A). The same effect occurs for the sleeper in Fig. 4.7c, where a 2.72 dB(A) in the 29th band (708 - 891 Hz) can be discerned, resulting in $\Delta L_{A,sl} = 0.14$ dB(A). When all three components are combined in the total SWL presented in Fig. 4.7d, the variation turns to $\Delta L_{A,T} = 0.17$ dB(A), with the greater gap being of 1.33 dB(A) in the 29th band likewise the sleeper case.

This way, it can be stated that the vibro-acoustic model developed in the present Thesis for the optimization procedures are in complete agreement with those returned by the software. No significant discrepancies are presented and, therefore, it can be safely implemented in order to compute the radiated noise of generated design candidates.

4.3 Optimization of wheel perforated schemes

In here, the results of the optimization of perforations schemes are discussed. Two set of optimizations are presented: first, using as a base geometry a wheel with a straight web shape; later, by applying the perforation scheme optimization algorithm into a curved web wheel design. Then, the effect of geometric parametric change is further analysed by making use of RSs and an exploratory study of the influence of the fluid-structure interaction in the optimization algorithm acoustic model is considered.

4.3.1 Straight web

For the optimization of a perforated scheme on a wheel with a straight web, the BFS design obtained consists in a unique layer of 6 holes with a radius $R_1 = 0.03031$ m and at distance to the axis $X_1 = 0.26039$ m. A reduction of 2 dB(A) is accomplished with this design, reducing the initial wheel noise of $L_{A,W} = 116.4$ dB(A) to a lower value of $L_{A,W} = 114.4$ dB(A), as shown in Fig. 4.8. The BFS is also structurally feasible with $\Delta A_m/\Delta \sigma_c = 1.48$. These characteristics are summarized in Table 4.3 and, in Fig. 4.9, the reference wheel together with the BFS can be seen.

With the intention of studying the variations observed along the noise spectrum due to the perforation pattern, an analysis of the modal shifting phenomenon between the initial unperforated wheel and the resulting BFS is performed. Even though the introduction of perforations alters the modeshapes of the wheel, it is still possible to visually identify them in the perforated candidates from the unperforated base design. Therefore, it is thought that their shift along the frequency domain and the consequent variation of the derived

Table 4.3: Perforation scheme BFS for the straight web case.

n_{layer}	X_1 [m]	R_1 [m]	N_1	$\Delta A_m/\Delta \sigma_c$	Generations	Time [h]
1	0.26039	0.03031	6	1.48	104	110.1

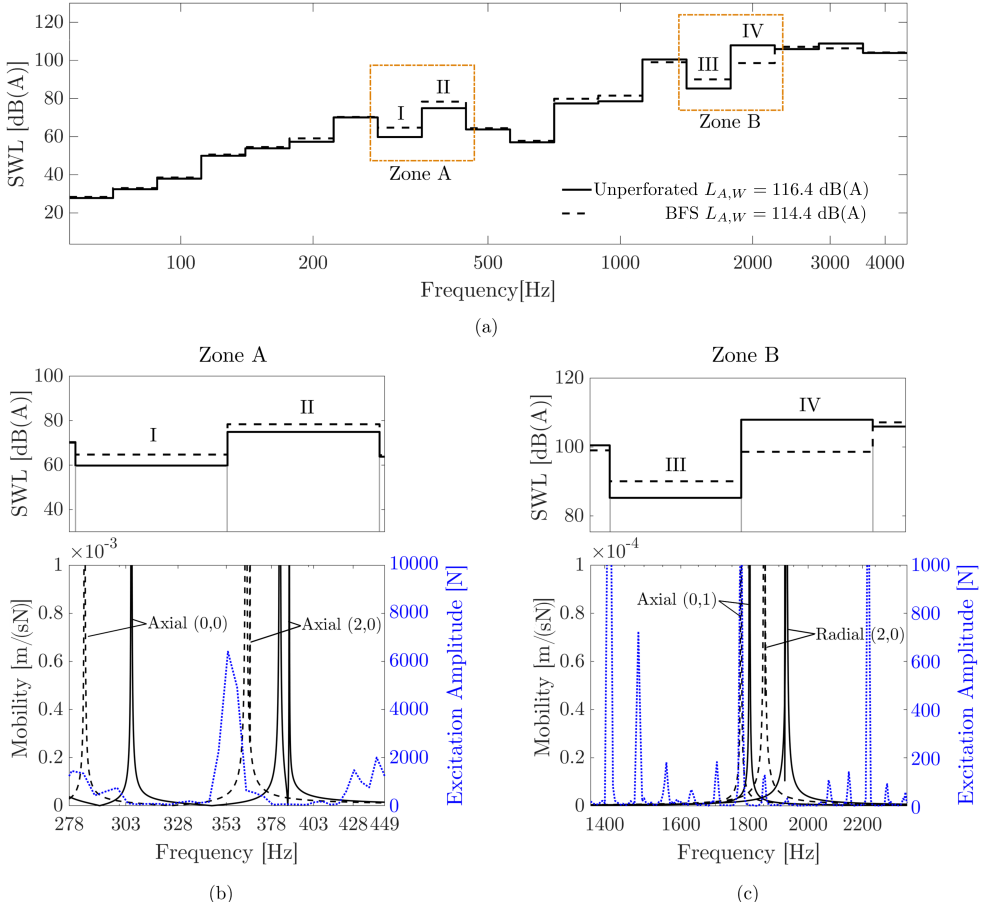


Figure 4.8: (a) SWL curves for the unperforated and BFS wheels for the straight web case; (b) detail of SWL, force amplitude (dotted line, in blue) and axial point mobility at contact for Zone A; (c) detail of SWL, force amplitude (dotted line, in blue) and radial point mobility at contact for Zone B. For all plots, continuous line refers to the unperforated wheel data and dashed lines to the perforated BFS.

mobility are responsible of some of the perceived changes in the SWL curves [249].

First, those more influential modes are determined. This is done by observing the acoustic energy contribution of individual mode shapes to the total SWL. In other words, by expressing the fraction $E_{L_{A,W}}$ of the sum of levels $L_{A,W}$ in energy of the wheel when considering just the selected modeshape compared to

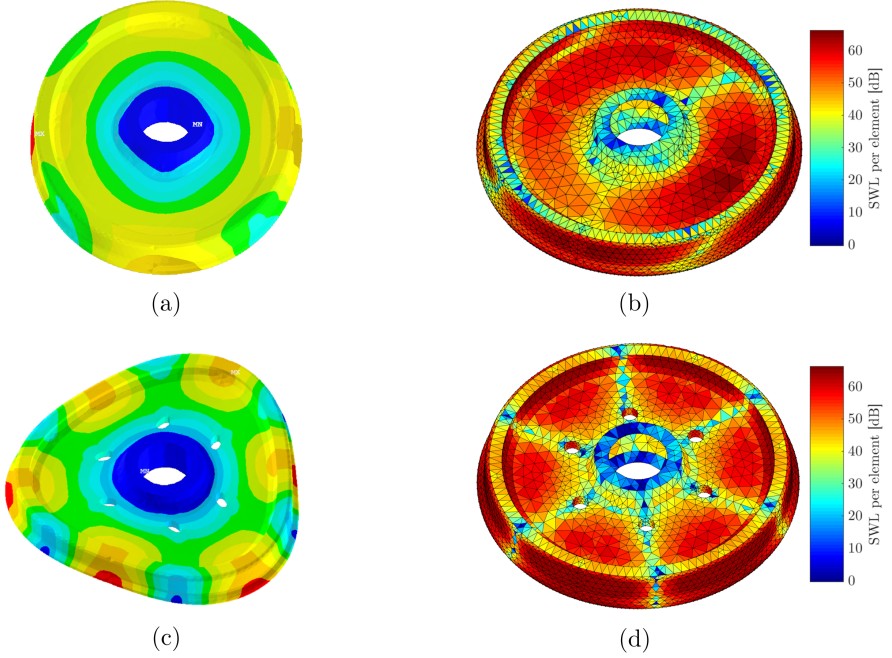


Figure 4.9: Radial (2,0) and (3,0) modeshapes ((a) and (c), respectively) and the SWL distribution along the surface at corresponding natural frequencies ((b) and (d), respectively).

when all modeshapes are considered. The three more influential mode shapes are described in Table 4.4. As it is observed, either for the unperforated or the BFS wheel, the most influential modeshapes are the radial ones, characterized by having predominant in-plane modal displacements in the radial direction. Such phenomenon is explained due to the fact that, for simplification reasons, only a purely radial contact force is introduced in the perforation scheme optimization. As a consequence, radial modeshapes are greater excited than its axial counterparts.

From Table 4.4, changes on the energy contribution share $E_{L_{A,W}}$ caused through the optimized perforation pattern can be appreciated. As an example, the modeshape listed as the most contributing in the base wheel, the radial (2,0) modeshape, only contributes in the BFS in $E_{L_{A,W}} = 0.05\%$. In addition, in Figure 4.9 radial modeshapes (2,0) and (3,0), the most radiating for the unperforated and BFS wheel respectively, are represented together with the computed SWL at their respective natural frequencies along the wheel surface.

It is noticed how the displacement distribution and the corresponding SWL depiction share the number of radial symmetry planes and present similar maxima points, with the highest noise radiation being produced at areas of maximum modal displacement. This effect is especially clear with the (3,0) modeshape, in Figs. 4.9 (c) and (d).

As for the general changes in the SWL, shown in Figure 4.8 (a), both curves are relatively similar. As the wheel is perforated, there are slight noise increments in most of the frequency domain and a considerable reduction is achieved in Band IV, which is largely responsible for the net noise decrease. With regard of the BFS resulting perforation scheme, it is noteworthy that is composed by just 1 layer with 6 holes in it, when the solution spaces allowed for a higher number of perforations that would further minimize the radiating area. Intuitively, it can be thought that as the presence of perforations reduces the radiating surface of the web, a higher number of them would be preferable. However, important radial velocity fields can appear at the hole surfaces. In the case of wheels with straight web, this phenomenon limits the amount of holes preferable for limiting rolling noise. In fact, the noise reduction contribution of the BFS due to the reduced axial surface is quantified in only 0.06 dB(A), representing just $\sim 3\%$ of the total reduction.

Returning to the above mentioned modal shifting concept, SWL variations can be explained by studying the redistribution of the mobility peaks in relation with the excitation frequency content. As an explanatory example, two samples of SWL curves in their respective frequency ranges are shown in Figure 4.8 and compared with the contact point mobility in the same range. Either axial or radial mobility components are chosen depending on the mode shape being described in each case.

An increase in the SWL in Bands I and II from Zone A is appreciated after the perforations are applied. As observed in Fig. 4.8 (b), this can be attributed to the displayed mobility peaks (corresponding to the axial (0,0) modeshape, inside Band I, and the axial (2,0), inside Band II) changing their

Table 4.4: Most contributing modeshapes for the unperforated base wheel and BFS design in the straight web case.

Mode shape	Unperforated		BFS		
	Frequency [Hz]	$E_{LA,W}$ [%]	Modeshape	Frequency [Hz]	$E_{LA,W}$ [%]
Radial, (2,0)	1926	27.0	Radial, (3,0)	2473	16.42
Radial, (4,0)	3167	11.6	Radial, (4,0)	3111	10.49
Radial, (5,0)	3845	8.7	Radial + Torsion, (1,0)	2878	7.82

positions to frequencies where the excitation is notably superior, near a local force maximum in the axial (2,0) case. The mobility peaks appear in pairs as a consequence of the symmetry duplicity of the modeshapes caused by slight asymmetries in the wheel FE mesh.

Regarding Zone B, the SWL variations can be explained by the frequency relocation of the modeshapes present in Figure 4.8 (c). Hence, an increase in SWL is observed in Band III together with a relatively large noise decrement in Band IV. As it can be seen, the axial modeshape (0,1) is shifted from Band IV to Band III, falling into an excitation peak, which derives in an energy transfer between both bands. Moreover, the modeshape with highest energy contribution in the unperforated wheel, the radial mode (2,0), is relocated near Band III where part of its energy content is added.

4.3.2 Curved web

For the optimization of a perforated scheme on a wheel with a curved web, the BFS design obtained consists in two layers of eight and fourteen holes each, with radius and distance to the axis, respectively, $R_1 = 0.03340$ m and $X_1 = 0.22381$ m for the first layer, and $R_2 = 0.03414$ m and $X_2 = 0.39852$ m for the second one. In this case, a notable reduction of 4.8 dB(A) is achieved, by reducing base wheel noise of $L_{A,W} = 121.3$ dB(A) to a resulting BFS with $L_{A,W} = 116.5$ dB(A), as shown in Fig. 4.10. Again, even though the higher number of holes compared to the straight wheel case, with a total of 22 perforations in the present approach, the resulting design is also structurally feasible with $\Delta A_m / \Delta \sigma_c = 1.41$. It is interesting to note that the computational cost of this optimization increases, reaching convergence in the generation 254. Main results for this optimization and respective BFS are summarized in Table 4.5, and the reference wheel together with the BFS can be observed in Fig. 4.11.

In Table 4.6, acoustic energy contribution of the predominant mode shapes for the BFS and unperforated designs when considering a curved web are shown. It is observed how, in the same manner as in the straight web case, radial modeshape are predominant, in consonance with the purely radial input force. Nevertheless, in this occasion an axial modeshape, the (0,1), appears among

Table 4.5: Perforation scheme BFS for the curved web case.

n_{layer}	X_1 [m]	R_1 [m]	N_1	X_2 [m]	R_2 [m]	N_2	$\Delta A_m / \Delta \sigma_c$	Gen.	Time [h]
2	0.22381	0.03340	8	0.39852	0.03414	14	1.41	254	428.2

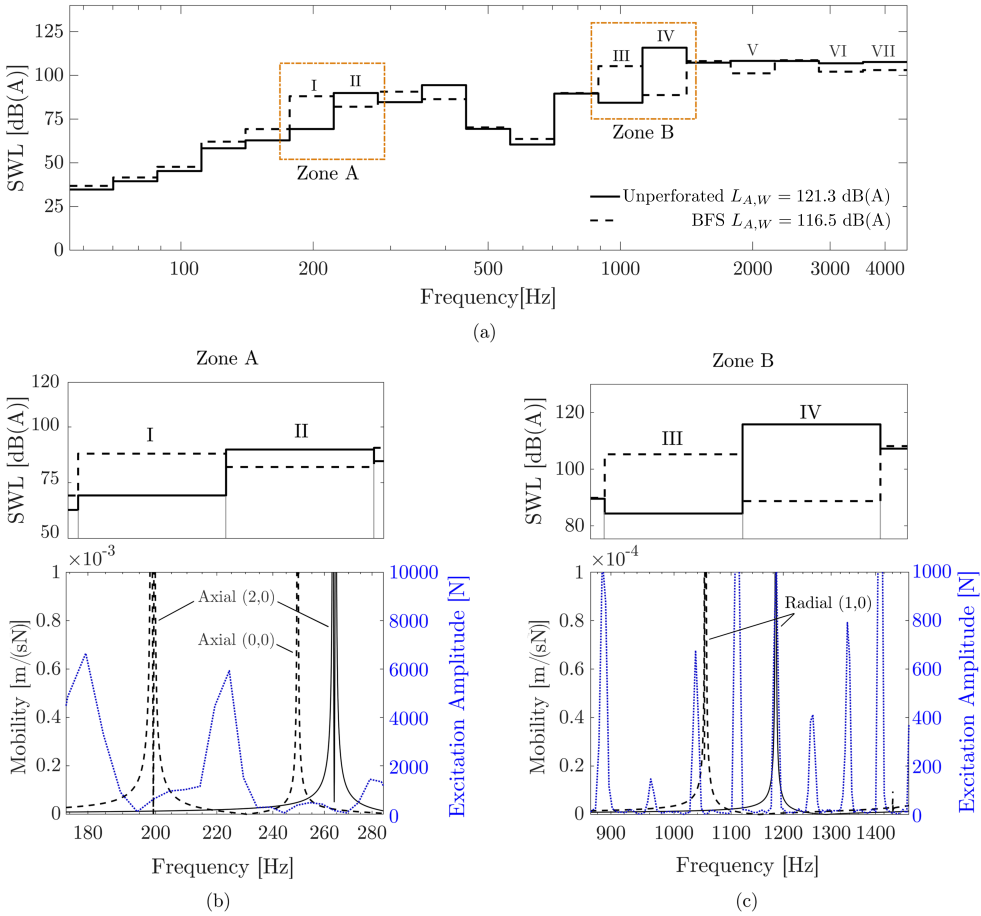


Figure 4.10: (a) SWL curves for the unperforated and BFS wheels for the curved web case; (b) detail of SWL, force amplitude (dotted line, in blue) and axial point mobility at contact for Zone A; (c) detail of SWL, force amplitude (dotted line, in blue) and radial point mobility at contact for Zone B. For all plots, continuous line refers to the unperforated wheel data and dashed lines to the perforated BFS.

the three most relevant modes. Such phenomenon, the excitation of an axial modeshape due to a radial excitation, is caused by the axial-radial coupling produced in railway wheels as a consequence of the curvature of the web. Anyway, after optimization this mode shape has reduced its contribution from 7.1% in the initial wheel to 1.3% in the BFS. The wheel with the BFS perforation scheme has its radiated energy more evenly shared between the different

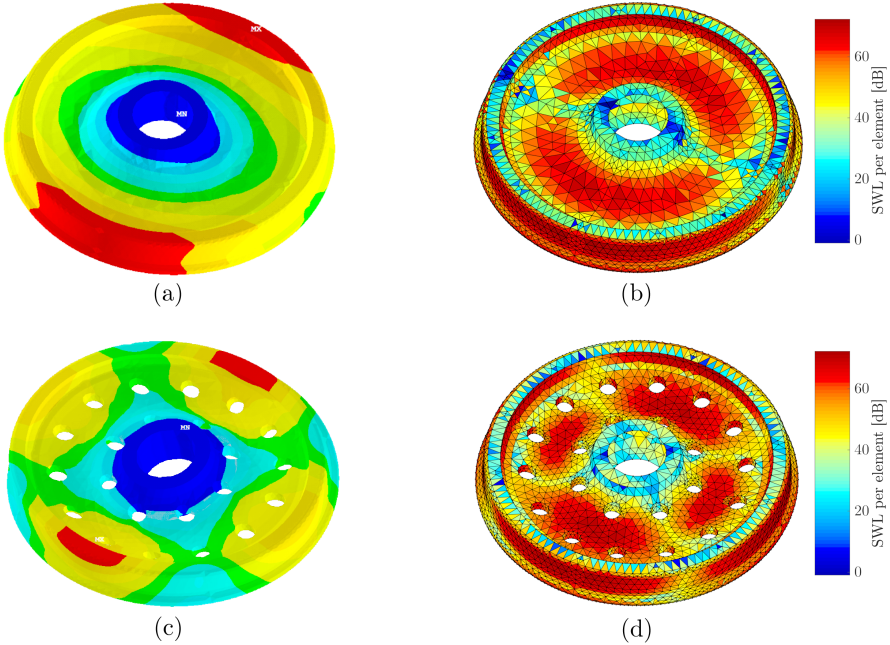


Figure 4.11: Radial (1,0) and (2,0) modeshapes ((a) and (c), respectively) and the SWL distribution along the surface at corresponding natural frequencies ((b) and (d), respectively).

modeshapes. Contrary to its unperforated counterpart, which has a single radial (1,0) modeshape being responsible for the 56.1% of the energy, in the BFS case the three main modes collect just a joint $E_{L_{A,W}} = 48.7\%$, with a maximum share for the radial (2,0) contribution of $E_{L_{A,W}} = 26.2\%$. This relates to the optimization algorithm relocating the most influential wheel resonances at lesser excited frequencies.

The most radiating modeshapes of Table 4.6 are represented in Fig. 4.11 together with the SWL distribution across wheel surface at their natural frequencies. As expected, modeshapes amplitudes and SWL distribution generally share the radial symmetry planes, with the zones of maximum radiation being coincident with the modal displacement maximums.

The aforementioned coupling is also one of the parameters that justifies the significant increase in the total number of holes obtained in the BFS perforation pattern when compared with the straight web approximation. As the resulting axial displacement is greater now and the web surface mostly radi-

Table 4.6: Most contributing modeshapes for the unperforated base wheel and BFS design in the curved web case.

Unperforated			BFS		
Modeshape	Frequency [Hz]	$E_{LA,w}$ [%]	Modeshape	Frequency [Hz]	$E_{LA,w}$ [%]
Radial, (1,0)	1185	56.1	Radial, (2,0)	1591	26.2
Radial, (4,0)	1820	8.9	Radial, (0,0)	2465	11.9
Axial, (0,1)	1775	7.1	Radial, (4,0)	2754	10.6

ates in the axial direction, its reduction by means of the perforations appear as a more effective noise mitigation mechanism in this wheel model than in the straight web case. Therefore, this might help understanding the variations in the achieved perforation patterns, with a total of 22 holes covering the inner and outer web surface in two layers contrasting to the inner single layer with $X_1 = 8$ holes of the straight web resulting candidate.

Besides, when the perforation pattern aligns near the anti-nodal circumferences of certain modeshapes, the mitigation effect of holes in vibration energy is especially significant. This can be clearly noticed in Table 4.7, where the normal velocity of wheel at the natural frequencies of selected axial modes is represented. As seen, the outer layer of perforations (meaning, at $X_2 = 0.399$ m) covers the circumferential areas of higher velocities, which explains, at least partially, their contribution reduction.

Anyhow, as in the straight web case, it should be noted that the SWL minimization directly attributed the reduction in the radiating area is quantified

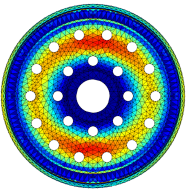
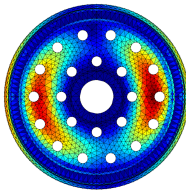
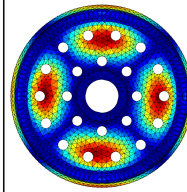
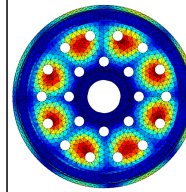
Normal Velocity Distribution				
Modeshape	Axial (0,1)	Axial (1,1)	Axial (2,1)	Axial (4,1)
Freq. (BFS)	1532 Hz	1684 Hz	2107 Hz	3387 Hz
$E_{LA,w}$ [%] Ini.	7.1	0.04	0.24	0.04
$E_{LA,w}$ [%] BFS	1.3	0.00014	0.007	0.001

Table 4.7: Normal velocity representation of wheel at the natural frequencies of a selected sample of axial modeshapes.

in just 0.26 dB(A) (or 5% of the total SWL reduction). Such influences is significantly less relevant than the SWL minimization through the modification of natural frequencies discussed below.

Then, in Fig. 4.10 the SWL curves of both the unperforated and BFS wheel are displayed in combination with their point mobilities and the contact force applied. This way, it is seen in Fig. 4.10 (b) that, in Zone A, the SWL curve of BFS increase in Band I respect the unperforated wheel meanwhile decrease in Band II. It can be seen in the mobility representation that such variation corresponds with the shift of axial (2,0) modeshape from a frequency located in Band II to one in Band I. Also, as the excitation amplitude in the new frequency is higher than in the original position, combined with the relocations of the axial modeshape (0,0) from a higher one-third octave band to Band II, the increase in Band I is greater than the corresponding Band II decrease when compared.

If the attention is fixed now in Zone B, Fig. 4.10 (c) shows a high SWL increment in Band III followed by an even larger decrease in Band IV. That can be explained by analysing the evolution of radial modeshape (1,0), whose related mobility peak matches a force maxima in Band IV for the unperforated wheel. This modeshape is reflected in Table 4.6, where it is shown its high energy contribution with $E_{L_{A,W}} = 56.1\%$. In contrast, after the optimization this mode relocates in Band III at a frequency with significantly less excited amplitude, leading to the important SWL changes observed in Zone B.

With regard Bands V - VII, an overall sound reduction is appreciated without the band content exchange pattern present in Zones A and B. Instead, at these bands the BFS configuration is such than the SWL is reduced in consecutive bands, with no existing counterbalance. It is worth noting that this situation is not given in the straight web wheel optimization, which could be associated with easiness in which modeshape relocation happens for each kind of wheel shape. Given the higher radial-axial coupling of the curved web wheel, the perforation patterns may have a larger influence on modeshape frequency shifts than in the straight web kind. Accordingly, a better positioning between excitation amplitude peaks of resonances is allowed which, at the same time, do not imply noise increments in the consecutive bands due to other undesired frequency shifts.

4.3.3 Response Surfaces

Visualizing the evolution of the objective function along the solution space is a useful tool to understand the behaviour and sensitivity of the designed optimization algorithm and its dependency on the chosen geometric parameters. With that goal in mind, in this section the RSs of the design domain in the surroundings of the resulting BFS wheels are presented.

First, the RS for the straight web procedure is introduced in Fig. 4.12. It is conformed by a uniformly distributed sampling grid of 20×20 points for the combination of the pair of design variables R_1 and X_1 , with a total of 400 different combinations. The selected interval, which covers the values of the BFS perforation scheme, are $R_1 = 0.02$ m to $R_1 = 0.045$ m and from $X_1 = 0.2$ m to $X_1 = 0.4$ m, with the values of n_{layer} and N_1 being kept constant and equal to those of the BFS with a straight web ($n_{layer} = 1, N_1 = 6$) during the samples evaluation. In each case, RSs are built by using cubic interpolation among sample points, represented as black markers

Thus, Figs. 4.12 (a) and (b) represent the $L_{A,W}$ RS for a straight web wheel. The topology observed is significantly complex, with low smoothness zones presenting a high sensitivity of the objective function and including multiple local minima/maxima. Minimum regions present a planar topology with soft variations of $L_{A,W}$. Besides, some relative $X_1 - R_1$ relationships generating high radiation values can be grasped.

Moreover, Figs. 4.12 (c) and (d) display noise reduction with respect to the unperforated base wheel. With the intention of helping to identify that areas more interesting in the present analysis, all solutions with greater value of $L_{A,W}$ than reference is depicted in grey. It is seen how, for the straight web wheel case, only a small fraction of the explored design domain produces better radiation levels than the unperforated case. Also, the RS minima, found in $X_1 = 0.266, R_1 = 0.0305$ and highlighted with an **M** sign, is almost identical to the BFS solution, that has a slightly 0.05 dB(A) lower $L_{A,W}$ value. Such difference is further studied in Fig. 4.13, where minima obtained through GA optimization (**M'**) and the RS (**M**) and the corresponding perforation patterns are compared. As seen, the RS minimum, although close in the studied set of the design space, does not correctly replicate the optimization BFS candidate **M'**. Together with the minimum $L_{A,W}$ value obtained with the RS being higher than that of **M'**, this suggests than a higher number of sample points would be necessary for sufficiently represent the solution field. That reinforces the adequacy of a stochastic global optimization algorithm such as GAs for complex

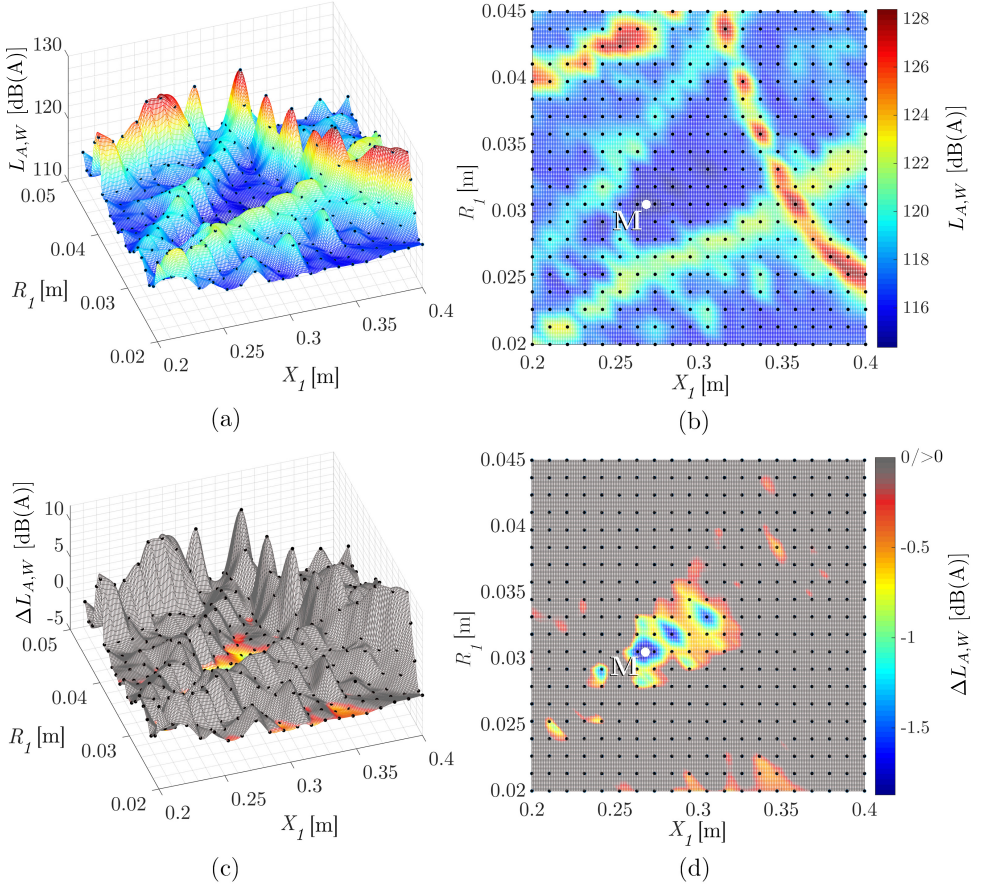


Figure 4.12: Response surfaces in the straight web wheel case for the geometric parameter pair of R_1 and X_1 using $Obj_{L_{A,W}}$. (a) and (b) represent $L_{A,W}$ absolute values in an isometric a two-dimensional view, respectively; (c) and (d) represent $L_{A,W}$ reduction with respect the unperforated base wheel ($L_{A,W} = 116.4$ dB(A)) in an isometric a two-dimensional view, respectively. In all cases the rest of the design parameters are kept fixed at $n_{layer} = 1$ and $N_1 = 6$.

problems like that treated in the present Thesis, especially when as many design as 10 design variables are considered [223].

In Fig. 4.14 the same representations are made but for the curved web geometry. It should be noted that, although the $n_{layer} = 1$ and $N_1 = 6$ case is not the BFS subspace for the curved web wheel, it is presented here as a comparative study with the straight web counterpart since the computational

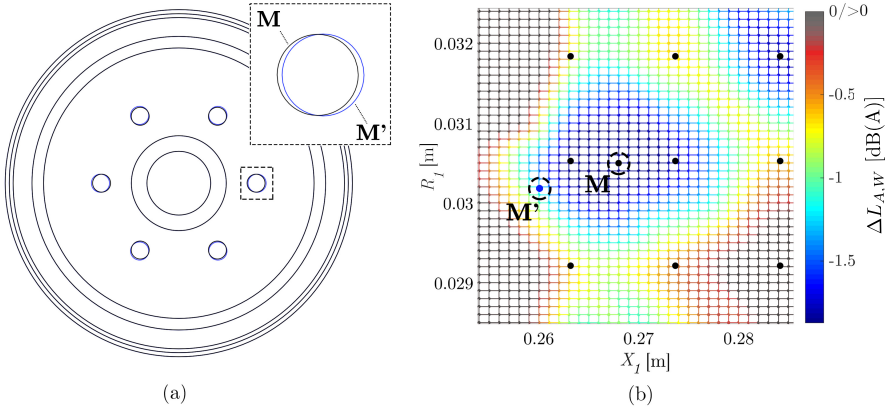


Figure 4.13: Comparison between the overall BFS (M') and the RS minima (M) for the straight web case. (a) Representation of each resulting perforation scheme. (b) Detailed view from Fig. 4.12 (d) where BFS and RS minima are marked.

cost of performing an RS study with two perforation layers is computationally infeasible with the resources available.

Thus, in Fig. 4.14, a complex topology is displayed again with multiple local maxima and minima. This time, the minimum point, at $X_1 = 0.342$ and $R_1 = 0.0312$, results in $\Delta L_{A,W} \simeq -3.7$ dB(A) with respect the curved web unperforated wheel. Generally, the RS reflects a greater effect of perforations than in the straight web approach, with some exceptions as the range between $X_1 = 0.23 - 0.27$ m. This is in accordance with that observed in the GA optimization, reassuring the idea than using perforation schemes as a methodology for rolling noise reduction is more effective in the case of curved web wheels. In addition, the SWL is less sensitive with respect to small geometric variations in this scenario, which could result in greater robustness to manufacturing tolerances.

4.3.4 Accuracy assessment of the acoustic model

The acoustic model used through the perforation scheme optimizations, as explained in Section 2.6, considers the sound radiation efficiency σ equal to unity for all wheel candidates. These approximation is made due to absence of analytical or computational efficient models for their calculation in the particular case of a railway wheel with perforations, and that considering an objective function based on solving the coupled Fluid-Structure Interaction (FSI) prob-

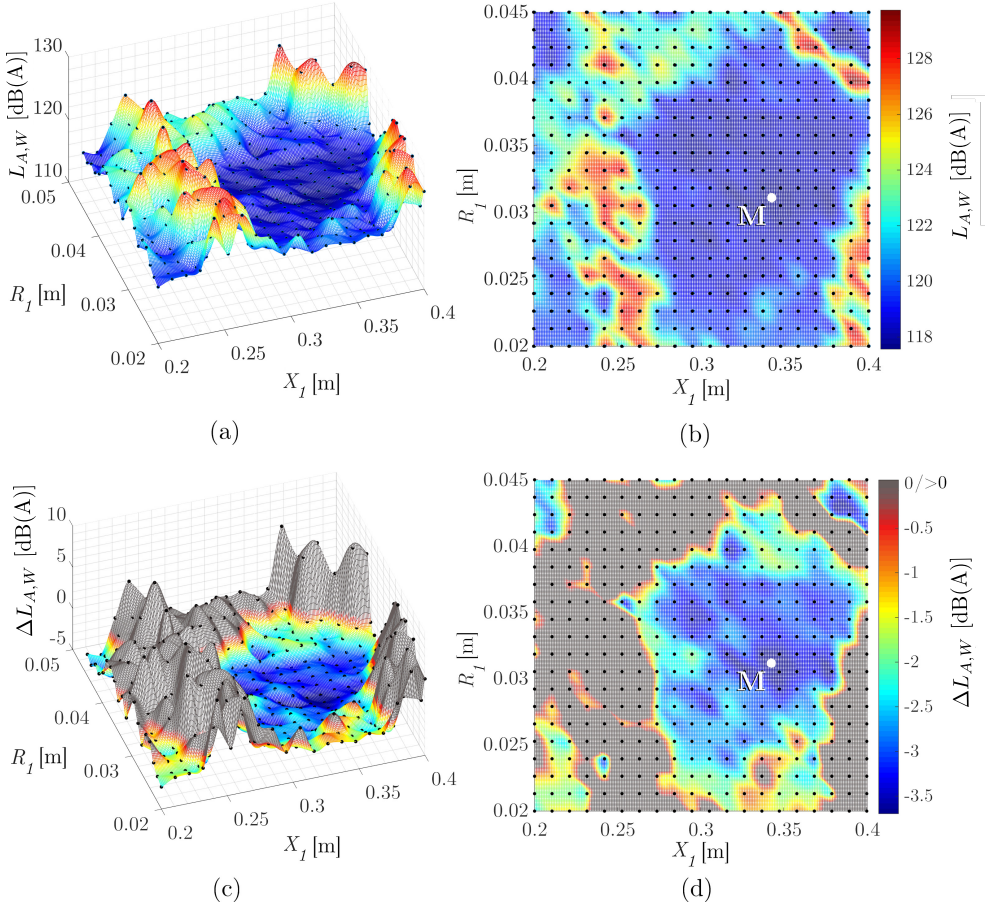


Figure 4.14: Response surfaces in the curved web wheel case for the geometric parameter pair of R_1 and X_1 using $Obj_{L_{A,W}}$. (a) and (b) represent $L_{A,W}$ absolute values in an isometric a two-dimensional view, respectively; (c) and (d) represent $L_{A,W}$ reduction with respect the unperforated base wheel ($L_{A,W} = 121.3$ dB(A)) in an isometric a two-dimensional view, respectively. In all cases the rest of the design parameters are kept fixed at $n_{layer} = 1$ and $N_1 = 6$.

lem for every design candidate is computationally unfeasible with the available resources. However, the $\sigma = 1$ approximation is considered to be a sensible one, as evidence exist that this holds true in the range above ~ 1500 Hz for either perforated plates [173] as unperforated wheels [4, 59]. Hence, it is expected that main differences when using an FSI approach would lie below a critical frequency lower than the point from which the wheel becomes the main com-

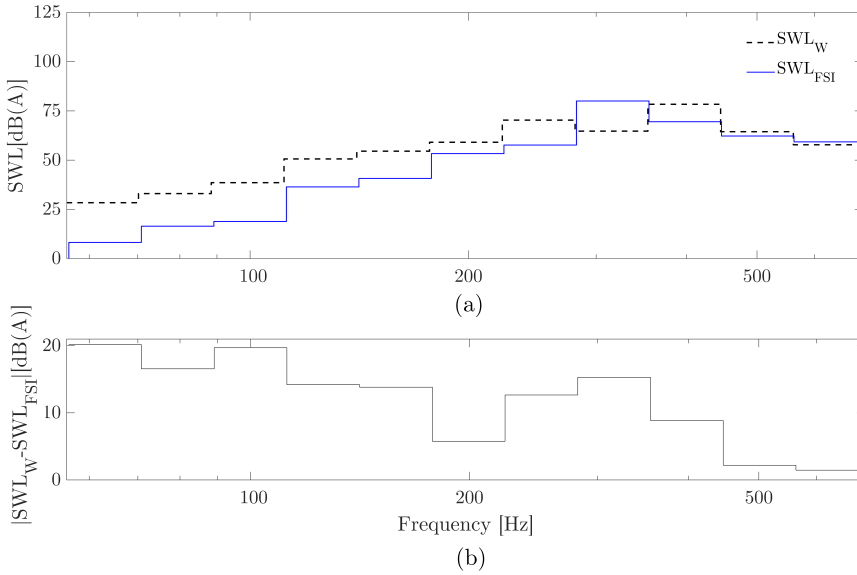


Figure 4.15: (a) SWL of the straight web BFS for the simplified methodology used through the optimization (SWL_W) and the FSI analysis (SWL_{FSI}). (b) Difference between SWL_W and SWL_{FSI} .

ponent of the rolling noise acoustic radiation (~ 2000 Hz [36]). Even though, in order to have a better understanding of the effects of such approximation in the perforated scheme optimization, the FSI problem is solved by means of an FE commercial software for the straight web BFS candidate obtained.

The vibrating velocity field in the wheel surface is derived from wheel modal properties by considering the same boundary and dynamic conditions than that used in the optimization procedure. For the acoustic problem, a spherical air enclosure is meshed around the candidate geometry and a radiation boundary condition is imposed in the outer surface of the enclosure. Due to license limitation in the available number of nodes for the acoustic mesh, the frequency range of study of the FSI is limited to 700 Hz with the enclosure mesh used. Although limited, this range is thought to be sufficient for a preliminary study of the relevant approach differences between the $\sigma = 1$ simplified approach and the FSI interaction problem here presented.

In Fig. 4.15, SWL curves for both the FSI calculations and the Section 2.6.1.2 simplified model are shown for the straight web wheel BFS. As expected, the highest discrepancies are appreciated at low frequencies, with the differences

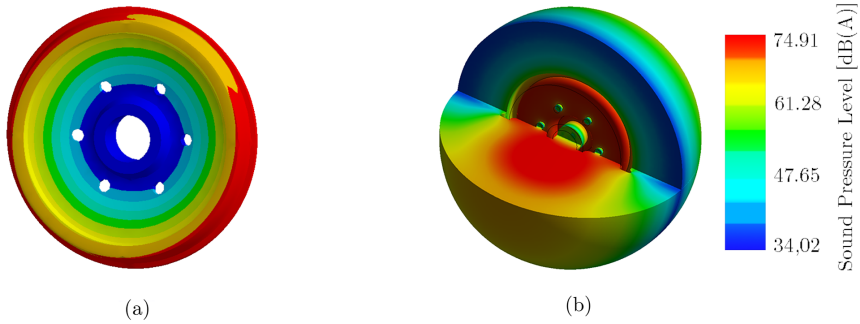


Figure 4.16: SPL_A distribution at 283 Hz and associated modeshape for the straight web wheel BFS: (a) representation of axial modeshape (0,0); (b) SPL_A distribution in the air enclosure.

shrinking with the increment of frequency up to the 28th one-third octave bands (the band that covers $f = 562 - 708$ Hz), where both curves overlap. This is better seen in Fig. 4.15(b), where the difference between SWL curves is represented explicitly. Hence, it is suggested that the critical frequency for this particular wheel model and conditions lies around 600 - 700 Hz. Such behaviour is compatible with that exposed in the literature for perforations in rectangular plates [173] and reinforces the idea the simplified model used through the optimization acting as a lower bound in the SWL reduction on railway wheel candidates.

As an example, an axial modeshape present at 283 Hz along with the corresponding A-weighted SPL (SPL_A) field is presented in Fig. 4.16. It is interesting to observe the drop in the SPL_A in the air enclosed by the perforations when compared with regions surrounding the wheel web surface. More precisely, this phenomenon is suggested as the mechanism behind the enhanced noise reduction effects of introducing perforations obtained with the FSI analysis. In any case, such phenomenon would be expected to be complementary to the modeshape shifting mechanism studied in previous sections.

Finally, it should be noted that approximately 16 h of computational time was required for solving the FSI problem presented using a PC with an Intel i7-8700K CPU at 3.70 GHz and 64 GB of RAM. Therefore, introducing this methodology in a GA optimization algorithm would imply an FSI analysis for each proposed viable design candidate, what is not computationally feasible with the available resources.

4.4 Cross-sectional wheel shape optimization

In this section, the results of the cross-sectional wheel shape optimization performed with the aim of reducing rolling noise through obtaining that geometry that minimizes acoustic radiation is presented. First, the optimized designs obtained with $L_{A,W}$ -min and NF-max methodologies, defined in Section 3.7, are explained for two different set of the geometric parameters shown in Fig. 3.12: one keeping the radius constant and another treating it as an additional design variable. Afterwards, the response surfaces obtained are displayed and their outcomes discussed in order to better understand the influence of the geometry in the objective functions. Lastly, the relation between the wheel natural frequencies and radiated noise is further analysed.

Regarding SWL computations, the configuration considered correspond to that used in the theoretical model validation in Section 4.2: an UIC54 rail with concrete bibloc sleeper separated 0.6 m, roughness defined by the standard DIN-prEN 13979-1 [200], train speed of $V = 80$ km/h and a contact filter applied to the roughness which takes into account the force attenuation due to the contact patch size [4] (Section 2.5.3 for further details). In relation to the wheel modal analysis, a rigid constraint is applied at the nodes on the inner surface of the wheel hub, thus providing better accuracy for those modeshapes with high contribution on rolling noise generation [4]. The number of wheel modeshapes considered is $N_m = 48$ and the maximum element size for the FE mesh is $h = 0.007$ m. Moreover, the reference wheel used as a guideline to compare the changes in wheel designs during the optimization processes is based on a simplified monobloc wheel with typical dimensions. The frequency range used in dynamic calculations varies from 50 to 5000 Hz with a resolution of 1 Hz, and SWL curves are represented until the last full one-third octave band (36th band).

4.4.1 Optimization with fixed radius

Among the different geometric parameters of the wheel, previously detailed in Fig. 3.12, the one corresponding to the radius should be treated carefully as it is not usually a completely free parameter. Due to constrains in the design process of the railway wheel, radius value x_1 is often linked with the other several geometric criterion that defines a complete railway wheel geometry and, therefore, it can not be freely modified independently of the other geometric parameters defining the wheel. For this reason, in the set of optimization runs presented below, the parameter x_1 corresponding to the radius has been kept

Table 4.8: Parameters of the reference wheel.

Geometric parameters	Sound power radiation values		
x_1	0.4500 m	Wheel $L_{A,W}$	101.29 dB(A)
x_2	0.0427 m	Rail $L_{A,R}$	98.65 dB(A)
x_3	0.0681	Sleeper $L_{A,Sl}$	93.92 dB(A)
x_4	0.0300 m	Superstructure $L_{A,Ss}$	93.24 dB(A)
Mass	285.92 kg	Total $L_{A,T}$	104.16 dB(A)
$\Delta A_m/\Delta \sigma_c$	1.03		

constant with the value corresponding to the radius of the reference wheel of $x_1 = 0.45$ m.

First, the properties of the reference wheel used are shown in Table 4.8. Then, the outcomes of BFSs obtained for the $L_{A,W}$ -min and NF-max methodologies are presented in Table 4.9. Together, in order to study possible transferences of radiated noise from the wheel to the other components of the system, Table 4.10 offers the SWL of each subcomponent derived using TWINS for each BFS in conjunction with the acoustic radiation of all components together. As with the wheel, SWL is summed in energy and expressed again in dB(A), the notation used being as follows: $L_{A,R}$ for the L_A corresponding to the rail, $L_{A,sl}$ for the one calculated for the sleeper, $L_{A,Ss}$ for the superstructure and $L_{A,T}$ for the total SWL radiated by all components together.

In all cases, there is a clear reduction in the final $L_{A,W}$ with respect to the reference wheel, with a prominent decreasing of $\Delta L_{A,W} = -3.94$ dB(A) for the $L_{A,W}$ -min methodology. Instead, the NF-max methodology presents a more modest reduction of $\Delta L_{A,W} = -1.11$ dB(A). This smaller effectiveness in diminishing the radiated $L_{A,W}$ should not distract from the fact that NF-max also presents some advantages over its alternative methodology. In return, the computational effort of the GA to perform an optimization with the NF-max approach is considerably lower, since the number of generations n_{gen} needed to achieve convergence, if compared to $L_{A,W}$ -min, is reduced by $\Delta n_{gen} = -24$,

Table 4.9: BFS values for the optimization considering a fixed wheel radius. x_1 , x_2 and x_4 are expressed in m. The mass of the wheel is expressed in kg. All L_A values are expressed in dB(A).

Methodology	x_1	x_2	x_3	x_4	$L_{A,W}$	$\Delta L_{A,W}$	Mass	$\Delta A_m/\Delta \sigma_c$
$L_{A,W}$-min	0.45	0.0484	0.10	-0.0128	97.35	-3.94	292.68	1.48
NF-max	0.45	0.0484	0.10	-0.0270	100.18	-1.11	292.66	1.74
Ref.	0.45	0.0427	0.07	0.0300	101.29	-	285.92	1.03

Table 4.10: L_A values of the rest of components of the system and total SWL radiated, calculated with each BFS for the optimization considering a fixed wheel radius. All L_A values are expressed in dB(A).

Methodology	$L_{A,R}$	$L_{A,Sl}$	$L_{A,Ss}$	$L_{A,T}$	$\Delta L_{A,T}$
$L_{A,W}$-min	97.59	94.33	94.82	102.28	-1.87
NF-max	98.01	94.35	96.47	103.73	-0.43
Ref.	98.65	93.92	93.24	104.16	-

thus evidencing that the computational effort by the GA to perform an optimization with this approach is considerably lower. Therefore, although the $L_{A,W}$ reduction achieved is smaller, its higher computational efficiency could represent an advantage in some situations as, for example, fast conceptual design or when there is limited amount of computational power available. Additionally, in both cases, the mean of the natural frequencies $\hat{\omega}_m$ is raised and natural frequencies are moderately shifted towards a higher frequency region, with almost identical variations of $\Delta\hat{\omega}_m \approx 238.30$ Hz for the $L_{A,W}$ -min and NF-max methodologies. This increase in the natural frequency of each mode-shape is represented in Fig. 4.17, where it is clear that the $\hat{\omega}_m$ shift, although present in both methodologies, is gentle. As seen later when compared with the optimization with all the geometric parameters, for a fixed radius and due to the great influence of x_1 over natural frequencies, the modal shifting is hindered.

Another factor that should be taken care of is the mass of the resulting wheels. When changing the geometry with respect of the reference wheel, it is possible to end with wheel design that, although less noise radiating, weight too much for a mechanical or cost effective design point of view. In the optimizations treated in the present section, as the radius is fixed, the possibility of having such a heavy wheel design is little, but to check for the final designs mass changes is still recommended. Thus, mass increase in all BFS, of about $\Delta m \approx 7$ kg, is negligible compared to the full weight of sprung masses (bogie frame and car body), representing around 2.4 % of the wheel mass. In addition, the safety factor obtained confirms the structural integrity of the solutions according to actual standards.

Concerning a possible transfer of radiated noise from the wheel to other components of the system, the SWL of each subcomponent has been derived using TWINS for each BFS wheel, as presented in Table 4.10. Hence, meanwhile the sleeper and superstructure components present consistently higher values, with a $\Delta L_{A,Sl} \approx 0.5$ dB(A) in both methodologies for the sleeper and a maximum

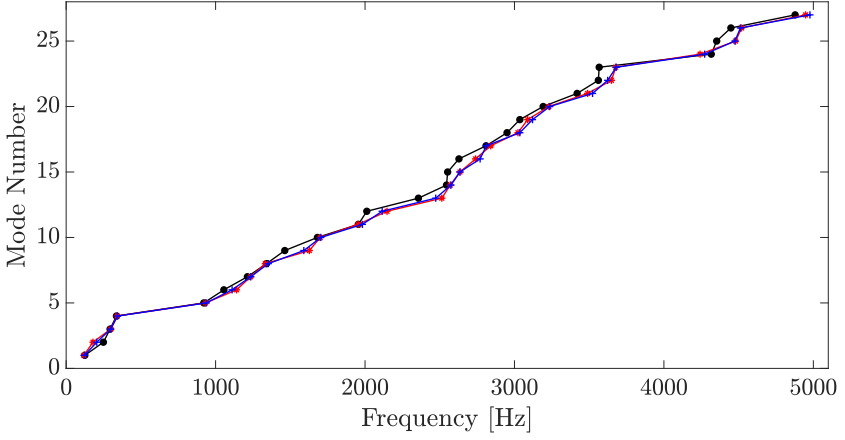


Figure 4.17: Comparison of natural frequencies distributions in the different wheel designs: continuous line for the fixed radius case ($-* -$ $L_{A,W}$ -min methodology, $-+ -$ NF-max methodology); $- \bullet -$ Reference wheel.

variation for the superstructure of $\Delta L_{A,Ss} = 3.23$ dB(A), the rail presents moderately lower SWL values with respect the ones of the reference wheel, with $\Delta L_{A,R}$ values of -1.06 and -0.64 dB(A) for the $L_{A,W}$ -min and NF-max methods, respectively. It is important to note that, despite the increases in some components like the superstructure are not negligible, the values of $L_{A,T}$ corresponding to the total SWL radiated by all the components together has also decreased for each optimal design, with $\Delta L_{A,T}$ values of -1.87 and -0.43 dB(A) for the $L_{A,W}$ -min and NF-max methods, respectively. Consequently, it is possible to state that the optimization has accomplished its aim even when considering the coupled system model in the optimization procedure.

As for the geometric parameters defining the resulting wheel designs, Table 4.9 shows that there are common patterns for the geometrical parameters in both methodologies which are consistent with literature [4, 182, 250]. When analysing the geometric changes that lead to less noise radiating solutions, it is observed how the factors determining fillet radius x_2 and web thickness x_3 are maximized in all designs. Moreover, for the web offset x_4 , the BFS presents values corresponding to straighter wheels, especially in the $L_{A,W}$ -min method. In order to better understand these geometric changes and have a more clear comparison with the reference wheel geometry, in Fig. 4.18 the cross-sections of each BFS in front of the reference wheel one are represented. It is important to point that x_2 and x_3 values are in the solution space boundary, which could

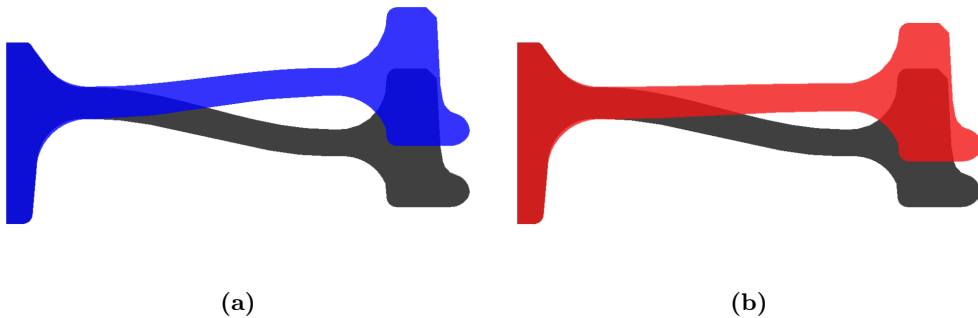


Figure 4.18: Cross-sections of the BFS of each methodology for the fixed radius case compared with the cross-section of the reference wheel (in black). (a) NF-max methodology and (b) $L_{A,W}$ -min methodology.

indicate a global optimum outside the solution space. Nevertheless, as the boundaries are strongly fixed by the wheel design and manufacturing process, it is not possible to broaden them and the search of a minimum beyond these limits is out of the scope of the present Thesis.

With the intention of studying changes in the acoustic radiation with greater detail, the SWL curves of each design together with the one corresponding to the reference wheel are shown in Fig. 4.19. Therefore, it is possible to appreciate how the biggest share of SWL reduction is focused on the mid and higher frequency regions, with the greatest improvements with respect the reference wheel above the 28th band (562 - 708 Hz). Particularly remarkable are bands as the 30th (891-1120 Hz) or 32nd (1410-1780 Hz), where reductions of up to 12 dB(A) with respect the reference wheel are obtained. On contrast, an increase on the SWL can be detected in the region from 75 to 600 Hz for all methodologies but nevertheless this range has a low energy contribution. As expected, the $L_{A,W}$ -min methodology improves the results with respect the NF-max methodology in almost all one-third octave bands considered.

Even though the description of the geometric changes obtained through the candidates during the optimization procedure is interesting, it is not a complete explanation of the causes in $L_{A,W}$ reduction if, at the same time, the underlying physical mechanisms for the changes in SWL among wheel candidates are not identified. Hence, in order to understand the causes for local SWL variations in shape optimized wheel designs, their receptances and the resulting contact forces are studied, since the main mechanism that causes the

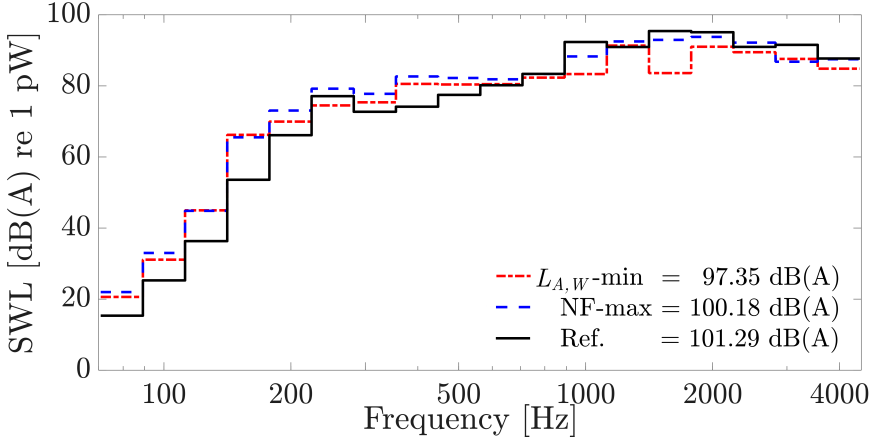


Figure 4.19: SWL of BFS wheels for an optimization considering the fixed wheel radius and the reference wheel (— $L_{A,W}$ -min, - - NF-max, — Ref. wheel).

wheel noise variation is the relocation of modeshapes in different one-third bands or frequencies where the excitation received is lower. Representative examples of such phenomenon are shown in Fig. 4.20, by means of comparing the contact force $|\mathbf{F}_c|$ and contact point receptance of the wheel \mathbf{H}_w for the axial direction $H_{w,yy}$ of the reference wheel and the BFS of the $L_{A,W}$ -min method in the fixed radius case. As it can be observed, Fig. 4.20 (left) reflects how the axial mode (1,0), present in the band B for the reference wheel, shifts towards band A in the optimized wheel, and since no other modeshapes are present in both the reference and optimized cases, the SWL increase in this band is justified. In band C, the SWL increase in the optimized wheel is explained by the displacement of the axial (0,2) modeshape to a point with higher excitation content. Another example can be found in Fig. 4.20 (right), where axial modes (2,1) in band D and (3,1) in band E shift after optimization to points in the frequency domain with less excitation inside their original one-third octave bands. Again, since there are no additional modeshape influences in those respective bands and for the receptance considered, the SWL of the BFS design lowers in relation to the reference wheel levels in both D and E one-third octave bands. Such shift influence is especially significant for the $\Delta L_{A,W}$ difference, as the axial modeshapes (2,1) and (3,1) are the most radiating modeshapes of the reference wheel, contributing from $\sim 55\%$ of the emitted energy to just $\sim 4\%$ in the BFS design. In addition, the effects described previously are also combined with the straightening of the web produced by the web offset x_4 variation, decreasing the coupling between axial and radial displacements.

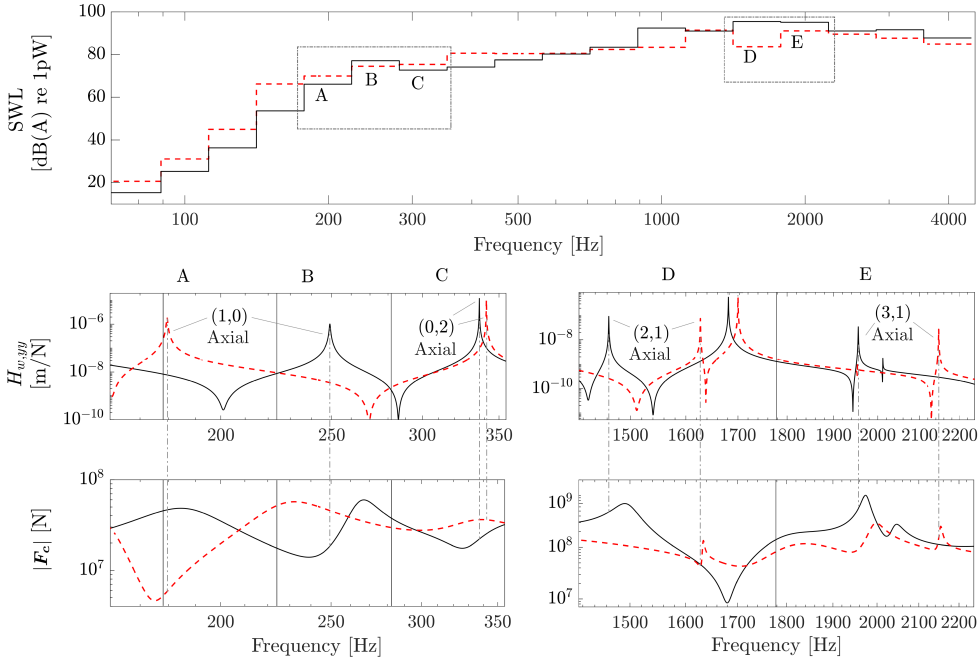


Figure 4.20: Receptance $H_{w,yy}$ and contact force $|\mathbf{F}_c|$ comparison between the BFS with $L_{A,W}$ -min method (---) for the fixed radius case and the reference wheel (—) for different frequency ranges. Black continuous vertical lines mark the limits of one-third octave bands and grey discontinuous vertical ones relates the amplitudes of $H_{w,yy}$ peaks and $|\mathbf{F}_c|$ for its corresponding frequency. Top: SWL curves with studied bands highlighted; left: bands 23 - 25 (178 - 355 Hz, named A, B and C); right: bands 32 - 33 (1410 - 2240 Hz, named D and E).

Thus, if the more relevant modes of the reference wheel (from an acoustic point of view) are observed, some degree of coupling effect can be found in all of them, unlike what happens in the $L_{A,W}$ -min BFS where the most influential modeset is entirely composed by uncoupled radial modes. In any case, it is important to note that, in order to carry out a quantitative study about the influence of the modeshape shifting mechanism over the SWL, it would be necessary to analyse more wheel receptances at different locations.

Table 4.11: Values of BFS when all $x_1 - x_4$ parameters are used in the optimization. x_1 , x_2 and x_4 are expressed in m. The mass of the wheel is expressed in kg. All L_A values are expressed in dB(A).

Methodology	x_1	x_2	x_3	x_4	$L_{A,W}$	$\Delta L_{A,W}$	Mass	$\Delta A_m / \Delta \sigma_c$
$L_{A,W}$-min	0.4222	0.0483	0.0999	-0.0102	96.33	-4.96	266.74	1.51
NF-max	0.4000	0.0484	0.1000	-0.0167	99.26	-2.03	247.04	1.84
Ref.	0.4500	0.0427	0.0681	0.0300	101.29	-	285.92	1.03

4.4.2 Optimization with all the geometric parameters

Even though that, as explained in section 4.4.1, the radius x_1 is a parameter that can not be usually freely changed due to design issues, the study the behaviour of the wheel radiated noise with the variation of this parameter could be useful. Thus, such study could be interesting at an industrial level under certain circumstances and provide valuable information about its influence in the wheel acoustic problem. Therefore, for the sake of completeness, in this section the results discussed correspond to optimization procedures where all the geometrical parameters described in Section 3.5.2 are treated as design variables.

In the same manner than in section 4.4.1, the parameters corresponding to BFSs obtained for the $L_{A,W}$ -min and NF-max methodologies are presented in Table 4.11, along with the different L_A corresponding to each subcomponent of the system together with the total radiated noise by all the components in Table 4.12.

As expected, $L_{A,W}$ reductions for both methodologies are greater than those described in section 4.4.1 with fixed wheel radius, with reductions of up to $\Delta L_{A,W} = -4.96$ dB(A) in the case of the $L_{A,W}$ -min optimization and $\Delta L_{A,W} = -2.03$ dB(A) in the NF-max approach. As x_1 is now allowed to change, the decrease in the amount of radiating surface on the wheel is a factor to take into account. This way, it is observed that, within these decrements, just ~ 0.8

Table 4.12: L_A values of the rest of components of the system and total SWL radiated, calculated with each BFS when all $x_1 - x_4$ parameters are used in the optimization. All L_A values are expressed in dB(A).

Methodology	$L_{A,R}$	$L_{A,SI}$	$L_{A,Ss}$	$L_{A,T}$	$\Delta L_{A,T}$
L_A-min	97.73	94.37	94.85	102.10	-2.05
NF-max	97.70	94.41	95.57	103.10	-1.05
Ref.	98.65	93.92	93.24	104.16	-

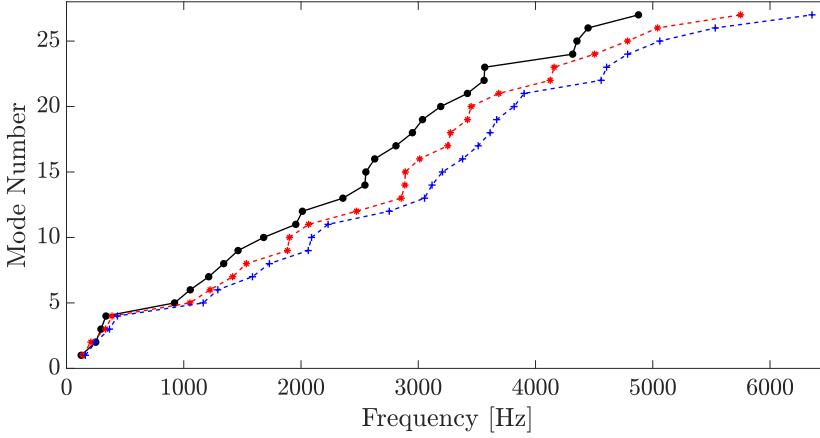


Figure 4.21: Comparison of natural frequencies distributions in the different wheel designs: discontinuous line for the optimization with all parameters allowed to change (-*- $L_{A,W}$ -min methodology, -+-NF-max methodology); —●— Reference wheel.

dB(A) are directly attributable to the radiating area reduction, reassuring that the drop in $L_{A,W}$ has its origin in the modal differences and not just to purely geometric modifications such as area reduction. Again, the mean of the natural frequencies $\hat{\omega}_m$ moves into a higher frequency region and, as shown in Fig. 4.21, it is immediate to realize that, due to the release of the constraint x_1 , a greater shift of the natural frequencies is produced compared to that obtained in the outcomes of the optimization with fixed wheel radius. In this occasion, the resulting variations in the mean of natural frequencies $\Delta\hat{\omega}_m$ are not just greater, but also with significant differences between methodologies, with $\Delta\hat{\omega}_m = \sim 264.18$ Hz for $L_{A,W}$ -min and $\hat{\omega}_m = \sim 288.55$ Hz for the NF-max case. Additionally, both Δm and the structural safety coefficient ($\Delta A_m / \Delta \sigma_c$) improved, since the resulting mass is lower and the structural safety coefficient higher than the corresponding for the BFS with a fixed x_1 . More precisely, BFSs presented a variation in mass of $\Delta m = -19.18$ kg for the $L_{A,W}$ -min method and $\Delta m = -38.88$ kg for the NF-max one. Therefore, not only noise emission levels have improved but also the structural integrity. In regard to the radiation emitted by the other components of the system, in Table 4.12, a decrease for the rail is observed, with $\Delta L_{A,R} \simeq -0.95$ dB(A) in both methodologies, and a slight increase for sleeper and superstructure, with a $\Delta L_{A,Sl}$ of 0.45 and 0.49 dB(A) and a $\Delta L_{A,Ss}$ of 1.61 and 2.33 dB(A) for the $L_{A,W}$ -min and NF-max methods, respectively. It is seen that, in this occasion, the change in the acoustic radiation of the different subsystems remains similar to section

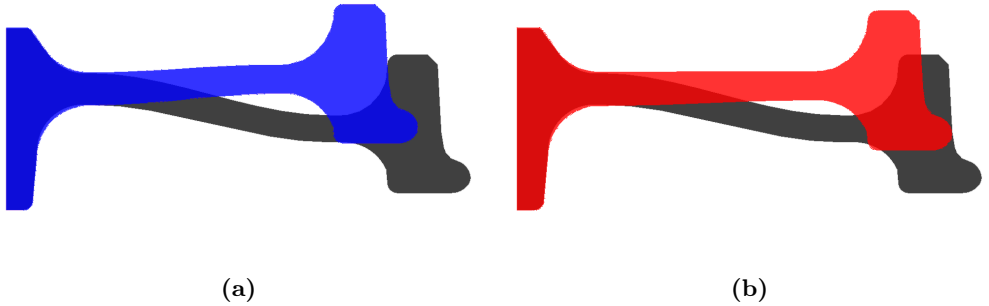


Figure 4.22: Cross-sections of the BFS of each methodology for an optimization considering all geometric parameters compared with the cross-section of the reference wheel (in black). (a) NF-max methodology and (b) $L_{A,W}$ -min methodology.

4.4.1, with the only exception of the superstructure, where the increases in L_{A,S_s} are smaller. In combination with a higher minimization of the wheel radiated noise it produces that, this time, the total radiation is further reduced than in the fixed radius case, with by $\Delta L_{A,T} = -2.05$ dB(A) for the $L_{A,W}$ -min methodology and a more modest reduction of $\Delta L_{A,T} = -1.05$ dB(A) for the NF-max one.

Concerning the geometric parameters, as represented in Table 4.11 and Fig. 4.22, the patterns observed in section 4.4.1 appear again: x_2 and x_3 are maximized and x_4 tends to describe a wheel with a straight web shape, with the particularity of x_1 playing a major role in both the $L_{A,W}$ and $\hat{\omega}_m$ values. As it was expected, in the NF-max process x_1 has converged to the minimum value possible. This is not the case for the $L_{A,W}$ -min approach, in which the final design presents a smaller radius than the reference wheel ($x_1 = 0.4222$ m) but has not converged to the defined lower design boundary. Such different behaviour can be attributed to the fact that NF-max approach, contrary to the $L_{A,W}$ -min case, does not solve the whole dynamic interaction. Observing the SWL representations described in Fig. 4.23, it is possible to appreciate how, in the same manner than in Fig. 4.19, most of the SWL reduction contribution of the BFSs is above the 600 Hz range, with lower noise increments at the low frequency region and more significant at higher frequencies, as compared to the fixed radius case. It should be noted that the results presented in this section should be treated with caution due to possible uncertainties caused by changes in the position of the calculation points $r_1 - r_6$, detailed in Fig. 2.20,

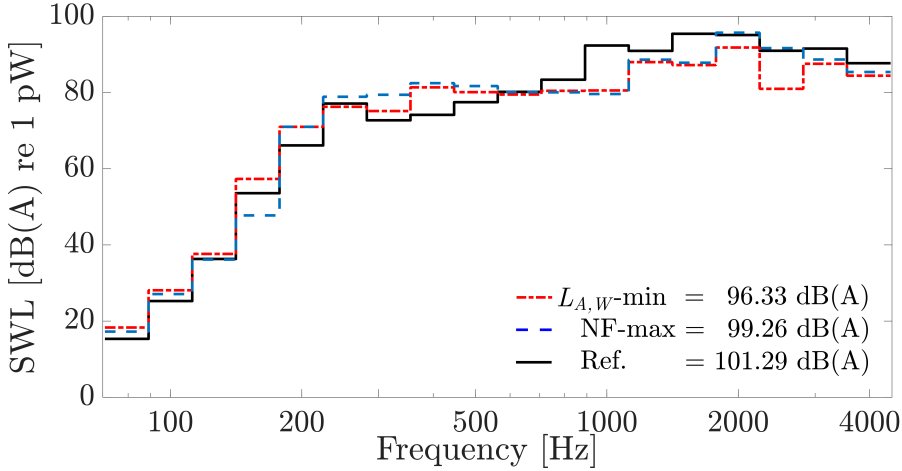


Figure 4.23: SWL of BFS wheels for an optimization considering all geometric parameters and the reference wheel (— $L_{A,W}$ -min, - - NF-max, — Ref. wheel).

which are chosen with the criterion of even distribution of surface area in the web.

4.4.3 Response Surfaces

Besides the optimization procedures, it is convenient to further study and analyse the objective functions behaviour and adequacy of the solutions found. For doing so, RSs are generated for each methodology and combination of geometric parameters possible, with special attention to those considered more relevant for the description of the problem. For the creation of RSs, each chosen combination of design variables conforming one of the BFS wheels is evaluated in 676 different points along the solution space, allocated in the form of a 26×26 evenly distributed sampling grid. With this analysis, it is intended to study the sensitivity of the SWL response with the design variables in the first place, and in the second, to evaluate the performance of the GA procedure and its suitability as a global optimization tool for the problem at hand, for both the $L_{A,W}$ -min and NF-max methodologies.

In Fig. 4.24, the RSs corresponding to NF-max methodology are presented. For every combination of geometric parameters, it is immediate to realize how, in the aforementioned approach the objective function presents approximately a planar behaviour and that, as expected, the maximization of natural frequencies is greater with the decrease of radius x_1 and broadening of the thickness

factor x_3 . Thus, by the slope that conforms the different Obj_{NF} levels, figures 4.24a, 4.24c and 4.24e make clear how, in this methodology, the radius x_1 and the web thickness factor x_3 are the predominant parameters in the objective function, together with the fillet radius x_2 . On the other hand, the web offset x_4 effect on Obj_{NF} is modest, as it can be appreciated on Fig. 4.24b, 4.24d and 4.24f. Consequently, in 4.24b and 4.24f the influence of x_4 is only visible by the slight curvature in the Obj_{NF} levels through the y axis while, in Fig. 4.24d, as the radius is predominant in the fixation of NF-max objective function, no effect produced by the web offset x_4 can be appreciated.

In all cases the minimum candidate in the RS fits the BFS for the respective methodology in the case of the GA optimization, and given the observed planar topology of RSs and the lack of local optima inside the design space analysed, it is clear that the NF-max methodology could be performed using local optimization algorithms, such a gradient-based algorithm. With this approach, the BFS will be probably obtained with a much lower number of objective function evaluations, which would emphasize the computational advantage of the NF-max technique.

Different outcomes are extracted from the RSs generated for the $L_{A,W}$ -min methodology, as it is seen in Fig. 4.25, where the RSs together with its contour level representations are observed. With the aim of reinforce that the BFSs obtained does not correspond to local minima, the minimum in each of the RSs made for $Obj_{L_{A,W}}$ has been compared with the results given by the optimization procedures. Therefore, Table 4.13 shows the minima obtained for all RSs made for the $L_{A,W}$ -min methodology. It is immediate to see that all minima are close to the BFS achieved through GA optimization and no RSs result in a lower $L_{A,W}$ than the lowest BFS one, reinforcing this way that, in the case of the $L_{A,W}$ -min problem, a global optimization technique such as GAs is the one most suited for accurately finding the best possible points in the solution domain.

The behaviour of $L_{A,W}$ with regard geometric parameters is presented in Fig. 4.25. Thus, Figs. 4.25a, 4.25c and 4.25e show how the offset variable x_4 is one of the most relevant parameters for defining a high quality solution subspace, corresponding to magnitudes related to straight web shapes. It is clear how in the x_4 value corresponding to a straight web a region of minima is conformed, whose final behaviour would be defined by its interaction with the corresponding x -axis parameter. In the case of Fig. 4.25a, when focusing in this region, the minimum point (marked with an M) is then given by the web thickness factor x_3 which has a visibly weaker relationship with the SWL level. The same applies for figs. 4.25c and 4.25e, with the radius x_1 and fillet radius x_2 ,

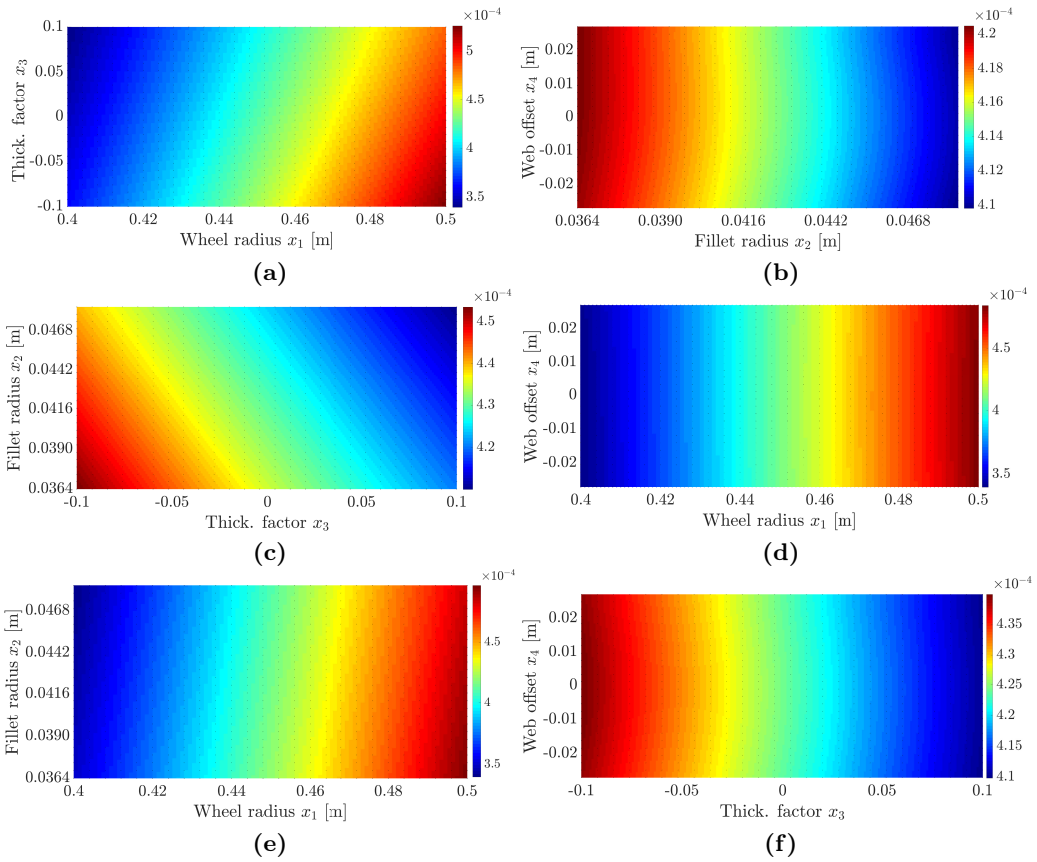


Figure 4.24: Response surfaces for different combinations of geometric parameters for $Obj_{NF} = \frac{1}{\bar{\omega}_m}$: (a) x_1 and x_3 ; (b) x_2 and x_4 ; (c) x_3 and x_2 ; (d) x_1 and x_4 ; (e) x_1 and x_2 ; (f) x_3 and x_4 .

respectively, playing the role that x_3 played in the previous case. A similar phenomenon can be described in the case of the radius x_1 and, more discretely, the web thickness factor x_3 and fillet radius x_2 , as reflected in Fig. 4.25b and 4.25d. Here, the minima region is dominated by the radius value $x_1 \simeq 0.42$ m, the best possible point (marked with an M) occurring at the intersection of this value with the highest allowed possible thickness (Fig. 4.25b) or fillet radius x_2 (Fig. 4.25d). In Fig. 4.25f, instead, the behaviour that the RS of a combination of the thickness factor x_3 and the fillet radius one x_2 shows relates to a planar tendency, evidencing the minor influence of this two geometric parameters in comparison with radius x_1 and web offset x_4 . Thus, the general

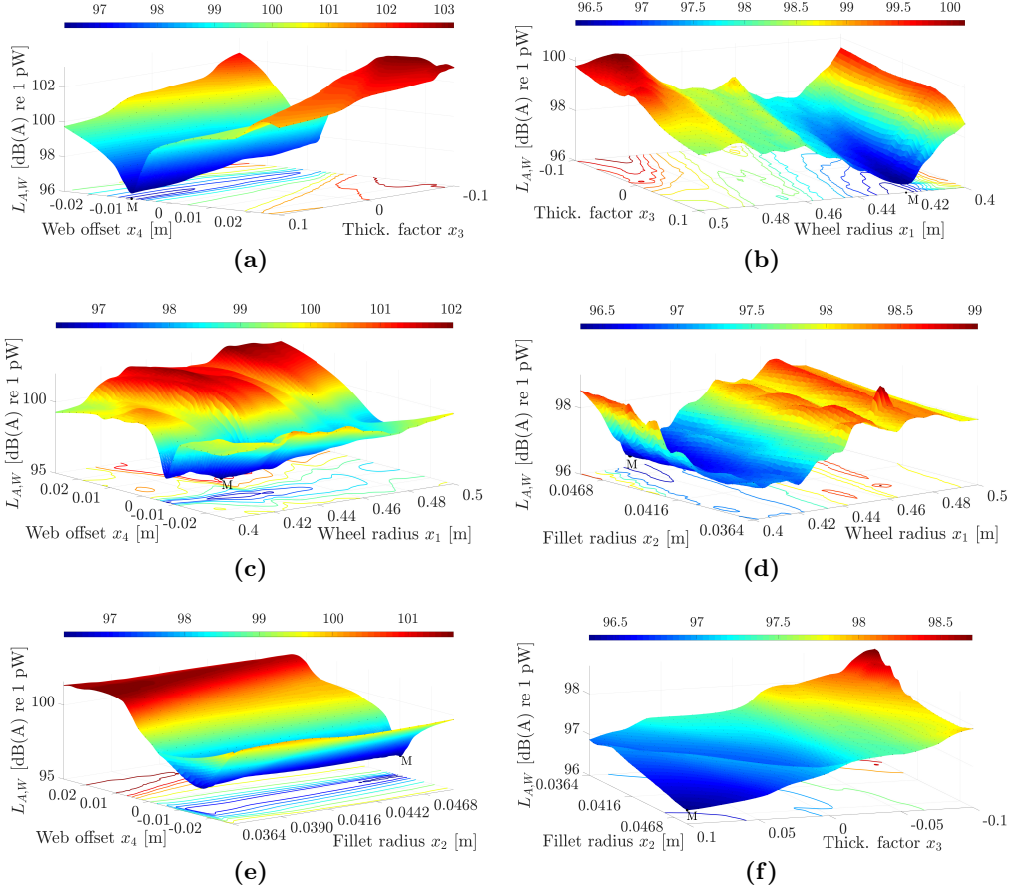


Figure 4.25: $Obj_{L_{A,W}}$ response surfaces for different combination of parameters. Fixed values correspond to those of the BFS as obtained with the $L_{A,W}$ -min methodology with no restrictions in the wheel radius x_1 : (a) x_3 and x_4 ; (b) x_1 and x_3 ; (c) x_1 and x_4 ; (d) x_1 and x_2 ; (e) x_2 and x_4 ; (f) x_3 and x_2 . Points M indicate the RS minima and are presented in Table 4.13.

design guidelines would be reducing wheel radius when possible, increasing thickness and fillet radius, together with a straightening of the web, which effectively decouples radial and axial modeshapes. The reduction of wheel radius, though, should be approached carefully, as the minimum radiating design does not always correspond with the minimum possible radius. Another important conclusion inferred from Fig. 4.25 is that relatively small changes in

Table 4.13: Geometric parameters together with its corresponding L_A value of each minimum in the RSs with the L_A -min objective function.

Geo. param.	x_1 [m]	x_2 [m]	x_3	x_4 [m]	L_A [dB(A)]
$\mathbf{x}_1, \mathbf{x}_3$	0.4240	0.0483	0.1000	-0.0102	96.36
$\mathbf{x}_1, \mathbf{x}_2$	0.4240	0.0484	0.0999	-0.0102	96.35
$\mathbf{x}_1, \mathbf{x}_4$	0.4200	0.0483	0.0999	-0.0097	96.39
$\mathbf{x}_2, \mathbf{x}_3$	0.4222	0.0479	0.1000	-0.0102	96.35
$\mathbf{x}_3, \mathbf{x}_4$	0.4222	0.0483	0.1000	-0.0097	96.39
$\mathbf{x}_2, \mathbf{x}_4$	0.4222	0.0484	0.0999	-0.0097	96.39

the web offset x_4 or the wheel radius x_1 can led to significant noise radiation variations. Such parameter sensitivity could have its importance from a production related perspective due to the variability inherent to manufacturing tolerances.

4.4.4 Studies on the correlation between natural frequencies and radiated noise

In order to further explore the relationship between Obj_{NF} and $Obj_{L_{A,W}}$, the objective function value $L_{A,W}$ for all candidates designs evaluated in the optimization runs is plotted against their natural frequencies mean in Fig. 4.26. In there, some correlations can be found locally, but not for the totality of sampled candidates. Some designs that reduce Obj_{NF} also increase their sound radiation and vice-versa, which is especially significant in the optimization with all design variables (black dots). In the region where x_1 is above the optimum value ($x_1 = 0.42$ m), the decreases of both objective functions value are coupled but, however, below this point the trend shift. Such behaviour is coherent with the minimum radiation level not occurring at the lower design bound for the wheel radius x_1 , as previously observed in the optimization results and shown in Figs. 4.24a and 4.25b in Section 4.4.3. A similar scheme occurs if the wheel radius variable is fixed (red dots). In such case, the candidates with maximum stiffness (minimum Obj_{NF}) present a wide range of emitted noise, several of them with high radiations levels $L_{A,W}$. That phenomenon is consistent with the existence of design variables with high influence on the acoustic behaviour but low in stiffness, as it could be the web offset x_4 , which has been shown in Section 4.4.3 to significantly affect $L_{A,W}$ levels (Fig. 4.25a) but presenting at the same time an almost negligible effect on the natural frequencies (Fig. 4.24b).

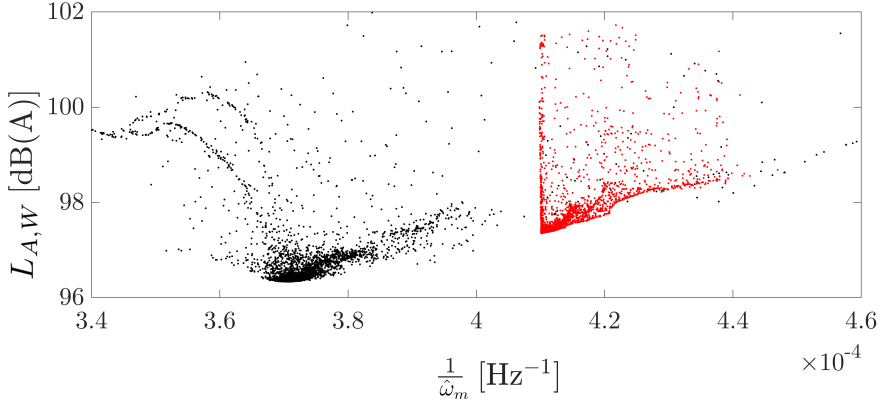


Figure 4.26: $Obj_{NF}(\frac{1}{\omega_m})$ and $Obj_{L_{A,W}}$ values for candidate evaluations corresponding to the optimization runs using the $L_{A,W}$ -min methodology. Black points are evaluations in a run with a design space consisting of all x_1 to x_4 variables. Red points are evaluations in a run considering a fixed wheel radius variable x_1 .

Hence, it can be stated that, although a certain correlation between both objective functions exists, this trend is not followed by some candidates with high rigidity but also greater noise generation (e.g. the BFS of the NF-max methodology in comparison to that of the $L_{A,W}$ -min one). Besides, it should be noted that if the noise rigidity relationship was totally monotonic, in the optimization with all geometric parameters presented in Section 4.4.2, the BFS for the $L_{A,W}$ -min approach would possibly present the lower bound for the wheel radius design variable x_1 (0.40 m) when considered for optimization, and not the value actually obtained ($x_1 = 0.42$ m).

4.5 Preliminary studies of the track shape influence on rolling noise

As mentioned several times along the present Thesis, track is a key component in the rolling noise. Along with the wheel, it is the component that accounts for the main share of the noise radiation [4, 34–38]. In addition, as shown in Section 4.4, reducing the sound emission of one source does not directly translate into a global SWL reduction. In the optimization procedure with all the geometric parameters, for example, the $L_{A,W}$ -min methodology BFS wheel achieves a variation in the total noise of $\Delta L_{A,T} = -2.05$ dB(A) even though that the improvement accomplished for the wheel is greater, with a

$\Delta L_{A,W} = 4.99$ dB(A). If attention is paid in the track components, it can be seen that even a slight increase in the sleeper of $\Delta L_{A,sl} = 0.45$ dB(A) is observed. Hence, it becomes necessary to study and analyse the track contribution if an integral minimization of the rolling noise is to be attained [4, 10].

In the present case, it is known that the track geometry and structural properties of its foundation have a significant influence on its dynamics and contribution to rolling noise [76, 155, 178]. In order to study these effects, SWL of two track cross-sectional shapes combined with different foundation characteristics are computed and compared. This way, a preliminary approach on how the track behaves respect to the variation of its geometry and foundation can be established, what serves as a survey on the feasibility of a search towards an optimal track geometry for minimizing rolling noise.

Thus, the rail cross-sectional shapes defined for the study are: the reference UIC54 shape used for the deformable track cross-section model in Section 4.2 and a modified geometry based on the UIC54 transition points defined in the standard UNE-EN 13674-1 [251]. Accordingly, in this second case the rail head width is lowered from 73 to 67 mm and the foot width is narrowed from 140 to 125 mm. Such variations can be better appreciated in Fig. 4.27, where the cross-sectional shapes of both designs are presented together. Although the cross-section area is reduced, it is expected to decrease the radiated SWL with these modifications as a consequence of diminishing the radiating area while maintaining the rail stiffness at similar levels.

In every case, a train speed of $V = 80$ km/h is considered during the computations and a contact filter is applied to the roughness in order to take into account the effects of the patch on the wheel/track excitation. For the wheel component, the BFS with the $L_{A,W}$ methodology of the optimization with all geometric parameters is selected, except for the reference case, in which the reference wheel is used.

Additionally, four different foundation are considered in combination with the modified geometry. In the first one, the reference values are kept unchanged, granting that the observed SWL variations can be attributed exclusively to the geometric differences of the rail profile. In the rest of foundations, ballast and rail pad properties are tuned: first, in the Foundation 1 the ballast stiffness and pad damping are increased while lowering the pad stiffness; then, in the Foundation 2, a new pad stiffness is assigned adapting the “optimal” stiffness defined for the pad in [155] to a train speed of $V = 80$ km/h; and for the Foundation 3, a high rail pad stiffness value is considered. Typical values of the foundations used are extracted from [37, 155] while, in the case of ballast

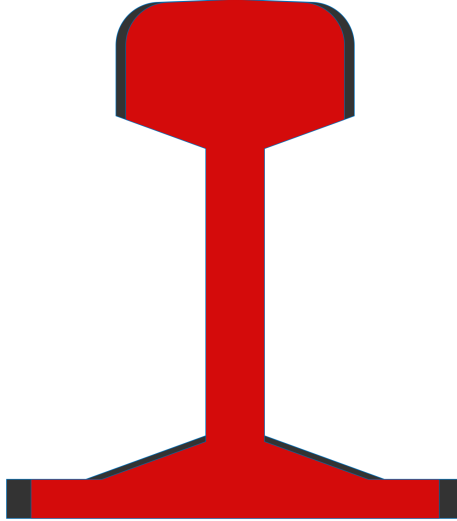


Figure 4.27: Cross-sections of the reference (in **black**) and modified shape (in **red**) tracks.

stiffness, it has been assured that the vertical/lateral relations remains equal to that of the reference foundation. For further detail, all parameters used for each foundation are specified in Table 4.14. Regarding the sleeper shape, the design used is the same as that used in the validation in Section 4.2 and it remains constant in all computations.

All obtained results are shown in Table 4.15 and represented in Figs. 4.28 and 4.29. As it can be seen in Table 4.15, reductions in $L_{A,T}$ are achieved in all cases when compared to the reference value, with a maximum of $\Delta L_{A,T} = -4.76$ dB(A) in the “Mod. Geo. + Found. 2” configuration (modified rail geometry and Foundation 2). In the case of sleeper $L_{A,Sl}$ and rail $L_{A,R}$, though, noise reductions are not always achieved. Therefore, increases of $\Delta L_{A,Sl} =$

Table 4.14: Parameters defined for each studied track foundation.

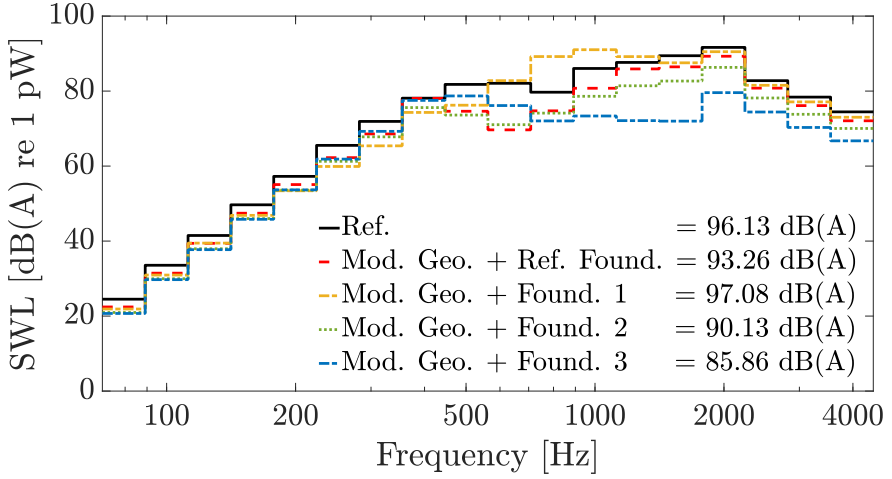
Foundation	Ref.		Found. 1		Found. 2		Found. 3	
	Lateral	Vertical	Lateral	Vertical	Lateral	Vertical	Lateral	Vertical
Pad stiffness k'_p [N/m ²]	$2.17 \cdot 10^9$	$1.67 \cdot 10^8$	$6.83 \cdot 10^8$	$5.27 \cdot 10^7$	$2.28 \cdot 10^9$	$1.75 \cdot 10^8$	$6.83 \cdot 10^9$	$5.27 \cdot 10^8$
Pad loss factor η_p	0.25	0.25	0.5	0.5	0.5	0.5	0.5	0.5
Ballast stiffness k'_b [N/m ²]	$1.17 \cdot 10^8$	$5.83 \cdot 10^7$	$1.67 \cdot 10^8$	$8.30 \cdot 10^7$	$1.67 \cdot 10^8$	$8.30 \cdot 10^7$	$1.67 \cdot 10^8$	$8.30 \cdot 10^7$
Ballast loss factor η_b	2	2	2	2	2	2	2	2

Table 4.15: L_A values for each component, total radiation of each component combined and their respective differences with the reference case for all studied track configurations. All values are expressed in dB(A).

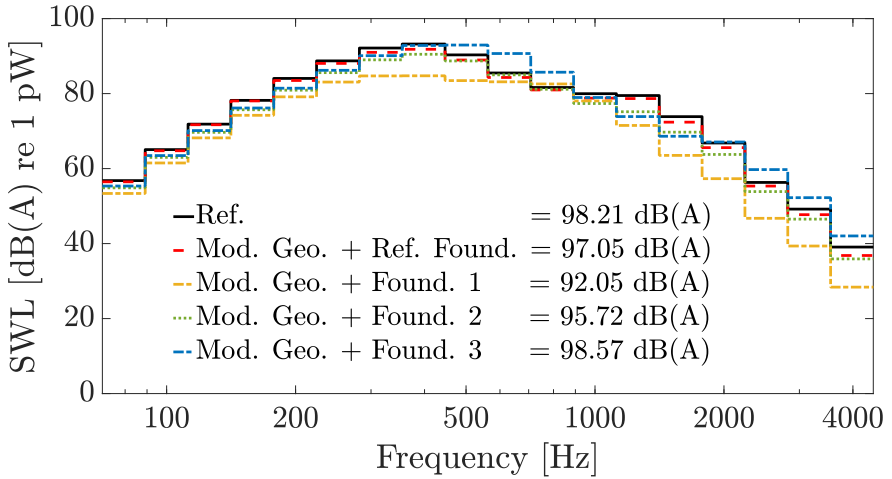
Case	$L_{A,R}$	$\Delta L_{A,R}$	$L_{A,SI}$	$\Delta L_{A,SI}$	$L_{A,W}$	$\Delta L_{A,W}$	$L_{A,T}$	$\Delta L_{A,T}$
Ref.	96.13	–	98.21	–	100.93	–	103.65	–
Mod. Geo. + Ref. Found.	93.26	-2.86	97.05	-1.15	94.79	-6.14	100.09	-3.56
Mod. Geo. + Found. 1	97.08	0.95	92.05	-6.16	95.87	-5.05	100.24	-3.41
Mod. Geo. + Found. 2	90.13	-6.00	95.72	-2.48	94.75	-6.18	98.89	-4.76
Mod. Geo. + Found. 3	85.86	-10.26	98.57	0.36	94.30	-6.63	100.11	-3.54

0.36 dB(A) and $\Delta L_{A,R} = 0.95$ dB(A) are observed when using Foundations 1 and 3, respectively. Such values are in agreement with what is found in literature [155, 179]. Consequently, when rail pad stiffness k'_p is lower than the reference as in the Foundation 1 case, rail SWL contribution raises while sleeper levels descend. However, when a remarkably stiff pad is considered as in Foundation 3, the huge gains in the rail leading to $\Delta L_{A,R} = -10.26$ dB(A) for this particular example are hindered by the surge in the sleeper influence. As seen in Fig. 4.28b, the noise contribution of sleeper in the low and medium frequency range increases with the stiffening of the rail pad and vice versa. Meanwhile, as show in Fig. 4.28a, rail behaves in an opposite manner in relation to the stiffening of the rail pad, since the rail is quieter when stiffer rail pads are considered (Foundation 3). Then, if attention is paid to the total radiation, considering the behaviour of the rail and the sleeper with respect to the stiffness of the rail pad, the minimum radiation level $L_{A,T}$ is expected in the surroundings of that in Foundation 2 (see Table 4.15 and Fig. 4.29). Such foundation uses an “optimal” rail pad stiffness k'_p defined in [155] and offers the greatest $L_{A,T}$ reduction of all the studied cases, since it reduces the radiation of the rail without increasing the sleeper too much. Regarding the variations attributed specifically to the modification of the rail cross-sectional shape, noise mitigation is still accomplished when the modified geometry is computed with the reference foundation. In such option, the rail and sleeper decrease with $\Delta L_{A,R} = -2.86$ dB(A) and $\Delta L_{A,SI} = -1.15$ dB(A), respectively, as it can be seen in Table 4.15 and Figure 4.28. When the total rolling noise SWL is considered, which also includes the $L_{A,W}$ -min BFS wheel design, a variation of $\Delta L_{A,T} = -3.56$ dB(A) is achieved (see Table 4.15 and Fig. 4.29).

It is also worth noting that no trade-off is appreciated between rail SWL reduction and a corresponding wheel noise radiation increase, as a result of the small influence that the track properties have on the wheel dynamics (increments of ± 1 dB(A)). So, due to the usage of a wheel optimized design in all the com-



(a)



(b)

Figure 4.28: SWL for all studied configurations and reference case: (a) rail and (b) sleeper (— Ref.; Mod. Geo.: - - Ref. Found., - - - Foundation 1, · · · Foundation 2 and - · - Foundation 3).

puted cases, the wheel noise is minimized, with a maximum variation in the “Mod. Geo. + Found. 3” configuration of $\Delta L_{A,W} = -6.63$ dB(A). The fact that the decrease observed in all cases is greater than that computed through the GA optimization in Section 4.4.2 is attributed to the lesser content of the

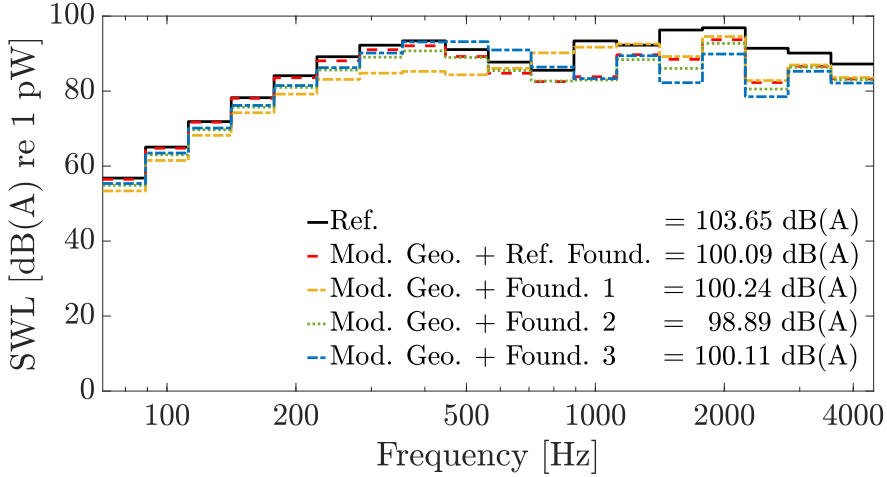


Figure 4.29: Total SWL of all components combined for all studied configurations and reference case (— Ref.; Mod. Geo.: - - Ref. Found., - · - Foundation 1, ···· Foundation 2 and - · · - Foundation 3).

interaction force generated when the deformable track cross-section model is adopted and, additionally, the lack of cross-coupling when the centre of the head of a symmetric rail is used as contact point, which is the case. Likewise, these same reasons explain the variation in the reference wheel radiation depending on the track model considered.

To conclude, it can be stated that both the foundation and track shape play a decisive role in rolling noise radiation. In the current preliminary study, when combined with an optimal wheel design, improvements in the total SWL of up to $\Delta L_{A,T} = -4.76$ dB(A) are achieved by tuning the track geometric and viscoelastic properties. Therefore, there is room for further research on rolling noise mitigation through the track shape modification and its introduction on a possible comprehensive optimisation that simultaneously considers all the components involved in rolling noise.

Conclusions and future work

5.1 Conclusions

The conclusions obtained in the present Thesis are presented in this section. The main objectives, consisting in the development of optimization procedures capable of attaining different geometric configurations of wheel which minimize their rolling noise radiation, have been achieved satisfactorily. In addition, some of the contributions made during the development of the Thesis and described in the previous chapters have been published in references [10, 11, 201, 238, 239, 247, 248, 250].

The following paragraphs provide detailed information about the main concluding remarks:

- It has been justified that rolling noise is a major contributor of the overall train noise and its most relevant sources are the wheel and the track. Additionally, it has been shown how the shape and structural characteristics of these components play a key role on the level and specificities of the sound radiated.
- Development and implementation of the different dynamic models involved in the rolling noise generation have been carried out successfully.

Wheel behaviour is characterized according to its modeshapes and the corresponding number of nodal diameters and circumferences, including both frequency and time domain approaches in the process. Regarding the track, two options are available: simpler and less computationally demanding Timoshenko beam, and a deformable cross-section model based on wave propagation theory, which is capable of providing better precision and taking into account geometric variations of the rail shape. Lastly, a full two-dimensional wheel/track interaction model has been implemented through a transfer function approach, including the effect of contact patch size on the roughness excitation with the use of a contact filter.

- Acoustic radiation has been characterized for both wheel and track, being able to compute their SWL on the basis of their dynamic behaviour. In the case of the wheel, that includes a two-dimensional model based on the velocity amplitude in the axial direction on six different positions over the cross-section combined with a semi-analytical formulation for the acoustic efficiencies; and a three-dimensional case capable of including non axisymmetric elements as the perforations, for which the acoustic efficiencies are not yet available and, consequently, a unitary value has to be used as an upper boundary. Regarding the track, an ESM has been incorporated allowing for a precise calculation of the radiation that includes the corresponding cross-section information for both the sleeper and the rail. A number of previously validated correction functions and wave propagation properties have been used for granting an accurate prediction of the whole track acoustic radiation from the two-dimensional cross-sectional information.
- A three-dimensional FEM approach has been developed for the creation of wheel models with several perforation schemes, allowing the consideration of a variable number of perforation layers (up to three) with different number of holes and size in each of them.
- A parametrization of the wheel cross-section has been defined according to those geometric features that have most influence on the radiated rolling noise: wheel radius, fillet radius, web thickness and web offset. Besides, the developed FEM makes use of the wheel axisymmetric properties in order to calculate the relevant set of modeshapes from the cross-section mesh information.
- A modal identification procedure has been designed in which modeshapes are classified according to their number of nodal diameters and circum-

ferences by using Fourier analysis on the corresponding modal amplitudes and inspecting their variation along the wheel surface.

- Two methodologies have been developed to improve wheel geometry through GA-based optimization, with the aim of tackling rolling noise: one focused on finding suitable perforation patterns and another that targets the search for an acoustically optimal geometric shape. In both approaches, quieter wheel designs are achieved. In all cases, structural requirements of the wheel are used as a “death penalty”, ensuring the resulting candidates to comply with the corresponding standard (UNE-EN 13979-1).
- Different strategies for rolling noise mitigation have been studied by using distinct objective functions, focused on either shifting modeshapes to a less excited frequency band or directly minimizing the radiated SWL through the whole frequency spectrum under analysis.
- All outcomes provided by the in-house code implementation have been validated with TWINS, the reference commercial program in the field, with a maximum discrepancy observed lower than 0.37 dB(A).
- Enhanced perforation schemes have been achieved with reductions of 2 and 4.8 dB(A) for straight and curved web wheel geometries, respectively. The greater mitigation in the curved case is attributed to a higher capacity for the natural frequencies of the modeshapes to be relocated and the relevance of the radial-axial coupling, both considered to have a more fundamental role in the noise reduction than the radiation surface decrease induced by the perforations. The considered assumptions are reinforced with an accuracy assessment of the acoustic model by means of a Fluid-Structure Interaction analysis, suggesting that improved results may be observed in the lower frequency region when such interaction is considered. Response surfaces show that arbitrary perforation schemes are prone to generate noisier wheel designs, emphasizing the need of optimization techniques for approaching the studied problem.
- Optimal wheel cross-section geometries have been accomplished, with improvements of up to 2 and 5 dB(A) in the computed radiated rolling noise for objective functions focused on the natural frequencies and on the direct minimization of SWL, respectively. Reductions are still attained when the whole system with all the components (wheel, rail, sleeper and superstructure) is considered. The evolution of the geometric parameters along the procedure has been established, with the final wheel designs presenting a higher thickness and fillet radius together with more straight

web shapes and, when allowed to change, smaller radii. Moreover, it has been shown that the differences in the noise calculated among wheel designs cannot be explained just with pure geometrical changes such as area reduction. Thus, the underlying physical mechanism for the changes in SWL among wheel candidates is identified and explained through the shift of modes along frequency spectrum and their relocation into frequencies with a lower amplitude content of the contact force.

- The natural frequency maximization methodology is suggested as a straightforward technique in cases where great precision is not required, obtaining optimized designs which are geometrically similar to those corresponding to a procedure requiring the SWL calculation, but in a computationally inexpensive manner. When studied, correlation between this approach and radiated noise is found in some cases, although that does not hold for the whole solution space.
- The methodology founded on direct minimization of the SWL is established as an effective approach appropriate for the reduction of rolling noise and the obtention of quieter wheel designs.
- A preliminary study on the influence of the track geometry on rolling noise has been performed by comparing two different track cross-sectional shapes, based on the UIC54 transition points defined in the corresponding standard (UNE-EN 13674-1), combined with four different foundations. It has been determined that the acoustic radiation of the rail decreases with the rail pad stiffness, while that of the sleeper increases, resulting in an improved stiffness that reduces the global noise. This configuration is the above-mentioned Foundation 2 which, when combined with wheel optimized designs, achieves reductions of up to 4.76 dB(A) in the total SWL. Improvements in the rail and sleeper acoustic radiation of 2.86 dB(A) and 1.15 dB(A), respectively, are accomplished when exclusively varying the track geometry.

5.2 Future work

The research exposed in the present Thesis attempts to minimize the rolling noise radiation through the modification of the railway component designs and the use of optimization techniques, accomplishing positive results in the process. To further develop the ideas expressed along the work and expand the scope of the investigation, some possible guidelines for future work are proposed in the following lines:

- Development and implementation of more detailed dynamic and sound power calculation methodologies, including Fluid-Structure Interaction analysis in the optimization algorithm.
- Study of the efficiency and feasibility of applying alternative evolutionary algorithms, checking if they could lead to faster convergence rates.
- Development of a wheel parametrization that includes more geometric variables, e.g. use of a different value for each fillet radius.
- Consideration of the inclusion of additional mitigation measures as damping layers or tuned absorbers in the optimization procedure.
- Parametrization of the track cross-section geometry and usage of the GA methodology for finding the shape that minimizes its emitted sound.
- Realization of a comprehensive optimization procedure which simultaneously considers wheel and track geometries to minimize the global rolling noise radiation. Hence, in such procedure, the final candidates obtained through the process would be achieved by minimizing global magnitudes, avoiding an eventual increase of sound emission in one of the components as a result of variations in the shape of another.
- Study of the possibility of using the optimization algorithm with alternative approaches focused on other relevant noise sources (e.g. squeal and aerodynamic noise). Development of ways to include additional railway components that play an important role in such noise (e.g. the superstructure for aerodynamic noise) into the algorithm.
- Manufacturing and test of the different designs, both perforated and modified wheel cross-sections, to experimentally measure the sound level mitigation and the resulting dynamic and structural properties.

Bibliography

- [1] P. de Vos, “Railway noise in Europe”, International Union of Railways, Tech. Rep., 2016.
- [2] U. Clausen, C. Doll, F. J. Franklin, G. V. Franklin, H. Heinrichmeyer, J. Kochsiek, W. Rothergatter, and N. Sieber, “Reducing railway noise pollution”, Policy Department Structural and Cohesion Policies, European Parliament, Tech. Rep., 2012.
- [3] World Health Organization European Centre for Environment and Health, “Burden of disease from environmental noise”, WHO, Tech. Rep., 2011.
- [4] D. J. Thompson, *Railway Noise and Vibration. Mechanisms, modelling and means of control*, 1st ed. Elsevier, 2010. DOI: 10.1016/B978-0-08-045147-3.X0023-0.
- [5] D. J. Thompson, “Wheel-rail noise generation, part I: Introduction and interaction model”, *Journal of Sound and Vibration*, vol. 161, no. 3, pp. 387–400, 1993. DOI: 10.1006/jsvi.1993.1082.
- [6] D. J. Thompson and P. E. Gautier, “Review of research into wheel/rail rolling noise reduction”, *Proceedings of the Institution of Mechanical Engineers, Part F: Journal of Rail and Rapid Transit*, vol. 220, no. 4, pp. 385–408, 2006. DOI: 10.1243/0954409JRRT79.

- [7] J. Oertli, “The STAIRRS project, work package 1: A cost-effectiveness analysis of railway noise reduction on a European scale”, *Journal of Sound and Vibration*, vol. 267, no. 3, pp. 431–437, 2003. DOI: 10.1016/S0022-460X(03)00705-3.
- [8] J. H. Holland, *Adaptation in Natural and Artificial Systems*, 1st ed. University of Michigan Press, 1975.
- [9] S. N. Sivanandam and S. N. Deepa, *Introduction to genetic algorithms*, 1st ed. Springer-Verlag Berlin Heidelberg, 2007, 1–442. DOI: 10.1007/978-3-540-73190-0.
- [10] X. Garcia-Andrés, J. Gutiérrez-Gil, J. Martínez-Casas, and F. D. Denia, “Wheel shape optimization approaches to reduce railway rolling noise”, *Structural and Multidisciplinary Optimization*, 2020. DOI: 10.1007/s00158-020-02700-6.
- [11] J. Gutiérrez-Gil, X. Garcia-Andrés, J. Martínez-Casas, E. Nadal, and F. D. Denia, “Optimized perforation schemes in railway wheels toward acoustic radiation mitigation”, *Journal of Vibration and Acoustics*, vol. 142, no. 4, 2020. DOI: 10.1115/1.4046681.
- [12] P. J. Remington, “Wheel/rail noise – Part IV: Rolling noise”, *Journal of Sound and Vibration*, vol. 46, no. 3, pp. 419–436, 1976. DOI: 10.1016/0022-460X(76)90864-6.
- [13] D. J. Thompson, “On the relationship between wheel and rail surface roughness and rolling noise”, *Journal of Sound and Vibration*, vol. 193, no. 1, pp. 149–160, 1996. DOI: 10.1006/jsvi.1996.0254.
- [14] M. H. A. Janssens, M. G. Dittrich, F. G. de Beer, and C. J. C. Jones, “Railway noise measurement method for pass-by noise, total effective roughness, transfer functions and track spatial decay”, *Journal of Sound and Vibration*, vol. 293, no. 3, pp. 1007–1028, 2006. DOI: 10.1016/j.jsv.2005.08.070.
- [15] Q. Li, D. J. Thompson, and M. G. R. Toward, “Estimation of track parameters and wheel-rail combined roughness from rail vibration”, *Proceedings of the Institution of Mechanical Engineers, Part F: Journal*

-
- of Rail and Rapid Transit*, vol. 232, no. 4, pp. 1149–1167, 2018. DOI: 10.1177/0954409717710126.
- [16] UNE, “Acoustics. Railway applications. Measurement of Noise Emmited by Railbound Vehicles. UNE-EN ISO 3095:2013”, Asociación Española de Normalización (UNE), Technical Standard, 2014.
- [17] O. Chiello, A. Le Bellec, M.-A. Pallas, P. Munoz, and V. Janillon, “Characterisation of wheel/rail roughness and track decay rates on a tram network”, 2019.
- [18] T. X. Wu and D. J. Thompson, “Theoretical investigation of wheel/rail non-linear interaction due to roughness excitation”, *Vehicle System Dynamics*, vol. 34, no. 4, pp. 261–282, 2000. DOI: 10.1076/vesd.34.4.261.2060.
- [19] R. Lewis and U. Olofsson, “Mapping rail wear regimes and transitions”, *Wear*, vol. 257, no. 7, pp. 721–729, 2004. DOI: 10.1016/j.wear.2004.03.019.
- [20] E. Sheinman, “Wear of rails. A review of the American press”, *Journal of Friction and Wear*, vol. 33, no. 4, pp. 308–314, 2012. DOI: 10.3103/S1068366612040101.
- [21] M. P. Vila Tortosa, “Modeling wave wear growth on rails. (In Spanish)”, PhD thesis, Universitat Politècnica de València (UPV), Departamento de Ingeniería Mecánica y de Materiales (DIMM), 2015.
- [22] S. L. Grassie and J. Kalousek, “Rail corrugation: Characteristics, causes and treatments”, *Proceedings of the Institution of Mechanical Engineers, Part F: Journal of Rail and Rapid Transit*, vol. 207, no. 1, pp. 57–68, 1993. DOI: 10.1243/PIME_PROC_1993_207_227_02.
- [23] S. L. Grassie, “Rail corrugation: Characteristics, causes, and treatments”, *Proceedings of the Institution of Mechanical Engineers, Part F: Journal of Rail and Rapid Transit*, vol. 223, no. 6, pp. 581–596, 2009. DOI: 10.1243/09544097JRRT264.

- [24] B. Hemsworth, “Recent developments in wheel/rail noise research”, *Journal of Sound and Vibration*, vol. 66, no. 3, pp. 297–310, 1979. DOI: 10.1016/0022-460X(79)90847-2.
- [25] P. C. Dings and M. G. Ditttrich, “Roughness on Dutch railway wheels and rails”, *Journal of Sound and Vibration*, vol. 193, no. 1, pp. 103–112, 1996. DOI: 10.1006/jsvi.1996.0250.
- [26] J. C. O. Nielsen and A. Johansson, “Out-of-round railway wheels—a literature survey”, *Proceedings of the Institution of Mechanical Engineers, Part F: Journal of Rail and Rapid Transit*, vol. 214, no. 2, pp. 79–91, 2000. DOI: 10.1243/0954409001531351.
- [27] T. Vernersson, “Thermally induced roughness of tread-braked railway wheels: Part 1: Brake rig experiments”, *Wear*, vol. 236, no. 1, pp. 96–105, 1999. DOI: 10.1016/S0043-1648(99)00260-4.
- [28] M. Petersson and T. Vernersson, “Noise-related roughness on tread braked railway wheels—experimental measurements and numerical simulations”, *Wear*, vol. 253, no. 1, pp. 301–307, 2002. DOI: 10.1016/S0043-1648(02)00121-7.
- [29] M. S. Walia, T. Vernersson, R. Lundén, F. Blennow, and M. Meinel, “Temperatures and wear at railway tread braking: Field experiments and simulations”, *Wear*, vol. 440-441, p. 203086, 2019. DOI: 10.1016/j.wear.2019.203086.
- [30] R. Bogacz and K. Frischmuth, “On dynamic effects of wheel-rail interaction in the case of polygonalisation”, *Mechanical Systems and Signal Processing*, vol. 79, pp. 166–173, 2016. DOI: 10.1016/j.ymsp.2016.03.001.
- [31] B. Hemsworth, “Railway noise prediction—data base requirements”, *Journal of Sound and Vibration*, vol. 87, no. 2, pp. 275–283, 1983. DOI: 10.1016/0022-460X(83)90563-1.
- [32] C. Stanworth, “Rolling noise”, in *Rolling Contact Phenomena*, B. Jacobson and J. J. Kalker, Eds., Springer Vienna, 2000, pp. 329–354.

-
- [33] C. Mellet, F. Létourneaux, F. Poisson, and C. Talotte, “High speed train noise emission: Latest investigation of the aerodynamic/rolling noise contribution”, *Journal of Sound and Vibration*, vol. 293, no. 3-5, pp. 535–546, 2006. DOI: 10.1016/j.jsv.2005.08.069.
- [34] P. J. Remington, “Wheel/rail rolling noise, II: Validation of the theory”, *Journal of the Acoustical Society of America*, vol. 81, no. 6, pp. 1824–1832, 1987. DOI: 10.1121/1.394747.
- [35] D. J. Thompson, “Predictions of acoustic radiation from vibrating wheels and rails”, *Journal of Sound and Vibration*, vol. 120, no. 2, pp. 275–280, 1988. DOI: 10.1016/0022-460X(88)90435-X.
- [36] D. J. Thompson, P. Fodiman, and H. Mahé, “Experimental validation of the TWINS prediction program for rolling noise, part 2: Results”, *Journal of Sound and Vibration*, vol. 193, no. 1, pp. 137–147, 1996. DOI: 10.1006/jsvi.1996.0253.
- [37] C. J. C. Jones and D. J. Thompson, “Extended validation of a theoretical model for railway rolling noise using novel wheel and track designs”, *Journal of Sound and Vibration*, vol. 267, no. 3, pp. 509–522, 2003. DOI: 10.1016/S0022-460X(03)00711-9.
- [38] D. J. Thompson, G. Squicciarini, J. Zhang, I. Lopez Arteaga, E. Zea, M. Dittrich, E. Jansen, K. Arcas, E. Cierco, F. Magrans, A. Malkoun, E. Iturritxa, A. Guiral, M. Stangl, G. Schleinzer, B. Martin Lopez, C. Chaufour, and J. Wändell, “Assessment of measurement-based methods for separating wheel and track contributions to railway rolling noise”, *Applied Acoustics*, vol. 140, pp. 48–62, 2018. DOI: 10.1016/j.apacoust.2018.05.012.
- [39] P. J. Remington, “Wheel/rail noise – Part I: Characterization of the wheel/rail dynamic system”, *Journal of Sound and Vibration*, vol. 46, no. 3, pp. 359–379, 1976. DOI: 10.1016/0022-460X(76)90861-0.
- [40] B. Hemsforth, “Vibration of a rolling wheel- preliminary results”, *Journal of Sound and Vibration*, vol. 87, no. 2, pp. 189–194, 1983. DOI: 10.1016/0022-460X(83)90553-9.

- [41] H. Irretier, “The natural and forced vibrations of a wheel disc”, *Journal of Sound and Vibration*, vol. 87, no. 2, pp. 161–177, 1983. DOI: 10.1016/0022-460X(83)90551-5.
- [42] R. D. Mindlin, “Influence of rotary inertia and shear on flexural motions of isotropic elastic plates”, *Journal of Applied Mechanics*, vol. 73, pp. 31–38, 1951.
- [43] E. Schneider, K. Popp, and H. Irretier, “Noise generation in railway wheels due to rail-wheel contact forces”, *Journal of Sound and Vibration*, vol. 120, no. 2, pp. 227–244, 1988. DOI: 10.1016/0022-460X(88)90431-2.
- [44] P. J. Remington, “Wheel/rail rolling noise, I: Theoretical analysis”, *Journal of the Acoustical Society of America*, vol. 81, no. 6, pp. 1805–1823, 1987. DOI: 10.1121/1.394746.
- [45] D. J. Thompson, “Wheel-rail noise generation, part II: Wheel vibration”, *Journal of Sound and Vibration*, vol. 161, no. 3, pp. 401–419, 1993. DOI: 10.1006/jsvi.1993.1083.
- [46] D. J. Thompson, “Wheel-rail noise generation, part V: Inclusion of wheel rotation”, *Journal of Sound and Vibration*, vol. 161, no. 3, pp. 467–482, 1993. DOI: 10.1006/jsvi.1993.1086.
- [47] Y. Honda, H. Matsuhisa, and S. Sato, “Modal response of a disk to a moving concentrated harmonic force”, *Journal of Sound and Vibration*, vol. 102, no. 4, pp. 457–472, 1985. DOI: 10.1016/S0022-460X(85)80107-3.
- [48] T. Zhong, G. Chen, X. Sheng, X. Zhan, L. Zhou, and J. Kai, “Vibration and sound radiation of a rotating train wheel subject to a vertical harmonic wheel-rail force”, *Journal of Modern Transportation*, vol. 26, no. 2, pp. 81–95, 2018. DOI: 10.1007/s40534-017-0154-6.
- [49] D. J. Thompson, N. Vincent, and P. E. Gautier, “Validation of a model for railway rolling noise using field measurements with sinusoidally profiled wheels”, *Journal of Sound and Vibration*, vol. 223, no. 4, pp. 587–609, 1999. DOI: 10.1006/jsvi.1998.2107.

-
- [50] A. Cigada, S. Manzoni, and M. Vanali, “Vibro-acoustic characterization of railway wheels”, *Applied Acoustics*, vol. 69, no. 6, pp. 530–545, 2008. DOI: 10.1016/j.apacoust.2007.01.002.
- [51] D. J. Thompson and M. G. Ditttrich, “Wheel response and radiation-laboratory measurements of five types of wheel and comparisons with theory”, Tech. Rep., 1991.
- [52] I. Merideño, J. Nieto, N. Gil-Negrete, A. Landaberea, and J. Iartza, “Numerical vibro-acoustic analysis of railway wheels with and without damping solutions”, *Noise Control Engineering Journal*, vol. 60, no. 4, pp. 458–472, 2012. DOI: 10.3397/1.3701024.
- [53] L. Baeza, J. Fayos, A. Roda, and R. Insa, “High frequency railway vehicle-track dynamics through flexible rotating wheelsets”, *Vehicle System Dynamics*, vol. 46, no. 7, pp. 647–659, 2008. DOI: 10.1080/00423110701656148.
- [54] J. Martínez-Casas, L. Mazzola, L. Baeza, and S. Bruni, “Numerical estimation of stresses in railway axles using a train-track interaction model”, *International Journal of Fatigue*, vol. 47, pp. 18–30, 2013. DOI: 10.1016/j.ijfatigue.2012.07.006.
- [55] J. Martínez-Casas, E. Di Gialleonardo, S. Bruni, and L. Baeza, “A comprehensive model of the railway wheelset-track interaction in curves”, *Journal of Sound and Vibration*, vol. 333, no. 18, pp. 4152–4169, 2014. DOI: 10.1016/j.jsv.2014.03.032.
- [56] J. Sadeghi and A. Hasheminezhad, “Correlation between rolling noise generation and rail roughness of tangent tracks and curves in time and frequency domains”, *Applied Acoustics*, vol. 107, pp. 10–18, 2016. DOI: 10.1016/j.apacoust.2016.01.006.
- [57] T. Bruneteau, C. J. C. Jones, and D. J. Thompson, “Numerical investigation into the radiation of sound from railway wheels”, Tech. Rep., 1999.
- [58] D. J. Thompson, B. Hemsworth, and N. Vincent, “Experimental validation of the TWINS prediction program for rolling noise, part 1: De-

- scription of the model and method”, *Journal of Sound and Vibration*, vol. 193, no. 1, pp. 123–135, 1996. DOI: 10.1006/jsvi.1996.0252.
- [59] D. J. Thompson and C. J. C. Jones, “Sound radiation from a vibrating railway wheel”, *Journal of Sound and Vibration*, vol. 253, no. 2, pp. 401–419, 2002.
- [60] D. J. Thompson and C. J. C. Jones, “Review of the modelling of wheel/rail noise generation”, *Journal of Sound and Vibration*, vol. 231, no. 3, pp. 519–536, 2000. DOI: 10.1006/jsvi.1999.2542.
- [61] C. J. C. Jones and D. J. Thompson, “Rolling noise generated by railway wheels with visco-elastic layers”, *Journal of Sound and Vibration*, vol. 231, no. 3, pp. 779–790, 2000. DOI: 10.1006/jsvi.1999.2562.
- [62] B. Blanco, “Development of new techniques for the numerical modelling of railway track dynamics. Application to rolling noise assessment”, PhD thesis, KTH Royal Institute of Technology, School of Engineering Sciences (SCI), Aeronautical and Vehicle Engineering., 2019.
- [63] L. Baeza, A. Roda, and J. C. O. Nielsen, “Railway vehicle/track interaction analysis using a modal substructuring approach”, *Journal of Sound and Vibration*, vol. 293, no. 1-2, pp. 112–124, 2006. DOI: 10.1016/j.jsv.2005.09.006.
- [64] B. Blanco, A. Alonso, L. Kari, N. Gil-Negrete, and J. Giménez, “Implementation of Timoshenko element local deflection for vertical track modelling”, *Vehicle System Dynamics*, vol. 57, no. 10, pp. 1421–1444, 2019. DOI: 10.1080/00423114.2018.1513538.
- [65] L.-H. Tran, T. Hoang, D. Duhamel, G. Foret, S. Messad, and A. Loaec, “A fast analytic method to calculate the dynamic response of railways sleepers”, *Journal of Vibration and Acoustics, Transactions of the ASME*, vol. 141, no. 1, 2019. DOI: 10.1115/1.4040392.
- [66] K. Knothe and S. L. Grassie, “Modelling of railway track and vehicle/track interaction at high frequencies”, *Vehicle System Dynamics*, vol. 22, no. 3-4, pp. 209–262, 1993. DOI: 10.1080/00423119308969027.

-
- [67] S. Timoshenko, “Method of analysis of statical and dynamical stresses in rail”, *Proceedings of the Second International Congress for Applied Mechanics*, pp. 407–418, 1926.
- [68] S. L. Grassie, R. W. Gregory, D. Harrison, and K. L. Johnson, “The dynamic response of railway track to high frequency vertical excitation”, *Journal of Mechanical Engineering Science*, vol. 24, no. 2, pp. 77–90, 1982. DOI: 10.1243/JMES_JOUR_1982_024_016_02.
- [69] S. L. Grassie, R. W. Gregory, and K. L. Johnson, “The dynamic response of railway track to high frequency lateral excitation”, *Journal of Mechanical Engineering Science*, vol. 24, no. 2, pp. 91–95, 1982. DOI: 10.1243/JMES_JOUR_1982_024_017_02.
- [70] S. L. Grassie, R. W. Gregory, and K. L. Johnson, “The dynamic response of railway track to high frequency longitudinal excitation”, *Journal of Mechanical Engineering Science*, vol. 24, no. 2, pp. 97–102, 1982. DOI: 10.1243/JMES_JOUR_1982_024_018_02.
- [71] D. J. Thompson, “Theoretical modelling of wheel-rail noise generation”, *Proceedings of the Institution of Mechanical Engineers, Part F: Journal of Rail and Rapid Transit*, vol. 205, no. 2, pp. 137–149, 1991. DOI: 10.1243/PIME_PROC_1991_205_227_02.
- [72] D. Kostovasilis, D. J. Thompson, and M. F. M. Hussein, “A semi-analytical beam model for the vibration of railway tracks”, *Journal of Sound and Vibration*, vol. 393, pp. 321–337, 2017. DOI: 10.1016/j.jsv.2016.12.033.
- [73] T. X. Wu and D. J. Thompson, “A double Timoshenko beam model for vertical vibration analysis of railway track at high frequencies”, *Journal of Sound and Vibration*, vol. 224, no. 2, pp. 329–348, 1999. DOI: 10.1006/jsvi.1999.2171.
- [74] T. X. Wu and D. J. Thompson, “Analysis of lateral vibration behavior of railway track at high frequencies using a continuously supported multiple beam model”, *Journal of the Acoustical Society of America*, vol. 106, no. 3, pp. 1369–1376, 1999. DOI: 10.1121/1.427171.

- [75] M. L. Munjal and M. Heckl, “Vibrations of a periodic rail-sleeper system excited by an oscillating stationary transverse force”, *Journal of Sound and Vibration*, vol. 81, no. 4, pp. 491–500, 1982. DOI: 10.1016/0022-460X(82)90292-9.
- [76] D. J. Thompson, “Wheel-rail noise generation, part III: Rail vibration”, *Journal of Sound and Vibration*, vol. 161, no. 3, pp. 421–446, 1993. DOI: 10.1006/jsvi.1993.1084.
- [77] M. A. Heckl, “Coupled waves on a periodically supported Timoshenko beam”, *Journal of Sound and Vibration*, vol. 252, no. 5, pp. 849–882, 2002. DOI: 10.1006/jsvi.2001.3823.
- [78] L. Brillouin, *Wave Propagation in Periodic Structures*, 1st ed. McGraw-Hill Publishing Company, 1946.
- [79] T. X. Wu and D. J. Thompson, “The influence of random sleeper spacing and ballast stiffness on the vibration behaviour of railway track”, *Acta Acustica united with Acustica*, vol. 86, pp. 313–321, 2000.
- [80] J. Ryue, D. J. Thompson, P. R. White, and D. Thompson, “Investigations of propagating wave types in railway tracks at high frequencies”, *Journal of Sound and Vibration*, vol. 315, no. 1-2, pp. 157–175, 2008. DOI: 10.1016/j.jsv.2008.01.054.
- [81] D. J. Mead, “A general theory of harmonic wave propagation in linear periodic systems with multiple coupling”, *Journal of Sound and Vibration*, vol. 27, no. 2, pp. 235–260, 1973. DOI: 10.1016/0022-460X(73)90064-3.
- [82] L. Gry, “Dynamic modelling of railway track based on wave propagation”, *Journal of Sound and Vibration*, vol. 195, no. 3, pp. 477–505, 1996. DOI: 10.1006/jsvi.1996.0438.
- [83] L. Gry and C. Gontier, “Dynamic modelling of railway track: A periodic model based on a generalized beam formulation”, *Journal of Sound and Vibration*, vol. 199, no. 4, pp. 531–558, 1997. DOI: 10.1006/jsvi.1995.0671.

-
- [84] L. Gavrić, “Computation of propagative waves in free rail using a finite element technique”, *Journal of Sound and Vibration*, vol. 185, no. 3, pp. 531–543, 1995. DOI: 10.1006/jsvi.1995.0398.
- [85] W. Li, R. A. Dwight, and T. Zhang, “On the study of vibration of a supported railway rail using the semi-analytical finite element method”, *Journal of Sound and Vibration*, vol. 345, pp. 121–145, 2015. DOI: 10.1016/j.jsv.2015.01.036.
- [86] X. Sheng, C. J. C. Jones, and D. J. Thompson, “Responses of infinite periodic structures to moving or stationary harmonic loads”, *Journal of Sound and Vibration*, vol. 282, no. 1-2, pp. 125–149, 2005. DOI: 10.1016/j.jsv.2004.02.050.
- [87] X. Sheng, “Generalization of the Fourier transform-based method for calculating the response of a periodic railway track subject to a moving harmonic load”, *Journal of Modern Transportation*, vol. 23, no. 1, pp. 12–29, 2015. DOI: 10.1007/s40534-015-0066-2.
- [88] X. Sheng, M. Li, C. J. C. Jones, and D. J. Thompson, “Using the Fourier-series approach to study interactions between moving wheels and a periodically supported rail”, *Journal of Sound and Vibration*, vol. 303, no. 3-5, pp. 873–894, 2007. DOI: 10.1016/j.jsv.2007.02.007.
- [89] X. Zhang, D. J. Thompson, Q. Li, D. Kostovasilis, M. Toward, G. Squicciarini, and J. Ryue, “A model of a discretely supported railway track based on a 2.5D finite element approach”, *Journal of Sound and Vibration*, vol. 438, pp. 153–174, 2019. DOI: 10.1016/j.jsv.2018.09.026.
- [90] D. J. Thompson, C. J. C. Jones, and N. Turner, “Investigation into the validity of two-dimensional models for sound radiation from waves in rails”, *Journal of the Acoustical Society of America*, vol. 113, no. 4, pp. 1965–1974, 2003. DOI: 10.1121/1.1555612.
- [91] M. H. A. Janssens, D. J. Thompson, F. G. de Beer, M. G. Dittrich, and H. W. Jansen, *TWINS version 3.3 Track-Wheel Interaction Noise Software theoretical manual*, TNO report, 2014.
- [92] C.-M. Nilsson, C. J. C. Jones, D. J. Thompson, and J. Ryue, “A waveguide finite element and boundary element approach to calculating the

- sound radiated by railway and tram rails”, *Journal of Sound and Vibration*, vol. 321, no. 3-5, pp. 813–836, 2009. DOI: 10.1016/j.jsv.2008.10.027.
- [93] D. Duhamel, “Efficient calculation of the three-dimensional sound pressure field around a noise barrier”, *Journal of Sound and Vibration*, vol. 197, no. 5, pp. 547–571, 1996. DOI: 10.1006/jsvi.1996.0548.
- [94] X. Zhang, D. J. Thompson, and G. Squicciarini, “Sound radiation from railway sleepers”, *Journal of Sound and Vibration*, vol. 369, pp. 178–194, 2016. DOI: 10.1016/j.jsv.2016.01.018.
- [95] X. Zhang, G. Squicciarini, and D. J. Thompson, “Sound radiation of a railway rail in close proximity to the ground”, *Journal of Sound and Vibration*, vol. 362, pp. 111–124, 2016. DOI: 10.1016/j.jsv.2015.10.006.
- [96] X. Zhang, H. Jeong, D. J. Thompson, and G. Squicciarini, “The noise radiated by ballasted and slab tracks”, *Applied Acoustics*, vol. 151, pp. 193–205, 2019. DOI: 10.1016/j.apacoust.2019.03.012.
- [97] X. Zhang, D. J. Thompson, E. Quaranta, and G. Squicciarini, “An engineering model for the prediction of the sound radiation from a railway track”, *Journal of Sound and Vibration*, vol. 461, 2019. DOI: 10.1016/j.jsv.2019.114921.
- [98] R. Bogacz, “On dynamics and stability of continuous systems subjected to a distributed moving load”, *Ingenieur-Archiv*, vol. 53, no. 4, pp. 243–255, 1983. DOI: 10.1007/BF00532244.
- [99] H. Ilias and S. Müller, “A discrete-continuous track-model for wheelsets rolling over short wavelength sinusoidal rail irregularities”, *Vehicle System Dynamics*, vol. 23, no. sup1, pp. 221–233, 1994. DOI: 10.1080/00423119308969517.
- [100] J. Martínez-Casas, J. Giner-Navarro, L. Baeza, and F. Denia, “Improved railway wheelset-track interaction model in the high-frequency domain”, *Journal of Computational and Applied Mathematics*, vol. 309, pp. 642–653, 2017. DOI: 10.1016/j.cam.2016.04.034.

- [101] J. Feldmann, “A theoretical model for structure-borne excitation of a beam and a ring in rolling contact”, *Journal of Sound and Vibration*, vol. 116, no. 3, pp. 527–543, 1987. DOI: 10.1016/S0022-460X(87)81382-2.
- [102] D. J. Thompson, “Wheel-rail noise generation, part IV: Contact zone and results”, *Journal of Sound and Vibration*, vol. 161, no. 3, pp. 447–466, 1993. DOI: 10.1006/jsvi.1993.1085.
- [103] H. Hertz, “Ueber die berührung fester elastischer körper”, *Journal für die Reine und Angewandte Mathematik*, vol. 1882, no. 92, pp. 156–171, 1882. DOI: 10.1515/crll.1882.92.156.
- [104] K. L. Johnson, *Contact Mechanics*, 1st ed. Cambridge University Press, 1985. DOI: 10.1017/CB09781139171731.
- [105] S. P. Timoshenko and J. N. Goodier, *Theory of elasticity*, 3rd ed. McGraw-Hill, 1982.
- [106] T. A. Harris, *Rolling bearing analysis*, 4th ed. John Wiley and Sons, 2001. DOI: 10.1201/9781482275148.
- [107] R. D. Mindlin, “Compliance of elastic bodies in contact”, *Journal of Applied Mechanics*, vol. 71, pp. 259–268, 1949.
- [108] J. J. Kalker, “Survey of wheel-rail rolling contact theory”, *Vehicle System Dynamics*, vol. 8, no. 4, pp. 317–358, 1979. DOI: 10.1080/00423117908968610.
- [109] J. J. Kalker, “Rolling with slip and spin in the presence of dry friction”, *Wear*, vol. 9, no. 1, pp. 20–38, 1966. DOI: 10.1016/0043-1648(66)90011-1.
- [110] J. J. Kalker, “The tangential force transmitted by two elastic bodies rolling over each other with pure creepage”, *Wear*, vol. 11, no. 6, pp. 421–430, 1968. DOI: 10.1016/0043-1648(68)90551-6.

- [111] J. J. Kalker, “The influence of the circulation of the balls in an unlubricated angular contact thrust ball bearing”, *Wear*, vol. 13, no. 4-5, pp. 293–300, 1969. DOI: 10.1016/0043-1648(69)90251-8.
- [112] J. J. Kalker, “Transient phenomena in two elastic cylinders rolling over each other with dry friction”, *Journal of Applied Mechanics, Transactions ASME*, vol. 37, no. 3, pp. 677–688, 1970. DOI: 10.1115/1.3408597.
- [113] K. Knothe and A. Gross-Thebing, “Derivation of frequency dependent creep coefficients based on an elastic half-space model”, *Vehicle System Dynamics*, vol. 15, no. 3, pp. 133–153, 1986. DOI: 10.1080/00423118608968848.
- [114] P. J. Vermeulen and K. L. Johnson, “Contact of nonspherical elastic bodies transmitting tangential forces”, *Journal of Applied Mechanics, Transactions ASME*, vol. 31, no. 2, pp. 338–340, 1964. DOI: 10.1115/1.3629610.
- [115] Z. Y. Shen, J. K. Hedrick, and J. A. Elkins, “A comparison of alternative creep force models for rail vehicle dynamic analysis”, *Vehicle System Dynamics*, vol. 12, no. 1-3, pp. 79–83, 1983. DOI: 10.1080/00423118308968725.
- [116] J. J. Kalker, *Three-Dimensional Elastic Bodies in Rolling Contact*, 1st ed. Springer Netherlands, 1990. DOI: 10.1007/978-94-015-7889-9.
- [117] K. E. Zaazaa and A. L. Schwab, “Review of Joost Kalker’s wheel-rail contact theories and their implementation in multibody codes”, in *7th International Conference on Multibody Systems, Nonlinear Dynamics, and Control, Parts A, B and C*, ser. International Design Engineering Technical Conferences and Computers and Information in Engineering Conference, San Diego, California, USA, Aug. 2009, pp. 1889–1900. DOI: 10.1115/DETC2009-87655.
- [118] J. J. Kalker, “A fast algorithm for the simplified theory of rolling contact”, *Vehicle System Dynamics*, vol. 11, no. 1, pp. 1–13, 1982. DOI: 10.1080/00423118208968684.

-
- [119] A. Alonso and J. G. Giménez, “Tangential problem solution for non-elliptical contact areas with the FastSim algorithm”, *Vehicle System Dynamics*, vol. 45, no. 4, pp. 341–357, 2007. DOI: 10.1080/00423110600999763.
- [120] J. G. Giménez, A. Alonso, and E. Gómez, “Introduction of a friction coefficient dependent on the slip in the FastSim algorithm”, *Vehicle System Dynamics*, vol. 43, no. 4, pp. 233–244, 2005. DOI: 10.1080/00423110412331282913.
- [121] E. A. H. Vollebregt and P. Wilders, “FASTSIM2: A second-order accurate frictional rolling contact algorithm”, *Computational Mechanics*, vol. 47, no. 1, pp. 105–116, 2011. DOI: 10.1007/s00466-010-0536-7.
- [122] P. Remington and J. Webb, “Estimation of wheel/rail interaction forces in the contact area due to roughness”, *Journal of Sound and Vibration*, vol. 193, no. 1, pp. 83–102, 1996. DOI: 10.1006/jsvi.1996.0249.
- [123] J. Boussinesq, *Application des potentiels à l’étude de l’équilibre et du mouvement des solides élastiques: principalement au calcul des déformations et des pressions que produisent, dans ces solides, des efforts quelconques exercés sur une petite partie de leur surface ou de leur intérieur; mémoire suivi de notes étendues sur divers points de physique mathématique et d’analyse*. Gauthier-Villars, 1885.
- [124] D. J. Thompson, “The influence of the contact zone on the excitation of wheel/rail noise”, *Journal of Sound and Vibration*, vol. 267, no. 3, pp. 523–535, 2003. DOI: 10.1016/S0022-460X(03)00712-0.
- [125] R. A. J. Ford and D. J. Thompson, “Simplified contact filters in wheel/rail noise prediction”, *Journal of Sound and Vibration*, vol. 293, no. 3-5, pp. 807–818, 2006. DOI: 10.1016/j.jsv.2005.08.049.
- [126] A. Pieringer, W. Kropp, and D. J. Thompson, “Investigation of the dynamic contact filter effect in vertical wheel/rail interaction using a 2D and a 3D non-hertzian contact model”, *Wear*, vol. 271, no. 1-2, pp. 328–338, 2011. DOI: 10.1016/j.wear.2010.10.029.
- [127] O. E. Lundberg, A. Nordborg, and I. Lopez Arteaga, “The influence of surface roughness on the contact stiffness and the contact filter effect

- in nonlinear wheel-track interaction”, *Journal of Sound and Vibration*, vol. 366, pp. 429–446, 2016. DOI: 10.1016/j.jsv.2015.12.026.
- [128] P. J. Remington, “Wheel/rail noise – Part I: Characterization of the wheel/rail dynamic system”, *Journal of Sound and Vibration*, vol. 46, no. 3, pp. 359–379, 1976. DOI: 10.1016/0022-460X(76)90861-0.
- [129] M. J. Rudd, “Wheel/rail noise – Part II: Wheel squeal”, *Journal of Sound and Vibration*, vol. 46, no. 3, pp. 381–394, 1976. DOI: 10.1016/0022-460X(76)90862-2.
- [130] I. L. Vér, C. S. Ventres, and M. M. Myles, “Wheel/rail noise – Part III: Impact noise generation by wheel and rail discontinuities”, *Journal of Sound and Vibration*, vol. 46, no. 3, pp. 395–417, 1976. DOI: 10.1016/0022-460X(76)90863-4.
- [131] A. G. Galaitis and E. K. Bender, “Wheel/rail noise – Part V : Measurement of wheel and rail roughness”, *Journal of Sound and Vibration*, vol. 46, no. 3, pp. 437–451, 1976. DOI: 10.1016/0022-460X(76)90865-8.
- [132] D. J. Thompson, “Wheel-rail noise: Theoretical modelling of the generation of vibrations”, PhD thesis, University of Southampton, 1991.
- [133] M. H. A. Janssens, D. J. Thompson, and F. G. de Beer, *TWINS version 3.3 Track-Wheel Interaction Noise Software user manual*, TNO report, 2014.
- [134] T. Kitagawa and D. J. Thompson, “Comparison of wheel/rail noise radiation on Japanese railways using the TWINS model and microphone array measurements”, *Journal of Sound and Vibration*, vol. 293, no. 3-5, pp. 496–509, 2006. DOI: 10.1016/j.jsv.2005.08.037.
- [135] E. K. Bender and P. J. Remington, “The influence of rails on train noise”, *Journal of Sound and Vibration*, vol. 37, no. 3, pp. 321–334, 1974. DOI: 10.1016/S0022-460X(74)80248-8.
- [136] P. J. Remington, “Wheel/rail rolling noise: What do we know? What don’t we know? Where do we go from here?”, *Journal of Sound and*

-
- Vibration*, vol. 120, no. 2, pp. 203–226, 1988. DOI: 10.1016/0022-460X(88)90430-0.
- [137] T. ten Wolde and C. J. M. van Ruitten, “Sources and mechanisms of wheel/rail noise: State-of-the-art and recent research”, *Journal of Sound and Vibration*, vol. 87, no. 2, pp. 147–160, 1983. DOI: 10.1016/0022-460X(83)90550-3.
- [138] H. Arai, “On the acoustic/dynamic characteristics of the resilient wheel (Part 1: Comparison with other anti-noise wheels in the running test).”, *Bulletin of the JSME*, vol. 26, no. 222, pp. 2200–2207, 1983. DOI: 10.1299/jsme1958.26.2200.
- [139] W. F. King III and D. Bechert, “On the sources of wayside noise generated by high-speed trains”, *Journal of Sound and Vibration*, vol. 66, no. 3, pp. 311–332, 1979. DOI: 10.1016/0022-460X(79)90848-4.
- [140] D. J. Thompson, “Predictions of acoustic radiation from vibrating wheels and rails”, *Journal of Sound and Vibration*, vol. 120, no. 2, pp. 275–280, 1988. DOI: 10.1016/0022-460X(88)90435-X.
- [141] T. Kitagawa, “The influence of wheel and track parameters on rolling noise”, *Quarterly Report of RTRI*, vol. 50, no. 1, pp. 32–38, 2009. DOI: 10.2219/rtriqr.50.32.
- [142] D. J. Thompson, G. Squicciarini, J. Zhang, I. Lopez Arteaga, E. Zea, M. Dittrich, E. Jansen, K. Arcas, E. Cierco, F. Magrans, A. Malkoun, E. Iturritxa, A. Guiral, M. Stangl, G. Schleinzer, B. Martin Lopez, C. Chaufour, and J. Wändell, “Assessment of measurement-based methods for separating wheel and track contributions to railway rolling noise”, *Applied Acoustics*, vol. 140, pp. 48–62, 2018. DOI: 10.1016/j.apacoust.2018.05.012.
- [143] B. Barsikow, W. F. King III, and E. Pfizenmaier, “Wheel/rail noise generated by a high-speed train investigated with a line array of microphones”, *Journal of Sound and Vibration*, vol. 118, no. 1, pp. 99–122, 1987. DOI: 10.1016/0022-460X(87)90257-4.
- [144] T. Kitagawa and D. J. Thompson, “The horizontal directivity of noise radiated by a rail and implications for the use of microphone arrays”,

- Journal of Sound and Vibration*, vol. 329, no. 2, pp. 202–220, 2010. DOI: 10.1016/j.jsv.2009.09.002.
- [145] J. Zhang, G. Squicciarini, and D. J. Thompson, “Implications of the directivity of railway noise sources for their quantification using conventional beamforming”, *Journal of Sound and Vibration*, vol. 459, pp. 114–841, 2019. DOI: 10.1016/j.jsv.2019.07.007.
- [146] S. Bühler, “Methods and results of field testing of a retrofitted freight train with composite brake blocks”, *Journal of Sound and Vibration*, vol. 293, no. 3-5, pp. 1041–1050, 2006. DOI: 10.1016/j.jsv.2005.08.055.
- [147] B. Asmussen, H. Onnich, R. Strube, L. M. Greven, S. Schröder, K. Jäger, and K. G. Degen, “Status and perspectives of the "specially monitored track"”, *Journal of Sound and Vibration*, vol. 293, no. 3-5, pp. 1070–1077, 2006. DOI: 10.1016/j.jsv.2005.08.066.
- [148] P. Remington and J. Webb, “Wheel/rail noise reduction through profile modification”, *Journal of Sound and Vibration*, vol. 193, no. 1, pp. 335–348, 1996. DOI: 10.1006/jsvi.1996.0274.
- [149] D. J. Thompson and P. J. Remington, “Effects of transverse profile on the excitation of wheel/rail noise”, *Journal of Sound and Vibration*, vol. 231, no. 3, pp. 537–548, 2000. DOI: 10.1006/jsvi.1999.2543.
- [150] P. J. Remington, “Control of wheel/rail rolling noise at the source”, *Heavy Vehicle Systems*, vol. 7, no. 1, pp. 1–21, 2000.
- [151] D. J. Thompson, “A continuous damped vibration absorber to reduce broad-band wave propagation in beams”, *Journal of Sound and Vibration*, vol. 311, no. 3-5, pp. 824–842, 2008. DOI: 10.1016/j.jsv.2007.09.038.
- [152] D. J. Thompson, C. J. C. Jones, T. P. Waters, and D. Farrington, “A tuned damping device for reducing noise from railway track”, *Applied Acoustics*, vol. 68, no. 1, pp. 43–57, 2007. DOI: 10.1016/j.apacoust.2006.05.001.

-
- [153] F. Ltourneaux, F. Margiocchi, and F. Poisson, “Complete assessment of rail absorber performances on an operated track in france”, in *Proceedings of the World Congress on Railway Research*, CDROM, Montreal, Canada, 2006, p. 8.
- [154] B. Asmussen, D. Stiebel, P. Kitson, D. Farrington, and D. Benton, “Reducing the noise emission by increasing the damping of the rail: Results of a field test”, in *Noise and Vibration Mitigation for Rail Transportation Systems*, Berlin, Heidelberg: Springer Berlin Heidelberg, 2008, pp. 229–235.
- [155] N. Vincent, P. Bouvet, D. J. Thompson, and P. E. Gautier, “Theoretical optimization of track components to reduce rolling noise”, *Journal of Sound and Vibration*, vol. 193, no. 1, pp. 161–171, 1996. DOI: 10.1006/jsvi.1996.0255.
- [156] D. J. Thompson, “But are the trains getting any quieter?”, in *14th International Congress on Sound and Vibration (ICSV14)*, Cairns, Australia, 2007, p. 20.
- [157] H. Ilias, “The influence of railpad stiffness on wheelset/track interaction and corrugation growth”, *Journal of Sound and Vibration*, vol. 227, no. 5, pp. 935–948, 1999. DOI: 10.1006/jsvi.1999.2059.
- [158] R. J. Diehl, R. Nowack, and G. Hölzl, “Solutions for acoustical problems with ballastless track”, *Journal of Sound and Vibration*, vol. 231, no. 3, pp. 899–906, 2000. DOI: 10.1006/jsvi.1999.2534.
- [159] S. Van Lier, “Vibro-acoustic modelling of slab track with embedded rails”, *Journal of Sound and Vibration*, vol. 231, no. 3, pp. 805–817, 2000. DOI: 10.1006/jsvi.1999.2564.
- [160] C. J. C. Jones, A. E. J. Hardy, R. R. K. Jones, and A. Wang, “Bogie shrouds and low track-side barriers for the control of railway vehicle rolling noise”, *Journal of Sound and Vibration*, vol. 193, no. 1, pp. 427–431, 1996. DOI: 10.1006/jsvi.1996.0286.
- [161] N. Vincent, “Rolling noise control at source: State-of-the-art survey”, *Journal of Sound and Vibration*, vol. 231, no. 3, pp. 865–876, 2000. DOI: 10.1006/jsvi.1999.2646.

- [162] I. Merideno, J. Nieto, N. Gil-Negrete, J. G. Giménez Ortiz, A. Landaberea, and J. Iartza, “Theoretical prediction of the damping of a railway wheel with sandwich-type dampers”, *Journal of Sound and Vibration*, vol. 333, no. 20, pp. 4897–4911, 2014. DOI: 10.1016/j.jsv.2014.05.034.
- [163] J. Färm, “Evaluation of wheel dampers on an intercity train”, *Journal of Sound and Vibration*, vol. 267, no. 3, pp. 739–747, 2003. DOI: 10.1016/S0022-460X(03)00737-5.
- [164] I. Merideno, J. Nieto, N. Gil-Negrete, A. Landaberea, and J. Iartza, “An experimental comparison between existing damping solutions for railway wheels”, *Noise Control Engineering Journal*, vol. 63, no. 5, pp. 448–459, 2015. DOI: 10.3397/1/376340.
- [165] I. Lopez, J. Vinolas, J. Busturia, and A. Castanares, “Railway wheel ring dampers”, in *Proceedings Inter-Noise 2000*, Nice, France, 2000, pp. 702–707.
- [166] Z. Wang, Y. Jiao, and Z. Chen, “Parameter study of friction damping ring for railway wheels based on modal analysis”, *Applied Acoustics*, vol. 153, pp. 140–146, 2019. DOI: 10.1016/j.apacoust.2019.04.025.
- [167] I. Lopez Arteaga, “Theoretical and experimental analysis of ring-damped railway wheels”, PhD thesis, Universidad de Navarra, Escuela Superior de Ingenieros Industriales, 1998.
- [168] P. Bouvet, N. Vincent, A. Coblenz, and F. Demilly, “Optimization of resilient wheels for rolling noise control”, *Journal of Sound and Vibration*, vol. 231, no. 3, pp. 765–777, 2000. DOI: 10.1006/jsvi.1999.2561.
- [169] A. Cigada, S. Manzoni, and M. Vanali, “Geometry effects on the vibro-acoustic behavior of railway resilient wheels”, *JVC/Journal of Vibration and Control*, vol. 17, no. 12, pp. 1761–1778, 2011. DOI: 10.1177/1077546310362452.
- [170] B. Suarez, J. A. Chover, P. Rodriguez, and F. J. Gonzalez, “Effectiveness of resilient wheels in reducing noise and vibrations”, *Proceedings of the Institution of Mechanical Engineers, Part F: Journal of Rail and Rapid*

-
- Transit*, vol. 225, no. 6, pp. 545–565, 2011. DOI: 10.1177/0954409711404104.
- [171] B. Hemsworth, P. E. Gautier, and R. Jones, “Silent freight and silent track projects”, in *Proceedings of Internoise*, Nice, France, 2000, pp. 714–719.
- [172] A. Putra and D. J. Thompson, “Sound radiation from a perforated un-baffled plate”, in *19th International Congress on Acoustics: Acoustics for the 21st Century*, A. Calvo-Manzano, A. Pérez-López, and S. Santiago, Eds., Madrid, Spain: Sociedad Española de Acústica, 2007.
- [173] A. Putra and D. J. Thompson, “Sound radiation from perforated plates”, *Journal of Sound and Vibration*, vol. 329, no. 20, pp. 4227–4250, 2010. DOI: 10.1016/j.jsv.2010.04.020.
- [174] A. Putra and D. J. Thompson, “Radiation efficiency of unbaffled and perforated plates near a rigid reflecting surface”, *Journal of Sound and Vibration*, vol. 330, no. 22, pp. 5443–5459, 2011. DOI: 10.1016/j.jsv.2011.05.033.
- [175] X.-Q. Tong, J. Lin, G.-Y. Zhang, and X. Zhu, “Influence of web plate holes on the radiation noise characteristics of wheels of the high speed train”, *Journal of Vibroengineering*, vol. 18, no. 7, pp. 4870–4884, 2016. DOI: 10.21595/jve.2016.17594.
- [176] E. Aggestam and J. C. O. Nielsen, “Multi-objective optimisation of transition zones between slab track and ballasted track using a genetic algorithm”, *Journal of Sound and Vibration*, vol. 446, pp. 91–112, 2019. DOI: 10.1016/j.jsv.2019.01.027.
- [177] S. Gregori, M. Tur, E. Nadal, and F. J. Fuenmayor, “An approach to geometric optimisation of railway catenaries”, *Vehicle System Dynamics*, vol. 56, no. 8, pp. 1162–1186, 2018. DOI: 10.1080/00423114.2017.1407434.
- [178] J. C. O. Nielsen, “Dynamic interaction between wheel and track – A parametric search towards an optimal design of rail structures”, *Vehicle System Dynamics*, vol. 23, no. 1, pp. 115–132, 1994. DOI: 10.1080/00423119408969053.

- [179] J. C. O. Nielsen, “Acoustic optimization of railway sleepers”, *Journal of Sound and Vibration*, vol. 231, no. 3, pp. 753–764, 2000. DOI: 10.1006/jjsvi.1999.2560.
- [180] Y. Zhao, X. Li, Q. Lv, H. Jiao, X. Xiao, and X. Jin, “Measuring, modelling and optimising an embedded rail track”, *Applied Acoustics*, vol. 116, pp. 70–81, 2017. DOI: 10.1016/j.apacoust.2016.07.021.
- [181] G. A. Efthimeros, D. I. Photeinos, Z. G. Diamantis, and D. T. Tsahalis, “Vibration/noise optimization of a FEM railway wheel model”, *Engineering Computations*, vol. 19, no. 7-8, pp. 922–931, 2002. DOI: 10.1108/026444400210450350.
- [182] J. C. O. Nielsen and C. R. Fredö, “Multi-disciplinary optimization of railway wheels”, *Journal of Sound and Vibration*, vol. 293, no. 3-5, pp. 510–521, 2006. DOI: 10.1016/j.jsv.2005.08.063.
- [183] J. R. Koch, N. Vincent, H. Chollet, and O. Chiello, “Curve squeal of urban rolling stock – Part 2: Parametric study on a 1/4 scale test rig”, *Journal of Sound and Vibration*, vol. 293, no. 3-5, pp. 701–709, 2006. DOI: 10.1016/j.jsv.2005.12.009.
- [184] S. S. Hsu, Z. Huang, S. D. Iwnicki, D. J. Thompson, C. J. C. Jones, G. Xie, and P. D. Allen, “Experimental and theoretical investigation of railway wheel squeal”, *Proceedings of the Institution of Mechanical Engineers, Part F: Journal of Rail and Rapid Transit*, vol. 221, no. 1, pp. 59–73, 2007. DOI: 10.1243/0954409JRRT85.
- [185] A. Pieringer, “A numerical investigation of curve squeal in the case of constant wheel/rail friction”, *Journal of Sound and Vibration*, vol. 333, no. 18, pp. 4295–4313, 2014. DOI: 10.1016/j.jsv.2014.04.024.
- [186] C. Glocker, E. Cataldi-Spinola, and R. I. Leine, “Curve squealing of trains: Measurement, modelling and simulation”, *Journal of Sound and Vibration*, vol. 324, no. 1-2, pp. 365–386, 2009. DOI: 10.1016/j.jsv.2009.01.048.
- [187] N. Vincent, J. R. Koch, H. Chollet, and J. Y. Guerder, “Curve squeal of urban rolling stock – Part 1: State of the art and field measurements”,

-
- Journal of Sound and Vibration*, vol. 293, no. 3-5, pp. 691–700, 2006. DOI: 10.1016/j.jsv.2005.12.008.
- [188] P. J. Remington, “Wheel/rail squeal and impact noise: What do we know? What don’t we know? Where do we go from here?”, *Journal of Sound and Vibration*, vol. 116, no. 2, pp. 339–353, 1987. DOI: 10.1016/S0022-460X(87)81306-8.
- [189] J. Giner Navarro, “Advanced techniques for the time-domain modelling of high-frequency train/track interaction”, PhD thesis, Universitat Politècnica de València (UPV), Departamento de Ingeniería Mecánica y de Materiales (DIMM), 2017.
- [190] C. Talotte, P. E. Gautier, D. J. Thompson, and C. Hanson, “Identification, modelling and reduction potential of railway noise sources: A critical survey”, *Journal of Sound and Vibration*, vol. 267, no. 3, pp. 447–468, 2003. DOI: 10.1016/S0022-460X(03)00707-7.
- [191] D. J. Thompson, E. L. Iglesias, X. Liu, J. Zhu, and Z. Hu, “Recent developments in the prediction and control of aerodynamic noise from high-speed trains”, *International Journal of Rail Transportation*, vol. 3, no. 3, pp. 119–150, 2015. DOI: 10.1080/23248378.2015.1052996.
- [192] C. Talotte, “Aerodynamic noise: A critical survey”, *Journal of Sound and Vibration*, vol. 231, no. 3, pp. 549–562, 2000. DOI: 10.1006/jsvi.1999.2544.
- [193] N. Frémion, N. Vincent, M. Jacob, G. Robert, A. Louisot, and S. Guerand, “Aerodynamic noise radiated by the intercoach spacing and the bogie of a high-speed train”, *Journal of Sound and Vibration*, vol. 231, no. 3, pp. 577–593, 2000. DOI: 10.1006/jsvi.1999.2546.
- [194] W.-Q. Dai, X. Zheng, Z.-Y. Hao, Y. Qiu, H. Li, and L. Luo, “Aerodynamic noise radiating from the inter-coach windshield region of a high-speed train”, *Journal of Low Frequency Noise Vibration and Active Control*, vol. 37, no. 3, pp. 590–610, 2018. DOI: 10.1177/1461348417747178.

- [195] M. H. A. Janssens and D. J. Thompson, “A calculation model for the noise from steel railway bridges”, *Journal of Sound and Vibration*, vol. 193, no. 1, pp. 295–305, 1996. DOI: 10.1006/jsvi.1996.0270.
- [196] X. Li, Q. Liu, S. Pei, L. Song, and X. Zhang, “Structure-borne noise of railway composite bridge: Numerical simulation and experimental validation”, *Journal of Sound and Vibration*, vol. 353, pp. 378–394, 2015. DOI: 10.1016/j.jsv.2015.05.030.
- [197] Q. Liu, D. J. Thompson, P. Xu, Q. Feng, and X. Li, “Investigation of train-induced vibration and noise from a steel-concrete composite railway bridge using a hybrid finite element-statistical energy analysis method”, *Journal of Sound and Vibration*, vol. 471, 2020. DOI: 10.1016/j.jsv.2020.115197.
- [198] W. Thomson, *Theory of Vibration with Applications*, 2nd ed. CRC Press, 1993. DOI: 10.1201/9780203718841.
- [199] S. P. Timoshenko and J. M. Gere, *Theory of elastic stability*, 2nd ed. McGraw-Hill International Book Company, 1963.
- [200] DIN, “Railway applications. Wheelsets and bogies. Monobloc wheels. Design assessment procedure. Part 1: Forged and rolled wheels. DIN-prEN-13979-1:2017”, Deutsches Institut für Normung (DIN), Technical Standard, 2017.
- [201] X. Garcia-Andrés, J. Martínez-Casas, F. D. Denia, and L. Baeza, “Cálculo 3D de la potencia acústica radiada por una rueda ferroviaria a partir de la respuesta temporal con efectos giroscópicos y comportamiento no lineal (In Spanish)”, in *Proceedings of the Congreso de Métodos Numéricos en Ingeniería (CMN 2017)*, València, Spain, 2017, pp. 23–36.
- [202] ISO, “Acoustics – Railway applications. Measurement of noise emitted by railbound vehicles ISO Standard 3095:2013”, International Organization for Standardization (ISO), Geneva, Technical Standard, 2014.
- [203] S. L. Grassie, R. W. Gregory, D. Harrison, and K. L. Johnson, “The dynamic response of railway track to high frequency vertical excitation”, *Journal of Mechanical Engineering Science*, vol. 24, no. 2, pp. 77–90, 1982. DOI: 10.1243/JMES_JOUR_1982_024_016_02.

-
- [204] K. F. Graff, *Wave motion in elastic solids*, 1st ed. Dover Publications Inc., 1991.
- [205] S. P. Timoshenko, “On the transverse vibrations of bars of uniform cross-section”, *The London, Edinburgh, and Dublin Philosophical Magazine and Journal of Science*, vol. 43, no. 253, pp. 125–131, 1922. DOI: 10.1080/14786442208633855.
- [206] K. F. Riley, M. P. Hobson, and S. J. Bence, *Mathematical Methods for Physics and Engineering: A Comprehensive Guide*, 3rd ed. Cambridge University Press, 2006. DOI: 10.1017/CB09781139164979.
- [207] S. Lang, *Complex Analysis*, 2nd ed. Springer, 1985. DOI: 10.1007/978-1-4757-1871-3_6.
- [208] J. J. Kalker, “On the rolling contact of two elastic bodies in the presence of dry friction”, PhD thesis, Technical University of Delft, 1967.
- [209] V. K. Garg and R. V. Dukkipati, *Dynamics of Railway Vehicle Systems*, 1st ed. Academic Press, 1984. DOI: 10.1016/B978-0-12-275950-5.X5001-9.
- [210] F. Fahy and P. Gardonio, *Sound and Structural Vibration*, 2nd ed. Academic Press, 2007, ch. 3, pp. 135–241. DOI: 10.1016/B978-012373633-8/50007-7.
- [211] S. Lee, “Review: The use of equivalent source method in computational acoustics”, *Journal of Computational Acoustics*, vol. 25, no. 1, 2017. DOI: 10.1142/S0218396X16300012.
- [212] A. D. Pierce, *Acoustics: An Introduction to Its Physical Principles and Applications*, 3rd ed. Springer International Publishing, 2019, pp. 1–60. DOI: 10.1007/978-3-030-11214-1.
- [213] H.-P. Schwefel, *Numerical Optimization of Computer Models*, 1st ed. John Wiley & Sons, Inc., 1981.

- [214] D. B. Fogel, “Artificial intelligence through simulated evolution”, in *Evolutionary Computation: The Fossil Record*. IEEE, 1998, pp. 227–296. DOI: 10.1109/9780470544600.ch7.
- [215] T. Bäck, *Evolutionary Algorithms in Theory and Practice: Evolution Strategies, Evolutionary Programming, Genetic Algorithms*, 1st ed. Oxford University Press, Inc., 1996.
- [216] C. Darwin, *On the Origin of Species by Means of Natural Selection, or the Preservation of Favored Races in the Struggle for Life*. Murray, 1859.
- [217] M. Mitchell, *An introduction to genetic algorithms*, 1st ed. MIT press, 1996, pp. 1–221.
- [218] L. M. Rios and N. V. Sahinidis, “Derivative-free optimization: A review of algorithms and comparison of software implementations”, *Journal of Global Optimization*, vol. 56, no. 3, pp. 1247–1293, 2013. DOI: 10.1007/s10898-012-9951-y.
- [219] R. T. Marler and J. S. Arora, “Survey of multi-objective optimization methods for engineering”, *Structural and Multidisciplinary Optimization*, vol. 26, no. 6, pp. 369–395, 2004. DOI: 10.1007/s00158-003-0368-6.
- [220] W. Hare, J. Nutini, and S. Tesfamariam, “A survey of non-gradient optimization methods in structural engineering”, *Advances in Engineering Software*, vol. 59, pp. 19–28, 2013. DOI: 10.1016/j.advengsoft.2013.03.001.
- [221] A. Chipperfield, P. Fleming, H. Pohlheim, and C. Fonseca, *Genetic Algorithm TOOLBOX for use with Matlab*, version 1.2, Automatic Control and Systems Engineering, University of Sheffield, 1994.
- [222] S. Boyd and L. Vandenberghe, *Convex Optimization*, 1st ed. Cambridge University Press, 2004, pp. 1–727.
- [223] D. E. Goldberg, *Genetic Algorithms in Search, Optimization, and Machine Learning*, 1st ed. Addison-Wesley Professional, 1989, pp. 1–432.

- [224] D. E. Goldberg and R. E. Smith, “Nonstationary function optimization using genetic algorithm with dominance and diploidy”, in *Proceedings of the Second International Conference on Genetic Algorithms on Genetic Algorithms and Their Application*, Cambridge, USA, 1987, pp. 59–68.
- [225] G. Pavai and T. V. Geetha, “New crossover operators using dominance and co-dominance principles for faster convergence of genetic algorithms”, *Soft Computing*, vol. 23, no. 11, pp. 3661–3686, 2019. DOI: 10.1007/s00500-018-3016-1.
- [226] K. A. De Jong, “An analysis of the behavior of a class of genetic adaptive systems.”, PhD thesis, 1975.
- [227] S. W. Mahfoud, “Crowding and preselection revisited”, in *Parallel Problem Solving From Nature*, North-Holland, 1992, pp. 27–36.
- [228] The MathWorks Inc. (2019). Global Optimization Toolbox, [Online]. Available: <https://es.mathworks.com/help/gads/> (visited on 03/18/2020).
- [229] J. T. Richardson, M. R. Palmer, G. E. Liepins, and M. R. Hilliard, “Some guidelines for genetic algorithms with penalty functions”, in *Proceedings of the 3rd International Conference on Genetic Algorithms*, San Francisco, CA, USA: Morgan Kaufmann Publishers Inc., 1989, pp. 191–197.
- [230] M. Gen and R. Cheng, “Survey of penalty techniques in genetic algorithms”, 1996, pp. 804–809.
- [231] B. Tessema and G. G. Yen, “An adaptive penalty formulation for constrained evolutionary optimization”, *IEEE Transactions on Systems, Man, and Cybernetics Part A: Systems and Humans*, vol. 39, no. 3, pp. 565–578, 2009. DOI: 10.1109/TSMCA.2009.2013333.
- [232] C. A. C. Coello, “Theoretical and numerical constraint-handling techniques used with evolutionary algorithms: A survey of the state of the art”, *Computer Methods in Applied Mechanics and Engineering*, vol. 191, no. 11-12, pp. 1245–1287, 2002. DOI: 10.1016/S0045-7825(01)00323-1.

- [233] J. C. Bean, “Genetic Algorithms and Random Keys for Sequencing and Optimization”, *ORSA Journal on Computing*, vol. 6, no. 2, pp. 154–160, 1994. DOI: 10.1287/ijoc.6.2.154.
- [234] Z. Michalewicz, *Genetic algorithms + data structures = evolution programs*, 2nd ed. Springer Science & Business Media, 2013. DOI: 10.1007/978-3-662-07418-3.
- [235] J. Paredis, “Coevolutionary computation”, *Artificial Life*, vol. 2, no. 4, pp. 355–375, 1995. DOI: 10.1162/artl.1995.2.4.355.
- [236] M. Shoenauer and S. Xanthakis, “Constrained GA optimization”, in *Proceedings of the 5th International Conference on Genetic Algorithms*, San Francisco, CA, USA: Morgan Kaufmann Publishers Inc., 1993, pp. 573–580.
- [237] UNE, “Railway applications. Wheelsets and bogies. Monobloc wheels. Technical approval procedure. Part 1: Forged and rolled wheels. UNE-EN-13979-1:2006”, Asociación Española de Normalización (UNE), Technical Standard, 2011.
- [238] J. Gutiérrez-Gil, X. Garcia-Andrés, J. Martínez-Casas, E. Nadal, and F. D. Denia, “Mitigation of railway wheel rolling noise by using advanced optimization techniques”, in *Proceedings of the 6th International Conference on Engineering Optimization (ENGOPT 2018)*, Lisboa, Portugal, 2018, pp. 1141–1153.
- [239] J. Gutiérrez-Gil, X. Garcia-Andrés, J. Martínez-Casas, E. Nadal, and F. D. Denia, “Reducción de ruido de rodadura en ruedas ferroviarias mediante técnicas avanzadas de optimización (In Spanish)”, in *Proceedings of the XXII Congreso Nacional de Ingeniería Mecánica (CNIM 2018)*, Madrid, Spain, 2018, pp. 626–636.
- [240] Ansys INC., *ANSYS elements reference*, version 11.0, Ansys INC., Canonsburg, USA, 2007.
- [241] Ansys INC., *ANSYS Mechanical APDL elements reference*, version 15.0, Ansys INC., Canonsburg, USA, 2013.

-
- [242] The MathWorks Inc. (2019). Partial Differential Equation Toolbox, [Online]. Available: <https://es.mathworks.com/help/pde/> (visited on 06/16/2020).
- [243] F. Irgens, *Continuum Mechanics*, 1st ed. Springer-Verlag Berlin Heidelberg, 2008. DOI: 10.1007/978-3-540-74298-2.
- [244] F. J. Fuenmayor, F. D. Denia, J. Albelda, and E. Giner, “H-adaptive refinement strategy for acoustic problems with a set of natural frequencies”, *Journal of Sound and Vibration*, vol. 255, no. 3, pp. 457–479, 2002. DOI: 10.1006/jsvi.2001.4165.
- [245] Ansys INC., *ANSYS Mechanical APDL theory reference*, version 15.0, Ansys INC., Canonsburg, USA, 2007.
- [246] L. L. Beranek, “Basic acoustical quantities: Levels and decibels”, in *Noise and Vibration Control Engineering*. John Wiley & Sons, Ltd, 2007, ch. 1, pp. 1–24. DOI: 10.1002/9780470172568.ch1.
- [247] J. Gutiérrez-Gil, X. Garcia-Andrés, J. Martínez-Casas, E. Nadal, and F. D. Denia, “A novel optimization technique for railway wheel rolling noise reduction”, in *Proceedings of the congress Mathematical Modelling in Engineering and Human Behaviour 2018*, València, Spain, 2018, pp. 79–84.
- [248] J. Gutiérrez-Gil, X. Garcia-Andrés, J. Martínez-Casas, E. Nadal, and F. D. Denia, “Mitigación del ruido de ruedas ferroviarias mediante un enfoque modal (In Spanish)”, in *Proceedings of the X Congreso de Métodos Numéricos en Ingeniería (CMN 2019)*, Guimarães, Portugal, 2019, pp. 155–160.
- [249] D. J. Thompson and C. J. C. Jones, “Brake and wheel design can cut train noise”, *Railway Gazette International*, vol. 159, no. 10, pp. 639–641, 2003.
- [250] X. Garcia-Andrés, J. Gutiérrez-Gil, J. Martínez-Casas, and F. Denia, “Sound power minimization of a railway wheel by means of a modal-based geometric optimization technique”, in *Proceedings of 48th International Congress and Exhibition on Noise Control Engineering (Inter-noise 2019)*, Madrid, Spain, 2019.

- [251] UNE, “Railway applications. Track. Rail. Part 1: Vignole railway rails 46 kg/m and above. UNE-EN 13674-1:2012+A1”, Asociación Española de Normalización (UNE), Technical Standard, 2018.

List of Publications

Some relevant contributions related to the present PhD Thesis are listed below:

1. International journals (JCR)

- I. X. Garcia-Andrés, J. Gutiérrez-Gil, J. Martínez-Casas and F. D. Denia, “Wheel shape optimization approaches to reduce railway rolling noise”, *Structural and Multidisciplinary Optimization*, 2020.
DOI: 10.1007/s00158-020-02700-6.
- II. J. Gutiérrez-Gil, X. Garcia-Andrés, J. Martínez-Casas, E. Nadal and F. D. Denia, “Optimized perforation schemes in railway wheels toward acoustic radiation mitigation”, *Journal of Vibration and Acoustics*, vol. 142, no. 4, 2020.
DOI: 10.1115/1.4046681.

2. International congresses

- I. X. Garcia-Andrés, J. Gutiérrez-Gil, J. Martínez-Casas and F. D. Denia, “Sound power minimization of a railway wheel by means of a modal-based geometric optimization technique”, in *Proceedings of 48th International Congress and Exhibition on Noise Control Engineering (Internoise 2019)*, Madrid, Spain, 2019.

- II. J. Gutiérrez-Gil, X. Garcia-Andrés, J. Martínez-Casas E. Nadal and F. D. Denia, “A novel optimization technique for railway wheel rolling noise reduction”, in *Proceedings of the congress Mathematical Modelling in Engineering and Human Behaviour 2018*, València, Spain, 2018, pp. 79-84.
- III. J. Gutiérrez-Gil, X. Garcia-Andrés, J. Martínez-Casas E. Nadal, and F. D. Denia, “Mitigation of railway wheel rolling noise by using advanced optimization techniques”, in *Proceedings of the 6th International Conference on Engineering Optimization (ENGOPT 2018)*, Lisboa, Portugal, 2018, pp. 1141-1153.

3. National congresses

- I. J. Gutiérrez-Gil, X. Garcia-Andrés, J. Martínez-Casas and F. D. Denia, “Mitigación del ruido de ruedas ferroviarias mediante un enfoque modal (In Spanish)”, in *Proceedings of the X Congreso de Métodos Numéricos en Ingeniería (CMN 2019)*, Guimarães, Portugal, 2019, pp. 155-160.
- II. J. Gutiérrez-Gil, X. Garcia-Andrés, J. Martínez-Casas E. Nadal, and F. D. Denia, “Reducción de ruido de rodadura en ruedas ferroviarias mediante técnicas avanzadas de optimización (In Spanish)”, in *Proceedings of the XXII Congreso Nacional de Ingeniería Mecánica (CNIM 2018)*, Madrid, Spain, 2018, pp. 626-636.
- III. X. Garcia-Andrés, J. Martínez-Casas, F. D. Denia and L. Baeza, “Cálculo 3D de la potencia acústica radiada por una rueda ferroviaria a partir de la respuesta temporal con efectos giroscópicos y comportamiento no lineal (In Spanish)”, in *Proceedings of the Congreso de Métodos Numéricos en Ingeniería (CMN 2017)*, València, Spain, 2017, pp. 23-36.